Cloud Condensation Nuclei and Ice-Nucleating Particles Over Tropical and Subtropical Regions in the Northern Hemisphere

Der Fakultät für Physik und Geowissenschaften
der Universität Leipzig
eingereichte

D I S S E R T A T I O N

zur Erlangung des Akademischen Grades

Doktor der Meteorologie
Dr. rer. nat.

vorgelegt von

M. Sc. Xianda Gong

geboren am April 01, 1990 in Shandong, China

UNIVERSITÄT
LEIPZIG

TROPOS
Leibniz Institute for
Tropospheric Research

Leipzig, den 22 June 2020

Xianda Gong
Cloud Condensation Nuclei and Ice-Nucleating Particles Over Tropical and Subtropical Regions in the Northern Hemisphere
Leibniz Institute for Tropospheric Research
Experimental Aerosol and Cloud Microphysics
Promoserstr. 15
04103 Leipzig

This work was supervised by Prof. Dr. Andreas Macke

Bibliographic description

Cloud Condensation Nuclei and Ice-Nucleating Particles Over Tropical and Subtropical Regions in the Northern Hemisphere

Gong, Xianda
Leipzig University, Dissertation
149 pages, 95 references, 9 figures, 1 tables, 5 appendices

Abstract A change in atmospheric aerosol particles, especially cloud condensation nuclei (CCN) and ice-nucleating particles (INPs), is bound to impact cloud properties, precipitation and cloud radiative effects.
In this thesis, two field campaigns were carried out in two representative locations, i.e. the anthropogenic polluted environment at Cyprus and the marine-dust intersect environment at Cabo Verde (a.k.a. Cape Verde) to understand the role of CCN and INPs over the tropical and subtropical regions in the northern hemisphere. On-line aerosol physical measurements were performed and samples from different environmental compartments were examined with respect to INPs: the oceanic sea surface microlayer (SML), underlying water (ULW), cloud water and atmospheric filters.
Both measurement sites differ in aerosol properties, such as particle number size distribution, CCN and INP concentrations and CCN-derived particle hygroscopicity, due to different environment backgrounds and air mass origins.
Aerosol particles at Cyprus were dominated by anthropogenic pollution, with small contributions of sea spray aerosol (SSA) and mineral dust. Particle aging process were observed through changes in CCN-derived particle hygroscopicity. New particle formation events with subsequent growth of the particles into the CCN size range were observed. INPs mainly originated from long-range transport. And anthropogenic pollution were found to be inefficient INPs at temperature range > -25 °C. However, aerosol particles at Cabo Verde featured a marine background with intrusions of dust. Dust and marine aerosols featured clearly different PNSDs. CCN number concentration at a supersaturation of 0.30% during the strongest observed dust periods was about 2.5 times higher than during marine periods. However, the CCN-derived hygroscopicity for marine and dust periods shows no significant difference. INPs at Cabo Verde were mainly in the supermicron size range, with a large contribution of biological particles. When comparing atmospheric INP number concentration to those found in seawater, it can be concluded that SSA only contributed a minor fraction to the atmospheric INP population.

Bibliographische Beschreibung

Wolkenkondensationskerne und eisnukleierende Partikel über den Tropen und subtropischen Regionen der nördlichen Hemisphäre

Gong, Xianda
Universität Leipzig, Dissertation
149 Seiten, 95 Literaturzitate, 9 Abbildungen, 1 Tabellen, 5 Anlagen

Referat Veränderungen im atmosphärischen Aerosol, speziell bei Wolkenkondensationskernen (CCN) und eisnukleierenden Partikeln (INPs), haben Auswirkungen auf Wolkeneigenschaften wie Niederschlagsbildung und Strahlung.
Für die hier vorgelegte Arbeit wurden zwei Feldmesskampagnen durchgeführt, im anthropogen verschmutzten Zypern und auf Cabo Verde (alias Kap Verde), einer Schnittstelle zwischen Meer und Wüste. Ziel war es, die Rolle von CCN und INPs in den tropischen und subtropischen Regionen der nördlichen Hemisphäre besser zu verstehen. Es wurden aerosol-physikalische online Messungen durchgeführt und verschiedene Proben auf INPs hin untersucht: die Meeresoberflächen-Mikroschicht (SML), das darunter liegende Wasser (ULW), das Wolkenwasser und atmosphärische Filter.
Die beiden verschiedenen Orte an denen die Messkampagnen stattfanden unterscheiden sich in den Aerosoleigenschaften wie z.B. Partikelanzahlgrößenverteilung (PNSD), CCN- und INP-Konzentration und der von CCN abgeleiteten Partikelhygroskopizität. Grund hierfür sind Unterschiede in der Umgebung und der Luftmassenherkunft.
Die Aerosolpartikel auf Zypern wurden von anthropogener Verschmutzung dominiert, mit kleinen Beiträgen von Partikeln aus Meeres-Gischt (SSA) und Mineralstaub. Partikelalterung ging einher mit einer Veränderung der Hygroskopizität der CCN. Partikelneubildung wurde beobachtet, mit anschließendem Wachstum der Partikel bis in den CCN-Größenbereich. INPs stammen hauptsächlich aus Ferntransport, und Partikel aus anthropogener Verschmutzung waren ineffiziente INPs im Temperaturbereich > -25 °C.
Das Aerosol in Cabo Verde speiste sich sowohl aus marinen Quellen als auch aus Wüstenstaub. Staub und marines Aerosol wiesen sehr verschiedene PNSDs auf. Die CCN-Anzahlkonzentration bei 0,30% Übersättigung war während der stärksten Staubperioden etwa 2,5 Mal höher als während der marinen Perioden. Die aus CCN abgeleitete Hygroskopizität zeigte jedoch keinen signifikanten Unterschied für marine und Staubperioden. Die INPs in Cabo Verde waren zum Großteil größer als ein Mikrometer, und waren zum Großteil biogenen Ursprungs. Aus dem Vergleich der atmosphärischen INP-Anzahlkonzentration mit der im Meerwasser gefundenen kann man schließen, dass SSA nur einen geringen Anteil zur atmosphärischen INP-Population beitrug.

Acknowledgement

Firstly, I would like to express my sincere gratitude to my advisers, Dr. Heike Wex and Dr. Frank Stratmann, for their continuous support of my Ph.D. study and related research, for their encouragement, patience and dedication. I greatly appreciate all of their contributions of time, ideas, and funding to make my Ph.D. experience so productive. There is no way I could have a better adviser and mentor for my PhD study.

I would also like to thank my committee members: Prof. Dr. Alfred Wiedensohler, Prof. Dr. Andreas Macke and Prof. Dr. Johannes Quaas, for their insightful comments and suggestions, as well as challenges which motivated me to broaden my research from various perspectives.

I will also extend my thank you to Dr. Manuela van Pinxteren, Dr. Khanneh Wadinga Fomba, Dr. Silvia Henning, Prof. Dr. Konrad Kandler, Dr. Kristina Höhler, Dr. Thomas Müller and Nadja Triesch for our wonderful partnership. Without their precious support it would be impossible to conduct the research.

The members of the Cloud group have greatly helped me both personally and professionally. The group has been a source of friendship as well as good advice and collaboration. I would like to give special call out to Thomas Conrath. We co-worked closely to make many filed measurements and laboratory experiments successful. It is always a pleasure to work with 'wolkis'. It is their kind help, thoughtful discussions and passion for life that made my past three years memorable.

I have harvested valuable friendship during my time at TROPOS. They are always valuable assets to my life– Lin, Johannes, Jiangyue, Jacob, Ying and Jia. I also thank my friends from Helmholtz Centre for Environmental Research (UFZ) for generously offering me support and joy when I needed.

It has been 10 years since I left my family to pursue my dream. I cannot make it without my family's love and encouragement. My deepest gratitude to my parents and brother who raised me with a love of science and support me in all my pursuits.

Lastly, I would like to thank my girlfriend for her support and love. I can not thank you enough for encouraging me throughout my PhD. In the past few years, we did not have many opportunities to spend time together. But we overcome all the difficult. I look forward to our wonderful life in the future.

Thank you!

Abbreviation

A-LIFE	**A**bsorbing Aerosol Layers in a Changing Climate: Aging, **Life**time and Dynamics
APS	Aerodynamic Particle Sizer
CCN	Cloud Condensation Nuclei
CCNC	Cloud Condensation Nuclei Counter
CFDC	Continuous-Flow Diffusion Chamber
CVAO	Cape Verde Atmospheric Observatory
d_{crit}	Critical Diameter
DMA	Differential Mobility Analyzer
EF	Enrichment Factor
f_{ice}	Frozen Fraction
INPs	Ice-Nucleating Particles
INDA	Ice Nucleation Droplet Array
INSEKT	Ice Nucleation SpEctrometer of the Karlsruhe Institute of Technology
LINA	Leipzig Ice Nucleation Array
MCS	Monte Carlo Simulation
MarParCloud	**Mar**ine Biological Production, Organic Aerosol **Par**ticles and Marine **Cloud**s: a Process Chain
MBL	Marine Boundary Layer
MPSS	Mobility Particle Size Spectrometer
MV	Monte Verde Station
N_{CCN}	Cloud Condensation Nuclei Number Concentration
N_{INP}	Ice-Nucleating Particle Number Concentration
NPF	New Particle Formation
n_{s}	Active Surface Site Density
N_{total}	Total Particle Number Concentration
OS	Ocean Station
PASD	Particle Surface Area Size Distribution
PDF	Probability Density Function
PNC	Particle Number Concentration
PNSD	Particle Number Size Distribution
RH	Relative Humidity

SML	Sea Surface Microlayer
SSA	Sea Spray Aerosol
STP	Standard Temperature and Pressure, 0 °C and 1013.25 hPa
TROPOS	Leibniz Institute for Tropospheric Research
ULW	Underlying Water

Contents

1 Introduction **1**

2 Methodology **5**

2.1 Particle Size and Cloud Condensation Nuclei 5

2.1.1 Measurement Setup 5

2.1.2 Particle Number Size Distribution 6

2.1.3 Cloud Condensation Nuclei 8

2.1.4 Particle Hygroscopicity 9

2.1.5 Measurement Uncertainty 10

2.2 Ice-Nucleating Particles 12

2.2.1 Sample Collection 12

2.2.2 Freezing Devices 15

2.2.3 Deriving N_{INP} 18

2.2.4 Ice Active Surface Site Density 20

3 Results and Discussion **21**

3.1 First Publication:
Characterization of Aerosol Properties at Cyprus, Focusing on Cloud Condensation Nuclei and Ice-Nucleating Particles 22

3.2 Second Publication:
Characterization of aerosol particles at Cabo Verde close to sea level and at the cloud level – Part 1: Particle number size distribution, cloud condensation nuclei and their origins 57

3.3 Third Publication:
Characterization of aerosol particles at Cabo Verde close to sea level and at the cloud level – Part 2: Ice-nucleating particles in air, cloud and seawater 89

4 Summary and Conclusions **127**

5 Outlook **131**

A Appendix **133**

A.1 Paper Included in This Doctoral Thesis and Author's Contribution . . 133

A.2 Co-authorship Publication During PhD 134

A.3 Conference Abstracts as Lead Author 136
A.4 PhD Commission 136
A.5 Supervisor Committee 137

Bibliography **139**

1 Introduction

One of the most interesting features of Earth are the ever-changing clouds. Clouds have an enormous influence on Earth's energy balance, climate, and weather. Aerosol particles, clouds and their interactions in the climate system contribute to the largest uncertainties in estimating the Earth's energy budget [1].

Clouds in the atmosphere form when water vapor condenses on aerosol particles that serve as cloud condensation nuclei (CCN). Back in the 1970s, Twomey [2] described that an increase in the number of aerosol particles that activate to cloud droplets lead to more but smaller droplets. Albrecht [3] suggested that smaller droplets then cause suppression in the formation of precipitation, leading to a prolonged cloud lifetime. Both of these effects enhance the shortwave reflection of clouds, i.e., they lead to a cooling of the atmosphere. In particular, warm low-level clouds located in the boundary layer significantly contribute to the cooling effects due to their abundance and strong cloud albedo effect [4].

Ice crystals in the atmosphere can be formed either via homogeneous nucleation below -38 °C or via heterogeneous nucleation aided by aerosol particles known as ice-nucleating particles (INPs) at any temperatures below 0 °C. Immersion freezing refers to the process when an INP becomes immersed in an aqueous solution e.g., through the process of cloud droplet activation [5]. Immersion freezing is suggested to be the most important freezing process for mixed phase clouds [6, 7].

The impact of aerosol particles on clouds, climate and global radiative forcing is mainly determined by their physical and chemical properties. The abundance, properties and sources of aerosol particles depend on location. Important constituents of the atmospheric aerosol, are e.g., dust, marine and anthropogenic particles. In the following, previous studies of dust, marine aerosol and anthropogenic aerosol particles and their contributions to CCN and INPs are shortly summarized.

Mineral dust from deserts contributes largely to tropospheric aerosols and impacts air quality of several regions and even of the globe [8, 9, 10]. Mineral dust aerosol in the atmosphere can affect the Earth's radiative budget by directly scattering and absorbing solar and infrared radiation [11, 12]. On the other hand, it can modify cloud properties, i.e., contribute as CCN or INPs [13, 14]. Karydis et al. [15] found that the predicted annual average contribution of insoluble mineral dust to CCN

number concentration (N_{CCN}) in cloud forming areas was up to 40% over North Africa and Asia (Arabian Peninsula and Gobi Desert).

Submicron dust particles were recognized as effective INPs below -20 °C [16] and super-micron dust particles were reported to be ice active even up to -10 °C [17, 18]. Laboratory studies on natural mineral dusts from different regions have been conducted to quantify the particle's ability to nucleate ice [19, 20]. Mineral dust particles from deserts are composed of a variety of minerals, and K-feldspar is supposed to be more active for ice nucleation than other minerals in the mixed-phase cloud temperature regime [21, 16, 22]. Boose et al. [23] found that ice activity of desert dust particles at temperatures between -35 and -28 °C can be attributed to the sum of the feldspar and quartz content.

Due to the vast coverage of the Earth's surface by the oceans, wind-driven particle production on the ocean surface is one of the largest global sources of primary atmospheric particle mass [24, 25]. Ambient measurements and laboratory studies indicated that the resulting marine aerosol with less than 10 μm diameter can have a trimodal size distribution, which suggests that several mechanisms are involved in marine aerosol production [26, 27]. Besides, ocean physics, biology, and chemistry ultimately control both particle hygroscopicity [28] and the number of particles that can act as CCN and INPs [29, 30, 31] in the marine aerosol. Together with newly formed particles originating from gaseous precursors which can also be emitted from the ocean, this sea spray aerosol (SSA) contributes to marine aerosols. On a global basis, SSA makes a contribution of less than 30% to the CCN number concentration [32].

Ocean water can be a potential source of INPs [33]. The source of INPs in ocean water might be associated with phytoplankton blooms [34]. Recently, Wilson et al. [30] and Irish et al. [35] found that organic material, with a diameter <0.2 μm, is the major ice nucleator in the sea surface microlayer (SML). DeMott et al. [31] found that the ice nucleation activity from laboratory generated SSA aligned well with measurements from diverse regions over the oceans. Furthermore, a connection between marine biological activity and INP number concentration (N_{INP}) was uncovered in their laboratory study [31]. In pristine marine conditions, such as the Southern Ocean, SSA was the main source of the INP population, but N_{INP} was relatively low in the Southern Ocean as well as in the clean marine Northeast Atlantic [36, 37]. These field measurements are consistent with the model work by Burrows et al. [38], which emphasizes the importance of SSA contribution to INPs in remote marine regions.

Regarding anthropogenic sources of aerosol particles, central Europe was identified as the major source of black carbon over the eastern Mediterranean [39]. In the Po

Valley, due to the comparable climatic conditions, Sandrini et al. [40] found that particles in the size range from 50 to 140 nm were mainly from traffic emissions. The photochemical oxidation of inorganic and organic gaseous precursors was identified as the important mechanism of secondary aerosol formation, which caused the accumulation mode (420-1200 nm) aerosol particles to be constituted mainly of ammonium nitrate, organic carbon and sulfate. In-situ observations of CCN on Crete were reported by Kalivitis et al. [41], highlighting new particle formation (NPF) as a source of CCN. At Finokalia, Crete, Bougiatioti et al. [42] found that air masses originating from central eastern Europe tend to be associated with higher N_{CCN}, and slightly lower hygroscopicity ($\kappa = 0.18$), than other air masses.

The INPs produced in urban regions have rarely been the focus of previous studies. Knopf et al. [43] studied the heterogeneous ice nucleation activity of predominantly organic (or coated with organic material) anthropogenic particles sampled within and around the polluted environment of Mexico City and found that anthropogenic particles dominated by organics can act as sufficient INPs under conditions relevant for cirrus cloud formation. Based on Continuous-Flow Diffusion Chamber (CFDC) and single particle mass spectrometer analysis, Corbin et al. [44] suggested that dust particles, biomass burning particles and particles containing elemental carbon might be sources of INPs in Toronto. Chen et al. [45] found that aerosol in Beijing did not contain higher N_{INP} during strong pollution events, compared with clean phases. N_{INP} might not be influenced directly by anthropogenic activities, at least not down to roughly -25 °C.

In order to understand the role of cloud CCN and INPs over the tropical and sub-tropical regions in the northern hemisphere, two field campaigns were carried out in two representative locations, i.e., the anthropogenic polluted environment at Cyprus and the marine-dust intersect environment at Cabo Verde.

Cyprus, an island located in the eastern Mediterranean region, is approximately 100 km south of the Turkish mainland, 100 km west of the Syrian coast, and 300 km north of the Egyptian coast. This geographical location makes Cyprus an unique spot in the eastern Mediterranean Sea, where a variety of aerosols (traffic emission, secondary biogenic, sea spray and mineral dust aerosols) from both continental and marine sources is present [46, 47, 48].

The first campaign took place in the framework of A-LIFE (**A**bsorbing aerosol layers in a changing climate: aging, **life**time and dynamics) project. The measurements were performed from 2 to 30 of April 2017, on the island of Cyprus, which had the purpose to investigate properties of absorbing aerosols during their atmospheric lifetime, and their distribution throughout the tropospheric column. As part of the A-LIFE campaign, ground-based measurements were carried out in Paphos, Cyprus,

to characterize the abundance, properties and sources of aerosol particles in general, CCN and INP in particular.

Cabo Verde is surrounded by the Atlantic Ocean and close to the largest dust sources (the Sahara and Sahel region) in the world. Significant seasonal intrusions of dust from the North West Africa affect Cabo Verde at surface level from usually October till March. An hourly PM_{10} value reached up to 710 μg m^{-3} at surface level at Cabo Verde [49]. Marine is the second important aerosol source at Cabo Verde when looking at particle mass [50, 51]. There is always a background of marine aerosol present at Cabo Verde [52].

The second campaign took place in the framework of the MarParCloud (**Mar**ine biological production, organic aerosol **par**ticles and marine **cloud**s: a process chain) project. The measurements were carried out on São Vicente island in Cabo Verde from 13 September to 13 October, 2017. The aim of this project was to investigate the entire process chain of biological production of organic matter in the oceans, the export of organic matter to marine aerosol particles and finally their abilities to act as CCN and INPs. As part of the MarParCloud campaign, a thorough characterization of the abundance, properties, and sources of aerosol particles, CCN and INPs close to both sea and cloud level heights with measurements was done at the Cape Verde Atmospheric Observatory (CVAO) and on the top of Monte Verde (MV), respectively. Furthermore, we collected samples from different environmental compartments: namely, the oceanic sea surface microlayer (SML), underlying water (ULW), cloud water and the atmospheric filter samples close to both sea and cloud level and measured INP number concentration (N_{INP}) with off-line freezing devices in our lab.

At the end of this introduction, I will give a brief overview on the content of the following chapters. In Chapter 2, all of the experimental methods will be explained in detail. Chapter 3.1, 3.2 and 3.3 form the cumulative part of the dissertation in that they consist of three publications, Gong et al. [53], Gong et al. [54] and Gong et al. [55]. In the end, the summary of the most important results as well as conclusions are given in Chapter 4 and an outlook is given in Chapter 5.

2 Methodology

In this chapter, all of the experimental methods will be explained in detail. There are three main topics, i.e., (1) Particle number concentration (PNC) and particle number size distribution (PNSD); (2) CCN number concentration (N_{CCN}) and particle hygroscopicity; (3) INP number concentration (N_{INP}) in different environmental compartments (sea surface microlayer (SML), underlying sea water (ULW), cloud water and ambient air).

2.1 Particle Size and Cloud Condensation Nuclei

2.1.1 Measurement Setup

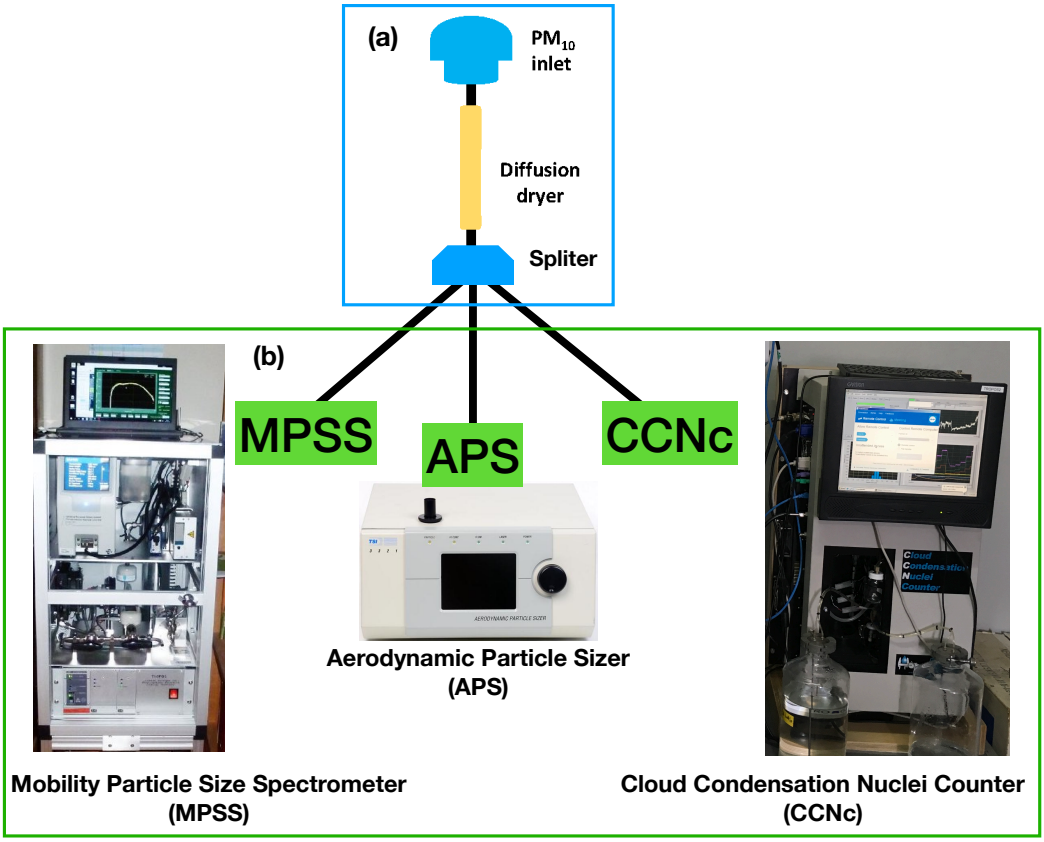

Fig. 2.1.: Schematic of the measurement system, including (a) sampling inlet and (b) on-line instruments TROPOS-type mobility particle size spectrometer (MPSS), aerodynamic particle sizer (APS) and cloud condensation cuclei counter (CCNC).

The instrumental setup used for particle size and cloud condensation nuclei measurements is shown in Fig. 2.1. An aerosol PM_{10} inlet, employed to remove particles larger than 10 μm in aerodynamic diameter, was installed on top of a measurement container. Downstream of the PM_{10} inlet, a vertical tube (inner diameter of 1.65 cm) and a diffusion dryer (130 cm) were arranged before the aerosol was led into the measurement container. The diffusion dryer was installed vertically to avoid gravitational losses of larger particles. Downstream of the dryer, the sampled aerosol was split to supply the aerosol to various instruments, including TROPOS-type mobility particle size spectrometer (MPSS), aerodynamic particle sizer (APS, model 3321, TSI Inc., St. Paul, MN, USA). and could condensation nuclei counter (CCNC, Droplet Measurement Technologies (DMT), Boulder, USA).

2.1.2 Particle Number Size Distribution

PNSDs were measured in the size range from 10 nm to 10 μm using a TROPOS-type MPSS and an APS.

Mobility Particle Size Spectrometer The TROPOS-type MPSS consists of a sequential setup of a bipolar diffusion charger (or traditionally named neutralizer), a DMA, and a CPC. First, the ambient aerosol sample flow has to be dried and a bipolar charge equilibrium is established using a bipolar diffusion charger. Second, the charged aerosol particles are fed into the DMA and then merged with the particle-free sheath air flow. In the DMA, charged particles are separated according to their electrical mobility. In the last step, the separated aerosol particle number concentration downstream of the DMA is measured by means of a CPC. Ramping or stepping the voltage yields an electrical particle mobility distribution. Fig. 2.2 shows the schematic of the TROPOS-type MPSS. The details of the TROPOS-type MPSS are described in Wiedensohler et al. [56].

Aerodynamic Particle Sizer The APS model 3321 is a time-of-flight spectrometer that measures the velocity of particles in an accelerating air flow through a nozzle. First, particles are confined to the center-line of an accelerating flow by sheath air. They then pass through two broadly focused laser beams, scattering light as they do so. Side-scattered light is collected by an elliptical mirror that focuses the collected light onto a solid-state photo-detector, which converts the light pulses to electrical pulses. From the time delay between the two pulses, the velocity can be calculated for each individual particle. Fig. 2.3 shows the schematic of the TSI APS model 3321.

Combined Particle number Size Distribution The electrical mobility distribution is converted to a size distribution by applying an inversion algorithm. The size

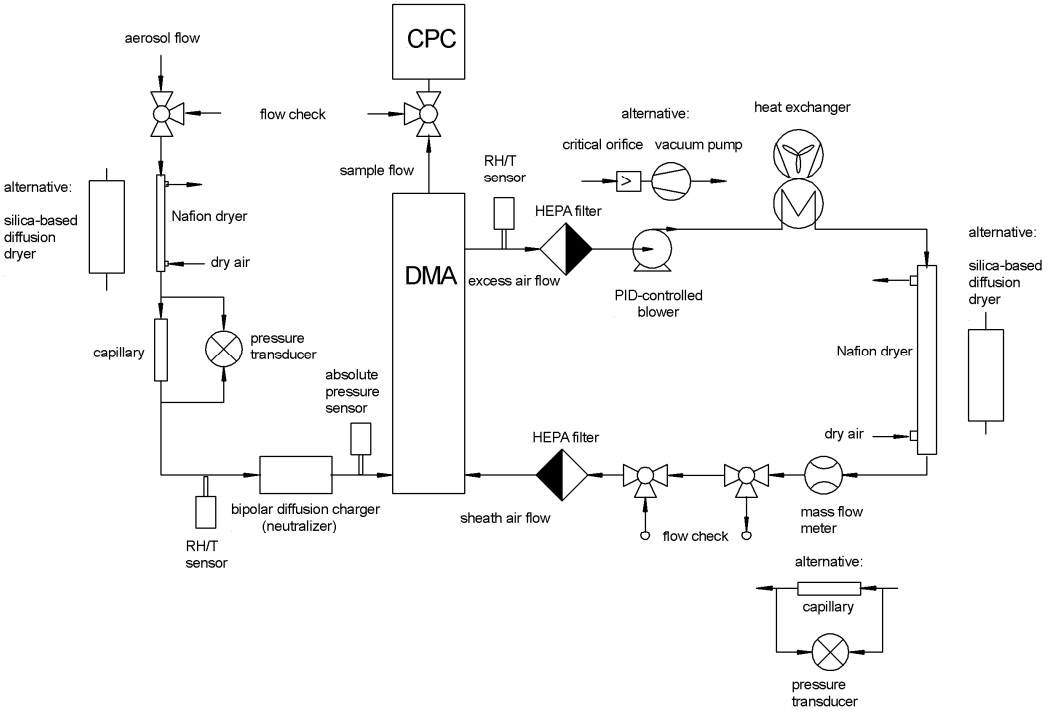

Fig. 2.2.: Schematic sketch of the TROPOS-type MPSS. MPSS consists of a sequential setup of a bipolar diffusion charger (neutralizer), a DMA, and a CPC, with some auxiliary flow and temperature controller and filters. This picture is taken from Wiedensohler et al. [56].

distribution is thereby corrected for multiply charged aerosol particles [58]. In this study, for the multiple charge correction of the MPSS data, the APS data was accounted for in the inversion of the measured PNSD [59]. The dry dynamic shape factor (χ) of mineral dust is $\chi = 1.25$ [60] for 1 μm particles, whereas the dynamic shape factor for sodium chloride is $\chi = 1.08$ [61, 62]. The average shape factor of 1.17 was used in this study. The dry density of Saharan dust particles was determined in a range of ρ = 2450-2700 kg m^{-3} [63]. The dry particle density of sodium chloride is known to be ρ = 2160 kg m^{-3}. The overall effective density of the dust and sea-salt fraction is approximately 2, as recommend in Schladitz et al. [64].

The combined PNSD is then given on the basis of the volume equivalent particle diameter. Size-dependent particle losses due to diffusion, deposition and sedimentation within the sampling inlet (between PM_{10} cutter and instruments) were corrected for utilizing the empirical particle loss calculator [65]. Total particle number concentrations (N_{total}) were calculated from the measured PNSDs and the size-dependent particle losses. The calibration of the MPSS before, during and after the intensive field study was done following the recommendations given in Wiedensohler et al. [66].

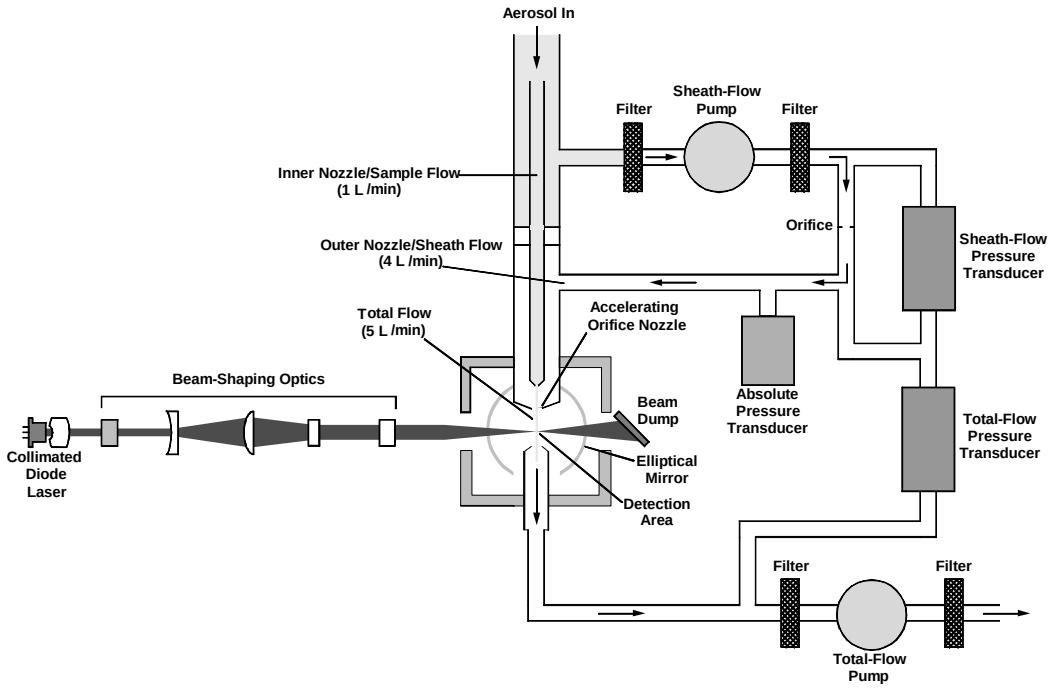

Fig. 2.3.: Schematic sketch of the TSI APS model 3321. APS mainly contains nozzles and a optics chamber, with some auxiliary flow and temperature controller and filters. The picture is taken from the TSI APS model 3321 instruction manual [57].

Based on these PNSDs, the particle surface area size distributions (PASDs) and the concentrations for the total surface area of particles were derived. This will be used for ice active surface site density (n_S) calculation.

2.1.3 Cloud Condensation Nuclei

N_{CCN} was measured using a CCNC. Fig. 2.4(a) shows the schematic of DMT CCNC. The main part of the CCNC is a 50 cm long cylindrical continuous flow thermal-gradient diffusion chamber, as shown in Fig. 2.4(b). In the diffusion chamber, a constant streamwise temperature gradient is established to adjust a quasi constant centerline supersaturation. The sampled aerosol particles are guided within a sheath flow through this chamber and can become activated into droplets, depending on the supersaturation and the particles' ability to act as CCN. The details of the CCNC are described in Roberts and Nenes [67].

During our study, the supersaturation was varied from $\sim$0.08 % to $\sim$0.77 % at a constant total flow rate of 0.5 L min^{-1}. To assure stable column temperatures, the first 5 minutes and the last 30 seconds of the 12-minute long measurement at each supersaturation, were excluded from the data analysis. The remaining data points were averaged. A supersaturation calibration (following the protocol by Gysel and Stratmann [69]) was done at the cloud laboratory of the Leibniz Institute for

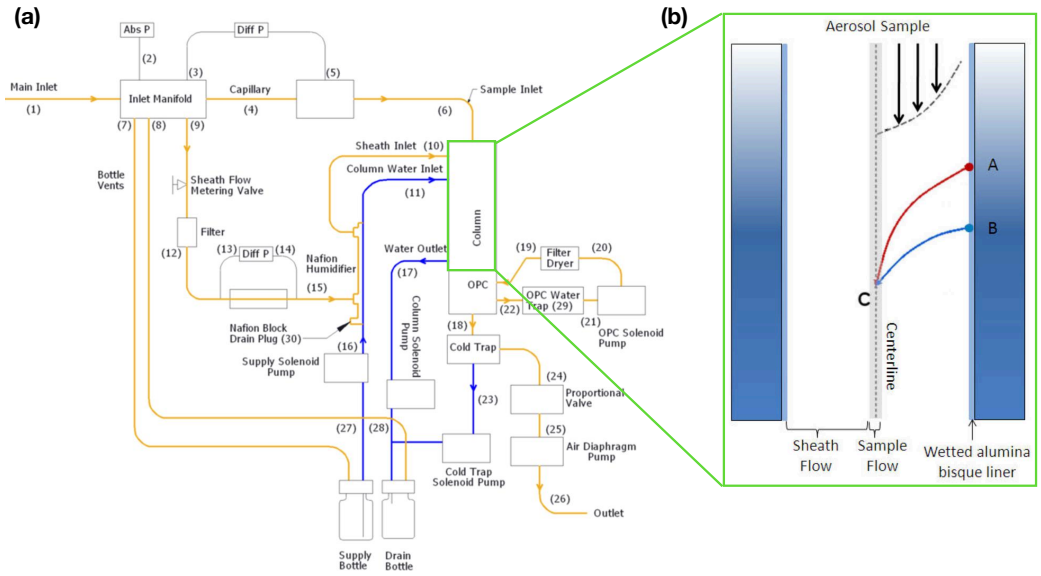

Fig. 2.4.: (a) Schematic sketch of the DMT CCNC and (b) the main part of CCNC, i.e., cylindrical continuous-flow thermal-gradient diffusion chamber. The picture is taken from DMT CCNC manual [68].

Tropospheric Research (TROPOS) prior to and after the measurement campaign, to determine the relationship between the temperature gradient along the column and the effective supersaturation.

2.1.4 Particle Hygroscopicity

According to Köhler theory [70], whether or not a particle can act as a CCN depends on its dry size, chemical composition and the maximum supersaturation it encounters. Petters and Kreidenweis [71] presented a method to describe the water activity term in the Köhler equation by utilizing the hygroscopicity parameter κ.

The κ values reported in this study were calculated as follows, assuming the surface tension of the examined solution droplets $\sigma_{s/\alpha}$ to be that of pure water:

$$\kappa = \frac{4A^3}{27 d_{\text{crit}}^3 \ln^2 S} \tag{2.1}$$

with

$$A = \frac{4\sigma_{s/\alpha} M_w}{RT\rho_w} \tag{2.2}$$

where d_{crit} is the critical diameter above which all particles activate into cloud droplets for a given saturation. S is the saturation ratio. M_w and ρ_w are the molar mass and density of water, while R and T are the ideal gas constant and the absolute temperature, respectively.

To derive d_{crit}, simultaneously measured N_{CCN} and PNSD are used. Thereto, it is assumed that all particles in the neighborhood of a given particle diameter have a similar κ, meaning that the aerosol particles are internally mixed. At a given supersaturation, a particle can be activated to a droplet once its dry size is equal to or larger than d_{crit}. Therefore, d_{crit} is the diameter at which N_{CCN} is equal to the value of cumulative particle number concentration, determined via integration from the upper towards the lower end of the PNSD. Fig. 2.5 shows the connection between the PNSD, a corresponding N_{CCN} and the resulting d_{crit}.

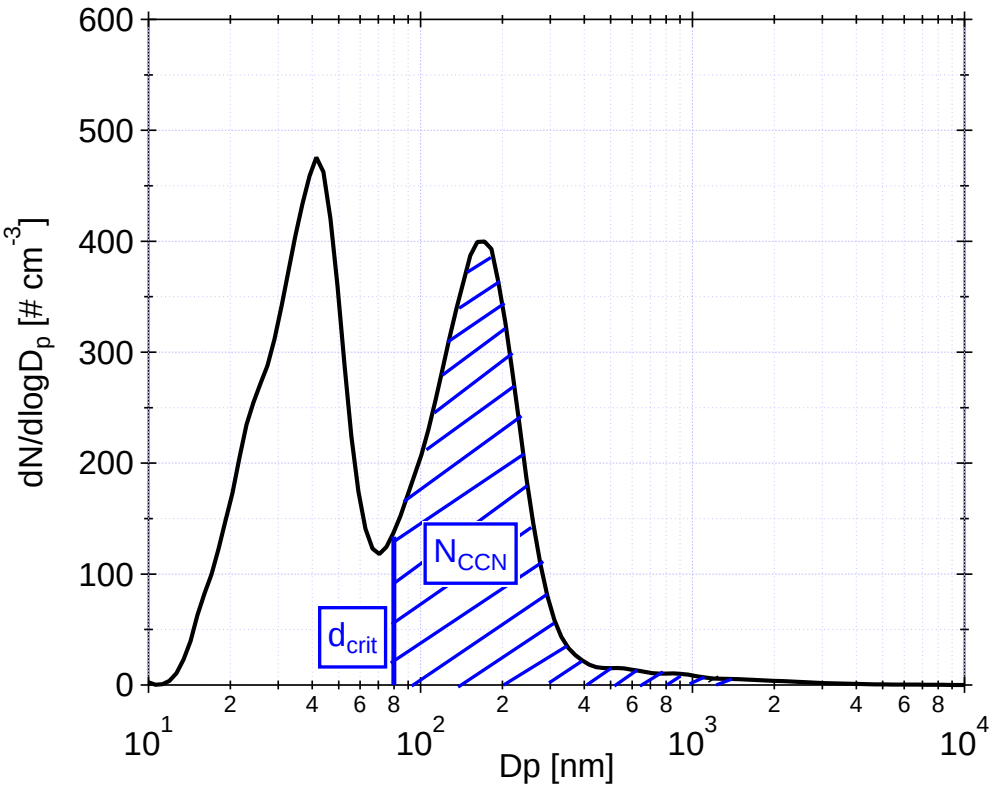

Fig. 2.5.: The connection between the PNSD, a corresponding N_{CCN} and the resulting d_{crit}. The critical diameter d_{crit} is determined by the integration of a PNSD starting from the largest diameter til it is equal to the value of a simultaneous measured N_{CCN}.

Hygroscopicity κ can be calculated with d_{crit} and the corresponding supersaturation, based on Eq.2.1. The inferred κ values correspond to particles with sizes of roughly d_{crit}.

2.1.5 Measurement Uncertainty

The uncertainty in κ, which results from uncertainties of the PNSD measurements and the supersaturations of the CCNC, was determined by applying a Monte Carlo simulation (MCS) in a similar fashion as done by Kristensen et al. [72] and Herenz et al. [73].

Based on results from laboratory calibrations and year-long application of the instruments, we assume the following uncertainties. The particle diameter which is selected with a DMA has an uncertainty of 3.0% (corresponding to one standard deviation). The measured particle number concentration has an uncertainty of 5.0% (corresponding to one standard deviation). In addition, the effective supersaturation in CCNC has a relative uncertainty of 3.5% (corresponding to one standard deviation) for supersaturation above 0.20%. Below a supersaturation of 0.20%, the same absolute uncertainty as for a supersaturation of 0.20% can be assumed. To consider the impact of these uncertainties on d_{crit} and κ in a realistic way, a MCS based on random normal distributions was used. This following general equation was applied:

$$s_{\text{MC}} = s + s * u * p \tag{2.3}$$

where u is the relative uncertainty, p is a normally distributed random number with a mean of 0, s is the measured signal and s_{MC} is the resulting MCS signal. This was done for 10 000 random numbers p, which then results in 10 000 values for s_{MC} with a variability that is characterized by u.

Firstly, the uncertainty in d_{crit} was obtained by a MCS based on one exemplary PNSD, the related N_{CCN} and a 5.0% uncertainty in the particle number concentration. Eq. 2.3 was used to vary the particle number concentration of each size bin of the PNSD to calculate 10 000 d_{crit} values, of which a distribution is shown in Fig. 2.6(a). The mean and 1 standard deviation of these 10 000 d_{crit} values can be taken from this distribution, and the overall uncertainty in d_{crit} was derived from those values together with the 3.0% uncertainty in the particle sizing due to the DMA, using error propagation. This was then done for all PNSDs.

Secondly, the effective supersaturation of the CCNC are 10 000 times Monte Carlo simulated (same procedure as for d_{crit}). Since the connection between κ and supersaturation is logarithmic, the resulting distribution of the 10 000 κ values is a log-normal distribution, as can be seen in Fig. 2.6(b) for one exemplary case. This was done for one specific measurement. Consequently, our final inferred κ and its uncertainty are the geometric mean and the one standard geometric standard deviation of this distribution, respectively.

Lastly, d_{crit} and κ uncertainties over the whole campaign were calculated. Combining all d_{crit} values in a certain period, the total d_{crit} distribution was derived. In this case, we took all of the d_{crit} at a supersaturation of 0.50% during the whole MarParCloud campaign. The mean value and one standard deviation of d_{crit} can be taken from this distribution. Using the same way, the distribution of κ values was

derived. The geometric mean value and one geometric standard deviation of κ can be taken from this distribution.

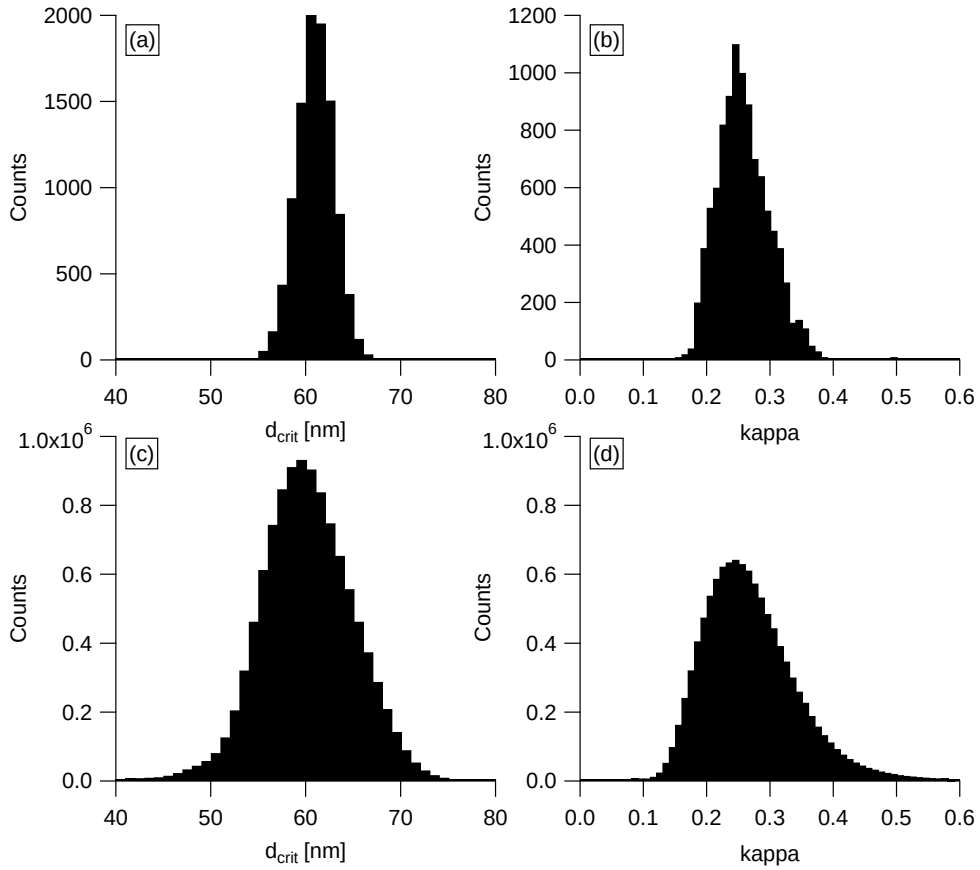

Fig. 2.6.: (a) Distribution of 10 000 d_{crit} values after applying the MCS. (b) Distribution of 10 000 κ values after applying the MCS. (c) Distribution of d_{crit} values during the whole MarParCloud campaign. (d) Distribution of κ values during the whole MarParCloud campaign.

Note that the particle losses inside the CCNC (discussed in Rose et al. [74]) are also considered before κ is calculated.

2.2 Ice-Nucleating Particles

2.2.1 Sample Collection

For A-LIFE campaign, only airborne samples were collected. For MarParCloud campaign, samples collected for INP analysis include: sea surface microlayer (SML) and underlying water (ULW) from the ocean wind of the island; filter samples of atmospheric aerosol; as well as cloud water collected during cloud events. Fig. 2.7 summarizes the sample collection strategy and corresponding sampling techniques during MarParCloud campaign.

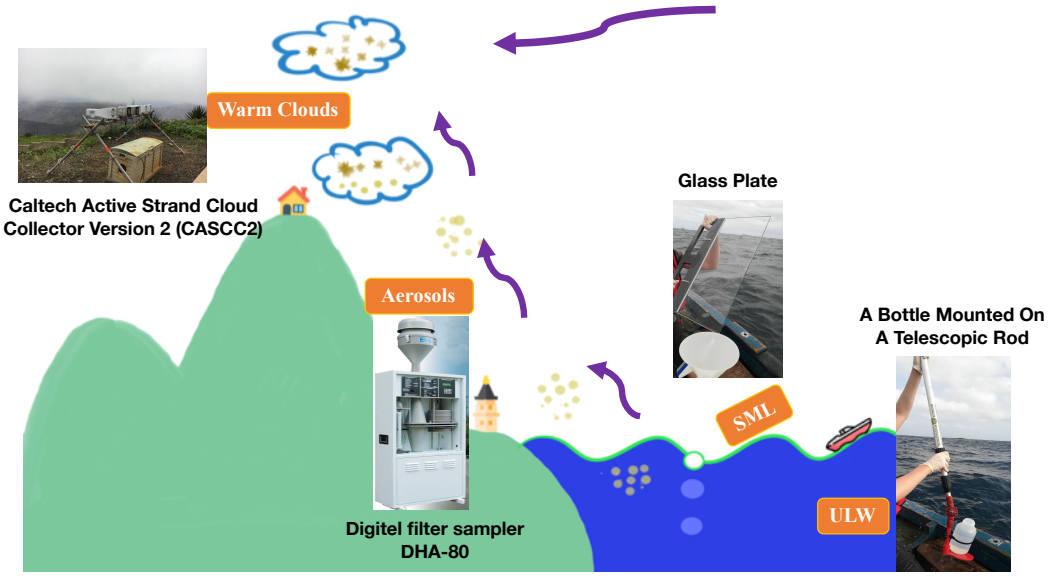

Fig. 2.7.: Schematic diagram of the sample collection strategy during MarParCloud campaign, including the sample collection of SML, ULW, filters of atmospheric aerosol and cloud water, and the corresponding sampling techniques.

Seawater Sampling

Seawater samples were taken by using of a fishing boat with a distance of at least 5 km from the coastal (off-shore samples). The SML samples were collected using a glass plate sampler [75, 35, 76]. The glass plate had a surface area of 2000 cm^{-2} and was immersed vertically into the ocean and then withdrawn at a slow rate (between 5 and 10 cm s^{-1}) allowed to drain for less than 5 s. The surface film adhered to the surface of the glass was scraped off from both sides of the glass plate with a framed Teflon wiper into a 1 Liter glass bottle. For each SML sample, approximately 1 Liter was collected, requiring ∼55 dips. Based on the amount of material collected, the number of dips and the area of the plate, the averaged thickness of the layer collected was calculated as ∼91.0 μm. ULW samples were collected at the same times and locations as the SML samples. ULW was collected from a depth of 1 m by a glass bottle mounted on a telescopic rod in order to monitor sampling depth. The bottle was opened underwater at the intended sampling depth with a specifically designed seal-opener.

Aerosol Particle Sampling

a. Polycarbonate filter The polycarbonate filters were deployed during the A-LIFE campaign in Cyprus. We used two setups to sample airborne particles for further analysis.

With the first setup, particles were collected on 200 nm pore size polycarbonate filters (Nuclepore Track-Etch Membrane, Whatman) with ∼20 hours time resolution and a flow rate of ∼10 L min^{-1}. We used a computer-based system to switch between filters based on wind directions. Two sectors were distinguished, i.e., the ocean sector comprising wind directions from 120 to 240 degree, and the land sector, covering the remaining directions. Blind filters were obtained by inserting the filters into the sampler for a period of 24 hours without loading them.

For the second filter-based sampling system, 200 nm pore size polycarbonate filters (Nuclepore Track-Etch Membrane, Whatman) were pre-treated with 10% H_2O_2 solution, washed with particle free ultrapure water and dried prior to insertion into the filter holder. Daily filter samples with an air flow rate of ∼15 L min^{-1} for ∼8 hours were taken. Blind filters were obtained by inserting the filters into the sampler for a period of 24 hours without loading them.

b. Quartz fiber filter The quartz fiber filters were deployed during the MarPar-Cloud campaign at Cabo Verde.

Particle sampling was done using a high-volume sampler with PM_{10}-inlet and PM_1-inlet (Digitel filter sampler DHA-80, Walter Riemer Messtechnik, Germany) that operated with an average flow rate of ∼500 L min^{-1} in a 24 hours sampling period. The high-volume samples were collected on 150 mm quartz fiber filters (Munktell, MK 360) with an effective sampling area of 140 mm in diameter. The filters were preheated in our laboratory at 110 °C for 24 hours to minimize the organic carbon background content. Blind filters were obtained by inserting the filters into the sampler for a period of 24 hours without loading them.

Cloud Water Sampling

Cloud water were collected with CASCC2 (Caltech Active Strand Cloud Collector Version 2). All cloud drops sizes are collected into one bulk sample. Drops are collected by inertial impaction on Teflon strands with a diameter of 508 μm. The 50% lower size cut for the CASCC2 is approximately 3.5 μm diameter. The flow rate through the CASCC2 was approximately 5.8 m^3 min^{-1}. The CASCC2 is described in more details in Demoz et al. [77]. Between cloud events, the cloud water sampler was cleaned with a large amount (∼5 L) of ultrapure water. Once the collector was cleaned, a blank was taken by spraying about 200 mL of ultrapure water into the collection strands in the collector.

Storage and Shipment

After sampling, the water and filter samples were stored in a freezer (−20 °C). The long-term storage and transportation of the collected samples from the measurement location to Leibniz Institute for Tropospheric Research (TROPOS), Germany was always carried out in aluminum boxes at −20 °C. At TROPOS, all samples were stored at −20 °C until they were prepared for the measurement.

2.2.2 Freezing Devices

Two droplet freezing devices called LINA (Leipzig Ice Nucleation Array) and INDA (Ice Nucleation Droplet Array) have been set up at TROPOS. An droplet freezing device called INSEKT (SpEctrometer of the Karlsruhe Institute of Technology) designed at KIT was used to compare the INP measurement with LINA.

LINA

The design of LINA was inspired by Budke and Koop [78]. A picture of LINA setup is shown in Fig. 2.8(a). Briefly, 90 droplets with the volume of 1 μL each were pipetted from the samples onto a thin hydrophobic glass slide, with the droplets being separated from each other inside individual compartment. The compartments were sealed at the top with another glass slide, to prevent the droplets from evaporation and ice seeding from neighboring droplets. The droplets were cooled on a Peltier element with a cooling rate of 1 K min^{-1} down to −35 °C. Once the cooling process started, pictures were taken every 6 secs by a camera corresponding a resolution of 0.1 K. An exemplary image is shown in Fig. 2.8(b). The number of frozen versus unfrozen droplets was derived automatically by an image identification program written in Python. More detailed parameters and temperature calibration of LINA and its application can be found in previous studies [45, 53].

In this study, LINA was used to measure seawater, cloud water and polycarbonate filter. The water samples can be directly measured by LINA. As for polycarbonate filters, each filter was immersed into 1 mL ultrapure water (Type 1, Millipore) and shaken for 25 minutes to wash off the particles. The resulting water samples were analyzed with LINA.

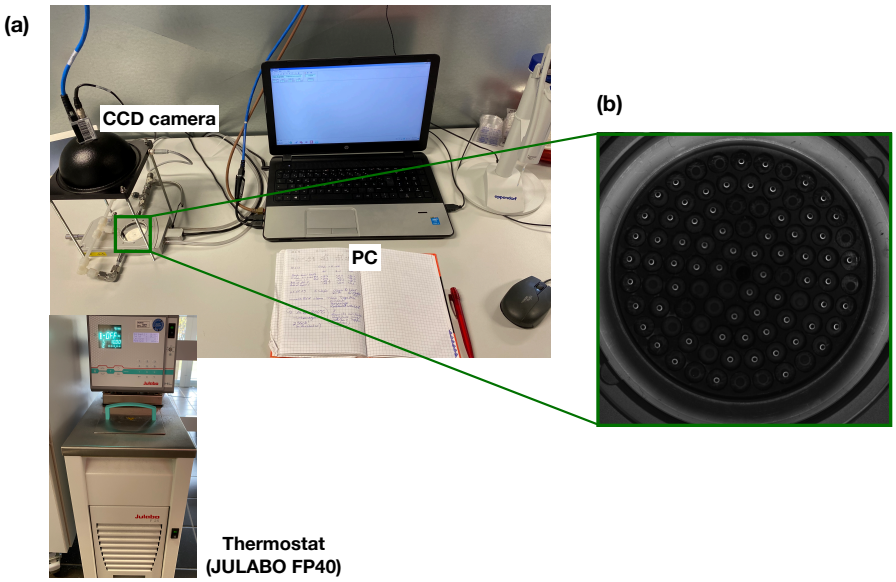

Fig. 2.8.: (a) Picture of LINA setup. (b) Image recording of a droplet freeze assay.

INDA

The design of INDA was inspired by Conen et al. [79], but deploying PCR-trays instead of separate tubes [80]. A picture of INDA is shown in Fig. 2.9(a). For quartz fiber filters, circular pieces with a diameter of 1 mm were punched out. Each of the 96 wells of a PCR-tray was filled with one filter piece together with 50 μL of ultrapure water. For SML, ULW and cloud water samples, 50 μL of the water samples were filled in each PCR-tray. After being sealed by a transparent foil, the PCR-tray was placed on a sample holder and immersed into a bath thermostat. The bath thermostat then decreases temperature with a cooling rate of approximately 1 K min^{-1}. Real-time images of the PCR-tray were recorded every 6 secs by a CCD (charge-coupled device) camera. A LED light was fixed to the bottom of the cooling bath to ensure contrast between frozen and unfrozen droplets on the recorded photos. Frozen droplets could be identified according to the brightness change during the freezing process. An exemplary image recording is shown in Fig. 2.9(b). A program recorded the current temperature of the cooling bath and related it to the real-time images from the CCD camera. The temperature in the PCR-trays had been calibrated. More detailed parameters and temperature calibration of INDA and its application can be found in previous studies [45, 81].

INSEKT

INSEKT is a droplet freezing device, the design of which was inspired by the Colorado State University Ice Spectrometer [82]. For the analysis, each filter (polycarbonate

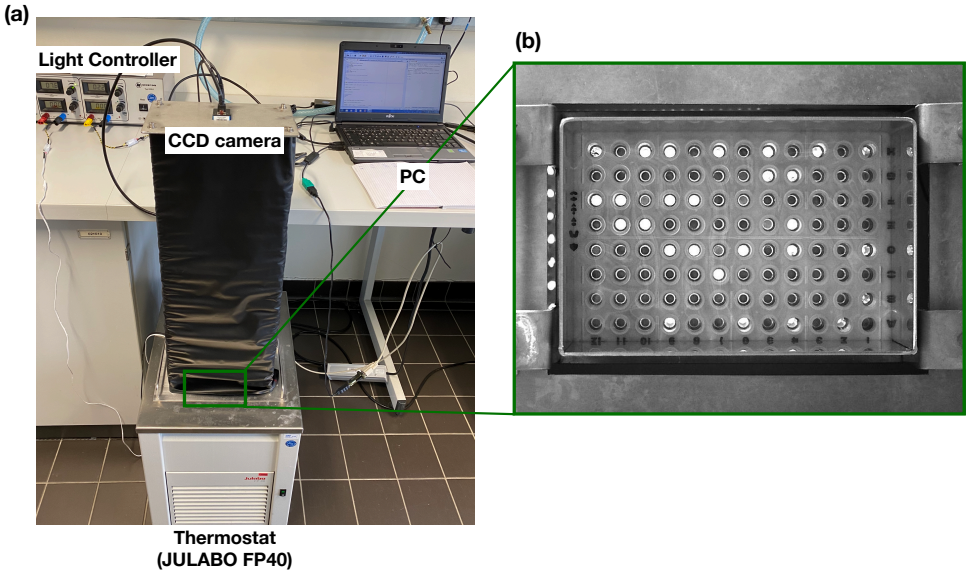

Fig. 2.9.: (a) Picture of INDA setup. (b) Image recording of a PCR tray.

filters from A-LIFE campaign in Cyprus) was washed with 8 mL ultrapure water, which had been passed through a 0.1 μm filter (Nuclepore Track-Etch Membrane, Whatman). 50 μL samples of the resulting suspension/solution were pipetted into 24 to 36 sections of two 96-well PCR trays. Other wells of the trays were filled with 15- and 225-fold (and for some samples also 3375-fold) dilutions of the filter washing water. Also, in each experiment at least 24 wells were filled with pure and particle free water, to be able to account for impurities resulting from the washing water and PCR tray surfaces. The PCR trays were then placed into aluminum cooling blocks. Those blocks have been customized by drilling channels into the bulk aluminum, through which the cooling agent thermostated by means of an external chiller (LAUDA PROLINE RP 855) is directed. The temperature of the cooling agent is then lowered by 0.33 K min^{-1} and monitored by eight calibrated temperature sensors inserted into the aluminum blocks. The number of frozen versus unfrozen wells was derived visually in 0.5 K steps.

A summary of sample types, treatment methods, instrumentation and sampling locations can be found in Tab. 2.1

Tab. 2.1.: Sample type, treatment method, instrumentation and sample location.

Sample type	Treatment	Instrumentation	Location
Polycarbonate filters	1 mL ultrapure water wash	LINA	Cyprus
Polycarbonate filters	8 mL ultrapure water wash	INSEKT	Cyprus
Quartz fiber filters	punched to 50 μL ultrapure water	INDA	Cabo Verde
SML	-	LINA, INDA	Cabo Verde
ULW	-	LINA, INDA	Cabo Verde
Cloud water	-	LINA, INDA	Cabo Verde

2.2.3 Deriving N_{INP}

Basic calculation

Based on Vali [83], the cumulative concentration of INP (N_{INP}) per air volume or water volume as a function of temperature can be calculated by:

$$N_{\mathrm{INP}}(\theta) = \frac{-\ln(1 - f_{\mathrm{ice}}(\theta))}{V} \tag{2.4}$$

with

$$f_{\mathrm{ice}}(\theta) = \frac{N(\theta)}{N_{\mathrm{total}}} \tag{2.5}$$

where N_{total} is the number of droplets and N(θ) is the number of frozen droplets at the temperature of θ.

Eq. 2.4 accounts for the possibility of the presence of multiple INPs in one vial by assuming that INPs are Poisson distributed. This way, the cumulative number of INP active at any temperature is obtained although only the most ice active INP (nucleating ice at the highest temperature) present in each droplet/well is observed. As for the SML, ULW and cloud water, V means the volume of droplet/well (V_{LINA}=1 μL, V_{INDA}=50 μL). As for the polycarbonate filters and quartz fiber filters, V means the volume of air distributed in each droplet/well. INDA features larger sample volumes. Assuming similar INP concentrations in each droplet/well, the larger volume implies a higher probability of INP being present in the sample, and consequently INP featuring the lower detection limit, and being more suitable for investigating warm temperature INP.

Uncertainty

Because the number (order of tens and lower per examined droplet/well) of INPs present in the washing water is usually small, and the number of droplets/wells considered in our measurements is limited, statical errors need to be considered in the data evaluation. Previous studies [36, 84] used the method suggested by Agresti and Coull [85] to calculate the freezing devices measurement uncertainties. Following this approach, the confidence intervals for the f_{ice} can be calculated by:

$$\left(f_{\mathrm{ice}} + \frac{z_{a/2}^2}{2n} \pm z_{a/2}\sqrt{[f_{\mathrm{ice}}(1 - f_{\mathrm{ice}}) + z_{a/2}^2/(4n)]/n}\right) / \left(1 + z_{a/2}^2/n\right) \tag{2.6}$$

where n is the droplet/well number. $z_{a/2}$ is the standard score at a confidence level $a/2$, which for a 95% confidence interval is 1.96.

Background

For filter samples, the background freezing signal of water samples resulting from punching/washing of blind filters is determined. Subtraction of the background was done by converting f_{ice} to concentrations of INPs per volume of droplet/well. N_{INP} from the field blanks was then subtracted from that of the filter samples, and the result was converted to background corrected atmospheric INP number concentrations. Ultimately this procedure can be summarized as:

$$N_{\text{INP,corr}} = \left(-ln(1 - f_{\text{ice,s}}) + ln(1 - f_{\text{ice,b}})\right) / V \tag{2.7}$$

The corrected atmospheric INP number concentration is $N_{\text{INP,corr}}$, the frozen fractions measured for the filter samples and the field blanks are $f_{\text{ice,s}}$ and $f_{\text{ice,b}}$, respectively. In this thesis, we always show the corrected INP number concentrations. Note that for those samples that were already collected in a liquid state (ULW, SML and cloud water), a background correction was not done.

Salinity Correction of SML and ULW

N_{INP} in SML and ULW were adjusted to account for the freezing depression caused by dissolved salts in sea water. First, based on Kreidenweis et al. [86], the water activity can be calculated by:

$$a_{\text{W}} = \frac{n_{\text{water}}}{n_{\text{water}} + i * n_{\text{solute}}} \tag{2.8}$$

where the n_{solute} and n_{water} are the number of moles of solute and water in solution, respectively. i is the van't Hoff factor [87]. We assumed the sea salt is mainly sodium chloride. The van't Hoff factor is 2. Once we get the a_{W}, the freezing depression temperature as a function of a_{W} can be found in Koop and Zobrist [88]. In our study, this was roughly a correction by 2.2 °C.

2.2.4 Ice Active Surface Site Density

The ice nucleating properties of aerosol particles may be characterized by their ice active surface site density (n_S) [19]. The n_S is a measure of how well an aerosol acts as a seed surface for ice nucleation. n_S can be calculated as:

$$n_S = \frac{N_{INP}(\theta)}{A} \tag{2.9}$$

Where A is the particle surface area concentration.

For cases where a single type of aerosol, such as one type of mineral dust, is examined in laboratory studies, A can be the total particle surface area. However, when field experiments are done, using the total particle surface area of the atmospheric aerosol assumes that all particles contribute to INP and have the same n_S, while the vast majority of these particles will not even be an INP. On the other hand, singling out the contribution of separate INP types in the atmospheric aerosol and relying n_S only to them by using their contribution to the total surface area is at least demanding if not often impossible. This has to be kept in mind when interpreting heterogeneous ice nucleation in terms of n_S as done below.

3 Results and Discussion

This chapter is the cumulative part of the dissertation. The following publications are considered:

- Gong, X., Wex, H., Müller, T., Wiedensohler, A., Höhler, K., Kandler, K., Ma, N., Dietel, B., Schiebel, T., Möhler, O., and Stratmann, F.: Characterization of aerosol properties at Cyprus, focusing on cloud condensation nuclei and ice-nucleating particles, Atmos. Chem. Phys., 19, 10883–10900, https://doi.org/10.5194/acp-19-10883-2019, 2019.

- Gong, X., Wex, H., Voigtlälnder, J., Fomba, K. W., Weinhold, K., van Pinxteren, M., Henning, S., Mülller, T., Herrmann, H., and Stratmann, F.: Characterization of aerosol particles at Cabo Verde close to sea level and at the cloud level – Part 1: Particle number size distribution, cloud condensation nuclei and their origins , Atmos. Chem. Phys., 20, 1431–1449, https://doi.org/10.5194/acp-20-1431-2020, 2020.

- Gong, X., Wex, H., van Pinxteren, M., Triesch, N., Fomba, K. W., Lubitz, J., Stolle, C., Robinson, T.-B., Müller, T., Herrmann, H., and Stratmann, F.: Characterization of aerosol particles at Cabo Verde close to sea level and at the cloud level – Part 2: Ice-nucleating particles in air, cloud and seawater, Atmos. Chem. Phys., 20, 1451–1468, https://doi.org/10.5194/acp-20-1451-2020, 2020.

The first publication is in the framework of the A-LIFE project, which took place in April 2017 on the island of Cyprus to investigate the aerosols prevailing in the eastern Mediterranean region. Ground-based measurements were carried out in Paphos, Cyprus, to characterize the abundance, properties (size distribution, hygroscopicity, ice activity), and sources of aerosol particles in general, CCN and INPs in particular.

The second and third publications are in the framework of MarParCloud project, which took place in September and October 2017 on the São Vicente island in Cabo Verde. Part 1 compared aerosol properties measured close to sea level and at a mountaintop to examine the representativeness of ground based measurements to the marine boundary layer (MBL) and present a thorough characterization of CCN with respect to their hygroscopicity and number concentrations for different air masses. Part 2 focused on INP properties. Samples collected for INPs analysis

include: SML and ULW from the ocean upwind of the island; quartz fiber filter samples of atmospheric aerosol, collected on a tower installed at the island shore (inlet height: 42 m a.s.l) and on a mountaintop (inlet height: 746 m a.s.l); cloud water collected during cloud events on the mountaintop.

3.1 First Publication: Characterization of Aerosol Properties at Cyprus, Focusing on Cloud Condensation Nuclei and Ice-Nucleating Particles

The content of this section has already been published under the title "Characterization of aerosol properties at Cyprus, focusing on cloud condensation nuclei and ice-nucleating particles" by Gong, X., Wex, H., Müller, T., Wiedensohler, A., Höhler, K., Kandler, K., Ma, N., Dietel, B., Schiebel, T., Möhler, O., and Stratmann, F. In 2019, the paper was published under the Creative Commons Attribution 4.0 License in *Atmos. Chem. Phys.* with the doi: https://doi.org/10.5194/acp-19-10883-2019.

Reprinted with permission by the authors from *Atmos. Chem. Phys.*, 19, 10883–10900, 2019.

Atmos. Chem. Phys., 19, 10883–10900, 2019
https://doi.org/10.5194/acp-19-10883-2019

Atmospheric Chemistry and Physics
Open Access
EGU

Characterization of aerosol properties at Cyprus, focusing on cloud condensation nuclei and ice-nucleating particles

Xianda Gong[1], Heike Wex[1], Thomas Müller[1], Alfred Wiedensohler[1], Kristina Höhler[2], Konrad Kandler[3], Nan Ma[1], Barbara Dietel[2], Thea Schiebel[2], Ottmar Möhler[2], and Frank Stratmann[1]

[1]Experimental Aerosol and Cloud Microphysics Department, Leibniz Institute for Tropospheric Research, Leipzig, Germany
[2]Institute for Meteorology and Climate Research – Atmospheric Aerosol Research,
Karlsruhe Institute of Technology, Karlsruhe, Germany
[3]Institute for Applied Geosciences, Technical University Darmstadt, Darmstadt, Germany

Correspondence: Xianda Gong (gong@tropos.de)

Received: 28 February 2019 – Discussion started: 27 March 2019
Revised: 30 July 2019 – Accepted: 31 July 2019 – Published: 29 August 2019

Abstract. As part of the A-LIFE (Absorbing aerosol layers in a changing climate: aging, LIFEtime and dynamics) campaign, ground-based measurements were carried out in Paphos, Cyprus, to characterize the abundance, properties, and sources of aerosol particles in general and cloud condensation nuclei (CCN) and ice-nucleating particles (INP) in particular. New particle formation (NPF) events with subsequent growth of the particles into the CCN size range were observed. Aitken mode particles featured κ values of 0.21 to 0.29, indicating the presence of organic materials. Accumulation mode particles featured a higher hygroscopicity parameter, with a median κ value of 0.57, suggesting the presence of sulfate and maybe sea salt particles mixed with organic carbon. A clear downward trend of κ with increasing supersaturation and decreasing d_{crit} was found. Super-micron particles originated mainly from sea-spray aerosol (SSA) and partly from mineral dust.

INP concentrations (N_{INP}) were measured in the temperature range from -6.5 to $-26.5\,°C$, using two freezing array-type instruments. N_{INP} at a particular temperature span around 1 order of magnitude below $-20\,°C$ and about 2 orders of magnitude at warmer temperatures ($T > -18\,°C$). Few samples showed elevated concentrations at temperatures $> -15\,°C$, which suggests a significant contribution of biological particles to the INP population, which possibly could originate from Cyprus. Both measured temperature spectra and N_{INP} probability density functions (PDFs) indicate that the observed INP (ice active in the temperature range between -15 and $-20\,°C$) mainly originate from long-range transport. There was no correlation between N_{INP} and particle number concentration in the size range > 500 nm ($N_{>500\,nm}$). Parameterizations based on $N_{>500\,nm}$ were found to overestimate N_{INP} by about 1 to 2 orders of magnitude. There was also no correlation between N_{INP} and particle surface area concentration. The ice active surface site density (n_s) for the polluted aerosol encountered in the eastern Mediterranean in this study is about 1 to 3 orders of magnitude lower than the n_s found for dust aerosol particles in previous studies. This suggests that observed N_{INP} PDFs such as those derived here could be a better choice for modeling N_{INP} if the aerosol particle composition is unknown or uncertain.

1 Introduction

The Mediterranean region is one of the hotspot areas of the globe being severely threatened by climate change (Giorgi and Lionello, 2008), with the direct and indirect effects of aerosol particles therein still remaining unclear. The Mediterranean region is rich in a variety of aerosols (fuel combustion, biomass burning, secondary biogenic, sea spray, and mineral dust aerosols) from both continental and marine sources (Chester et al., 1993; Piazzola and Despiau, 1997; Lelieveld et al., 2002). The sensitivity of this region, together with the large number of influencing factors, makes it a difficult task to understand all ongoing processes and their interconnections. This, however, is needed in order to better

be able to protect the region or mitigate upcoming changes. Our goal in this framework is to better understand the varied aerosol that occurs in this region. In the next paragraphs, we will start by giving an overview of what is known about the Mediterranean aerosol.

Regarding anthropogenic sources of aerosol particles, Sciare et al. (2003) found that the major contributions in the eastern Mediterranean were from Turkey and central Europe. Central Europe was identified as the major source of black carbon over the eastern Mediterranean. In the Po Valley, which is in the western Mediterranean, but which we still consider here, due to the comparable climatic conditions, Sandrini et al. (2016) found that particles in the size range from 50 to 140 nm were mainly from traffic emissions. The photochemical oxidation of inorganic and organic gaseous precursors was identified as the important mechanism of secondary aerosol formation, which caused the accumulation mode (420–1200 nm) aerosol particles to be constituted mainly of ammonium nitrate, organic carbon, and sulfate. Bougiatioti et al. (2013) found that organic carbon and element carbon concentrations made up $2/3$ of the PM_1, with organic carbon being mostly secondary and therefore highly oxidized and water-soluble to a great extent.

Biomass burning is another important anthropogenic aerosol source over the Mediterranean, and it was mainly observed in the driest months of the year, July and August (Pace et al., 2005). Long-term observations of absorbing aerosol particles have clearly shown that they originated from agriculture waste burning (post-harvest wheat residual) in the countries surrounding the Black Sea (Sciare et al., 2008). Bougiatioti et al. (2016) examined in the eastern Mediterranean potential cloud condensation nuclei (CCN) and hygroscopicity properties and found that an increased organic content in the aerosol particles decreased the values of the hygroscopicity parameter κ for all particle sizes. Furthermore, they observed CCN concentrations (N_{CCN}) to be enhanced by a factor from 1.6 to 2.5 during biomass burning plumes compared to background conditions.

Natural aerosol particles such as mineral dust and sea salt are however the major contributing factors to particle mass in the Mediterranean (Rodríguez et al., 2002). Mineral dust particles from the Sahara Desert were regularly observed at different locations across the Mediterranean. A record-breaking dust storm originating from desert regions in northern Syria and Iraq occurred over the eastern Mediterranean in September 2015. The PM_{10} concentrations were close to $8000\,\mu g\,m^{-3}$ and the observed meteorological optical range (MOR) was reduced to 300–750 m (Mamouri et al., 2016). By using the Weather Research and Forecasting model in a Sahara outflow region, Smoydzin et al. (2012) found that the presence of mineral dust can enhance the CCN concentration and formation of ice crystals.

Sea-spray aerosols (SSA) are another main natural aerosol type observed in the Mediterranean. Claeys et al. (2017) found that primary marine aerosols mass concentration reached up to $6.5\,\mu g\,m^{-3}$, representing more than 40 % of the total PM_{10} mass in the western Mediterranean. Salameh et al. (2007) reported AOD around 0.15–0.20 (at 865 nm) within a SSA plume during strong wind events with wind speeds up to $18\,m\,s^{-1}$.

Clouds in the atmosphere form when water vapor condenses on aerosol particles that serve as CCN. Clouds in the atmosphere glaciate at temperatures above $-38\,°C$ if droplet freezing is initiated by aerosol particles called ice-nucleating particles (INP) or at temperatures below $-38\,°C$, also through homogeneous freezing (without INP) (Pruppacher and Klett, 2010). Therefore, a change in atmospheric aerosol particles, especially CCN and INP, is bound to impact cloud properties, precipitation, and cloud radiative effects (Fan et al., 2016). Even though clouds are omnipresent in the Earth's atmosphere, and play an important role in regulating the radiative budget of the planet, the response of clouds to climate change remains highly uncertain, in particular with regard to aerosol–cloud interactions and feedback mechanisms.

In situ observations of CCN on Crete were reported by Kalivitis et al. (2015), highlighting new particle formation (NPF) as a source of CCN. At Finokalia, Crete, Bougiatioti et al. (2011) found that air masses originating from central eastern Europe tend to be associated with higher N_{CCN}, and slightly lower hygroscopicity ($\kappa = 0.18$), than other air masses.

Rarely have measurements of INP been carried out in the Mediterranean. Excluding situations characterized by high-altitude transport of dust plumes, Rinaldi et al. (2017) found that at a measurement station in the Po Valley basin, INP number concentration (N_{INP}) was roughly double that of what they observed at the top of an Apennine mountain. Schrod et al. (2017) found that mineral dust, or a constituent related to dust, was a major contributor to INP on Cyprus. However, due to Sahara dust plumes travelling at several kilometers in altitude, N_{INP} at higher altitudes were 10 times higher than at ground level (height ~ 700 m).

As outlined above, the aerosol in the Mediterranean region represents a complex mixture of primary and secondary aerosol particles from both natural and anthropogenic sources, with these sources being non-uniformly distributed across the greater Mediterranean region. Most regional and global climate simulations have investigated impacts of global warming on the Mediterranean climate without detailed considerations of possible radiative influences and climatic feedback from different types of Mediterranean aerosols (Mallet et al., 2016). Besides, to the best of our knowledge, seldom have studies paid attention to the CCN and INP simultaneously, which both have an effect on climate. The aim of this study is to provide a quantitative understanding concerning the abundance, properties and source of CCN and INP in the eastern Mediterranean.

2 Experiment

2.1 Sampling site and campaign setup

Measurements were performed from 2 to 30 April 2017, on the island of Cyprus, as part of the A-LIFE (Absorbing aerosol layers in a changing climate: aging, LIFEtime and dynamics) project, which had the purpose of investigating properties of absorbing aerosols during their atmospheric lifetime, and their distribution throughout the tropospheric column. Cyprus, an island located in the eastern Mediterranean region, is approximately 100 km south of the Turkish mainland, 100 km west of the Syrian coast, and 300 km north of the Egyptian coast. This geographical location makes Cyprus an unique spot in the eastern Mediterranean Sea, where different and complex aerosol mixtures occur. On the one hand, the Sahara Desert in the southwest, and the desert of the Arabian Peninsula in the southeast favor a regular occurrence of mineral-dust-rich air masses. One the other hand, Cyprus is influenced by anthropogenic emissions from southeastern Europe, as well as the Middle East, and, of course, local pollution. This exposure to diverse air masses makes Cyprus an ideal place for investigating the abundance and properties of climate relevant aerosol particles in general, and CCN and INP in particular. As shown in Fig. 1, the measurement site was located in Paphos, Cyprus (34°43′ N, 32°29′ E). The measurements took place at the side of a fairly calm coastal highway, facing the Mediterranean Sea. On the northeastern side of the measurement site, 1 km away, is Paphos International Airport.

The instrumental setup used for these investigations is shown in Fig. S1 in the Supplement. An aerosol PM_{10} inlet, employed to remove particles larger than 10 µm in aerodynamic diameter, was installed on top of a measurement container. Downstream of the PM_{10} inlet, a vertical tube (inner diameter of 1.65 cm) and a diffusion dryer (130 cm) were arranged before the aerosol was led into the measurement container. The diffusion dryer was installed vertically to avoid gravitational losses of larger particles. Downstream of the dryer and inside the container, the sampled aerosol was split to supply the aerosol to various instruments, measuring particle number size distribution (PNSD), number concentration, as well as hygroscopic and optical (not discussed in this paper) properties.

For the measurement of N_{INP}, two different filter-based sampling systems were utilized. For one set of samples, total suspended particles were collected with a flow rate of $\sim 10\,L\,min^{-1}$. For a second set of samples, a separate PM_{10} inlet was used as the inlet, and an air flow of $\sim 15\,L\,min^{-1}$ was sampled onto the filters. No dryer was arranged in the filter sampling system.

The CCN hygroscopicity was derived from N_{CCN} combined with the PNSD. INP freezing behavior and N_{INP} were determined by filter sampling and off-line analysis using freezing array-type instruments. In the following, we will briefly introduce the different measurement techniques applied in this study, including calibrations, measurements, and data processing.

And lastly, to get additional information on the presence of super-micron particles, depositing aerosol particles were collected at ambient conditions outside of the measurement container.

2.2 Particle number size distribution

PNSDs were measured in the size range from 10 nm to 10 µm using a TROPOS-type MPSS (Mobility Particle Size Spectrometer) (Wiedensohler et al., 2012), and an APS (Aerodynamic Particle Sizer, model 3321, TSI Inc., St. Paul, MN, USA). For the multiple charge correction (Wiedensohler, 1988) of the MPSS data, the APS data were accounted for in the inversion of the measured PNSD (Pfeifer et al., 2016). The combined PNSD is then given on the basis of the volume-equivalent particle diameter, where a dynamic shape factor of 1.17 was used for particles > 1 µm, based on Schladitz et al. (2011). More details about the combined MPSS and APS PNSD can be found in Schladitz et al. (2011). Size-dependent particle losses due to diffusion, deposition, and sedimentation within the inlet were corrected for utilizing the empirical particle loss calculator (von der Weiden et al., 2009), as shown in Fig. S2. Total particle number concentrations (N_{total}) were calculated from the measured PNSDs and the size-dependent particle losses. The calibration of the MPSS before, during, and after the intensive field study was done following the recommendations given in Wiedensohler et al. (2018).

2.3 Cloud condensation nuclei

N_{CCN} was measured using a Cloud Condensation Nuclei counter (CCNc, Droplet Measurement Technologies (DMT), Boulder, USA). The CCNc is a cylindrical continuous-flow thermal-gradient diffusion chamber, establishing a constant streamwise temperature gradient to adjust a quasi-constant centerline supersaturation. The sampled aerosol particles are guided within a sheath flow through this chamber and can become activated into droplets, depending on the supersaturation and the particles' ability to act as CCN. The details of the CCNc are described in Roberts and Nenes (2005).

During our study, the supersaturation was varied from $\sim 0.08\,\%$ to $\sim 0.77\,\%$ at a constant total flow rate of $0.5\,L\,min^{-1}$. To ensure stable column temperatures, the first 5 min and the last 30 s of the 12 min long measurement at each supersaturation were excluded from the data analysis. The remaining data points were averaged. A supersaturation calibration (following the protocol by Gysel and Stratmann, 2013) was done at the cloud laboratory of the Leibniz Institute for Tropospheric Research (TROPOS) prior to and after the measurement campaign to determine the relationship between the temperature gradient along the column and the ef-

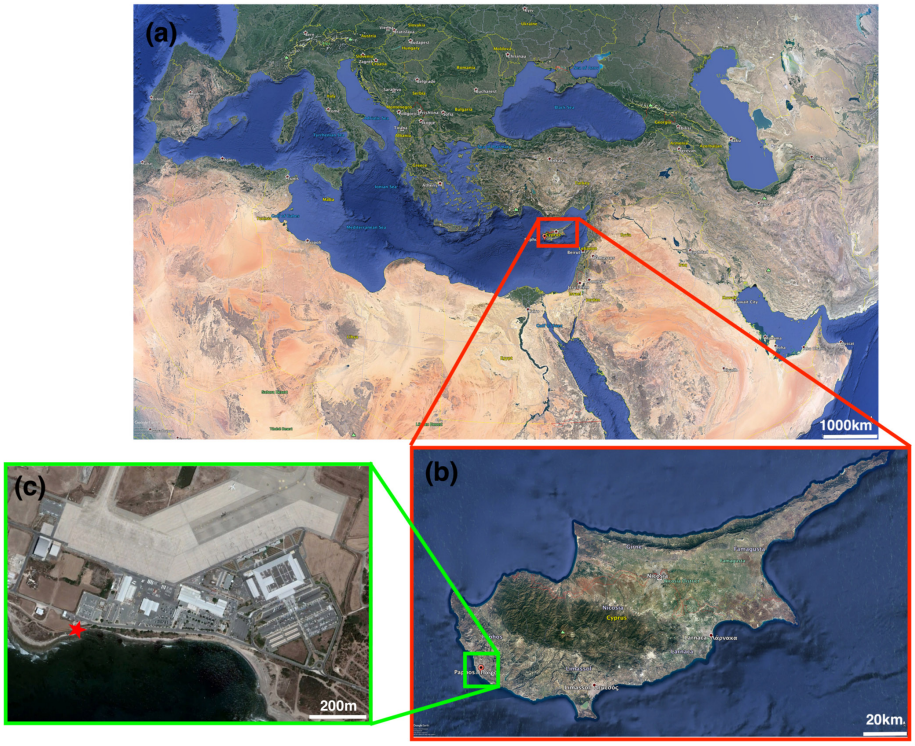

Figure 1. Maps of the Mediterranean region, Cyprus, and the sampling location. **(a)** Position of Cyprus in the Mediterranean region. **(b)** Position of Paphos in Cyprus. **(c)** The sampling site is displayed as a red star. Northeast of the sampling site is Paphos International Airport.

fective supersaturation. Calibrated supersaturation set points were 0.08 %, 0.19 %, 0.31 %, 0.54 %, and 0.77 %. These calibrated values were used for further calculations.

According to Köhler theory (Köhler, 1936), whether or not a particle can act as CCN depends on its dry size, chemical composition, and the maximum supersaturation it encounters. Petters and Kreidenweis (2007) presented a method to describe the water activity term in the Köhler equation by utilizing the hygroscopicity parameter κ. The κ values reported in this study were calculated as follows, assuming the surface tension of the examined solution droplets $\sigma_{s/\alpha}$ to be that of pure water:

$$\kappa = \frac{4A^3}{27 d_{\mathrm{crit}}^3 \ln^2 S}, \quad (1)$$

with

$$A = \frac{4\sigma_{s/\alpha} M_{\mathrm{w}}}{RT\rho_{\mathrm{w}}}, \quad (2)$$

where d_{crit} is the critical diameter above which all particles activate into cloud droplets for a given supersaturation. M_{w} and ρ_{w} are the molar mass and density of water, while R and T are the ideal gas constant and the absolute temperature, respectively. To derive d_{crit}, simultaneously measured N_{CCN} and PNSD are used. Thereto, it is assumed that all particles in the neighborhood of a given particle diameter have a similar κ, meaning that the aerosol particles are internally mixed. At a given supersaturation, a particle can be activated to a droplet once its dry size is equal to or larger than d_{crit}. Therefore, d_{crit} is the diameter at which N_{CCN} is equal to the value of cumulative particle number concentration, determined via integration from the upper towards the lower end of the PNSD. Hygroscopicity κ can be calculated with d_{crit} and the corresponding supersaturation, based on Eq. (1). Note that the particle losses inside the CCNc (discussed in Rose et al., 2008) are also considered before κ is calculated. More details about the correction method and data processing can be found in the previous literature (Kristensen et al., 2016; Herenz et al., 2018).

2.4 Ice-nucleating particles

We used two setups to sample airborne particles for further analysis. With the first setup, particles were collected on 200 nm pore size polycarbonate filters (Nuclepore Track-Etch Membrane, Whatman) with ∼ 20 h time resolution and a flow rate of ∼ 10 L min^{-1}. As shown in Fig. S1, we used a computer-based system to switch between filters based on wind directions. Two sectors were distinguished, i.e., the ocean sector comprising wind directions from 120 to 240° and the land sector covering the remaining directions. During the campaign, we collected 4 filters with air from the ocean sector, 17 from the land sector, and 2 blind filter samples

in total. All of the filters were stored at −18 °C on Cyprus and cooled below 0 °C during transportation. The start and end times of sampling, flow rates, duration, and total sample volumes are shown in Table S1 in the Supplement. These filters were transported to TROPOS for analysis. At TROPOS, all filters were stored at −18 °C until they were prepared for the measurement. Each filter was immersed into 1 mL ultrapure water (Type 1, Millipore) and shaken for 25 min to wash off the particles. The resulting water samples were characterized with the Leipzig Ice Nucleation Array (LINA). It should be mentioned that results from separate tests using 1 and 10 mL of washing water were well in agreement (see Fig. S3). LINA is based on the freezing array technique and follows the design described in Budke and Koop (2015). Briefly, 90 droplets with a volume of 1 µL are pipetted from the water samples onto a thin hydrophobic glass slide, with the droplets being separated from each other inside individual compartments. The compartments are sealed at the top with another glass slide to minimize evaporation of the droplets and to prevent ice seeding from neighboring droplets. The bottom glass slide is cooled with a Peltier element with a cooling rate of 1 K min^{-1}. A camera takes pictures every 6 s, corresponding to a temperature resolution of 0.1 K. The number of frozen versus unfrozen droplets was derived automatically. More details concerning the experimental parameters and temperature calibration of LINA can be found in Chen et al. (2018).

For the second filter-based sampling system, 200 nm pore size polycarbonate filters (Nuclepore Track-Etch Membrane, Whatman) were pre-treated with 10 % H_2O_2 solution, washed with particle free ultrapure water, and dried prior to insertion into the filter holder. Daily filter samples with an air flow rate of ∼ 15 L min^{-1} for ∼ 8 h were taken. In total 25 d time and two blind filter samples were collected. All of the filters were stored at −18 °C in Cyprus and cooled below 0 °C during transportation. The start and end times of sampling, flow rates, and duration are shown in Table S2. These filters were transported to the Karlsruhe Institute of Technology (KIT) for analysis with the Ice Nucleation SpEctrometer of the Karlsruhe Institute of Technology (INSEKT). INSEKT is a droplet freezing device, the design of which was inspired by the Colorado State University Ice Spectrometer (Hiranuma et al., 2015). For the analysis, each filter was washed with 8 mL ultrapure water which had been passed through a 0.1 µm filter (Nuclepore Track-Etch Membrane, Whatman); 50 µL samples of the resulting suspension/solution were pipetted into 24 to 36 sections of two 96-well PCR trays. Other wells of the trays were filled with 15- and 225-fold (and for some samples also 3375-fold) dilutions of the filter washing water. Also, in each experiment at least 24 wells were filled with pure and particle-free water to be able to account for impurities resulting from the washing water and PCR tray surfaces. The PCR trays were then placed into aluminum cooling blocks. Those blocks have been customized by drilling channels into the bulk aluminum, through which the cooling agent thermostated by means of an external chiller (LAUDA PROLINE RP 855) is directed. The temperature of the cooling agent is then lowered by 0.33 K min^{-1} and monitored by eight calibrated temperature sensors inserted into the aluminum blocks. The number of frozen versus unfrozen wells was derived visually in 0.5 K steps.

For both measurement systems, the cumulative concentration of INP per air volume as a function of temperature can be calculated based on Vali (1971):

$$N_{\mathrm{INP}}(\theta) = \frac{\ln N_{\mathrm{t}} - \ln N(\theta)}{V}, \quad (3)$$

where N_{t} is the number of droplets/wells and $N(\theta)$ is the number of unfrozen droplets/wells at temperature θ. V means the volume (at 0 °C and 1013 hPa) of air distributed into each droplet/well.

The background freezing signal of ultrapure water and water samples resulting from washing of blind filters is determined for the two sampling systems as well. Measured N_{INP} is corrected by subtracting the background concentrations determined for the blind filters and the ultrapure water.

Due to the usually small number (order of tens and lower per examined droplet/well) of INP present in the washing water and the limited number of droplets/wells considered in our measurements, statical errors need to be considered in the data evaluation. Therefore, confidence intervals for the frozen fraction (f_{ice}) were determined using the method suggested by Agresti and Coull (1998). More details about the background subtraction and measurement uncertainties can be found in the Supplement.

2.5 Chemical composition

Aerosol particle dry deposition was collected with a flat-plate-type sampler (Ott and Peters, 2008) on carbon adhesive mounted on standard electron microscopy stubs. Sample substrates were exposed for approximately 24 h, collecting particles approximately between 1 and 100 µm particle diameter at ambient conditions. Samples were subject to automated electron microscopy single-particle analysis, yielding the particle size (projected area diameter) and average elemental composition for each particle. Particles were classified according to the composition in groups based on a static rules set. For more information on sampling, analysis, and data processing, refer to Kandler et al. (2018). In this study, we calculated the particle mass deposition rate in the size range from 1 to 8 µm.

3 Results and discussion

3.1 Overview of the meteorology and air quality

Time series of meteorological and air quality parameters as measured from 2 to 30 April are shown in Fig. 2. The relative humidity (RH), temperature, wind speed, wind direction,

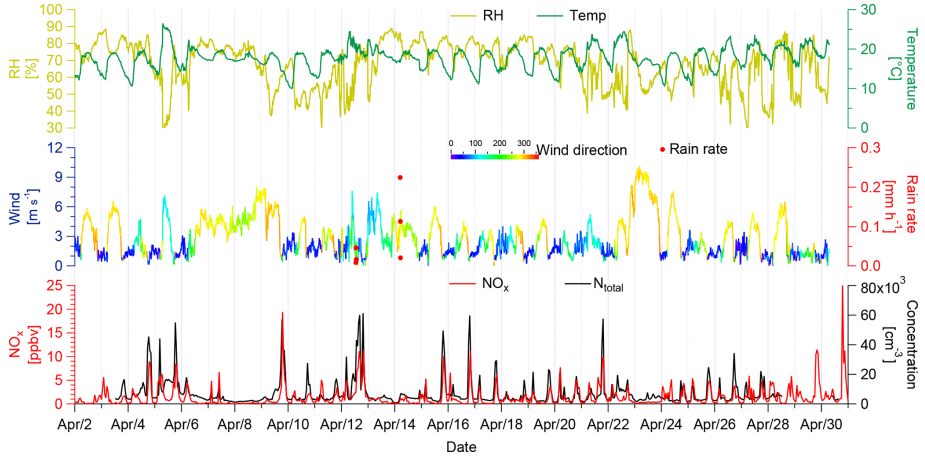

Figure 2. Time series of RH, temperature, wind speed, and wind direction with 10 min resolution, NO_x, and N_{total} with 1 h resolution.

NO_x, and N_{total} (retrieved from MPSS- and APS-measured PNSD) were determined at the measurement site. Note that all times presented here are in UTC (corresponding to local time −3).

RH exhibited large variability throughout the campaign, varying from 22.6 % to 89.2 %, with a mean of 68.4 %. Temperature varied from 10.0 to 26.5 °C, with a mean of 17.5 °C. The local wind speeds ranged from 0.1 to 10.1 m s^{-1}, with a mean of 2.8 m s^{-1}. Figure S4 shows the wind rose plot based on a 10 min mean of wind speed and wind direction. It is clear that winds are mainly from northwest, west, and northeast. The winds from northwest and west featured higher wind speeds, while winds from northeast featured lower wind speeds.

NO_x varied from 0.0027 to 25 ppbv, with a median of 0.67 ppbv. N_{total} varied from 658 to 61 308 cm^{-3}, with a median of 3954 cm^{-3}. The NO_x and N_{total} were relatively low during most of the campaign. However, sharp increases in NO_x and N_{total} were observed frequently, and extremely high concentrations ($NO_x > 1.6$ ppbv, $N_{total} > 8000$ cm^{-3}) only occurred for a few hours. A good correlation ($R^2 = 0.62$) was found between such extremely high concentrations of NO_x and N_{total} (Fig. S5), indicating a nearby pollution source. The extremely high concentrations of NO_x and N_{total} together with the wind direction typically connected to their occurrences suggest the nearby airport as the source of these pollutions, as will be discussed in more detail in Sect. 3.2.

To get indications concerning possible particle sources, we studied the air mass origin and transport by means of backward trajectory analysis. The calculations were performed with the HYSPLIT (HYbrid Single-Particle Lagrangian Integrated Trajectory) model (Stein et al., 2015; Rolph, 2003). Figure 3a shows the 6 d backward trajectories with 1 h time resolution ending at 500 m above the measurement site. Figure 3b shows the relative frequency of backward trajectories. The majority (more than 30 %) of the trajectories featured paths over central and southern Europe. Around 10 % of the trajectories were traced back to the northern Atlantic Ocean and travelled through the western Mediterranean Sea to the site. Approximately 5 % of the trajectories touched the Sahara Desert and the desert regions in Syria and Iraq, indicating that mineral dust particles could have been transported to Cyprus during the campaign.

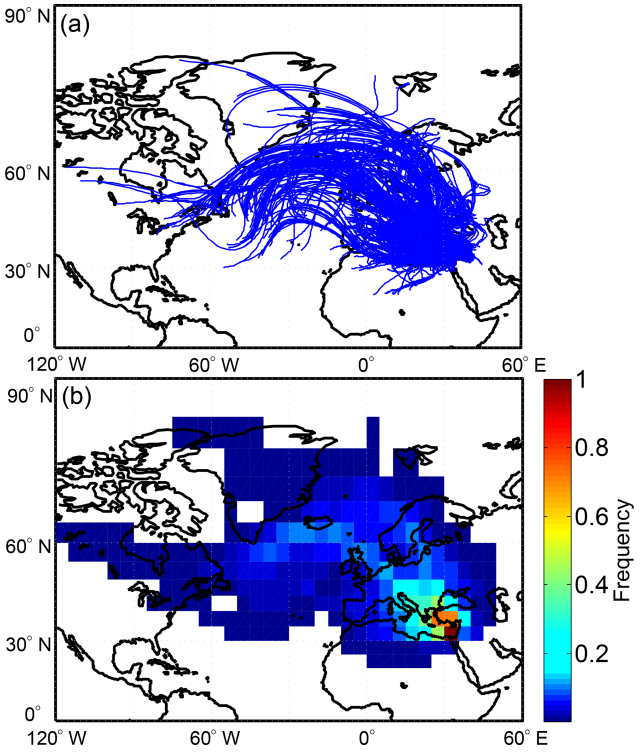

Figure 3. (a) 6 d backward trajectories (blue lines) ended at 500 m above the measurement station with 1 h resolution. **(b)** Relative frequency of trajectories arriving at the station, based on a 5° by 5° grid size.

3.2 Particle number size distribution and sources

Particles of different sizes have different formation pathways, sources, and behaviors. Figure 4a presents measured super-micron PNSDs as a contour plot, together with wind speed information. The super-micron particle concentration varied from 0 to 11 cm^{-3}, with a mean of 2 cm^{-3}. Figure 5 shows the time series of particle mass deposition rates for different compounds at Cyprus, for particles between 1 and 8 µm dry diameter. Overall, sea salt accounted for more than 60 % of the super-micron particle mass throughout the whole campaign.

Higher super-micron particle number concentrations were mainly observed from 6 to 7, 12 to 14, and 21 to 22 April, with the corresponding air masses originating from dust areas, as shown in Fig. 4a by brown dots. As shown in Fig. 5, high dust deposition rates of $\sim 1\,mg\,m^{-2}\,d^{-1}$ were also observed during these periods. Therefore, mineral dust was another important constituent of super-micron particle mass during these periods. However, the observed super-micron particle concentrations were relatively low compared to those reported in previous studies (Mamouri et al., 2016; Schrod et al., 2017) for Cyprus during dust plumes. Low concentrations of super-micron particles were observed on 15 April, although the respective backward trajectories featured paths over the Sahara dust region. In summary, the super-micron particles observed during the campaign were a mixture of ~ 60 % sea salt, ~ 32 % mineral dust, and ~ 8 % others (mainly sodium sulfate), with the relative contributions being dependent on the actual meteorological conditions and source regions.

Figure 4b presents contour plots of PNSDs observed for submicron particles. Extremely high concentrations of ultrafine particles (pronounced mode with a maximum at about 15 nm, median $dN/d\log Dp$ value larger than $10^4\,cm^{-3}$) were frequently observed throughout the whole campaign. When ultrafine particles featured high concentrations, extremely high concentrations of NO_x were also observed. An exemplary case is shown in Fig. S6. Such kinds of behavior usually appeared from 03:00 to 06:00 UTC and 17:00 to 22:00 UTC. A wind rose plot shown in the Supplement indicates that during these periods, winds were from the northeast (Fig. S7), i.e., the direction where Paphos International Airport is located. This is highly suggestive of the airport being the origin of the observed ultrafine particles and NO_x. Figure 6 shows the comparison of medians of PNSDs observed during airport-affected (PNSDa) and non-affected time periods. The error bars indicate the range between the 25 % and 75 % percentiles. It is clearly seen that airport-affected PNSDa exhibit a very pronounced ultrafine particle mode with a maximum at diameters of about 15 nm. Such a mode is indicative of a nearby particle source, such as the combustion of fuel at the airport. Previous studies found that airport-emitted particles featured similar PNSDs (Hudda and Fruin, 2016; Jasinski and Przylebska, 2018). Therefore, in the following, time periods affected by pollution from the airport were excluded from further analysis. The pollution-free median PNSD (black line in Fig. 6) features clear Atiken, accumulation, and coarse modes, with the Hoppel minimum (Hoppel et al., 1986) being located at approximately 80 nm.

Based on the criteria reported by Dal Maso et al. (2005), we identified several NPF and growth events during the campaign. The criteria are, first of all, the appearance of a distinct new mode (in the nucleation mode size range) in the size distribution. Secondly, the mode must prevail over a time span of hours. Lastly, the new mode must show signs of growth. For example, newly formed particles occurred at 07:00 UTC, 5 April, 08:00 UTC, 12 April, and 07:00 UTC, 22 April, with subsequent particle growth in the next few hours up to days. All observed NPF started during daytime, suggesting that photochemistry products were likely to contribute to the formation of the new particles. The NPF events, which occurred at 07:00 UTC, 5 April and 07:00 UTC, 22 April, featured continuous particle growth up to several tens of nanometers. The NPF event occurring at 08:00 UTC, 12 April exhibits a more complicated time evolution. Around 15:30 UCT, 12 April, the PNSDs were affected by pollution from the airport due to the wind direction shifting to the northeast. Around 00:00 UTC, 13 April, the wind speed increased and wind directions were from the clean ocean; i.e., clean air mass weakened the particle growth process. Later on, i.e., at 01:00 UTC, 14 April, precipitation occurred. This influenced the evolution of the NPF and growth event, but the growing trend in particle size is still to be seen. The observed particle growth events show that newly formed particles can grow up to sizes where they can act as CCN. However, there are several more NPF and growth events which we do not discuss here, because particles did not grow up to sizes making them potential CCN.

3.3 CCN and particle hygroscopicity

Figure 7 shows time series of N_{total} and N_{CCN} (corrected with particle losses) in the upper panel, d_{crit} in the middle panel, and κ in the lower panel. N_{CCN} exhibit large variability throughout the campaign, including a few remarkably elevated concentrations (maximum value $\sim 3730\,cm^{-3}$ at supersaturation of 0.31 %), and one exceptionally low concentration (minimum value $\sim 170\,cm^{-3}$ at supersaturation of 0.31 %). The median values of N_{CCN} at different supersaturations are given in Table 1 and vary from 295 cm^{-3} for a supersaturation of 0.08 % to 2004 cm^{-3} for a supersaturation of 0.77 %.

The low N_{CCN} around 03:00 UTC, 14 April were associated with precipitation, as can be seen in Fig. 2. Most of the time, high N_{CCN} are associated with NPF and growth events. For example, around 09:00 UTC, 5 April, N_{CCN} at higher supersaturations (0.54 % and 0.77 %) started to increase. The N_{CCN} at lower supersaturations (0.19 % and 0.31 %) followed at 04:00 UTC, 6 April. However, N_{CCN} at the lowest

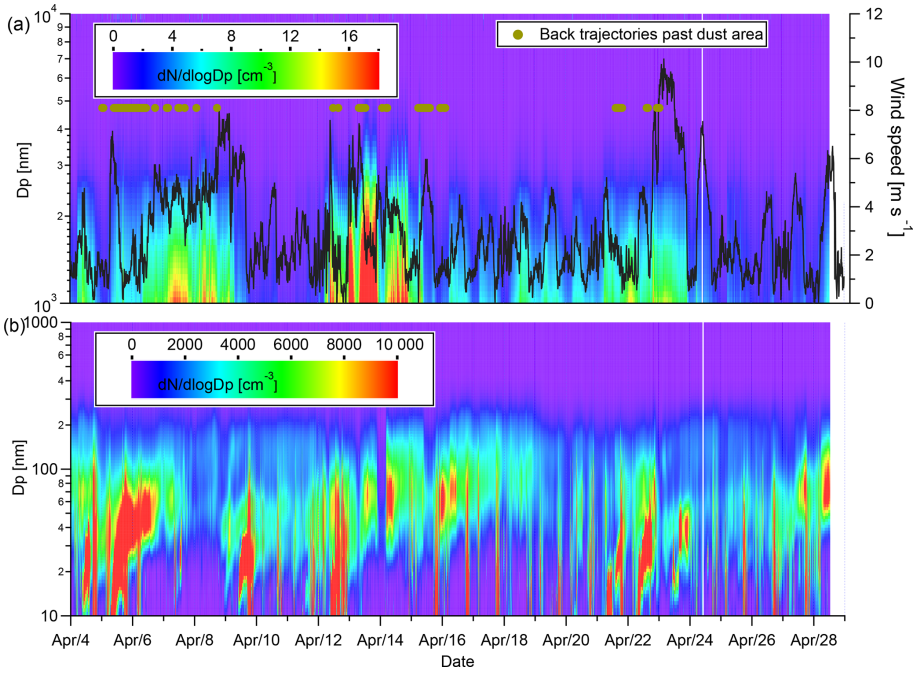

Figure 4. Contour plots for PNSDs during the whole campaign. The color scale indicates $\mathrm{d}N/\mathrm{d}\log Dp$ in cm^{-3}. **(a)** Contour plots for PNSDs of 1000 to 10 000 nm. Black line shows time series of wind speed and the brown dots show the time when backward trajectories passed the dust area. **(b)** Contour plots for PNSDs of 10 to 1000 nm.

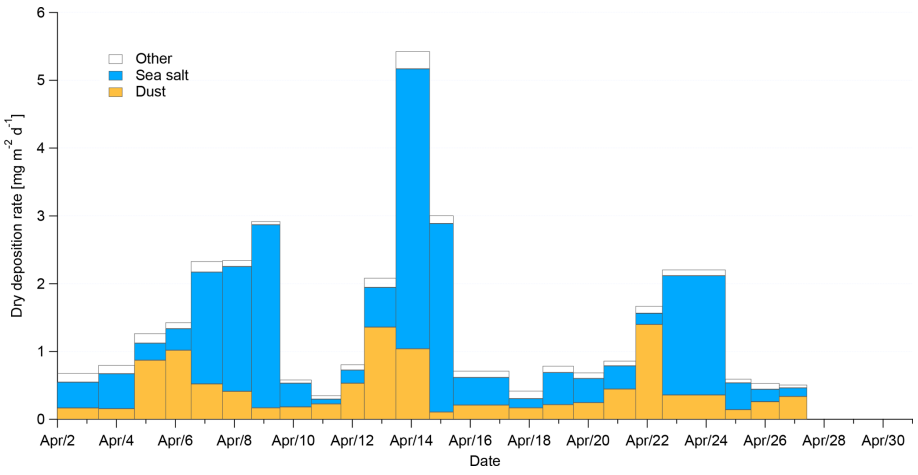

Figure 5. Time series of the dry mass deposition rate for different compounds for particles between 1 and 8 µm dry diameter. The "Dust" class includes silicate and carbonate particles, and the "Other" class mainly consists of sodium sulfate. Mixed particles are evenly distributed between the respective groups.

supersaturation (corresponding to the d_{crit} around 163 nm) did not increase in connection with the NPF and growth event. Newly formed particles did not grow into that size range; i.e., N_{CCN} at the lowest supersaturation was not affected. The same behavior was observed from 08:00 UTC, 22 April to 00:00 UTC, 23 April. From 13 to 14 April, the NPF and growth were affected by changing wind directions and precipitation. N_{CCN} also show respective influences, but the overall trend still can be seen.

The probability density functions (PDFs) of N_{CCN} at different supersaturations are shown in the upper panel of Fig. 8. As discussed, N_{CCN} at the lowest supersaturation was not affected by the NPF and growth events, so a unimodal PDF was observed. However, the PDFs of N_{CCN} at other supersaturations are bimodal, with the larger mode (higher concentrations) representing the NPF and growth events. Kalivitis et al. (2015) also found that CCN production resulted from NPF in the eastern Mediterranean during the summertime. The small

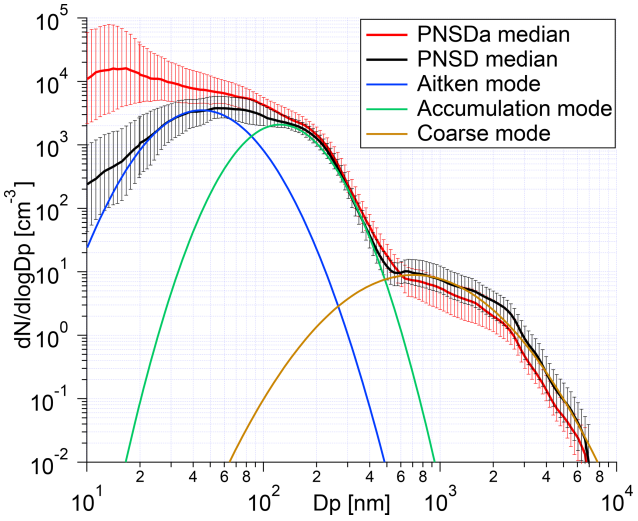

Figure 6. Comparison of the median PNSD during airport-affected (red line) and non-affected (black line) time periods. The error bar indicates the range between the 25 % and 75 % percentiles. Aitken, accumulation, and coarse modes are fitted with log-normal distribution, displayed in blue, green, and brown lines, respectively.

Table 1. Median values of N_{CCN}, d_{crit}, κ, and 1 standard deviation of d_{crit} and κ at different supersaturations.

Supersaturation (%)	N_{CCN} (cm^{-3})	d_{crit} (nm)	κ	$\sigma_{d_{crit}}$ (nm)	σ_κ
0.08	295	163	0.57	10	0.09
0.19	872	92	0.49	8	0.12
0.31	1332	70	0.42	8	0.13
0.54	1743	55	0.29	7	0.10
0.77	2004	48	0.21	8	0.10

modes (lower concentrations) of the PDFs are representative of the time periods without NPF and growth events.

The d_{crit} at different supersaturations were almost constant throughout the campaign, even during the NPF events. The PDFs of d_{crit} are unimodal, as shown in Fig. 8. The d_{crit} at different supersaturations and the standard deviations of their PDFs are included in Table 1. For the supersaturations of 0.77 % and 0.54 %, the d_{crit} were below 60 nm, i.e., inside the Aitken mode. However, for the lowest supersaturation of 0.08 %, d_{crit} is located in the accumulation mode. Consequently, hygroscopicities derived at these supersaturations can be assumed to be representative of the Aitken (at supersaturations of 0.77 % and 0.54 %) and accumulation (at a supersaturation of 0.08 %) modes, respectively.

The particle hygroscopicity, expressed as κ, can be seen as a measure for average particle chemical composition. Time series of calculated κ values are depicted in the lower panel of Fig. 7. The κ values at different supersaturations show little variability over time, with 1 standard deviation from 0.09 to 0.13; i.e., there is no clear trend in κ over time during the campaign. At the supersaturations of 0.54 % and 0.77 %, corresponding to d_{crit} of 40 ± 8 and 55 ± 7 nm (median $\pm$ 1 standard deviation), the medians of κ are 0.21 ± 0.10 and 0.29 ± 0.10, respectively. These low κ values in Aitken mode suggest the presence of organic material, which has also been observed in previous studies (Kalivitis et al., 2015; Kristensen et al., 2016). At the lowest supersaturation of 0.08 %, corresponding to the d_{crit} of 163 ± 10 nm, the median of κ is 0.57 ± 0.09. Particles in this size range are members of the accumulation mode and have undergone cloud processing and aging. This results in higher amounts of sulfates being present, and consequently higher hygroscopicities. A few sea salt particles mixed with organic carbon might also be present in the accumulation mode, according to a previous study (Prather et al., 2013). But the absolute number concentration of sea salt mixed with organic carbon particles in the size range < 200 nm is likely limited. A clear downward trend of κ is observed with increasing supersaturations and decreasing d_{crit} (Fig. 9). The κ values in the Aitken and accumulation modes are clearly different, with the error bars considered, indicating significant differences in particle chemical composition for the two modes.

The PDFs of κ change from unimodal to bimodal to unimodal with decreasing supersaturation. As mentioned above, the κ values at supersaturations of 0.77 % and 0.54 % are representative for the Aitken mode particles, while the κ values at supersaturation of 0.08 % are a measure for the accumulation mode particles. Therefore, the κ values at these supersaturations feature unimodal distributions. κ at supersaturations of 0.31 % and 0.19 %, corresponding to d_{crit} of 92 ± 8 and 70 ± 8 nm, respectively, exhibit bimodal distributions. These κ values are influenced by both Aitken and accumulation mode particles, indicating an external mixture of particles in that size range.

The determined particle hygroscopicities confirm those given in previous studies. For example, Kalivitis et al. (2015) reported that κ values in the Aitken mode were 0.20–0.40 lower than those in the accumulation mode during the NPF events in the eastern Mediterranean, and highlighted NPF as a source of CCN. Pringle et al. (2010) used an atmospheric chemistry model to derive global distributions of effective particle hygroscopicity κ. The annual mean value at the surface of the eastern Mediterranean was roughly 0.45, with an annual cycle ranging from 0.35 in December to 0.50 in February. For April, the period of this study, a value of 0.40 was reported, which is consistent with what we obtained ($\kappa = 0.39$) for this campaign.

3.4 Ice-nucleating particles

3.4.1 Temperature spectra of cumulative N_{INP}

Ice fractions (f_{ice}) as determined with both LINA and INSEKT are shown in Fig. S8. The corresponding N_{INP} from both instruments are shown in Fig. 10 as a function of tem-

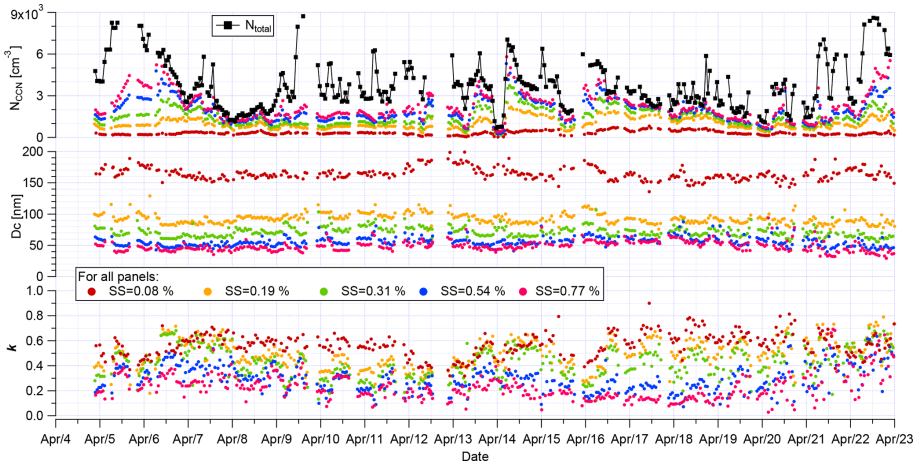

Figure 7. Time series of N_{total}, N_{CCN}, the inferred d_{crit}, and κ values at different supersaturations.

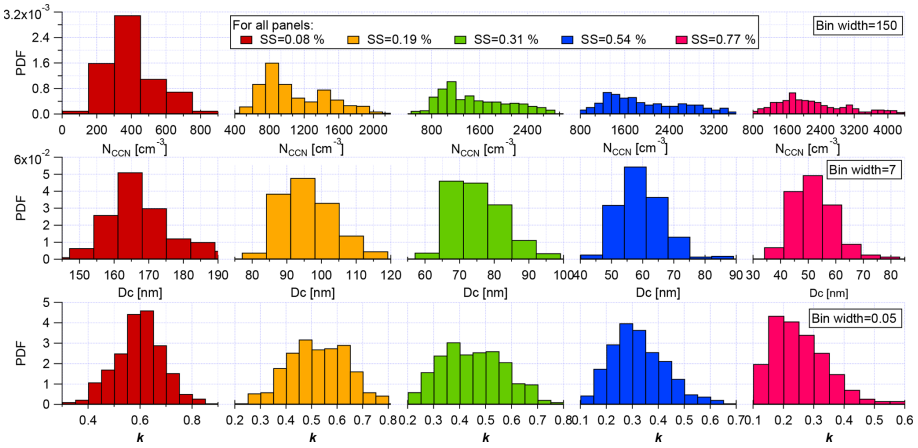

Figure 8. PDFs of N_{CCN}, d_{crit}, and κ values at different supersaturations.

perature. Samples collected from the land and ocean sectors (measured by LINA) are represented by black circles and red rectangles, respectively. These filter samples were all active at −16 °C and the highest freezing temperature was found to be −6.5 °C. Samples collected during daytime (measured by INSEKT) are represented by blue rectangles. With two or three dilution steps, by measuring suspensions with different aerosol concentrations, the INSEKT measurements cover a larger temperature range from −7.5 to −26.5 °C. The measurement uncertainty for both instruments is shown in Fig. S9. As mentioned in the experimental section, filters examined with LINA were switched according to the wind direction. From Fig. 10, it is obvious that there is no very pronounced difference in N_{INP} between the land and ocean sectors. It is, however, noticeable that the freezing curves from the ocean sector are rather at the lower end of the measured curves. To test whether there was a pronounced contribution to INP from the land sector, we examined the INSEKT data in more depth. Figure S10 shows the N_{INP} from the INSEKT measurements in dependence on the fraction of time sampled from the ocean sector. No clear trend was found. A source apportionment for INP examined in this study is therefore difficult to do. Considering that Cyprus is only a small island surrounded by the Mediterranean Sea, its effect might be limited. Besides, for a location such as Cyprus, it is difficult to determine sources for different air masses only based on wind direction alone.

The measured N_{INP} in this study are within the N_{INP} range presented by Welti et al. (2018), who characterized INP sampled at the Cape Verde Atmospheric Observatory (CVAO) over a time period of 4 years (shown in Fig. 10 as yellow shadow). This is surprising as those atmospheric aerosols at CVAO and Cyprus should be expected to be different. It might, however, point towards a similar background of INP worldwide. N_{INP} are lower than those proposed in Fletcher (1962), while the slope is similar to that of the Fletcher (1962) line. N_{INP} increased exponentially from −10 to −25 °C, indicating the presence of a broad variety of INP, featuring, e.g., different size, composition, and ice active surface sites.

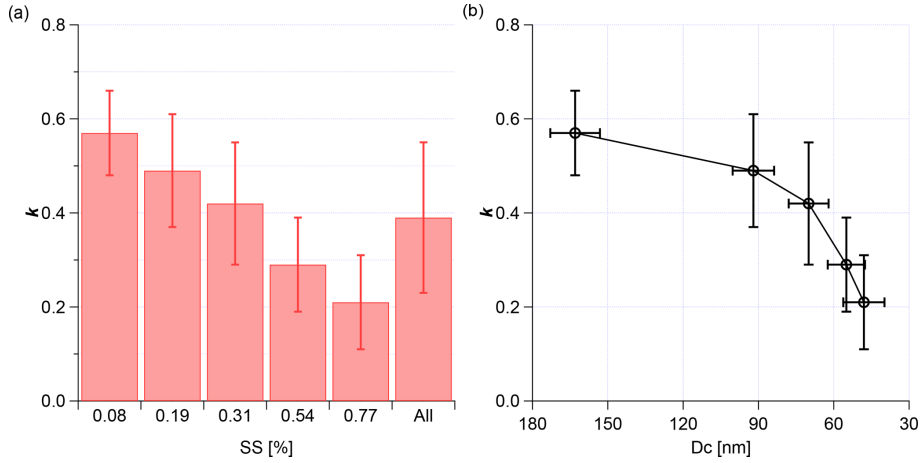

Figure 9. (a) Derived κ values at different supersaturations. **(b)** κ values as a function of the corresponding d_{crit}. Error bar represents the 1 standard deviation.

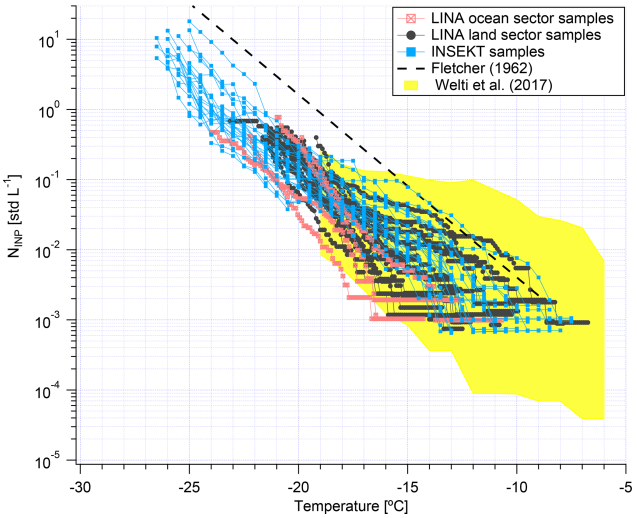

Figure 10. N_{INP} (measured by LINA and INSEKT) as a function of temperature. Parameterization from Fletcher (1962) in the valid temperature range is given for comparison, as shown in dashed line. The yellow shadow represents the measured N_{INP} from a ground-based station at CVAO (Welti et al., 2018).

N_{INP} at a particular temperature span about 1 order of magnitude below −20 °C and about 2 orders of magnitude at the warmer temperatures ($T > -18$ °C). This is consistent with the previous study of O'Sullivan et al. (2018), who carried out field measurement in northwestern Europe. Few samples (LINA sample05, 20, 22 and INSEKT sample01, 06, 12, 13, 19, 28) showed elevated concentrations at temperatures above −15 °C. Biological particles (e.g., bacteria, fungal spores, pollen, viruses, and plant fragments) usually contributed to the INP at these moderate supercooling temperatures (Kanji et al., 2017; O'Sullivan et al., 2018). These high signals observed in both instruments might have been caused by biogenic INP, originating from Cyprus, as such high signals did not occur for the four samples from the ocean sector. However, as there are only four samples from the ocean sector, and as no additional tests were possible with the limited amount of sampled material, it should suffice to express this hypothesis here.

Overall, N_{INP} of the land samples are not clearly different from those of the ocean samples, besides for some samples at > -15 °C for which a biogenic contribution is expected. Therefore, a contribution of INP from pollution from the airport is not expected. This would be in line with Chen et al. (2018), who found that aerosol in Beijing did not contain higher N_{INP} during strong pollution events, compared with clean phases.

3.4.2 Time series and PDFs

Figure 11a shows the time series of N_{INP} during the campaign. Here we present N_{INP} derived from LINA (ocean sector in green and land sector in red) and INSEKT (in blue) measurements at −15, −18, and −20 °C. N_{INP} varied from 0.001 to 0.1, 0.004 to 0.2, and 0.03 to 0.4 std L^{-1} at −15, −18, and −20 °C, respectively. N_{INP} varies non-synchronously at different temperatures. Here we compared data from different temperatures with each other and determined a regression line between them. Taking, e.g., the results from the LINA measurements, the coefficients of determination (R^2) are 0.45, 0.26, and 0.0033 for −15 to −18, −18 to −20, and −15 to −20 °C, indicating the different natures and origins of the INP active at different temperatures.

Welti et al. (2018) found that log-normal distributions best approximate the measured variability in concentrations at each individual temperature. Here we used two methods to test our N_{INP} frequency distributions, which are both described in more detail in the Supplement. Both methods indicate that the INP distributions at −15, −18, and −20 °C

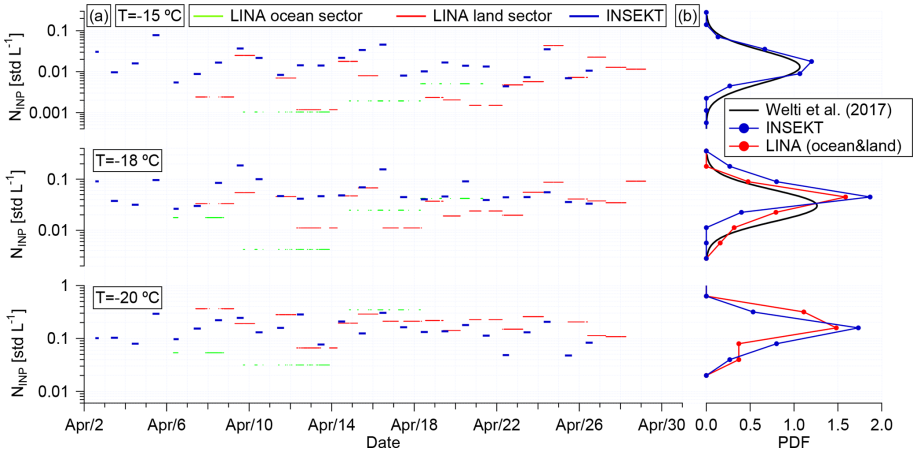

Figure 11. (a) Time series and **(b)** PDFs of N_{INP} at −15, −18, and −20 °C.

are indeed log-normally distributed. This analysis was only done for these temperatures, as only in this temperature range did almost all samples contribute data. As log-normally distributed N_{INP} are indicative of the observed INP population having undergone a series of random dilutions while being transported (Welti et al., 2018), the performed tests yield proof of the INP (ice active at $-20 \leq T \leq -15$ °C) sampled during our measurements originating from long-range transport rather than local sources, as the proximity of sources would cause a more strongly skewed frequency distribution (Ott, 1990; Welti et al., 2018).

Figure 11b depicts the PDFs of N_{INP} at different temperatures. Thereby, a PDF is shown if at the particular temperature most of the investigated samples featured a quantifiable ($0 < f_{ice} < 1$) freezing behavior. For example, there were three LINA-measured samples which did not freeze at −15 °C ($f_{ice} = 0$); therefore, we do not show the PDF of LINA-measured N_{INP} at −15 °C. At −20 °C the data from Welti et al. (2018) are omitted, because more than half of all the samples were fully frozen ($f_{ice} = 1$). As can be seen from Fig. 11b, our results are comparable to those given in Welti et al. (2018) (black curves) derived from long-term measurement at CVAO. Note that it is not possible to directly compare the N_{INP} measured by LINA and INSEKT, as they always had different sampling times and INSEKT always sampled air from all directions, whereas LINA got it from the different sectors separately. But in general, no systematic deviation can be seen, as can be seen when looking at the PDFs. To the best of our knowledge, the only in situ observations at −20 °C for supersaturated conditions (101 %) in the eastern Mediterranean were reported by Schrod et al. (2017) during a heavy dust plume at high altitude with 0.03 to 3 std L^{-1}.

3.4.3 Correlation of N_{INP} with particle number/surface area concentration and parameterization

Scatter plots of LINA- and INSEKT-measured N_{INP} at temperatures of −15, −18, and −20 °C against particle number concentration in the size range > 500 nm ($N_{>500\,nm}$) are shown in Fig. 12a and b. The averaged $N_{>500nm}$ during each filter sample varied from 2 to 14 cm^{-3}. The $N_{>500\,nm}$ in this study is much lower than that observed during the dust plume period in Cyprus (maximum 75 cm^{-3} Schrod et al., 2017). The R^2 between $N_{>500\,nm}$ and N_{INP} are shown in Table S4. The R^2 were all below 0.25, indicating no correlation between N_{INP} and $N_{>500\,nm}$.

Based on nine field studies occurring at a variety of locations over 14 years, DeMott et al. (2010) proposed a parameterization of the "global" average INP distribution. Besides, Tobo et al. (2013) present a similar parameterization method with adjusted coefficients to predict INP populations in a forest ecosystem. Figure 12c and d compare the N_{INP} we measured with LINA and INSEKT to the predicted N_{INP} on the basis of the DeMott et al. (2010) and Tobo et al. (2013) parameterizations. As can be seen, the DeMott et al. (2010) parameterization overestimates the observed values by about 2 orders of magnitude on average. The Tobo et al. (2013) parameterization can reproduce only 24 % and 25 % of the N_{INP} measured by LINA and INSEKT within a factor of 2, respectively. The Tobo et al. (2013) parameterization overestimates the observed values by about 1 order of magnitude on average. This, together with N_{INP} not being correlated with $N_{>500\,nm}$ (see Table S4), indicates that the application of parameterizations in connection with measured particle number concentrations has to be done with extreme caution, as the encountered particle populations may significantly differ from those considered when developing the parameterizations.

Figure S12 shows the median particle surface area size distribution (PSSD) for the whole campaign (excluding the air-

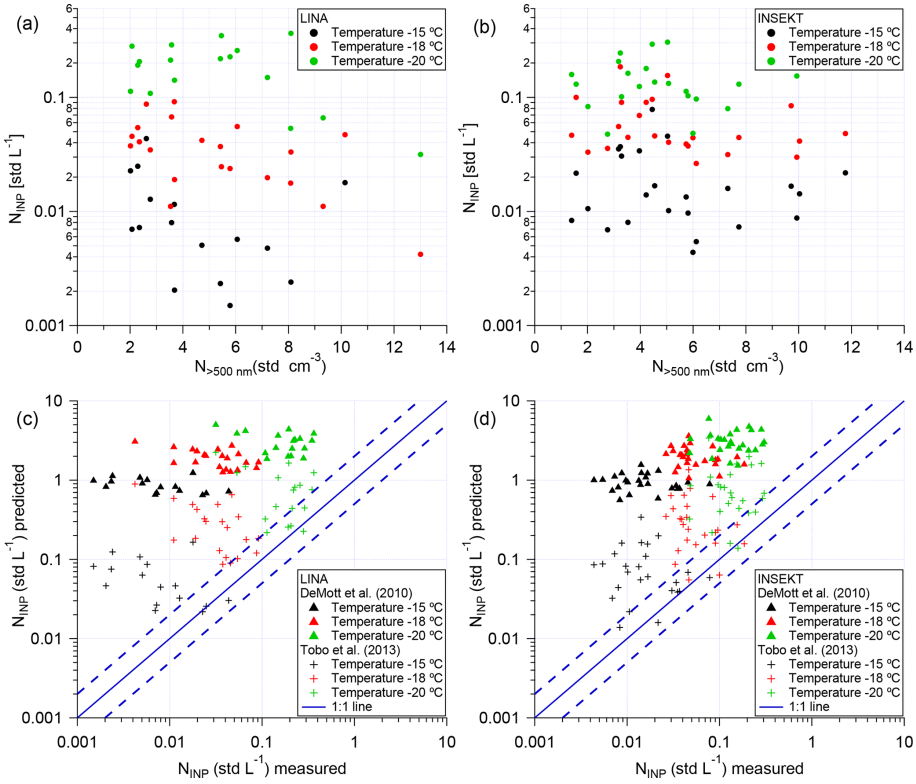

Figure 12. Scatter plot of N_{INP} measured by LINA **(a)** and INSEKT **(b)** against $N_{>500\,nm}$. Scatter plot of N_{INP} measured by LINA **(c)** and INSEKT **(d)** against the N_{INP} predicted by DeMott et al. (2010) and Tobo et al. (2013). The dashed lines outline a range of a factor of 2 about the 1 : 1 line (solid line).

port pollution events). Two different modes were observed, i.e., a small mode (20–500 nm) and a larger mode (500–7000 nm). Based on the PSSD, the concentrations for the total surface area of the small mode ($S_{<500\,nm}$), the large mode ($S_{>500\,nm}$), and for both modes combined (S_{all}) were calculated. The $S_{<500\,nm}$ is about 4 times higher than $S_{>500\,nm}$. Scatter plots of LINA- and INSEKT-measured N_{INP} against $S_{<500\,nm}$, $S_{>500\,nm}$, and S_{all} are shown in Fig. S13a and b. The R^2 between N_{INP} and particle surface area concentration are shown in Table S5. The R^2 are all below 0.20, indicating no correlation between N_{INP} and particle surface area concentration.

The ice-nucleating properties of aerosol particles may be characterized by its ice active surface site density (n_s). The n_s is a measure of how well an aerosol acts as a seed surface for ice nucleation. The n_s can be calculated as

$$n_s = \frac{N_{INP}(\theta)}{S}, \quad (4)$$

where S is the particle surface area concentration.

Depending on which particle size range was investigated, previous studies calculated n_s based on either the total surface area concentration (S_{all}) or on the surface area concentration of particles larger than 500 nm ($S_{>500\,nm}$). Here, both approaches were used, resulting in n_{s_all} and $n_{s>500\,nm}$, respectively. Figure 13 shows the $n_{s>500\,nm}$ as a black box plot and the n_{s_all} as a red box plot at −15, −18, and −20 °C. As can be seen, n_s increases towards lower temperature, which is expected. The n_s results, calculated using LINA- and INSEKT-measured N_{INP}, are shown in Fig. 13a and b, respectively. The n_s values determined from LINA measurements are consistent with those from INSEKT measurements.

To the best of our knowledge, many studies dealt with the n_s for dust aerosol particles, while no study investigated the n_s for the type of polluted aerosol we encountered in the eastern Mediterranean. In the following, we compare our n_{s_all} for the polluted aerosol on Cyprus, with n_{s_all} based on existing parameterizations (Niemand et al., 2012; Ullrich et al., 2017) for dust aerosols (Fig. 13). However, the n_{s_all} values from the parameterizations are more than 2 orders of magnitude larger than the n_{s_all} found in this study. Price et al. (2018) carried out an airborne measurement in dust-laden air over the tropical Atlantic. The n_{s_all} reported in Price et al. (2018) (shown in Fig. 13 as yellow shadow) is about 1 to 2 orders of magnitude higher than our results. Based on airborne measurement, Schrod et al. (2017) found that the $n_{s>500\,nm}$ at Cyprus ranged between 10^5 and 10^8 m^{-2} at $T = -20$ °C, $RH_{water} = 101$ %, shown as green shadow in Fig. 13.

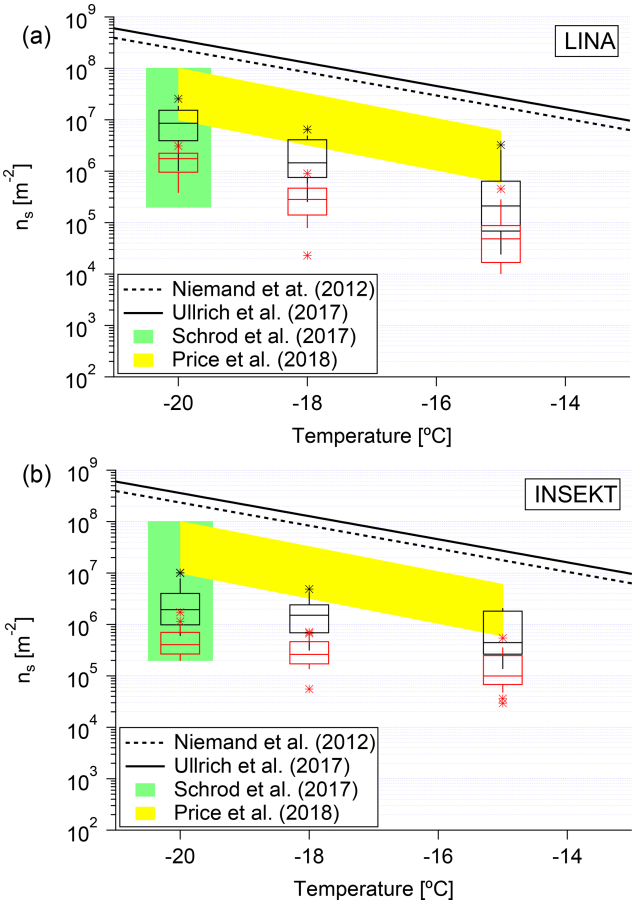

Figure 13. $n_{s>500\,nm}$ (black box plot) and n_{s_all} (red box plot) as a function of temperature. The results were determined based on LINA-measured N_{INP} in panel **(a)** and INSEKT-measured N_{INP} in panel **(b)**. The boxes represent the interquartile range. Data not included between the whiskers are plotted as an outlier with a star. Two n_s parameterizations (Niemand et al., 2012; Ullrich et al., 2017) for desert dust are shown in dashed and solid line. We also compare this to recent data from airborne measurement by Schrod et al. (2017) and Price et al. (2018), as shown in green and yellow shadow, respectively.

In short summary, parameterizations purely based on $N_{>500\,nm}$ or particle surface area concentration in mineral-dust-dominated model systems overestimate the N_{INP} of the polluted aerosol we encountered on Cyprus. Although we cannot clearly say to which extent the aerosol we observed was influenced by anthropogenic pollution, our results here fit to what was found in a different context, anthropogenically polluted air masses in Beijing (Chen et al., 2018), and is based on the fact that more strongly polluted air masses have larger numbers of particles in the size range above 500 nm than natural ones.

4 Conclusions

The A-LIFE campaign took place in April 2017 on the island of Cyprus to investigate the aerosols prevailing in the eastern Mediterranean region. As part of the A-LIFE campaign, ground-based measurements were carried out in Paphos, Cyprus, to characterize the abundance, properties (size distribution, hygroscopicity, ice activity), and sources of aerosol particles in general, CCN and INP in particular.

During these activities, NPF and growth events were observed. Following NPF, during some events, on timescales of a few hours to days, particles grew into the CCN size range. In fact, the highest observed N_{CCN} were connected with NPF and growth events, which confirms the importance of NPF as a source of CCN in the eastern Mediterranean.

Usually, trimodal (Aitken, accumulation, coarse mode) PNSDs were observed. Aitken mode particles featured low hygroscopicities (κ values about 0.21 to 0.29), indicating the presence of organic materials. Accumulation mode particles featured higher κ values of about 0.57, indicating that particles in the accumulation mode underwent cloud processing and aging, resulting in higher amounts of sulfate being present. A few sea salt particles mixed with organic carbon might also be present in the accumulation mode. The supermicron particles were mainly from SSA and partly mineral dust.

PDFs of κ in both the Aitken and accumulation modes exhibit a unimodal structure, while the κ-PDFs for particle sizes close to the Hoppel minimum feature a bimodal shape. This indicates the presence of both non-cloud-processed (Aitken mode) and cloud-processed (accumulation mode) particles in the size range around the Hoppel minimum. The average observed κ of 0.39 confirms values found in previous field measurements (Kalivitis et al., 2015) and in model results (Pringle et al., 2010) for the Mediterranean region.

Atmospheric N_{INP} were determined in the temperature range from -6.5 to $-26.5\,°C$, using two freezing array type instruments (LINA, TROPOS, and INSEKT, KIT). N_{INP} at a particular temperature span around 1 order of magnitude below $-20\,°C$ and about 2 orders of magnitude at warmer temperatures ($T > -18\,°C$). Few samples showed elevated concentrations at temperatures $T > -15\,°C$, which suggests a significant contribution of biological particles to the INP population, which might have originated from Cyprus. No significant differences in N_{INP} were found when selectively sampling wind directions from the land or sea sector for INP that were ice active in the temperature range between -15 and $-20\,°C$. PDFs of N_{INP} at a particular temperature follow log-normal distributions. For example, at $-18\,°C$, the N_{INP} ranged from 0.004 to 0.2 std L^{-1} during the campaign, which is consistent with the previous study of Welti et al. (2018). This indicates that these sampled INP which are ice active below $-15\,°C$ originate from long-range transport rather than local sources.

No correlations were found between N_{INP} and $N_{>500\,nm}$. Parameterizations (DeMott et al., 2010; Tobo et al., 2013) based on $N_{>500\,nm}$ were found to overestimate the N_{INP} by about 1 to 2 orders of magnitude. There was also no correlation between N_{INP} and particle surface area concentration. The n_s for the polluted aerosol we encountered on Cyprus was found to be 1 to 3 orders of magnitude lower than the n_s for dust aerosol particles resulting from previous studies (Niemand et al., 2012; Ullrich et al., 2017; Price et al., 2018). This clearly highlights that usage of such parameterizations just based on measured particle number or surface area size distributions is not always feasible for predicting N_{INP}, as the parameterizations were derived for particular aerosol types. In other words, basing modeling efforts on, e.g., PDFs from observed N_{INP}, rather than on parameterizations, might be the method of choice if the aerosol particle and/or INP composition are unknown.

Data availability. The data will be available through the World Data Center PANGAEA (https://doi.pangaea.de/10.1594/PANGAEA.904758, Gong et al., 2019) in the near future. A link to the data can be found under this paper's assets tab on ACP's journal website.

Supplement. The supplement related to this article is available online at: https://doi.org/10.5194/acp-19-10883-2019-supplement.

Author contributions. XG wrote the manuscript with contributions from HW, FS, KH, KK, TM, and AW. NM and TM performed particle number size distribution measurement and XG performed data evaluation. Chemical composition measurements and data evaluation were performed by KK. CCN measurements and data analysis were performed by XG. LINA measurements and data evaluation were performed by XG. INSEKT measurements and data evaluation were performed by BD, TS, KH, and XG. XG, HW, and FS discussed the results and did further analysis after the campaign. All the co-authors proofread and commented on the manuscript.

Competing interests. The authors declare that they have no conflict of interest.

Acknowledgements. The works were carried out in the framework of the A-LIFE project. This project has received funding from the European Research Council (ERC) under the European Union's Horizon 2020 research and innovation program under grant agreement no. 640458. We would like to thank Umar Javed from the Institute of Energy and Climate Research, Troposphere (IEK-8), and Anywhere Tsokankunku from the Max Planck Institute for Chemistry for providing the NO_x data. Konrad Kandler is funded by the Deutsche Forschungsgemeinschaft (DFG, German Research Foundation) – 264907654, 264912134, 378741973, 416816480.

Financial support. The publication of this article was funded by the Open Access Fund of the Leibniz Association.

Review statement. This paper was edited by Pedro Jimenez-Guerrero and reviewed by two anonymous referees.

References

Agresti, A. and Coull, B. A.: Approximate is Better than "Exact" for Interval Estimation of Binomial Proportions, The American Statistician, 52, 119–126, https://doi.org/10.1080/00031305.1998.10480550, 1998.

Bougiatioti, A., Nenes, A., Fountoukis, C., Kalivitis, N., Pandis, S. N., and Mihalopoulos, N.: Size-resolved CCN distributions and activation kinetics of aged continental and marine aerosol, Atmos. Chem. Phys., 11, 8791–8808, https://doi.org/10.5194/acp-11-8791-2011, 2011.

Bougiatioti, A., Zarmpas, P., Koulouri, E., Antoniou, M., Theodosi, C., Kouvarakis, G., Saarikoski, S., Mäkelä, T., Hillamo, R., and Mihalopoulos, N.: Organic, elemental and water-soluble organic carbon in size segregated aerosols, in the marine boundary layer of the Eastern Mediterranean, Atmos. Environ., 64, 251–262, https://doi.org/10.1016/j.atmosenv.2012.09.071, 2013.

Bougiatioti, A., Bezantakos, S., Stavroulas, I., Kalivitis, N., Kokkalis, P., Biskos, G., Mihalopoulos, N., Papayannis, A., and Nenes, A.: Biomass-burning impact on CCN number, hygroscopicity and cloud formation during summertime in the eastern Mediterranean, Atmos. Chem. Phys., 16, 7389–7409, https://doi.org/10.5194/acp-16-7389-2016, 2016.

Budke, C. and Koop, T.: BINARY: an optical freezing array for assessing temperature and time dependence of heterogeneous ice nucleation, Atmos. Meas. Tech., 8, 689–703, https://doi.org/10.5194/amt-8-689-2015, 2015.

Chen, J., Wu, Z., Augustin-Bauditz, S., Grawe, S., Hartmann, M., Pei, X., Liu, Z., Ji, D., and Wex, H.: Ice-nucleating particle concentrations unaffected by urban air pollution in Beijing, China, Atmos. Chem. Phys., 18, 3523–3539, https://doi.org/10.5194/acp-18-3523-2018, 2018.

Chester, R., Nimmo, M., Alarcon, M., Saydam, C., Murphy, K., Sanders, G., and Corcoran, P.: Defining the chemical character of aerosols from the atmosphere of the Mediterranean-Sea and surrounding regions, Oceanol. Acta, 16, 231–246, 1993.

Claeys, M., Roberts, G., Mallet, M., Arndt, J., Sellegri, K., Sciare, J., Wenger, J., and Sauvage, B.: Optical, physical and chemical properties of aerosols transported to a coastal site in the western Mediterranean: a focus on primary marine aerosols, Atmos. Chem. Phys., 17, 7891–7915, https://doi.org/10.5194/acp-17-7891-2017, 2017.

Dal Maso, M., Kulmala, M., Riipinen, I., Wagner, R., Hussein, T., Aalto, P. P., and Lehtinen, K. E.: Formation and growth of fresh atmospheric aerosols: eight years of aerosol size distribution data from SMEAR II, Hyytiala, Finland, Boreal Environ. Res., 10, 323–336, 2005.

DeMott, P. J., Prenni, A. J., Liu, X., Kreidenweis, S. M., Petters, M. D., Twohy, C. H., Richardson, M. S., Eidhammer, T., and Rogers, D. C.: Predicting global atmospheric ice nuclei distribu-

tions and their impacts on climate, P. Natl. Acad. Sci. USA, 107, 11217–11222, https://doi.org/10.1073/pnas.0910818107, 2010.

Fan, J., Wang, Y., Rosenfeld, D., and Liu, X.: Review of Aerosol–Cloud Interactions: Mechanisms, Significance, and Challenges, J. Atmos. Sci., 73, 4221–4252, https://doi.org/10.1175/jas-d-16-0037.1, 2016.

Fletcher, N. H.: The physics of rainclouds, Cambridge University Press, New York, 1962.

Giorgi, F. and Lionello, P.: Climate change projections for the Mediterranean region, Global Planet. Change, 63, 90–104, https://doi.org/10.1016/j.gloplacha.2007.09.005, 2008.

Gong, X. Wex, H., Müller, T., Wiedensohler, A., Höhler, K., Kandler, K., Ma, N., Dietel, B., Schiebel, T., Möhler, O., Stratmann, F.: Ground-based measurements on aerosol particles at Paphos, Cyprus, in March–April 2017, PANGAEA, https://doi.pangaea.de/10.1594/PANGAEA.904758, last access: 16 August 2019.

Gysel, M. and Stratmann, F.: WP3 – NA3: In-situ chemical, physical and optical properties of aerosols, Deliverable D3.11: Standardized protocol for CCN measurements, Tech. rep., available at: http://www.actris.net/Publications/ACTRISQualityStandards/tabid/11271/language/en-GB/Default.aspx (last access: 18 August 2019), 2013.

Herenz, P., Wex, H., Henning, S., Kristensen, T. B., Rubach, F., Roth, A., Borrmann, S., Bozem, H., Schulz, H., and Stratmann, F.: Measurements of aerosol and CCN properties in the Mackenzie River delta (Canadian Arctic) during spring–summer transition in May 2014, Atmos. Chem. Phys., 18, 4477-4496, https://doi.org/10.5194/acp-18-4477-2018, 2018.

Hiranuma, N., Augustin-Bauditz, S., Bingemer, H., Budke, C., Curtius, J., Danielczok, A., Diehl, K., Dreischmeier, K., Ebert, M., Frank, F., Hoffmann, N., Kandler, K., Kiselev, A., Koop, T., Leisner, T., Möhler, O., Nillius, B., Peckhaus, A., Rose, D., Weinbruch, S., Wex, H., Boose, Y., DeMott, P. J., Hader, J. D., Hill, T. C. J., Kanji, Z. A., Kulkarni, G., Levin, E. J. T., McCluskey, C. S., Murakami, M., Murray, B. J., Niedermeier, D., Petters, M. D., O'Sullivan, D., Saito, A., Schill, G. P., Tajiri, T., Tolbert, M. A., Welti, A., Whale, T. F., Wright, T. P., and Yamashita, K.: A comprehensive laboratory study on the immersion freezing behavior of illite NX particles: a comparison of 17 ice nucleation measurement techniques, Atmos. Chem. Phys., 15, 2489–2518, https://doi.org/10.5194/acp-15-2489-2015, 2015.

Hoppel, W., Frick, G., and Larson, R.: Effect of nonprecipitating clouds on the aerosol size distribution in the marine boundary layer, Geophys. Res. Lett., 13, 125–128, https://doi.org/10.1029/GL013i002p00125, 1986.

Hudda, N. and Fruin, S. A.: International Airport Impacts to Air Quality: Size and Related Properties of Large Increases in Ultrafine Particle Number Concentrations, Environ. Sci. Technol., 50, 3362–3370, https://doi.org/10.1021/acs.est.5b05313, 2016.

Jasinski, R. and Przylebska, K.: Analysis of the particle size distribution near the civil airport runway, IOP Conference Series: Materials Science and Engineering, 421, 042030, https://doi.org/10.1088/1757-899x/421/4/042030, 2018.

Kalivitis, N., Kerminen, V.-M., Kouvarakis, G., Stavroulas, I., Bougiatioti, A., Nenes, A., Manninen, H. E., Petäjä, T., Kulmala, M., and Mihalopoulos, N.: Atmospheric new particle formation as a source of CCN in the eastern Mediterranean marine boundary layer, Atmos. Chem. Phys., 15, 9203–9215, https://doi.org/10.5194/acp-15-9203-2015, 2015.

Kandler, K., Schneiders, K., Ebert, M., Hartmann, M., Weinbruch, S., Prass, M., and Pöhlker, C.: Composition and mixing state of atmospheric aerosols determined by electron microscopy: method development and application to aged Saharan dust deposition in the Caribbean boundary layer, Atmos. Chem. Phys., 18, 13429–13455, https://doi.org/10.5194/acp-18-13429-2018, 2018.

Kanji, Z. A., Ladino, L. A., Wex, H., Boose, Y., Burkert-Kohn, M., Cziczo, D. J., and Krämer, M.: Overview of Ice Nucleating Particles, Meteor. Mon., 58, 1.1–1.33, https://doi.org/10.1175/amsmonographs-d-16-0006.1, 2017.

Köhler, H.: The nucleus in and the growth of hygroscopic droplets, T. Faraday Soc., 32, 1152–1161, 1936.

Kristensen, T. B., Müller, T., Kandler, K., Benker, N., Hartmann, M., Prospero, J. M., Wiedensohler, A., and Stratmann, F.: Properties of cloud condensation nuclei (CCN) in the trade wind marine boundary layer of the western North Atlantic, Atmos. Chem. Phys., 16, 2675–2688, https://doi.org/10.5194/acp-16-2675-2016, 2016.

Lelieveld, J., Berresheim, H., Borrmann, S., Crutzen, P. J., Dentener, F. J., Fischer, H., Feichter, J., Flatau, P. J., Heland, J., Holzinger, R., Korrmann, R., Lawrence, M. G., Levin, Z., Markowicz, K. M., Mihalopoulos, N., Minikin, A., Ramanathan, V., de Reus, M., Roelofs, G. J., Scheeren, H. A., Sciare, J., Schlager, H., Schultz, M., Siegmund, P., Steil, B., Stephanou, E. G., Stier, P., Traub, M., Warneke, C., Williams, J., and Ziereis, H.: Global Air Pollution Crossroads over the Mediterranean, Science, 298, 794–799, https://doi.org/10.1126/science.1075457, 2002.

Mallet, M., Dulac, F., Formenti, P., Nabat, P., Sciare, J., Roberts, G., Pelon, J., Ancellet, G., Tanré, D., Parol, F., Denjean, C., Brogniez, G., di Sarra, A., Alados-Arboledas, L., Arndt, J., Auriol, F., Blarel, L., Bourrianne, T., Chazette, P., Chevaillier, S., Claeys, M., D'Anna, B., Derimian, Y., Desboeufs, K., Di Iorio, T., Doussin, J.-F., Durand, P., Féron, A., Freney, E., Gaimoz, C., Goloub, P., Gómez-Amo, J. L., Granados-Muñoz, M. J., Grand, N., Hamonou, E., Jankowiak, I., Jeannot, M., Léon, J.-F., Maillé, M., Mailler, S., Meloni, D., Menut, L., Momboisse, G., Nicolas, J., Podvin, T., Pont, V., Rea, G., Renard, J.-B., Roblou, L., Schepanski, K., Schwarzenboeck, A., Sellegri, K., Sicard, M., Solmon, F., Somot, S., Torres, B., Totems, J., Triquet, S., Verdier, N., Verwaerde, C., Waquet, F., Wenger, J., and Zapf, P.: Overview of the Chemistry-Aerosol Mediterranean Experiment/Aerosol Direct Radiative Forcing on the Mediterranean Climate (ChArMEx/ADRIMED) summer 2013 campaign, Atmos. Chem. Phys., 16, 455–504, https://doi.org/10.5194/acp-16-455-2016, 2016.

Mamouri, R.-E., Ansmann, A., Nisantzi, A., Solomos, S., Kallos, G., and Hadjimitsis, D. G.: Extreme dust storm over the eastern Mediterranean in September 2015: satellite, lidar, and surface observations in the Cyprus region, Atmos. Chem. Phys., 16, 13711–13724, https://doi.org/10.5194/acp-16-13711-2016, 2016.

Niemand, M., Möhler, O., Vogel, B., Vogel, H., Hoose, C., Connolly, P., Klein, H., Bingemer, H., DeMott, P., Skrotzki, J., and Leisner, T.: A Particle-Surface-Area-Based Parameterization of Immersion Freezing on Desert Dust Particles, J. Atmos. Sci., 69, 3077–3092, https://doi.org/10.1175/jas-d-11-0249.1, 2012.

O'Sullivan, D., Adams, M. P., Tarn, M. D., Harrison, A. D., Vergara-Temprado, J., Porter, G. C. E., Holden, M. A., Sanchez-

Marroquin, A., Carotenuto, F., Whale, T. F., McQuaid, J. B., Walshaw, R., Hedges, D. H. P., Burke, I. T., Cui, Z., and Murray, B. J.: Contributions of biogenic material to the atmospheric ice-nucleating particle population in North Western Europe, Sci. Rep.-UK, 8, 13821, https://doi.org/10.1038/s41598-018-31981-7, 2018.

Ott, D. K. and Peters, T. M.: A Shelter to Protect a Passive Sampler for Coarse Particulate Matter, $PM_{10-2.5}$, Aerosol Sci. Technol., 42, 299–309, https://doi.org/10.1080/02786820802054236, 2008.

Ott, W. R.: A Physical Explanation of the Lognormality of Pollutant Concentrations, J. Air Waste Manage. Assoc., 40, 1378–1383, https://doi.org/10.1080/10473289.1990.10466789, 1990.

Pace, G., Meloni, D., and Di Sarra, A.: Forest fire aerosol over the Mediterranean basin during summer 2003, J. Geophys. Res.-Atmos., 110, https://doi.org/10.1029/2005JD005986, 2005.

Petters, M. D. and Kreidenweis, S. M.: A single parameter representation of hygroscopic growth and cloud condensation nucleus activity, Atmos. Chem. Phys., 7, 1961–1971, https://doi.org/10.5194/acp-7-1961-2007, 2007.

Pfeifer, S., Müller, T., Weinhold, K., Zikova, N., Martins dos Santos, S., Marinoni, A., Bischof, O. F., Kykal, C., Ries, L., Meinhardt, F., Aalto, P., Mihalopoulos, N., and Wiedensohler, A.: Intercomparison of 15 aerodynamic particle size spectrometers (APS 3321): uncertainties in particle sizing and number size distribution, Atmos. Meas. Tech., 9, 1545–1551, https://doi.org/10.5194/amt-9-1545-2016, 2016.

Piazzola, J. and Despiau, S.: Contribution of marine aerosols in the particle size distributions observed in Mediterranean coastal zone, Atmos. Environ., 31, 2991–3009, https://doi.org/10.1016/S1352-2310(97)00088-5, 1997.

Prather, K. A., Bertram, T. H., Grassian, V. H., Deane, G. B., Stokes, M. D., DeMott, P. J., Aluwihare, L. I., Palenik, B. P., Azam, F., Seinfeld, J. H., Moffet, R. C., Molina, M. J., Cappa, C. D., Geiger, F. M., Roberts, G. C., Russell, L. M., Ault, A. P., Baltrusaitis, J., Collins, D. B., Corrigan, C. E., Cuadra-Rodriguez, L. A., Ebben, C. J., Forestieri, S. D., Guasco, T. L., Hersey, S. P., Kim, M. J., Lambert, W. F., Modini, R. L., Mui, W., Pedler, B. E., Ruppel, M. J., Ryder, O. S., Schoepp, N. G., Sullivan, R. C., and Zhao, D.: Bringing the ocean into the laboratory to probe the chemical complexity of sea spray aerosol, P. Natl. Acad. Sci. USA, 110, 7550–7555, https://doi.org/10.1073/pnas.1300262110, 2013.

Price, H. C., Baustian, K. J., McQuaid, J. B., Blyth, A., Bower, K. N., Choularton, T., Cotton, R. J., Cui, Z., Field, P. R., Gallagher, M., Hawker, R., Merrington, A., Miltenberger, A., Neely III, R. R., Parker, S. T., Rosenberg, P. D., Taylor, J. W., Trembath, J., Vergara-Temprado, J., Whale, T. F., Wilson, T. W., Young, G., and Murray, B. J.: Atmospheric Ice-Nucleating Particles in the Dusty Tropical Atlantic, J. Geophys. Res.-Atmos., 123, 2175–2193, https://doi.org/10.1002/2017JD027560, 2018.

Pringle, K. J., Tost, H., Pozzer, A., Pöschl, U., and Lelieveld, J.: Global distribution of the effective aerosol hygroscopicity parameter for CCN activation, Atmos. Chem. Phys., 10, 5241–5255, https://doi.org/10.5194/acp-10-5241-2010, 2010.

Pruppacher, H. and Klett, J.: Microphysics of Clouds and Precipitation, vol. 18, Springer Science & Business Media, Dordrecht, 2010.

Rinaldi, M., Santachiara, G., Nicosia, A., Piazza, M., Decesari, S., Gilardoni, S., Paglione, M., Cristofanelli, P., Marinoni, A., Bonasoni, P., and Belosi, F.: Atmospheric Ice Nucleating Particle measurements at the high mountain observatory Mt. Cimone (2165 m a.s.l., Italy), Atmos. Environ., 171, 173–180, https://doi.org/10.1016/j.atmosenv.2017.10.027, 2017.

Roberts, G. C. and Nenes, A.: A Continuous-Flow Streamwise Thermal-Gradient CCN Chamber for Atmospheric Measurements, Aerosol Sci. Technol., 39, 206–221, https://doi.org/10.1080/027868290913988, 2005.

Rodríguez, S., Querol, X., Alastuey, A., and Plana, F.: Sources and processes affecting levels and composition of atmospheric aerosol in the western Mediterranean, J. Geophys. Res.-Atmos., 107, AAC 12-1–AAC 12-14, https://doi.org/10.1029/2001JD001488, 2002.

Rolph, G.: Real-time environmental applications and display system (READY) website, available at: https://www.ready.noaa.gov/index.php (last access: 15 August 2019), 2003.

Rose, D., Gunthe, S. S., Mikhailov, E., Frank, G. P., Dusek, U., Andreae, M. O., and Pöschl, U.: Calibration and measurement uncertainties of a continuous-flow cloud condensation nuclei counter (DMT-CCNC): CCN activation of ammonium sulfate and sodium chloride aerosol particles in theory and experiment, Atmos. Chem. Phys., 8, 1153–1179, https://doi.org/10.5194/acp-8-1153-2008, 2008.

Salameh, T., Drobinski, P., Menut, L., Bessagnet, B., Flamant, C., Hodzic, A., and Vautard, R.: Aerosol distribution over the western Mediterranean basin during a Tramontane/Mistral event, Ann. Geophys., 25, 2271–2291, https://doi.org/10.5194/angeo-25-2271-2007, 2007.

Sandrini, S., van Pinxteren, D., Giulianelli, L., Herrmann, H., Poulain, L., Facchini, M. C., Gilardoni, S., Rinaldi, M., Paglione, M., Turpin, B. J., Pollini, F., Bucci, S., Zanca, N., and Decesari, S.: Size-resolved aerosol composition at an urban and a rural site in the Po Valley in summertime: implications for secondary aerosol formation, Atmos. Chem. Phys., 16, 10879–10897, https://doi.org/10.5194/acp-16-10879-2016, 2016.

Schladitz, A., Müller, T., Nowak, A., Kandler, K., Lieke, K., Massling, A., and Wiedensohler, A.: In situ aerosol characterization at Cape Verde, Tellus B, 63, 531–548, https://doi.org/10.1111/j.1600-0889.2011.00569.x, 2011.

Schrod, J., Weber, D., Drücke, J., Keleshis, C., Pikridas, M., Ebert, M., Cvetković, B., Nickovic, S., Marinou, E., Baars, H., Ansmann, A., Vrekoussis, M., Mihalopoulos, N., Sciare, J., Curtius, J., and Bingemer, H. G.: Ice nucleating particles over the Eastern Mediterranean measured by unmanned aircraft systems, Atmos. Chem. Phys., 17, 4817–4835, https://doi.org/10.5194/acp-17-4817-2017, 2017.

Sciare, J., Bardouki, H., Moulin, C., and Mihalopoulos, N.: Aerosol sources and their contribution to the chemical composition of aerosols in the Eastern Mediterranean Sea during summertime, Atmos. Chem. Phys., 3, 291–302, https://doi.org/10.5194/acp-3-291-2003, 2003.

Sciare, J., Oikonomou, K., Favez, O., Liakakou, E., Markaki, Z., Cachier, H., and Mihalopoulos, N.: Long-term measurements of carbonaceous aerosols in the Eastern Mediterranean: evidence of long-range transport of biomass burning, Atmos. Chem. Phys., 8, 5551–5563, https://doi.org/10.5194/acp-8-5551-2008, 2008.

Smoydzin, L., Teller, A., Tost, H., Fnais, M., and Lelieveld, J.: Impact of mineral dust on cloud formation in a Saharan outflow region, Atmos. Chem. Phys., 12, 11383–11393, https://doi.org/10.5194/acp-12-11383-2012, 2012.

Stein, A. F., Draxler, R. R., Rolph, G. D., Stunder, B. J. B., Cohen, M. D., and Ngan, F.: NOAA's HYSPLIT Atmospheric Transport and Dispersion Modeling System, B. Am. Meteorol. Soc., 96, 2059–2077, https://doi.org/10.1175/bams-d-14-00110.1, 2015.

Tobo, Y., Prenni, A. J., DeMott, P. J., Huffman, J. A., McCluskey, C. S., Tian, G., Pöhlker, C., Pöschl, U., and Kreidenweis, S. M.: Biological aerosol particles as a key determinant of ice nuclei populations in a forest ecosystem, J. Geophys. Res.-Atmos., 118, 10100–10110, https://doi.org/10.1002/jgrd.50801, 2013.

Ullrich, R., Hoose, C., Möhler, O., Niemand, M., Wagner, R., Höhler, K., Hiranuma, N., Saathoff, H., and Leisner, T.: A New Ice Nucleation Active Site Parameterization for Desert Dust and Soot, J. Atmos. Sci., 74, 699–717, https://doi.org/10.1175/jas-d-16-0074.1, 2017.

Vali, G.: Quantitative Evaluation of Experimental Results an the Heterogeneous Freezing Nucleation of Supercooled Liquids, J. Atmos. Sci., 28, 402–409, https://doi.org/10.1175/1520-0469(1971)028<0402:qeoera>2.0.co;2, 1971.

von der Weiden, S.-L., Drewnick, F., and Borrmann, S.: Particle Loss Calculator – a new software tool for the assessment of the performance of aerosol inlet systems, Atmos. Meas. Tech., 2, 479–494, https://doi.org/10.5194/amt-2-479-2009, 2009.

Welti, A., Müller, K., Fleming, Z. L., and Stratmann, F.: Concentration and variability of ice nuclei in the subtropical maritime boundary layer, Atmos. Chem. Phys., 18, 5307–5320, https://doi.org/10.5194/acp-18-5307-2018, 2018.

Wiedensohler, A.: An approximation of the bipolar charge distribution for particles in the submicron size range, J. Aerosol Sci., 19, 387–389, https://doi.org/10.1016/0021-8502(88)90278-9, 1988.

Wiedensohler, A., Birmili, W., Nowak, A., Sonntag, A., Weinhold, K., Merkel, M., Wehner, B., Tuch, T., Pfeifer, S., Fiebig, M., Fjäraa, A. M., Asmi, E., Sellegri, K., Depuy, R., Venzac, H., Villani, P., Laj, P., Aalto, P., Ogren, J. A., Swietlicki, E., Williams, P., Roldin, P., Quincey, P., Hüglin, C., Fierz-Schmidhauser, R., Gysel, M., Weingartner, E., Riccobono, F., Santos, S., Grüning, C., Faloon, K., Beddows, D., Harrison, R., Monahan, C., Jennings, S. G., O'Dowd, C. D., Marinoni, A., Horn, H.-G., Keck, L., Jiang, J., Scheckman, J., McMurry, P. H., Deng, Z., Zhao, C. S., Moerman, M., Henzing, B., de Leeuw, G., Löschau, G., and Bastian, S.: Mobility particle size spectrometers: harmonization of technical standards and data structure to facilitate high quality long-term observations of atmospheric particle number size distributions, Atmos. Meas. Tech., 5, 657–685, https://doi.org/10.5194/amt-5-657-2012, 2012.

Wiedensohler, A., Wiesner, A., Weinhold, K., Birmili, W., Hermann, M., Merkel, M., Müller, T., Pfeifer, S., Schmidt, A., Tuch, T., Velarde, F., Quincey, P., Seeger, S., and Nowak, A.: Mobility particle size spectrometers: Calibration procedures and measurement uncertainties, Aerosol Sci. Technol., 52, 146–164, https://doi.org/10.1080/02786826.2017.1387229, 2018.

Supplement of Atmos. Chem. Phys., 19, 10883–10900, 2019
https://doi.org/10.5194/acp-19-10883-2019-supplement

Atmospheric Chemistry and Physics
Open Access
EGU

Supplement of

Characterization of aerosol properties at Cyprus, focusing on cloud condensation nuclei and ice-nucleating particles

Xianda Gong et al.

Correspondence to: Xianda Gong (gong@tropos.de)

S1 Instrumentation

As shown in Fig. S1.

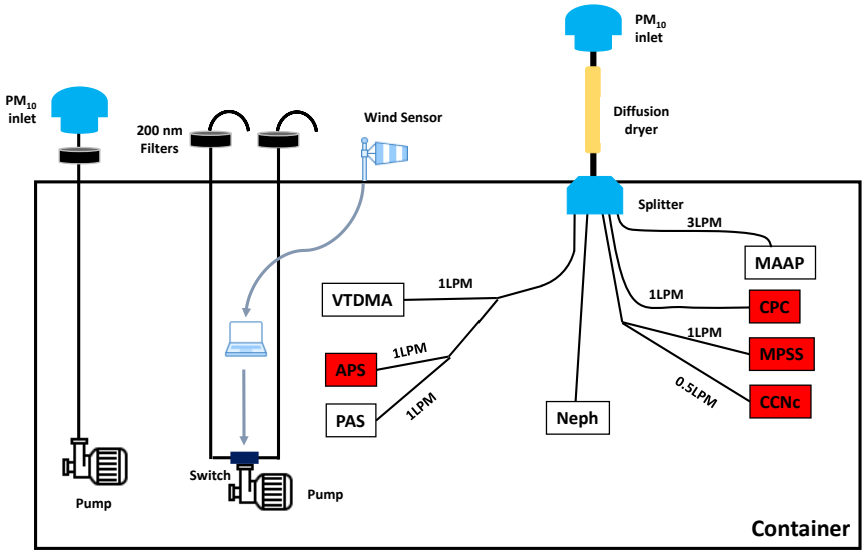

Figure S1. A schematic diagram of the measurement system and flow rate partitioning to the measurement devices. Indicated by the word "Switch" is a computer-based system that switched between two filters according to wind directions. The on-line instruments discussed in this paper are marked with red background. MPSS, APS and CCNc represent Mobility Particle Size Spectrometer, Aerodynamic Particle Sizer and Cloud Condensation Nuclei counter, respectively.

S2 Accounting for particle losses

The particle losses related to the transport of aerosol particles within the inlet tube system are determined using the Particle Loss Calculator (PLC) (von der Weiden et al., 2009). Size-dependent particle losses due to diffusion, sedimentation, turbulent inertial deposition, inertial deposition in a bend, and inertial deposition in a contraction are accounted for. The result is shown in Fig. S2, which depicts particle losses in % as a function of particle size.

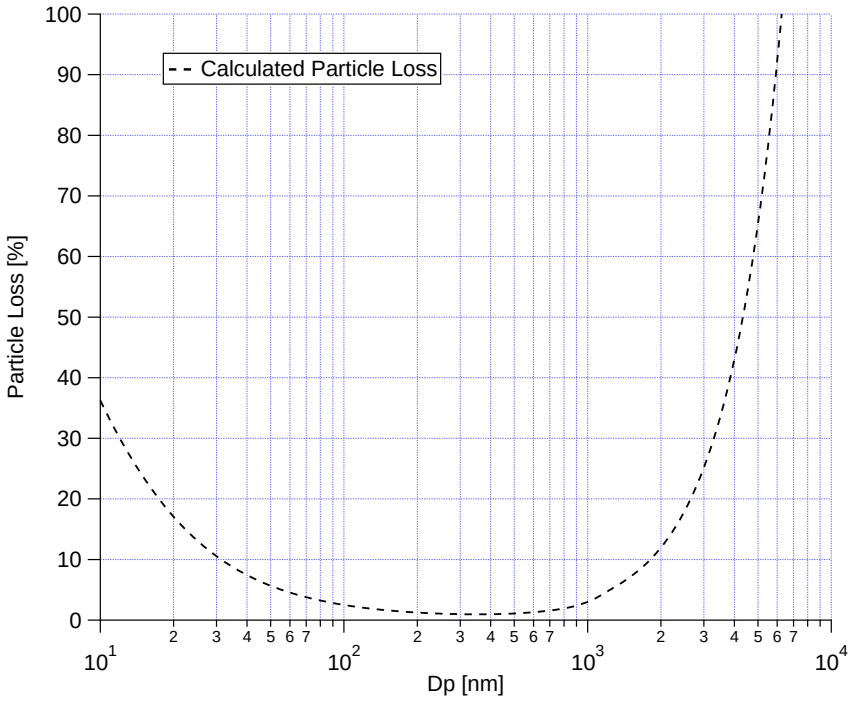

Figure S2. Size-dependent particle loss through the inlet.

S3 Filter sample information and pre-experiment

Table S1. The information of TROPOS filter samples, including the sample number, start time, start flow, stop time, end flow, duration and status.

Sample number	Start time (UTC)	Start flow (L min^{-1})	Stop time (UTC)	End flow (L min^{-1})	Duration (h)	Status
Sample 01	2017/04/06 07:50:00	10.76	2017/4/09 06:10:00	9.95	23.07	Ocean sector
Sample 02	-	-	-	-	-	Blind filter
Sample 03	2017/04/07 09:50:00	10.00	2017/4/09 06:10:00	7.92	26.09	Land sector
Sample 04	2017/04/09 07:30:00	10.61	2017/4/14 06:30:00	12.10	23.76	Ocean sector
Sample 05	2017/04/09 07:30:00	9.85	2017/4/10 06:20:00	8.74	22.63	Land sector
Sample 07	2017/04/11 07:00:00	9.73	2017/4/12 06:30:00	8.89	22.00	Land sector
Sample 08	2017/04/12 07:00:00	9.86	2017/4/14 06:30:00	8.68	25.65	Land sector
Sample 09	2017/04/14 07:50:00	9.83	2017/4/18 07:10:00	4.19	20.65	Ocean sector
Sample 10	2017/04/14 07:50:00	9.55	2017/4/15 06:20:00	6.11	21.04	Land sector
Sample 11	2017/04/15 06:40:00	9.80	2017/4/16 06:40:00	8.79	23.73	Land sector
Sample 12	2017/04/16 07:00:00	9.67	2017/4/18 11:00:00	7.74	18.21	Land sector
Sample 13	2017/04/18 07:30:00	9.68	2017/4/21 08:00:00	8.4	20.87	Ocean sector
Sample 14	2017/04/18 11:20:00	9.60	2017/4/19 09:40:00	8.12	18.12	Land sector
Sample 15	2017/04/19 09:50:00	9.49	2017/4/20 09:20:00	9.07	19.83	Land sector
Sample 16	2017/04/20 09:40:00	9.70	2017/4/22 06:30:00	9.34	26.20	Land sector
Sample 17	-	-	-	-	-	Blind filter
Sample 18	2017/04/22 06:40:00	9.74	2017/4/23 06:20:00	8.28	22.20	Land sector
Sample 19	2017/04/23 06:40:00	9.53	2017/4/24 06:20:00	7.95	23.05	Land sector
Sample 20	2017/04/24 06:40:00	9.65	2017/4/25 06:20:00	8.08	23.61	Land sector
Sample 21	2017/04/25 06:40:00	9.65	2017/4/26 09:40:00	8.71	20.42	Land sector
Sample 22	2017/04/26 09:50:00	9.65	2017/4/27 06:50:00	8.91	20.95	Land sector
Sample 23	2017/04/27 07:00:00	9.67	2017/4/28 06:30:00	8.11	22.95	Land sector
Sample 24	2017/04/28 06:40:00	9.57	2017/4/29 06:20:00	6.67	23.16	Land sector

Table S2. The information of KIT filter samples, including the sample number, start time, stop time, flow and duration.

Sample number	Start time (UTC)	Stop time (UTC)	Flow (L min^{-1})	Duration (h)
Sample01	2017/04/02 13:00:00	2017/04/02 17:00:00	15	4.00
Sample02	2017/04/03 07:08:00	2017/04/03 15:13:00	15	8.08
Sample04	2017/04/04 07:29:00	2017/04/04 15:17:00	15	7.80
Sample06	2017/04/05 07:34:00	2017/04/05 15:36:00	15	8.03
Sample08	2017/04/06 08:06:00	2017/04/06 13:58:00	15	5.87
Sample10	2017/04/07 07:31:00	2017/04/07 15:40:00	15	8.15
Sample11	2017/04/08 08:20:00	2017/04/08 16:20:00	15	8.00
Sample12	2017/04/09 09:35:00	2017/04/09 17:35:00	15	8.00
Sample13	2017/04/10 07:30:00	2017/04/10 15:30:00	15	8.00
Sample14	2017/04/11 08:30:00	2017/04/11 16:30:00	15	8.00
Sample15	2017/04/12 07:35:00	2017/04/12 15:35:00	15	8.00
Sample16	2017/04/13 07:35:00	2017/04/13 15:35:00	15	8.00
Sample17	2017/04/14 07:35:00	2017/04/14 15:35:00	15	8.00
Sample18	2017/04/15 07:35:00	2017/04/15 15:35:00	15	8.00
Sample19	2017/04/16 07:35:00	2017/04/16 15:35:00	15	8.00
Sample20	2017/04/17 07:43:00	2017/04/17 15:43:00	15	8.00
Sample21	2017/04/18 07:43:00	2017/04/18 15:43:00	15	8.00
Sample22	2017/04/19 07:43:00	2017/04/19 15:43:00	15	8.00
Sample23	2017/04/20 07:43:00	2017/04/20 15:43:00	15	8.00
Sample24	2017/04/21 07:43:00	2017/04/21 15:43:00	15	8.00
Sample25	2017/04/22 06:55:00	2017/04/22 14:20:00	15	7.42
Sample27	2017/04/23 07:15:00	2017/04/23 15:15:00	15	8.00
Sample28	2017/04/24 06:42:00	2017/04/24 14:42:00	15	8.00
Sample30	2017/04/25 07:26:00	2017/04/25 15:26:00	15	8.00
Sample32	2017/04/26 07:32:00	2017/04/26 15:32:00	15	8.00

When data evaluation was started for this set of samples, tests were made (as these were the first atmospheric samples on polycarbonate for which we did an analysis). A set of measurements was done in which filters were washed off with 1 mL of ultrapure water, first. This was done by shaking the centrifuge tube in which filter and water were situated. From this, 0.1 mL was used for a first analysis, directly taken from the tube in which the shaking had been done. Then 9.1 mL were added to the tube and the sample was shaken again, followed by a second analysis. The results from both dilutions can be seen in Fig. S3, and data in the overlapping temperature region are well in agreement. Based on this, we decided to use only 1 mL for washing, as this allows us to retrieve INP concentrations already at higher temperatures.

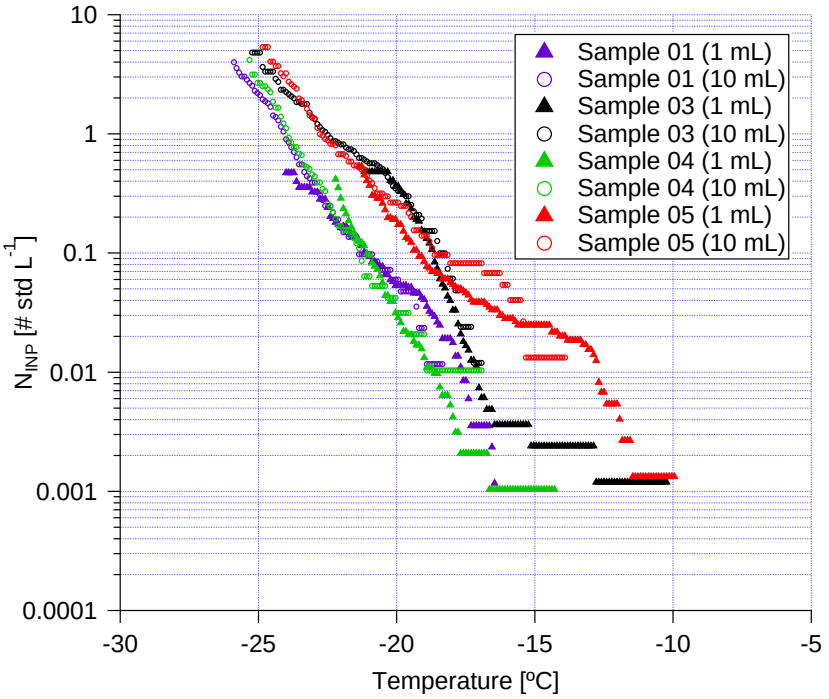

Figure S3. N_{INP} measured by LINA as a function of temperature. The solid triangles and hollow circles show N_{INP} from the samples washed with 1 mL and 10 mL ultrapure water, respectively.

S4 Wind speed and direction

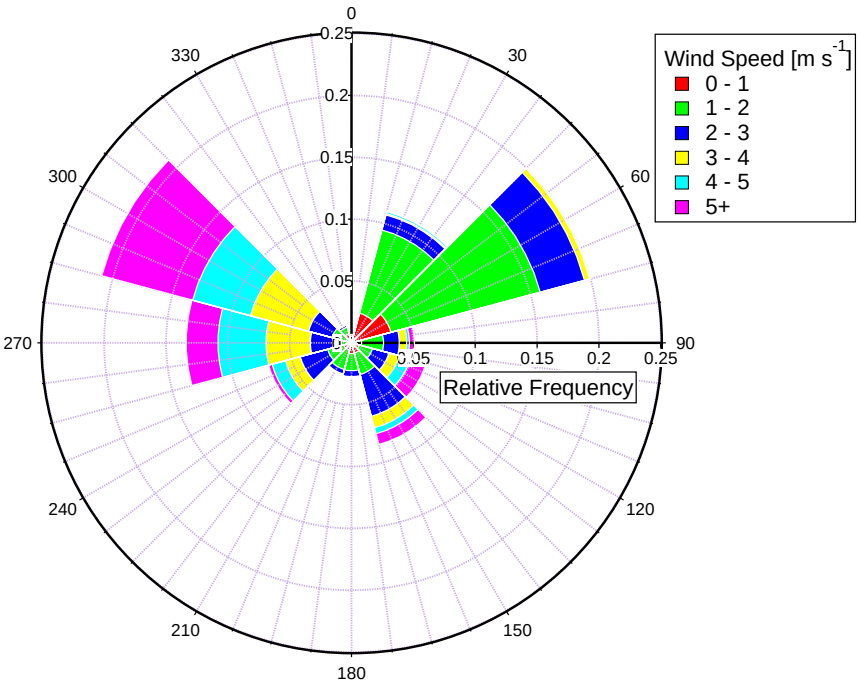

Figure S4. Wind rose based on 10 minutes mean of wind speed and direction measured at the station for whole campaign.

S5 Correlation of NO_x and N_{total}

Fig. S5 shows the scatter plot of N_{total} against NO_x. A good correlation (R^2=0.62) was found between extremely high concentrations of NO_x and N_{total} (upper panel in Fig. S5). No correlation was observed at lower concentrations of NO_x and N_{total} (lower panel in Fig. S5).

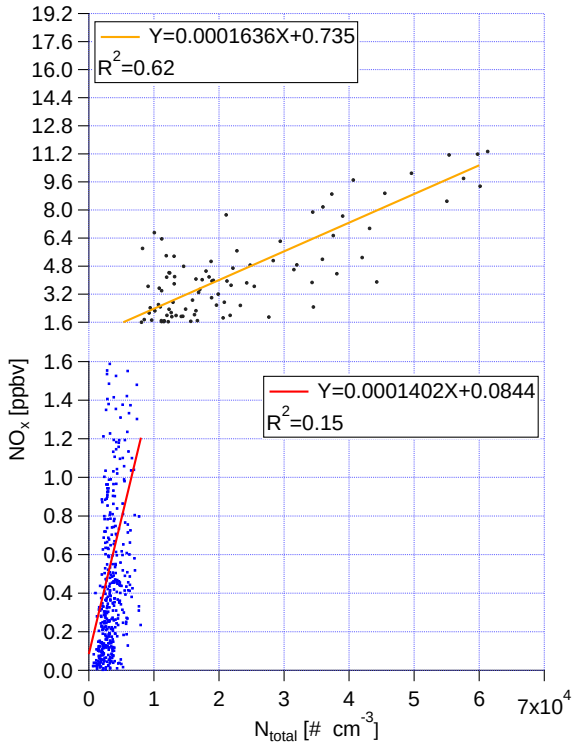

Figure S5. Scatter plot of N_{total} versus NOx. R^2 and fitting function are given in the panels.

S6 Identification of pollution periods

Fig. S6 shows the measured super-micron PNSDs as contour plot, together with NO_x information from 06:00 UTC 16 to 00:00 UTC 18 April. Pollution events were identified based on the PNSDs. The criteria are, first of all, the appearance of a distinct ultrafine particle mode with a dN/dlogDp value large than 3000 cm^{-3} at 15 nm. Secondly, the ultrafine particle mode featured similar PNSDs, without any sign of growth.

The resulting PNSDs during the pollution events featured a pronounced mode with a maximum at about 15 nm (median dN/dlogDp value larger than 10^4 cm^{-3}). Three pollution periods were observed in the example shown here, i.e., from 18:10

to 22:20 UTC 16 Apr, 04:50 to 05:10 UCT, 17:30 to 20:50 UTC 17 Apr. During the pollution periods, high concentrations of NO_x were also observed.

Once we identified all the pollution periods. We made the wind rose plot for all the pollution periods, as shown in Fig. S7.

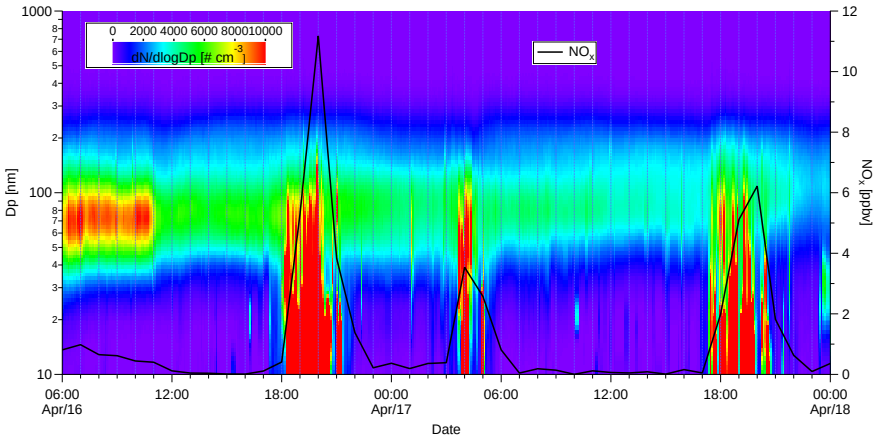

Figure S6. Contour plots for PNSDs from 06:00 UTC 16 to 00:00 UTC 18 April. Black line shows time series of NO_x concentration.

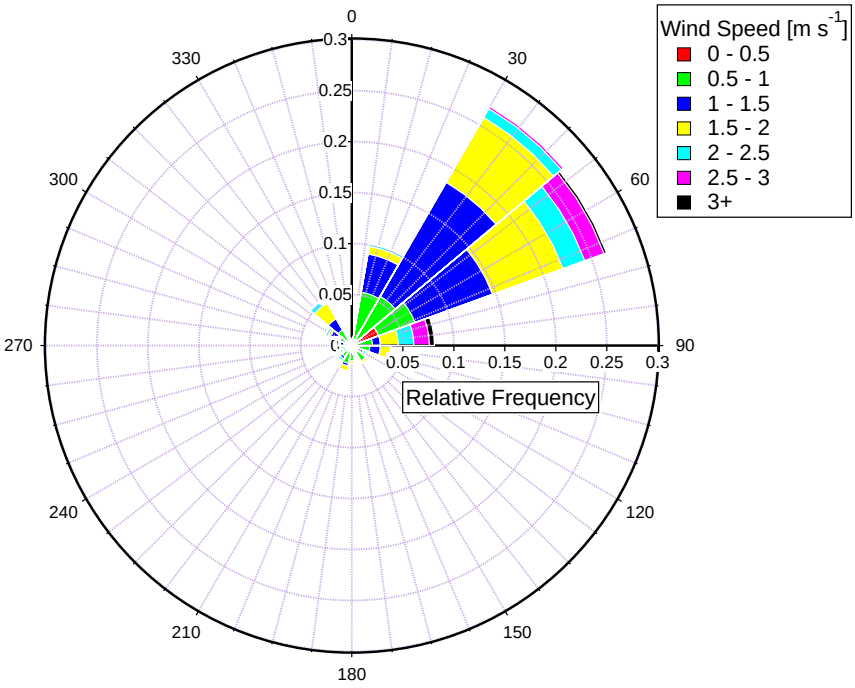

Figure S7. Wind rose based on 10 minutes average of wind speed and direction measured at the station for pollution periods.

S7 Filter background and measurement uncertainty

As shown in Fig. S8, the background of LINA and INSEKT measurement is tested. The ultrapure water droplets started to freeze at -20 °C. Compared to the ultrapure water, the frozen fraction (f_{ice}) curve from blind filters washed with ultrapure water is shifted approx 1 °C towards higher temperatures. The f_{ice} curves determined for atmospheric filter samples are clearly above those obtained for the blind filters, while the f_{ice} of 225- and 3375-fold dilutions of the filter washing water is close to that of ultrapure water.

For the subtraction of background, we used the same method as proposed by Umo et al. (2015). Thereto, the cumulative concentration of INP per air volume determined for the blind filters (KT_{blind}) was subtracted from that for filter samples (KT_{filter}):

$$N_{\text{INP}} = KT_{\text{filter}} - KT_{\text{blind}} \tag{1}$$

Based on Agresti and Coull (1998), the confidence interval of f_{ice} can be calculated by:

$$\left(f_{\text{ice}} + \frac{z_{\alpha/2}^2}{2n} \pm z_{\alpha/2}\sqrt{[f_{\text{ice}}(1-f_{\text{ice}}) + z_{\alpha/2}^2/(4n)]/n}\right) / \left(1 + \frac{z_{\alpha/2}^2}{n}\right) \tag{2}$$

where $z_{\alpha/2}^2$ is the standard score at a confidence level $\alpha/2$, which for a 95% confidence interval is 1.96. n is the droplet number of each experiment.

The uncertainty of N_{INP} is calculated based on the uncertainty of the f_{ice} as we outlined above. The error bar in Fig. S9 represents 95% confidence interval for N_{INP}.

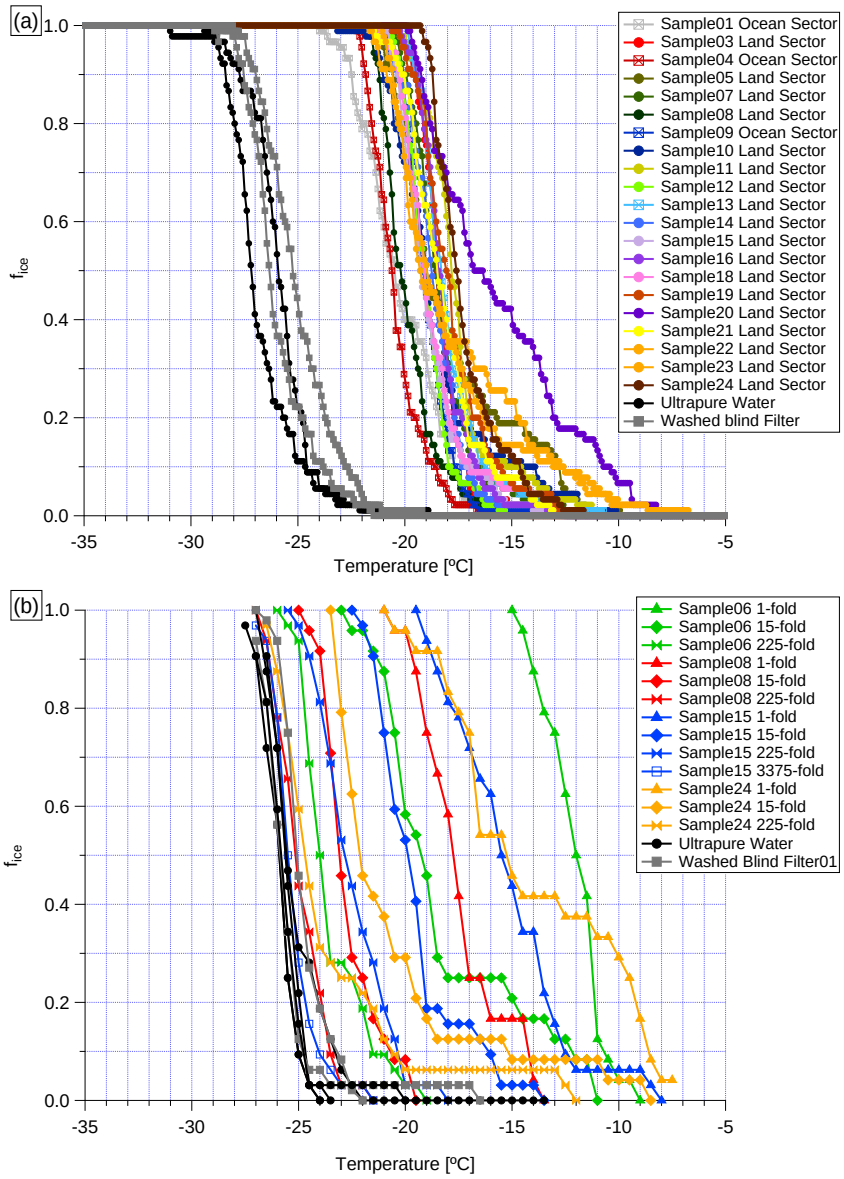

Figure S8. The f_{ice} of washed filter samples, together with background signals of ultrapure water and ultrapure water washed blind filter samples of LINA (a) and INSEKT (b) measurement results. For INSEKT, only a subset of all samples is shown exemplarily, to enable seeing curves for the same sample from different dilutions.

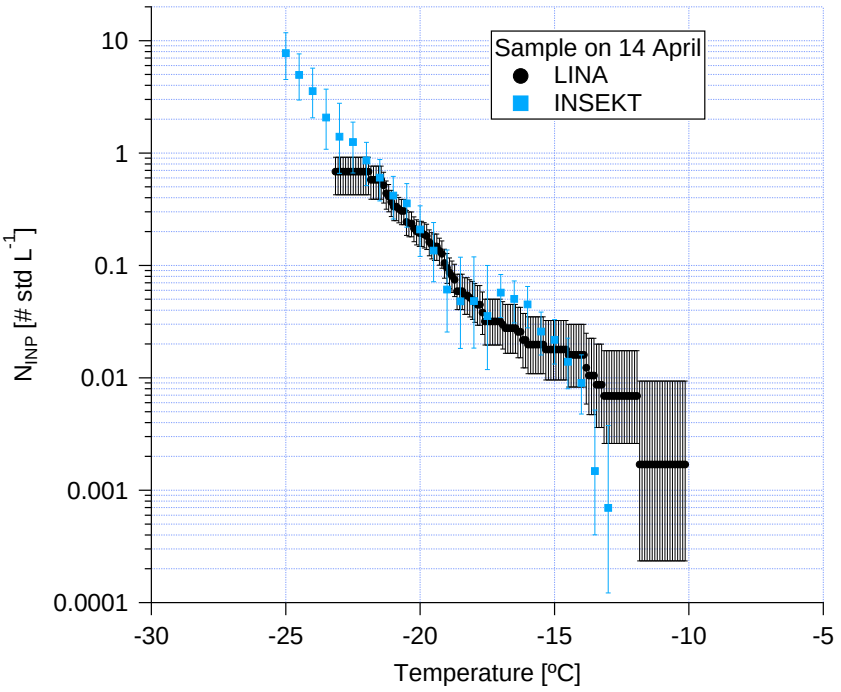

Figure S9. N_{INP} measured by LINA (black) and INSEKT (blue) as a function of temperature. For comparison, the LINA and INSEKT results here were both sampled on 14 April. The error bar shows the 95% confidence interval in N_{INP}.

S8 INSEKT measured N_{INP} against the ratio of time sampling from the ocean sector

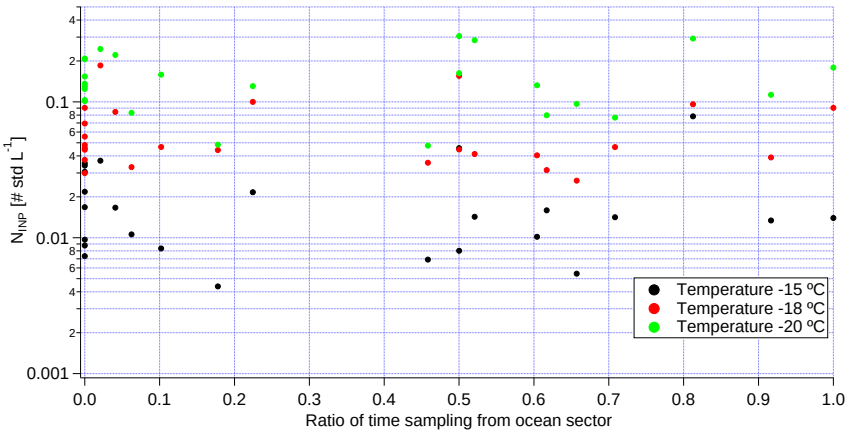

Figure S10. Scatter plot of N_{INP} (measured by INSEKT) versus the ratio of time sampling from the ocean sector at -15, -18 and -20 °C.

S9 Log-normal distribution of N_{INP} test

Here we used two methods to test our N_{INP} frequency distributions. The quantile-quantile plot was originally proposed by Wilk and Gnanadesikan (1968) to compare two distributions by plotting quantiles of one versus quantiles of the other. Here, we plot logarithmic N_{INP} at -18 °C versus a standard normal distribution, as shown in Fig. S11. The measured N_{INP} is close to the reference line, indicating that the N_{INP} follows the log-normal distribution. Note that the quantile-quantile plot provides only a rough measure how similar the compared distributions are.

Table S3. Lillifors test results.

Temperature	LINA		INSEKT	
	h	p	h	p
-15 °C	0	0.3455	0	0.4461
-18 °C	0	0.1810	0	0.1400
-20 °C	0	0.0355	0	0.5000

Furthermore, we used the Lilliefors test (Lilliefors, 1967) to determine if the observed N_{INP} frequency distributions follow a log-normal distribution. In statistics, the Lilliefors test is a normality test based on the Kolmogorov-Smirnov test (Sachs, 2012). It is used to test the null hypothesis of the data following a normal distribution, with the null hypothesis not including the actual

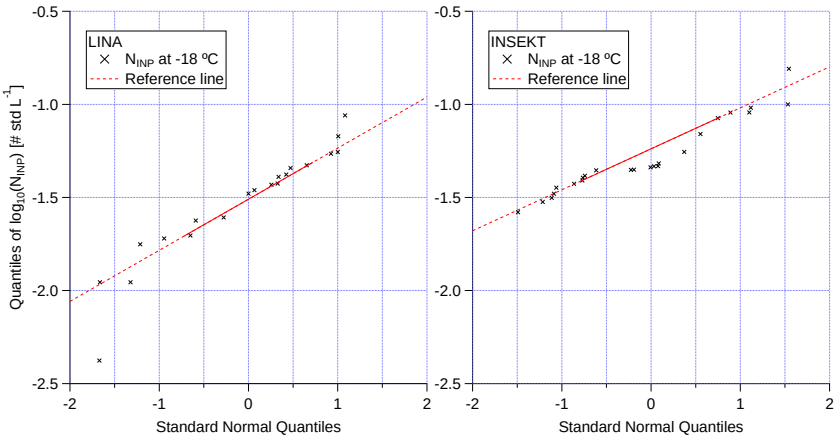

Figure S11. The quantile-quantile plot of logarithmic N_{INP} measured by LINA and INSEKT at -18 °C with a random normal distribution.

parameters (mean and standard deviation) of the normal distribution. Results (h-value and p-value) of the carried out Lilliefors tests are shown in Tab. S3. A return value of h = 0 indicates that the logarithmic N_{INP} (measured by LINA and INSEKT) follow normal distributions at -15, -18 and -20 °C. As log-normally distributed N_{INP} are indicative for the observed INP population having undergone a series of random dilutions while being transported (Welti et al., 2018), the performed Lilliefors tests yield additional prove for the INP sampled during our measurements originating from long-range transport rather than local sources.

S10 Correlation of N_{INP} with particle number/surface area concentration

Table S4. Coefficient of determination (R^2) of LINA and INSEKT measured N_{INP} with $N_{>500\mathrm{nm}}$.

Temperature	LINA	INSEKT
-15 °C	0.0877	0.0277
-18 °C	0.2369	0.0602
-20 °C	0.0950	0.0006

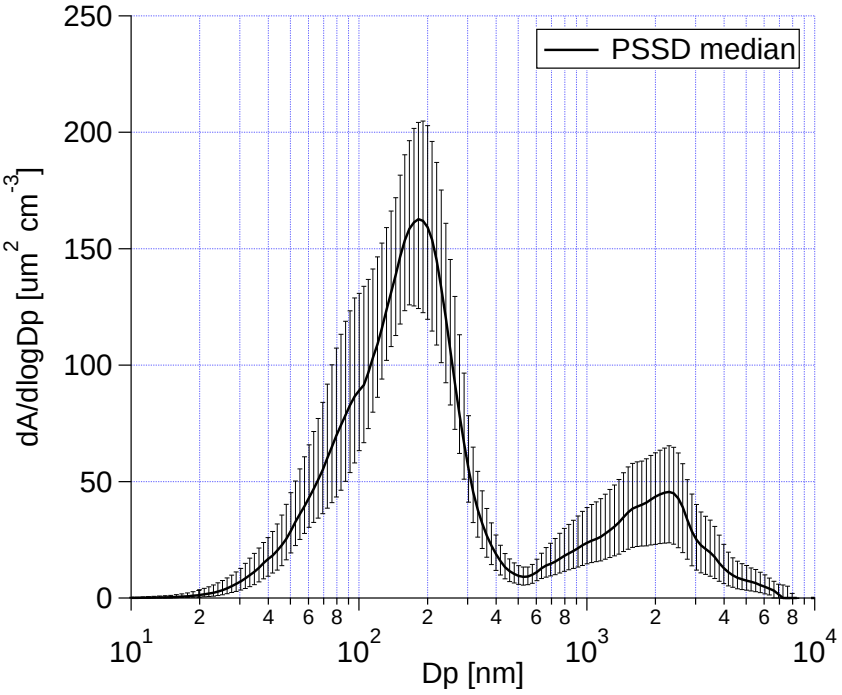

Figure S12. The median PSSD (excluding airport pollution period) during the whole campaign. The error bar indicates the range between the 25 % and 75 % percentiles.

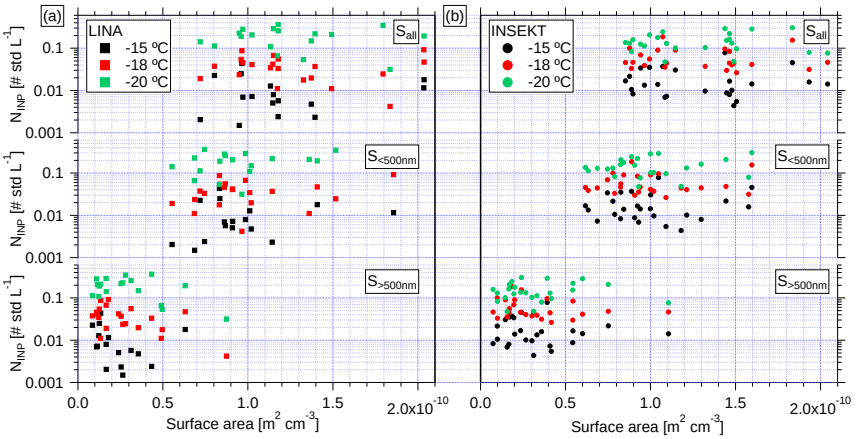

Figure S13. Scatter plot of N_{INP} (measured by LINA (a) and INSEKT (b)) against S_{all}, S_1, S_2 at -15, -18 and -20 °C.

Table S5. R^2 of LINA and INSEKT measured N_{INP} with particle surface area concentration.

Temperature	LINA			INSEKT		
	S_{all}	S_1	S_2	S_{all}	S_1	S_2
−15 °C	0.0009	0.0011	0.0319	0.0016	0.0153	0.0055
−18 °C	0.0002	0.0905	0.1945	0.0059	0.0079	0.0521
−20 °C	0.0001	0.0852	0.1255	0.0395	0.0362	0.0057

References

Agresti, A. and Coull, B. A.: Approximate is Better than "Exact" for Interval Estimation of Binomial Proportions, The American Statistician, 52, 119–126, https://doi.org/10.1080/00031305.1998.10480550, https://doi.org/10.1080/00031305.1998.10480550, 1998.

Lilliefors, H. W.: On the Kolmogorov-Smirnov Test for Normality with Mean and Variance Unknown, Journal of the American Statistical Association, 62, 399–402, https://doi.org/10.1080/01621459.1967.10482916, https://amstat.tandfonline.com/doi/abs/10.1080/01621459.1967.10482916, 1967.

Sachs, L.: Applied statistics: a handbook of techniques, Springer Science & Business Media, 2012.

Umo, N., Murray, B., Baeza-Romero, M., Jones, J., Lea-Langton, A., Malkin, T., O'Sullivan, D., Neve, L., Plane, J., and Williams, A.: Ice nucleation by combustion ash particles at conditions relevant to mixed-phase clouds, Atmospheric Chemistry and Physics, 15, 5195–5210, 2015.

von der Weiden, S. L., Drewnick, F., and Borrmann, S.: Particle Loss Calculator - a new software tool for the assessment of the performance of aerosol inlet systems, Atmos. Meas. Tech., 2, 479–494, https://doi.org/10.5194/amt-2-479-2009, http://www.atmos-meas-tech.net/2/479/2009/, 2009.

Welti, A., Müller, K., Fleming, Z. L., and Stratmann, F.: Concentration and variability of ice nuclei in the subtropical maritime boundary layer, Atmospheric Chemistry and Physics, 18, 5307–5320, 2018.

Wilk, M. B. and Gnanadesikan, R.: Probability plotting methods for the analysis for the analysis of data, Biometrika, 55, 1–17, https://doi.org/10.1093/biomet/55.1.1, http://dx.doi.org/10.1093/biomet/55.1.1, 1968.

3.2 Second Publication: Characterization of aerosol particles at Cabo Verde close to sea level and at the cloud level – Part 1: Particle number size distribution, cloud condensation nuclei and their origins

The content of this section has already been published under the title "Characterization of aerosol particles at Cabo Verde close to sea level and at the cloud level – Part 1: Particle number size distribution, cloud condensation nuclei and their origins" by Gong, X., Wex, H., Voigtländer, J., Fomba, K. W., Weinhold, K., van Pinxteren, M., Henning, S., Müller, T., Herrmann, H., and Stratmann, F. In 2020, the paper was published under the Creative Commons Attribution 4.0 License in *Atmos. Chem. Phys.* with the doi: https://doi.org/10.5194/acp-20-1431-2020.

Reprinted with permission by the authors from *Atmos. Chem. Phys.*, 20, 1431–1449, 2020.

Atmos. Chem. Phys., 20, 1431–1449, 2020
https://doi.org/10.5194/acp-20-1431-2020

Atmospheric Chemistry and Physics
Open Access
EGU

Characterization of aerosol particles at Cabo Verde close to sea level and at the cloud level – Part 1: Particle number size distribution, cloud condensation nuclei and their origins

Xianda Gong, Heike Wex, Jens Voigtländer, Khanneh Wadinga Fomba, Kay Weinhold, Manuela van Pinxteren, Silvia Henning, Thomas Müller, Hartmut Herrmann, and Frank Stratmann

Leibniz Institute for Tropospheric Research, Leipzig, Germany

Correspondence: Xianda Gong (gong@tropos.de)

Received: 19 June 2019 – Discussion started: 11 July 2019
Revised: 7 December 2019 – Accepted: 13 January 2020 – Published: 6 February 2020

Abstract. In the framework of the MarParCloud (Marine biological production, organic aerosol particles and marine clouds: a Process Chain) project, measurements were carried out on the islands of Cabo Verde (a.k.a. Cape Verde) to investigate the abundance, properties and sources of aerosol particles in general, and cloud condensation nuclei (CCN) in particular, both close to sea level and at the cloud level.

A thorough comparison of particle number concentration (PNC), particle number size distribution (PNSD) and CCN number concentration (N_{CCN}) at the Cape Verde Atmospheric Observatory (CVAO, sea-level station) and Monte Verde (MV, cloud-level station) reveals that during times without clouds the aerosols at CVAO and MV are similar and the boundary layer is generally well mixed. Therefore, data obtained at CVAO can be used to describe the aerosol particles at cloud level. Cloud events were observed at MV during roughly 58 % of the time, and during these events a large fraction of particles was activated to cloud droplets.

A trimodal parameterization method was deployed to characterize PNC at CVAO. Based on number concentrations in different aerosol modes, four well-separable types of PNSDs were found, which were named the marine type, mixture type, dust type1 and dust type2. Aerosol particles differ depending on their origins. When the air masses came from the Atlantic Ocean, sea spray can be assumed to be one source for particles besides new particle formation. For these air masses, PNSDs featured the lowest number concentration in Aitken, accumulation and coarse modes. Particle number concentrations for sea spray aerosol (SSA, i.e., the coarse mode for these air masses) accounted for about 3.7 % of $N_{CCN,0.30\,\%}$ (CCN number concentration at 0.30 % supersaturation) and about 1.1 % to 4.4 % of N_{total} (total particle number concentration). When the air masses came from the Sahara, we observed enhanced Aitken, accumulation and coarse mode particle number concentrations and overall increased N_{CCN}; $N_{CCN,0.30\,\%}$ during the strongest observed dust periods is about 2.5 times higher than that during marine periods. However, the particle hygroscopicity parameter κ for these two most different periods shows no significant difference and is generally similar, independent of air mass.

Overall, κ averaged 0.28, suggesting the presence of organic material in particles. This is consistent with previous model work and field measurements. There is a slight increase in κ with increasing particle size, indicating the addition of soluble, likely inorganic, material during cloud processing.

1 Introduction

Clouds in the atmosphere are formed when excess water vapor condenses on aerosol particles that serve as cloud condensation nuclei (CCN). Back in the 1970s, Twomey (1974) described that an increase in the number of aerosol particles that activate to clouds led to more but smaller droplets. Albrecht (1989) suggested that smaller droplets then cause suppression in the formation of precipitation, leading to a prolonged cloud lifetime. Both of these effects enhance the shortwave reflection of clouds, i.e., they lead to a cooling of the atmosphere. In particular, warm low-level clouds located in the boundary layer constitute an important role in the cool-

ing effects due to their abundance and strong cloud albedo effect (Christensen et al., 2016). In recent years, many more aspects of aerosol–cloud interactions were discussed. Considerable progress has been made in understanding the chemical composition and microphysical properties of aerosol particles that enable them to act as CCN (Andreae and Rosenfeld, 2008). The ability of particles to act as CCN is largely controlled by aerosol particle size rather than composition (Dusek et al., 2006). However, we still lack understanding of the overall roles of aerosol particles, clouds and their interactions in the climate system, which contribute to the largest uncertainties to estimate the Earth's energy budget (Stocker, 2014).

Mineral dust from deserts contributes largely to tropospheric aerosols and impacts the air quality of several regions, even of the globe (Ginoux et al., 2001; Huang et al., 2006; Tanaka and Chiba, 2006). The largest dust source is located in the Northern Hemisphere in the Sahara and Sahel regions (Goudie and Middleton, 2001; Prospero et al., 2002; Ginoux et al., 2012), with millions of tonnes of mineral dust being transported to Europe and the Middle East, as well as to the Americas, yearly (including the Caribbean and the Amazon basin) (Swap et al., 1992; Salvador et al., 2013; Wex et al., 2016). Mineral dust aerosol in the atmosphere can affect the Earth's radiative budget by directly scattering and absorbing solar and infrared radiation (Goudie and Middleton, 2001; Shao et al., 2011). On the other hand, it can modify cloud properties, i.e., serve as CCN or ice-nucleating particles (INPs) (Sassen et al., 2003; DeMott et al., 2003). Karydis et al. (2011) found that the predicted annual average contribution of insoluble mineral dust to CCN number concentration in cloud-forming areas is up to 40 % over northern Africa and Asia (Arabian Peninsula and Gobi Desert).

Based on a 3-week field campaign in summer 1973 at Cabo Verde, Jaenicke and Schütz (1978) investigated the aerosol properties, such as total size distribution, mass, sea salt, mineral and organic compound content, and found that a total mass of $100\,\mu g\,m^{-3}$ during dust plumes is 5 times higher than the $20\,\mu g\,m^{-3}$ of clean air masses. Kandler et al. (2011b) also found that the total particle mass concentration during dust plumes was raised by a factor of more than 10 over the maritime mass concentration, demonstrating a strong impact of Saharan dust advection on the aerosol load at Cabo Verde. Significant seasonal intrusions of dust from northwest Africa affect Cabo Verde at surface level from October till March. An hourly PM_{10} value reached up to $710\,\mu g\,m^{-3}$ at surface level at Cabo Verde (Gama et al., 2015). Schladitz et al. (2011b) found that mineral dust particles were mainly in the coarse mode. The variation in the amount of mineral dust is much larger than the variation in the sea salt content in the coarse mode. Also pesticides, polycyclic aromatic hydrocarbons (PAHs), and polychlorinated biphenyl (PCB), all of which originate from the Sahara and Sahel regions, can be incorporated with Saharan dust and then transported to Cabo Verde (Garrison et al., 2014).

Many studies investigated the marine aerosol in laboratory or in field measurements, but few of them were carried out at Cabo Verde or nearby regions. Due to the vast coverage of the Earth's surface by the oceans, wind-driven particle production on the ocean surface is one of the largest global sources of primary atmospheric particle on a mass concentration basis (Warneck, 1999; Modini et al., 2015). Together with newly formed particles originating from gaseous precursors which can also be emitted from the ocean, this sea spray aerosol (SSA) contributes to marine aerosols. Ambient measurements and laboratory studies indicated that the resulting marine aerosol with less than 10 µm diameter can have a trimodal size distribution, which suggests that several mechanisms are involved in marine aerosol production (Prather et al., 2013; Quinn et al., 2015; Brooks and Thornton, 2018). Marine aerosol number and mass concentrations, chemical composition, and optical and cloud-nucleating properties can be changed during transportation, e.g., marine aerosol can carry continental emissions up to thousands of kilometers downwind (Quinn et al., 2015). Marine aerosol impacts Earth's radiation balance by directly scattering solar radiation (Quinn et al., 2017). Ocean physics, biology and chemistry ultimately control both particle hygroscopicity (Fuentes et al., 2011) and the number of particles that can act as CCN and INPs (Andreae and Rosenfeld, 2008; Wilson et al., 2015; DeMott et al., 2016) in the marine aerosol. On a global basis, SSA makes a contribution of less than 30 % to the CCN population (Quinn et al., 2017).

Marine aerosol is the second important aerosol source at Cabo Verde when looking at particle mass (Fomba et al., 2014; Salvador et al., 2016). There is always a background of marine aerosol present at Cabo Verde (Kandler et al., 2011a). Based on a 5-year measurement at Cabo Verde, Fomba et al. (2014) found that the mean mass concentration of sea salt was $11.00 \pm 5.10\,\mu g\,m^{-3}$ (corresponding to total mass of $47.20 \pm 55.50\,\mu g\,m^{-3}$). Additionally during summer, elevated concentrations of organic material were observed to originate from marine emissions. A summer maximum was observed for non-sea-salt sulfate, and it was connected to periods when air mass inflow was predominantly of marine origin, indicating that marine biogenic emissions were a significant source. Schladitz et al. (2011b) found that the Aitken mode and accumulation mode particles were mainly composed of marine aerosol, whereas coarse mode particles were composed of sea salt and a variable fraction of Saharan mineral dust.

As outlined above, Saharan dust and sea salt dominate PM_{10} particle composition (more than 70 %) near the surface at Cabo Verde (Fomba et al., 2014; Salvador et al., 2016). In addition, Cabo Verde is rich in other kinds of aerosols from both continental and marine sources. Biomass burning aerosols produced from October to November in sub-Sahelian latitudes had a clear influence on the content of elemental carbon (EC) recorded at Cabo Verde but a small impact on PM_{10} (Salvador et al., 2016), as particles originating from the biomass burning layer usually stay at high

altitude (1500–5000 m) (Tesche et al., 2009; Heinold et al., 2011; Lieke et al., 2011).

Overall, there are diverse sources of less or more hygroscopic particles which might contribute to aerosols at Cabo Verde. Pringle et al. (2010) used an atmospheric chemistry model to simulate global fields of the effective hygroscopicity parameter, represented by κ (Petters and Kreidenweis, 2007), which roughly describes the influence of chemical composition on CCN activity of aerosol particles. An annual cycle of monthly-mean κ values at the surface of Cabo Verde was reported in Pringle et al. (2010). The only field measurement of particle hygroscopicity at Cabo Verde was carried out by Schladitz et al. (2011a). Here, these model results and field measurement values will be compared with those obtained from in situ measurements during our measurement campaign in the framework of the MarParCloud (Marine biological production, organic aerosol particles and marine clouds: a Process Chain) project.

The atmospheric boundary layer (ABL) is the region in the lowest part of the troposphere (below 1000 m above the ground) where the Earth's surface strongly influences temperature, moisture and wind through the turbulent transfer of air masses. Most particles are emitted or formed in the ABL with temporally varying sources (Rosati et al., 2016b). Extensive data sets from ground-based aerosol property studies are available. One major point of interest is to know whether ground-based measurements can be used to infer aerosol properties at cloud level. Previous field measurements at Po Valley and the Netherlands found that during the development of a newly mixed layer the estimation of altitude-specific data from surface measurements may be problematic (Rosati et al., 2016a, b). Once the ABL was fully mixed, a constant extinction coefficient (Rosati et al., 2016b) and particle hygroscopicity (Rosati et al., 2016a) were observed at all altitudes within the ABL. Wex et al. (2016) found, for marine aerosol on Barbados, that the particle number size distribution (PNSD) on the ground and throughout the subcloud level showed good agreement.

During the MarParCloud project, we set up two measurement stations, one close to the sea level (10 m a.s.l.) and one on a mountaintop (744 m a.s.l.), to characterize aerosol properties, including particle number concentration (PNC), PNSD and CCN number concentration (N_{CCN}). In addition, a measurement from a kite and balloon (Helikite) was carried out to characterize vertical profiles of meteorological parameters at Cabo Verde. This offered a unique opportunity to compare particle properties close to the sea level and higher up in the marine boundary layer (MBL).

In a series of companion papers (Gong et al., 2020), we aim to provide a quantitative understanding regarding the abundance, properties and source of aerosol particles in general, and CCN and INPs in particular, close to both sea-level and cloud-level heights. In this paper, we will (1) compare aerosol properties measured close to sea level and at a mountaintop to examine the representativeness of ground-based measurements to the MBL and (2) present a thorough characterization of CCN with respect to their hygroscopicity and number concentrations for different air masses. Both of these will be presented here for the Cabo Verde for the first time. In a companion paper, we will examine the abundance and properties of INPs from several different sources, namely sea surface microlayer and under layer water from the ocean, airborne close to sea and cloud level, and cloud water of warm cloud. This study is the first in a series of publications to come from the MarParCloud project. For more information about the campaign itself and a more detailed analysis of the meteorological situation, we refer the reader to the overview paper (van Pinxteren et al., 2019), which will also cover a thorough size-resolved chemical composition analysis of particles close to the sea level and on the mountaintop.

2 Experiment and methods

2.1 Sampling sites and campaign setup

The measurements were carried out on São Vicente island in Cabo Verde from 13 September to 13 October 2017. Located in the Atlantic Ocean, São Vicente island is ~ 900 km off the African coast. The region experiences constant northeasterly winds. The average annual temperature at Cabo Verde is 23.6 ± 4.0 °C (mean ± 1 standard deviation). It is an arid region with a maximum of 24–350 mm rainfall per year. The precipitation frequency is about 3 to 10 events annually, mainly between August and October (Carpenter et al., 2010; Fomba et al., 2013). More details of the meteorological conditions at Cabo Verde can be found in Carpenter et al. (2010).

Three measurement stations were set up at Cabo Verde, i.e., Cape Verde Atmospheric Observatory (CVAO), Monte Verde station (MV) and an ocean station (OS, this station will be discussed only in the companion paper). CVAO (16°51′49″ N, 24°52′02″ W) is located at the northeastern shore of the São Vicente island, 70 m from the coastline at about 10 m a.s.l. An aerosol PM_{10} inlet, employed to remove particles larger than 10 µm in aerodynamic diameter, was installed on top of a 32 m tower. Downstream of the aerosol inlet there was a vertical stainless-steel sampling pipe (32 m long, 1/2 in. outer diameter), installed together with a diffusion dryer, which was placed directly on top of the measurement container. Aerosol entered the inlet on top of the mast and was transported through the tube and the dryer. Downstream of the dryer and inside of the container, the aerosol was split isokinetically and distributed to various instruments, including a mobility particle sizer spectrometer (MPSS), an aerodynamic particle sizer (APS) and a cloud condensation nuclei counter (CCNC). Besides, airborne measurements were carried out at CVAO using a Helikite to characterize the vertical profiles of temperature, relative humility (RH), and wind speed and direction.

MV (16°52′11″ N, 24°56′02″ W) is located on the top of Monte Verde (744 m a.s.l.), ∼ 7 km away to the west of CVAO. An aerosol inlet was installed on the roof of a building, which overall had a cut-off size of 4 µm. A vertical stainless-steel sampling pipe (2 m long, 1 in. diameter) and a diffusion dryer were placed downstream of the aerosol inlet. Downstream of the dryer and inside the building, the sample aerosol was split isokinetically to an MPSS and CCNC. An overview of the sampling site and instruments is given in Table 1. In the following, we will briefly introduce the different measurement techniques applied in this study, including calibrations, measurements and data processing.

2.2 Balloon measurements

The vertical profile of meteorological parameters was taken at CVAO. The measurements were achieved using a 16 m^3 Helikite (Allsopp Helikites Ltd, Hampshire, UK), a unique combination of a tethered balloon and a kite. Helikites are designed to be operated under extreme weather conditions. The kite was attached to a 3 mm Dyneema rope (2000 m long, ∼ 4.6 g m^{-1}, Lyros D-Pro 3 mm, breaking load 950 daN, working elongation < 1 %) and operated by a winch. Under calm conditions, the Helikite has a net load capacity of ∼ 8 kg. Under windy condition, the pull increases significantly, and the net load capacity reaches about 16 kg at 6 m s^{-1}. Depending on the prevailing conditions, meteorological measurements of up to an altitude of about 1200 m could be carried out. The measuring system, built by the Leibniz Institute for Tropospheric Research (TROPOS), was attached to the rope 20 m below the Helikite. All sensors were selected and tested individually in the laboratory at TROPOS. Wind speed was measured using a differential pressure sensor together with a pitot tube; wind direction was determined from an orientation sensor (compass) of a wind vane. Data were recorded with a measuring frequency of 2 Hz, stored in a Secure Digital memory card and additionally transmitted to a ground station (via Digi XBee radio modules). Our aim was to characterize the atmospheric boundary layer in terms of mixing state, which can provide insights into uncertainties regarding the connection between ground-based measurements and the free troposphere.

2.3 Particle number size distribution

PNSDs were measured in the size range from 10 nm to 10 µm using a TROPOS-type MPSS (Wiedensohler et al., 2012) and an APS (aerodynamic particle sizer, model 3321, TSI Inc., St. Paul, MN, USA). The APS data accounted for the multiple charge correction of MPSS data in the inversion of measured PNSD (Wiedensohler, 1988; Pfeifer et al., 2016). The combined PNSD is then given on the basis of the volume equivalent particle diameter. More details about the combined MPSS and APS PNSDs can be found in the Supplement and Schladitz et al. (2011b). Size-dependent particle losses caused by diffusion, deposition and sedimentation within the inlet were corrected for by utilizing the empirical particle loss calculator (von der Weiden et al., 2009). The size-dependent particle losses are shown in the Supplement, Fig. S1. Total particle number concentrations (N_{total}) were calculated from the measured PNSDs accounting for the size-dependent particle losses. The MPSS and APS were calibrated before, during and after the intensive field study. Overall, fewer than 3 % of the particles were lost when passing the inlet. More details about calibration methods can be found in Wiedensohler et al. (2018).

2.4 Cloud condensation nuclei

N_{CCN} was measured using a cloud condensation nuclei counter (CCNC, Droplet Measurement Technologies, Boulder, USA; Roberts and Nenes, 2005). The CCNC is a cylindrical continuous-flow thermal-gradient diffusion chamber, establishing a constant streamwise temperature gradient to adjust a quasi constant centerline supersaturation. The sampled aerosol particles are guided within a sheath flow through this chamber and can become activated to droplets, depending on the supersaturation level and the ability of the particles to act as CCN.

During our study, the supersaturation was varied between ∼ 0.15 % and ∼ 0.79 % at a constant total flow rate of 0.5 L min^{-1}. To ensure stable column temperature, the first 5 min and the last 30 s of each 12 min long measurement at each supersaturation were excluded from the data analysis. The remaining data points were averaged. A supersaturation calibration (following the protocol by Gysel and Stratmann, 2013) was done at the cloud laboratory of the TROPOS prior to and after the measurement campaign in order to determine the relationship between the temperature gradient along the column and the effective supersaturation. Calibrated supersaturation set points were 0.15 %, 0.20 %, 0.30 %, 0.50 % and 0.70 % of CVAO CCNC and 0.15 %, 0.21 %, 0.33 %, 0.56 %, and 0.79 % of MV CCNC. These values were used for further calculations.

According to Köhler theory (Köhler, 1936), whether or not a particle can act as a CCN depends on its dry size, chemical composition and the maximum supersaturation it encounters. Petters and Kreidenweis (2007) presented a method to describe the relationship between particle dry diameter and CCN activity using the hygroscopicity parameter κ; κ values reported in this study were calculated as follows, assuming the surface tension of the examined solution droplets, $\sigma_{s/\alpha}$, to be that of pure water:

$$\kappa = \frac{4A^3}{27 d_{\mathrm{crit}}^3 \ln^2 S} \tag{1}$$

with

$$A = \frac{4\sigma_{s/\alpha} M_\omega}{RT\rho_\omega}, \tag{2}$$

Table 1. Measured and derived parameters and the respective instrumentation used at CVAO and MV. Note, SS represents supersaturation.

Measurement site	Location	Parameter	Abbreviation	Instrument	Measurement range
CVAO	16°51′49″ N, 24°52′02″ W; inlet height 42 m a.s.l.	Particle number size distribution	PNSD	MPSS and APS system	10 to 10 000 nm
		Particle number concentration	N_{total}	Integrated PNSD	–
		CCN number concentration	N_{CCN}	CCNC	–
		Particle hygroscopicity	κ	CCNC with MPSS and APS system	SS = 0.15 %, 0.20 %, 0.30 %, 0.50 %, and 0.70 %
		Vertical profile of temperature and RH	–	Balloon	Height up to 1200 m
MV	16°52′11″ N, 24°56′02″ W; inlet height 746 m a.s.l.	Particle number size distribution	PNSD	MPSS system	10 to 850 nm
		Particle number concentration	N_{total}	Integrated PNSD	–
		CCN number concentration	N_{CCN}	CCNC	–
		Particle hygroscopicity	κ	CCNC with MPSS system	SS = 0.15 %, 0.21 %, 0.33 %, 0.56 %, and 0.79 %

where d_{crit} is the critical diameter above which all particles activate into cloud droplets for a given supersaturation. S is the supersaturation. M_ω and ρ_ω are the molar mass and density of water, respectively, and R and T are the ideal gas constant and the absolute temperature, respectively. To derive d_{crit}, simultaneously measured N_{CCN} and PNSD are used. Therefore, it is assumed that all particles in the neighborhood of a given particle diameter have a similar κ, meaning that the aerosol particles are internally mixed. At a given supersaturation, a particle can be activated to a droplet once its dry size is equal to or larger than d_{crit}. Therefore, d_{crit} is the diameter at which N_{CCN} is equal to the value of the cumulative particle number concentration, determined via integration from the upper towards the lower end of the PNSD. Values for κ can be calculated with d_{crit} and the corresponding supersaturation based on Eq. (1). The inferred κ values correspond to particles with sizes of roughly d_{crit}. The uncertainty in κ, which results from uncertainties of the PNSD measurements and the supersaturations of the CCNC, was determined by applying a Monte Carlo simulation (MCS) in a similar fashion as done by Kristensen et al. (2016) and Herenz et al. (2018). A detailed description of this method is provided in the Supplement. Note that the particle losses inside the CCNC (discussed in Rose et al., 2008) were also considered before κ was calculated.

3 Results and discussion

3.1 Overview of the meteorology

Time series of meteorological parameters, including the wind speed, temperature and RH at CVAO and MV, as well as wind direction at CVAO, are shown in Fig. 1. The wind speed varied from 0.6 to 9.7 m s^{-1}, with a mean of 6.0 m s^{-1} at CVAO. The variation in wind speed at MV is similar to that at CVAO. Figure 2 shows the wind rose plot based on hourly average of wind speed and direction at CVAO. Clearly, the CVAO station experienced constant northeasterly winds during this campaign. The temperature and RH were measured by a digital temperature and humidity sensor (Davis Instruments, 7346.070). The accuracy of the temperature sensor is ±0.3 °C; the accuracy of the humidity sensor is ±2 % below 90 % and ±4 % above 90 %. The temperature and RH at CVAO varied from 25.6 to 28.3 °C and 70.0 % to 90.5 %, with means of 26.6 °C and 81.0 %, respectively. Obviously, temperature at MV was lower than that at CVAO, ranging from 18.9 to 25.4 °C, with a mean of 21.2 °C. The measured RH was 100 % during more than half of the campaign at MV. Note that due to the instrument detection limit, RH = 100 % is not accurate. However, the RH = 100 % result indicates that the MV station was often in a cap cloud. More precise determination of cloud events and influences of cloud on aerosol particles will be discussed in Sect. 3.3. Note that all the times presented here are in UTC (corresponding to LT+1). For better comparison, all PNC and N_{CCN} data reported in this study are given for standard temperature and pressure (STP, 0 °C and 1013.25 hPa).

During the MarParCloud campaign, 19 vertical profiles on 10 different days were taken. Profiles of up to about 1200 m could be measured. The inversion layer heights were determined by the measurements. The MBL was typically well mixed with boundary layer heights between about 550 and 1100 m, as shown by blue rectangles in Fig. 1. It is indicated that there were three cases of a decoupled boundary layer during the whole campaign, as shown by red dots in Fig. 1. Therefore, to be sure to represent aerosol collected at Cabo Verde, we used backward trajectories starting at 200 m altitude to represent MBL air mass origins in this study. Exemplary data from one balloon measurement can be found in the Supplement (Sect. S3).

3.2 Particle characterization

This section will first discuss PNSDs and PNC at CVAO. A well-known trimodal lognormal parameterization method is adopted to characterize the temporal variation in PNC in three modes. It is used to classify the particles into different types based on PNC in different modes. Lastly, to get insights into possible particle sources, we studied the air

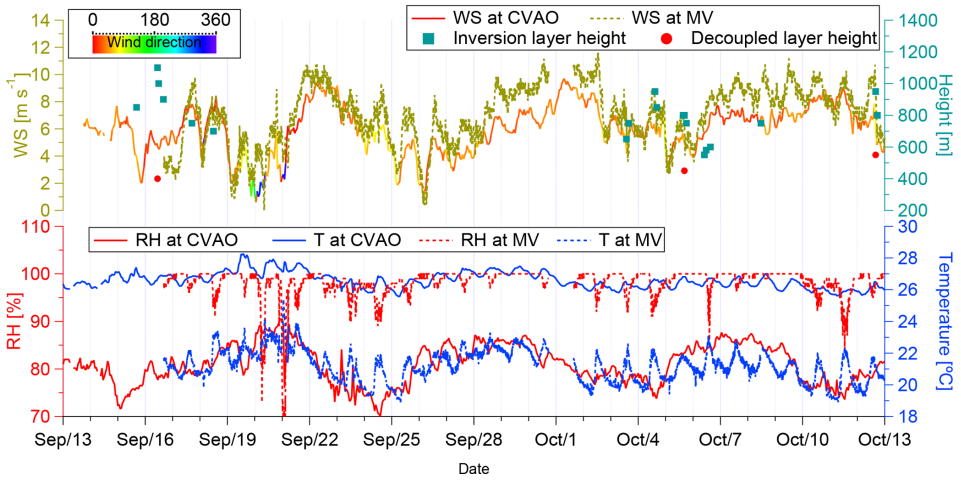

Figure 1. Time series of wind speed (WS), wind direction (CVAO only), RH and temperature. Parameters measured at CVAO are shown by solid lines and at MV in dashed lines. Time series of inversion layer height are shown by blue squares and decoupled layer height in red dots.

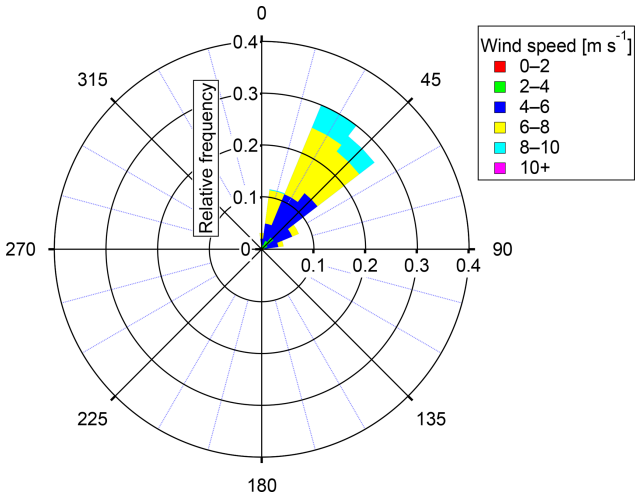

Figure 2. Wind rose based on hourly averages of wind speed and direction (measured at CVAO).

mass origin and transport through backward trajectory analysis. Calculations were performed with the HYSPLIT (HYbrid Single-Particle Lagrangian Integrated Trajectory) model (Stein et al., 2015; Rolph, 2003).

3.2.1 Particle number size distribution and concentration

Particle size is one of the most important parameters to characterize the atmospheric aerosol. Figure 3 presents contour plots for PNSDs of supermicron particles in Fig. 3a and submicron particles in Fig. 3b. In order to show details of supermicron particles, we adopted different color bar scales for submicron and supermicron particles. Most of the time, two submicron modes (Aitken and accumulation mode) and one supermicron mode (coarse mode) are observed. The Aitken mode is observed from ~ 10 to ~ 80 nm, and the accumulation mode is observed from ~ 80 to ~ 1000 nm. However, from 03:30 to 20:00 21 September and from 09:30 28 September to 18:30 30 September, the submicron particles only exhibited a unimodal distribution. The supermicron particles exhibited a high concentration during those periods. N_{total} was changed significantly, from ~ 200 to $\sim 1500\,\text{cm}^{-3}$ with a median of $\sim 700\,\text{cm}^{-3}$, shown as black line in Fig. 3b.

Particles of different sizes have different formation routes, sources and behaviors. To better define the modes of our data, we fitted the PNSDs to three lognormal functions. The lognormal distribution was expressed by Seinfeld and Pandis (2016), and the parameterization function is as follows:

$$\frac{\mathrm{d}N}{\mathrm{d}\log D_{\mathrm{p}}} = \sum_{i=1}^{n} \frac{N_i}{\sqrt{2\pi}\log_{10}\sigma_i} \exp\left(-\frac{(\log_{10}D_{\mathrm{p}} - \log_{10}D_i)^2}{2(\log_{10}\sigma_i)^2}\right), \quad (3)$$

where N_i is the total number concentration of the ith mode, D_i is the geometric mean diameter of the ith mode and σ_i is the geometric standard deviation of the ith mode distribution. Every PNSD was individually parameterized by a trimodal distribution, where the number of i, $i = 1, 2, 3$, stands for Aitken, accumulation or coarse mode, receptively. For each PNSD, we searched for an optimal fitting function, until the coefficient of determination (R^2) was larger than 0.97.

Time series of PNC in Aitken mode (N_{Aitken}), accumulation mode ($N_{\text{accumulation}}$) and coarse mode (N_{coarse}), together with sum of N_i and measured N_{total}, are shown in Fig. 4. Due to the unimodal distribution of submicron particles from 03:30 to 20:00 21 September and from 09:30 28 September to 18:30 30 September, the trimodal lognormal fitting did not work properly, so we did a bimodal lognormal fitting instead,

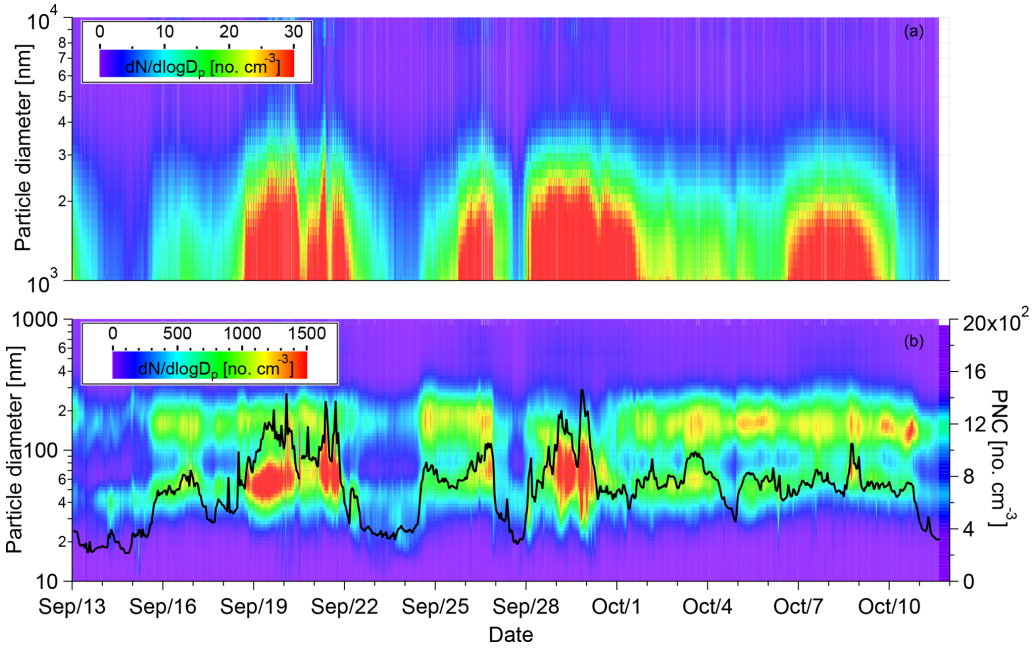

Figure 3. Contour plots for PNSDs of 1000 nm to 10 µm in panel **(a)** and 10 to 1000 nm in panel **(b)**. The color scale indicates $dN/d\log D_p$ in cubic centimeters (cm^{-3}). Time series of N_{total} is shown by the black line in panel **(b)**.

with one submicron mode ($N_{submicron}$, as shown by purple dots) and one coarse mode.

PNC showed large variability during our measurement. N_{Aitken} and $N_{accumulation}$ varied from 41 to 789 and 89 to 639 cm^{-3}, with medians of 244 and 354 cm^{-3}, respectively. Generally, Aitken mode particles are produced by homogeneous and heterogeneous nucleation processes, formed during natural gas-to-particle condensation. Aitken mode particles are transferred to the accumulation mode through cloud processing (Hoppel et al., 1994). And accumulation mode particles are furthermore formed by coagulation of smaller particles or condensation of vapors onto existing particles, during which they grow into that size range (Seinfeld and Pandis, 2016). Therefore, when $N_{accumulation}$ is higher than N_{Aitken}, this indicates long-range transport and a more aged aerosol. N_{coarse} varied from 3 to 71 cm^{-3}, with a median of 21 cm^{-3}. Coarse mode particles are mostly emitted to the atmosphere from natural sources, e.g., marine aerosol, mineral dust or biological materials.

3.2.2 Particle classification and origins

To better understand the particle sources and features, we divided the data from the campaign into different periods. An overview of the classification criteria and features of the different resulting aerosol types are summarized in Table 2. Details about the classification criteria are discussed in the Supplement. Classification results are shown as different background colors in Fig. 4. Note that from 00:00:00 27 September to 00:00:00 28 September, N_{total} suddenly decreased. This might due to the wet deposition that happened before the air masses arrived at the measurement site. The precipitation is an output parameter of the calculated NOAA HYSPLIT backward trajectories. From 00:00:00 27 September to 00:00:00 28 September, the total precipitation (sum of precipitation of 144 segment endpoints) exceeded a value of 7 mm in the past 144 h (corresponding to 6 d) of each backward trajectory history. Therefore, this period was not included in the aerosol classification.

Figure 5 shows the median of PNSDs of the four different aerosol types, with a linear (top) and a logarithmic (bottom) scaling on the y axis. The error bar indicates the range between 25th and 75th percentiles. PNSDs which have N_{Aitken} larger than $N_{accumulation}$ and $N_{coarse} < 25$ cm^{-3} are attributed to the "marine type" in this work. PNSDs resembling those show three modes, i.e., Aitken, accumulation and coarse modes, which can be clearly distinguished, as shown in blue lines in Fig. 5. For the separation of this marine type, trajectories were additionally examined. The marine type featured the lowest N_{Aitken}, $N_{accumulation}$ and N_{coarse} median values of 189, 143 and 7 cm^{-3}, respectively. The minimum between the Aitken and accumulation mode of PNSDs (Hoppel minimum; see Hoppel et al., 1986) at roughly 70 nm indicates the sizes above which particles had previously been activated to cloud droplets during the history of the air mass at least once. When passing through a cloud, soluble material is added to the activated particles by aqueous-phase chemistry, increasing particulate mass and hence the size of those particles. The coarse mode particles can also be assumed to be sea spray aerosol (SSA) during the marine type period,

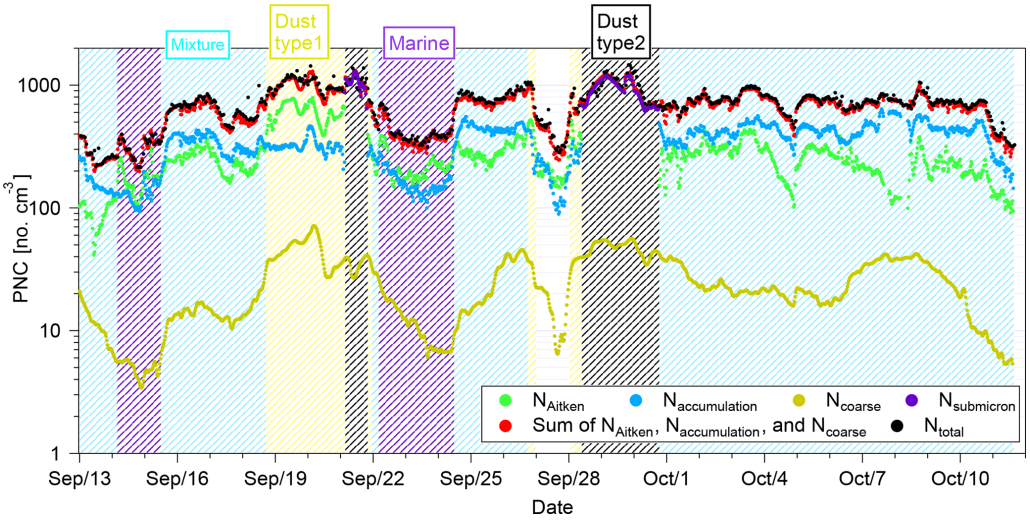

Figure 4. Time series of N_{Aitken}, $N_{\text{accumulation}}$, N_{coarse}, $N_{\text{submicron}}$, sum of N_i and N_{total} at CVAO. The different shading colors indicate different aerosol type periods.

Table 2. Classification criteria and features of four different particle types.

Aerosol type	Criteria	Features					
		N_1 (cm^{-3}) median ± SD*	N_2 (cm^{-3}) median± SD	N_3 (cm^{-3}) median ± SD	N_{total} (cm^{-3}) median ± SD	$N_{\text{CCN,0.30\%}}$ (cm^{-3}) median ± SD	Shape of PNSD
Marine	$N_{\text{Aitken}} > N_{\text{accumulation}}$ $N_{\text{coarse}} < 25\,\text{cm}^{-3}$	189 ± 58	143 ± 41	7 ± 6	369 ± 124	190 ± 49	visible Hoppel minimum at 70 nm
Mixture	$N_{\text{Aitken}} < N_{\text{accumulation}}$	247 ± 78	405 ± 102	20 ± 10	725 ± 173	478 ± 76	visible Hoppel minimum at 80 nm
Dust type1	$N_{\text{Aitken}} > N_{\text{accumulation}}$ $N_{\text{coarse}} > 25\,\text{cm}^{-3}$	556 ± 134	312 ± 50	39 ± 11	952 ± 173	332 ± 44	visible Hoppel minimum at 100 nm
Dust type2	Single mode in submicron $N_{\text{coarse}} > 25\,\text{cm}^{-3}$	–	–	44 ± 8	994 ± 218	503 ± 105	no visible Hoppel minimum

* 1 standard deviation

as discussed in previous studies (Modini et al., 2015; Wex et al., 2016). A decent correlation ($R^2 = 0.69$, $p < 0.01$) was found between SSA number concentration and wind speed (Supplement, Fig. S6). Modini et al. (2015) also observed that SSA number concentration correlated with local wind speed, which is consistent with the fact that SSAs are generated from the process associated with the agitation of the sea surface by air moving above it. The SSA accounted for 1.1 % to 4.4 % of N_{total} at CVAO (wind speed from 4 to 10 m s^{-1}), which is relatively low when comparing to Wex et al. (2016), who found the SSA particles contributed 4 % to 10 % of N_{total} (wind speed up to 14 m s^{-1}) for the marine aerosol on Barbados. Figure 6 shows the 6 d backward trajectories with 1 h time resolution ending at 200 m above CVAO. Looking at Fig. 6a, which displays the marine periods, the backward trajectories clearly featured paths over the Atlantic Ocean and traveled to Cabo Verde. None of the backward trajectories touched the European or African continents.

PNSDs that have a larger $N_{\text{accumulation}}$ than N_{Aitken} are attributed to the "mixture type" in this work, shown as green lines in Fig. 5, with three modes, i.e., Aitken, accumulation and coarse modes, which can be clearly distinguished. N_{Aitken}, $N_{\text{accumulation}}$ and N_{coarse} have median values of 247, 405 and 20 cm^{-3}, respectively. The Hoppel minimum of the mixture type is at roughly 80 nm. The respective backward trajectories, colored in green in Fig. 6b, showed that the related air mass came from the north Atlantic Ocean and spent some days over southern Europe and northern Africa. Anthropogenic aerosol and mineral dust may be incorporated into air parcels and transported to Cabo Verde, causing higher levels of Aitken, accumulation and coarse mode particles than in the marine type.

PNSDs with larger N_{Aitken} than $N_{\text{accumulation}}$ and $N_{\text{coarse}} > 25\,\text{cm}^{-3}$ are attributed to the "dust type1" in this work, shown as red lines in Fig. 5. PNSDs attributed to this type show three modes, i.e., Aitken, accumulation and coarse modes, which can be clearly distinguished. N_{Aitken},

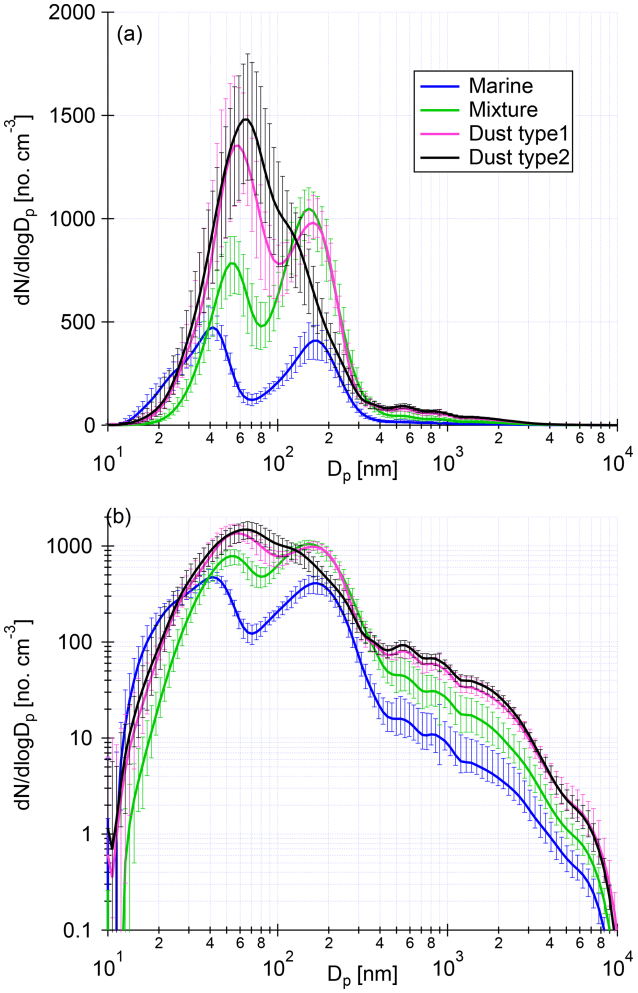

Figure 5. The median of PNSDs of marine type (blue), mixture type (green), dust type1 (purple) and dust type2 (black), with a linear **(a)** and a logarithmic **(b)** scaling on the y axis. The error bar indicates the range between 25th and 75th percentiles.

$N_{\text{accumulation}}$ and N_{coarse} had median values of 556, 312 and 39 cm^{-3}, respectively. The Hoppel minimum of the mixture type is at roughly 100 nm. The respective backward trajectories, colored in red in Fig. 6c, featured two pathways. One air mass group originated from the north Atlantic Ocean and stayed a few days over southern Europe and northern Africa. Another air mass group came from the Sahara.

It is interesting to note that the Hoppel minimum is at the lowest diameter for the marine air mass ($\sim$ 70 nm), compared to all other air masses. This suggests that the supersaturation in the clouds forming in the clean marine air masses is highest, as there is less surface area for the water vapor to condense onto during cloud formation.

PNSDs which featured a single mode in the submicron size range are attributed to "dust type2", shown as black lines in Fig. 5. No visible Hoppel minimum can be seen. The dust type2 featured highest N_{total} and N_{coarse} median values of 994 and 44 cm^{-3}, respectively. It is worth mentioning that previous field measurements at the Sahara found similar PNSDs to what we observed in this study (Kaaden et al., 2009; Kandler et al., 2009; Weinzierl et al., 2009). We assumed that dust type2 is the heaviest dust plume period during this campaign. The respective backward trajectories, colored in black in Fig. 6d, showed that related air masses originated from the Sahara.

The higher N_{coarse} during dust type1 and type2 periods is due to the direct dust aerosol from the Sahara. Schladitz et al. (2011b) also found that the higher coarse mode number concentration at Cabo Verde originated from the Sahara. Besides, a very high concentration of Aitken mode particles was observed during dust type1 and dust type2 periods. A previous study also found that an African-influenced period showed a great enhancement in the Aitken mode particles and an overall increase in the number of particles of all sizes (Allan et al., 2009). Nie et al. (2014) found that new particle formation and growth happened in the remote ambient atmosphere during the strongest observed dust episodes. Both the formation and growth rates of particles in the diameter range of 15–50 nm were enhanced during the dust episodes. In our data, we found that backward trajectories often traveled from the upper troposphere down to the marine boundary layer during dust periods, which means that Aitken mode particles could have been transported from the upper troposphere. Therefore, there are different factors contributing to the observed high N_{Aitken} and $N_{\text{accumulation}}$ during dust plumes, such as direct transport of particles from the desert and Sahel region, and additional new particle formation and growth in the vicinity or in the upper troposphere.

To summarize Sect. 3.2, based on number concentrations in different aerosol modes, an aerosol classification was done, and four well-separable types of PNSDs were found, i.e., the marine type, mixture type, dust type1 and dust type2. Marine type particles are mainly from the Atlantic Ocean, while dust type particles are mainly from the Sahara. Mixture type particles are a combination of marine, anthropogenic and dust particles. Backward trajectories support this classification and analysis. The marine, mixture, dust type1 and dust type2 in this study are comparable to type A, D, C and B in Fomba et al. (2014), respectively, who characterized particle chemical composition at CVAO over a time period of 4 years.

3.3 Comparison of CVAO and MV

In this section, we will compare the PNC, PNSDs and N_{CCN} at CVAO and MV. Cloud events are identified based on the difference in integrated PNC between MV and CVAO. Cloud effects on PNSDs and N_{CCN} will also be discussed.

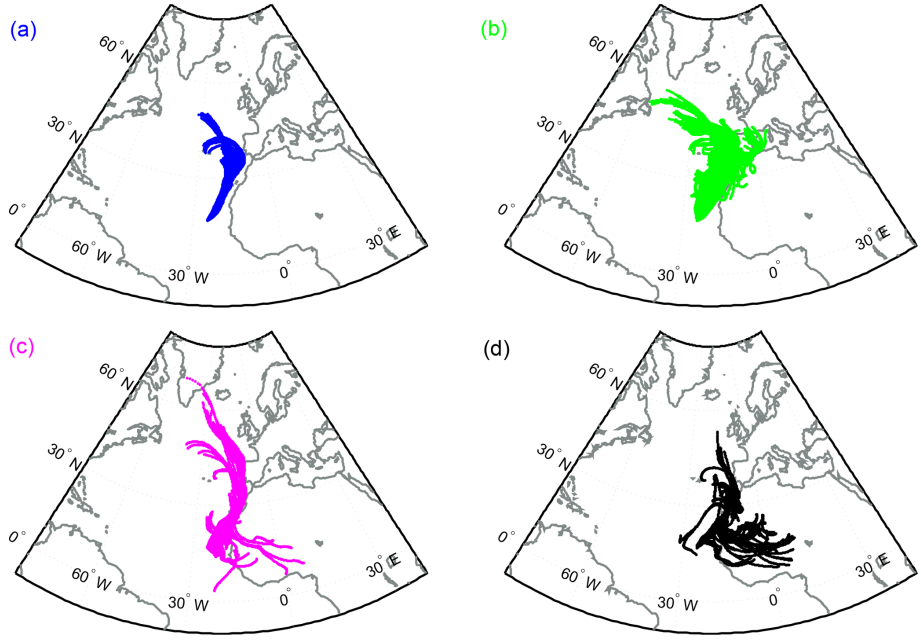

Figure 6. The 6 d backward trajectories arriving at CVAO at a height of 200 m with 1 h resolution for marine type **(a)**, mixture type **(b)**, dust type1 **(c)** and dust type2 **(d)**. Each calculation is shown as a separate dot, which is separately visible when air masses moved fast.

3.3.1 Comparison of PNC and PNSD

PNSDs from 10 to 800 nm were measured by MPSS and a bimodal lognormal parameterization was adopted to calculate N_{Aitken} and $N_{\mathrm{accumulation}}$ at MV. Figure 7 shows the time series of PNC in the size range between 10 and 800 nm at CVAO ($N^{\mathrm{CVAO}}_{10\text{–}800\,\mathrm{nm}}$) and MV ($N^{\mathrm{MV}}_{10\text{–}800\,\mathrm{nm}}$) in Fig. 7a, PNC of accumulation mode at CVAO ($N^{\mathrm{CVAO}}_{\mathrm{accumulation}}$) and MV ($N^{\mathrm{MV}}_{\mathrm{accumulation}}$) in Fig. 7b, and PNC of Aitken mode at CVAO ($N^{\mathrm{CVAO}}_{\mathrm{Aitken}}$) and MV ($N^{\mathrm{MV}}_{\mathrm{Aitken}}$) in Fig. 7c. The variation in $N^{\mathrm{CVAO}}_{10\text{–}800\,\mathrm{nm}}$ and $N^{\mathrm{MV}}_{10\text{–}800\,\mathrm{nm}}$ was similar sometimes, e.g., from 23 to 25 September. However, sometimes the concentrations at MV were obviously lower than the respective values at CVAO, at least for $N^{\mathrm{MV}}_{10\text{–}800\,\mathrm{nm}}$ and $N^{\mathrm{MV}}_{\mathrm{accumulation}}$, as, for example, from 5 to 9 October. Such a decrease was sometimes, but not always, also observed for $N^{\mathrm{MV}}_{\mathrm{Aitken}}$. This is a typical observation for cloudy air, in which particles from the accumulation mode and maybe also some from the Aitken mode are activated to cloud droplets which are then removed in the aerosol inlet on MV. When the ratio of $N^{\mathrm{MV}}_{\mathrm{accumulation}}$ to $N^{\mathrm{CVAO}}_{\mathrm{accumulation}}$ was lower than 0.85, we assumed that MV is in the cloud. When the trimodal fitting function did not work for the CVAO data set (from 03:30 to 20:00 21 September and from 09:30 28 September to 18:30 30 September), a slightly different approach was needed. For that, we used the ratio of PNC in the size range between 80 and 800 nm at MV ($N^{\mathrm{MV}}_{80\text{–}800\,\mathrm{nm}}$) to that at CVAO ($N^{\mathrm{CVAO}}_{80\text{–}800\,\mathrm{nm}}$) (replacing the ratio of $N^{\mathrm{MV}}_{\mathrm{accumulation}}$ to $N^{\mathrm{CVAO}}_{\mathrm{accumulation}}$). When this ratio was lower than 0.75, we assumed that MV is in the cloud. It is described in more detail in the Supplement how this ratio was derived separately for cases with trimodal and bimodal fitting. The time for cloud events is shown as red shading in Fig. 7. As outlined above in the meteorology part, we observed RH = 100 % at MV. Figure S8 shows the time series of RH at MV together with the time for cloud events as red shading. It is clear that times with RH = 100 % are consistent with cloud events identified as described above, which verifies our identification of cloud events.

To better understand the cloud effect of PNSDs, we compared the PNSDs at CVAO and MV during cloud events and noncloud events of different aerosol types. Figure 8 shows the median PNSDs of different particle types during cloud events and noncloud events. During noncloud events, PNSDs at CVAO ($\mathrm{PNSD}^{\mathrm{CVAO}}_{\text{non-cloud}}$) and MV ($\mathrm{PNSD}^{\mathrm{MV}}_{\text{non-cloud}}$) were similar for marine, mixture or dust type1 periods. During dust type2, there is only a very short period of noncloud event with 15 PNSDs observed. Therefore, we did not include the comparison of $\mathrm{PNSD}^{\mathrm{CVAO}}_{\text{non-cloud}}$ and $\mathrm{PNSD}^{\mathrm{MV}}_{\text{non-cloud}}$ during the dust type2 period in Fig. 8.

During noncloud events, PNSDs at CVAO and MV were the same, as shown in Fig. 8. For periods with clouds, PNSDs in the size range > 80 nm at MV are lower than that at CVAO for all the particle types. For dust type1 and dust type2, depending on the clouds, i.e., the highest supersaturation the particles encounter, particles in Aitken mode were also activated to cloud droplets. For particles in the size range $<$ 40 nm, PNSDs are similar during cloud and noncloud events. This is because the particle size is not large enough to activate to cloud droplets. Furthermore, it also indicates that PNSDs are similar at CVAO and MV during cloud events, at least in

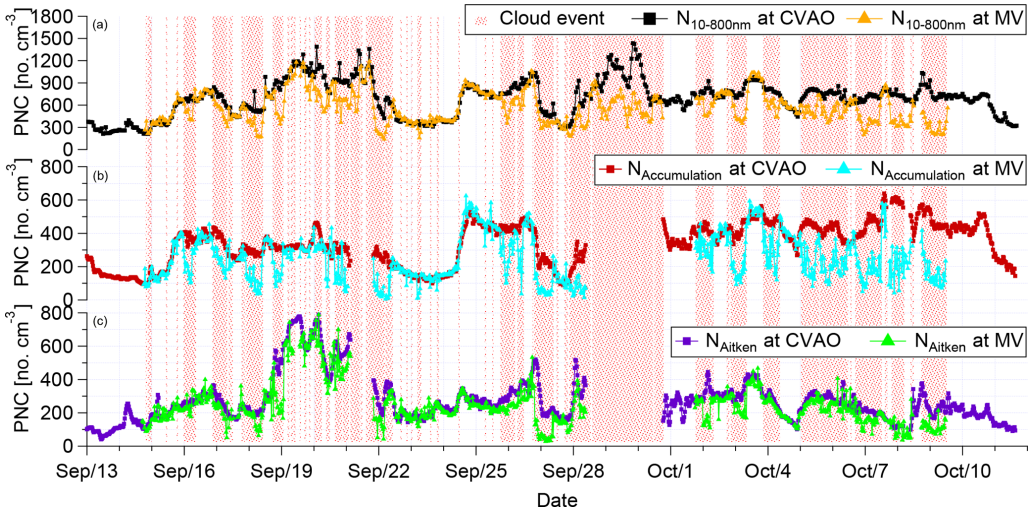

Figure 7. Time series of $N^{\mathrm{CVAO}}_{10\text{–}800\,\mathrm{nm}}$ and $N^{\mathrm{MV}}_{10\text{–}800\,\mathrm{nm}}$ in panel **(a)**, $N^{\mathrm{CVAO}}_{\mathrm{Aitken}}$ and $N^{\mathrm{MV}}_{\mathrm{Aitken}}$ in the panel **(b)**, and $N^{\mathrm{CVAO}}_{\mathrm{accumulation}}$ and $N^{\mathrm{MV}}_{\mathrm{accumulation}}$ in panel **(c)**. The times of cloud events are shown by red shading.

the size range < 40 nm. For a more detailed comparison of PNSDs at CVAO and MV, contour plots for PNSDs can be found in Fig. S9 in the Supplement.

During the campaign, a decoupled marine boundary layer was observed with our balloon measurements in three cases, i.e., 10:30 to 11:00 16 September, 16:00 to 16:30 5 October and 17:20 to 17:50 12 October (shown as red dots in Fig. 1). Only for the first decoupling case (10:30 to 11:00 16 September) was MV cloud free; otherwise, PNSDs were similar at CVAO and MV (Fig. S10). Therefore, the MBL may be generally well mixed, maybe still from times before the decoupling of the layers formed. On the other hand, lifting of the air masses over the mountain might also partially explain this observation. However, due to the fact that there is only this one decoupled case, a thorough analysis of the influence of coupling and decoupling can not be done.

3.3.2 Comparison of N_{CCN}

Figure 9 shows the scatter plot of N_{CCN} at CVAO ($N^{\mathrm{CVAO}}_{\mathrm{CCN}}$) against that at MV ($N^{\mathrm{MV}}_{\mathrm{CCN}}$) during cloud events (green dots) and noncloud events (red rectangles) at different supersaturations. During cloud events, large particles that had been activated to cloud droplets were removed by the aerosol inlet on MV. Therefore, $N^{\mathrm{CVAO}}_{\mathrm{CCN,cloud}}$ is larger than $N^{\mathrm{MV}}_{\mathrm{CCN,cloud}}$ at each supersaturation. During noncloud events, all the data points are close to the 1 : 1 line (for the slopes see Fig. 9), and R^2 values between $N^{\mathrm{CVAO}}_{\mathrm{CCN,non\text{-}cloud}}$ and $N^{\mathrm{MV}}_{\mathrm{CCN,non\text{-}cloud}}$ are all above 0.90, indicating N_{CCN} is similar at CVAO and MV. Although there were slight differences in supersaturation at CVAO and MV due to the CCNC calibration, the similarity between N_{CCN} at the two stations conveys the same message as what was discussed before concerning the comparison of

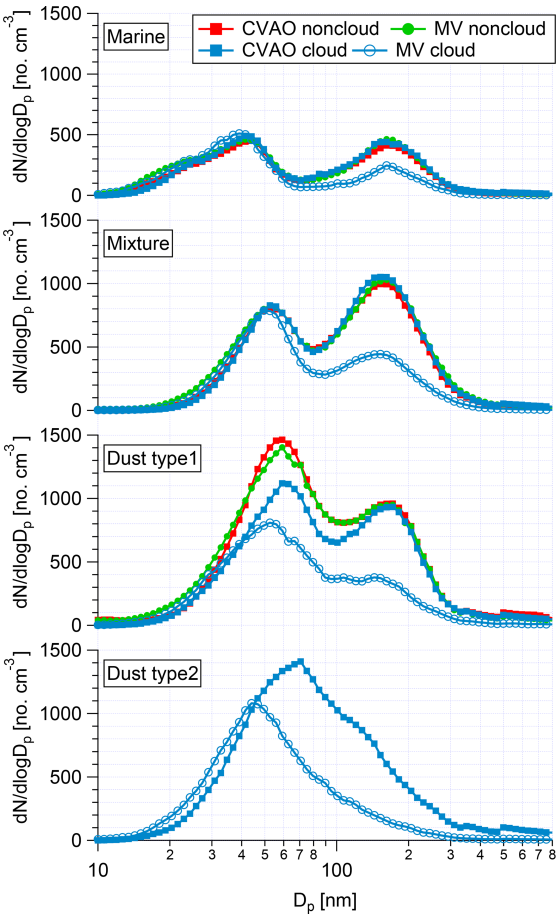

Figure 8. The median of PNSDs for four different particle types during cloud events and noncloud events at CVAO and MV.

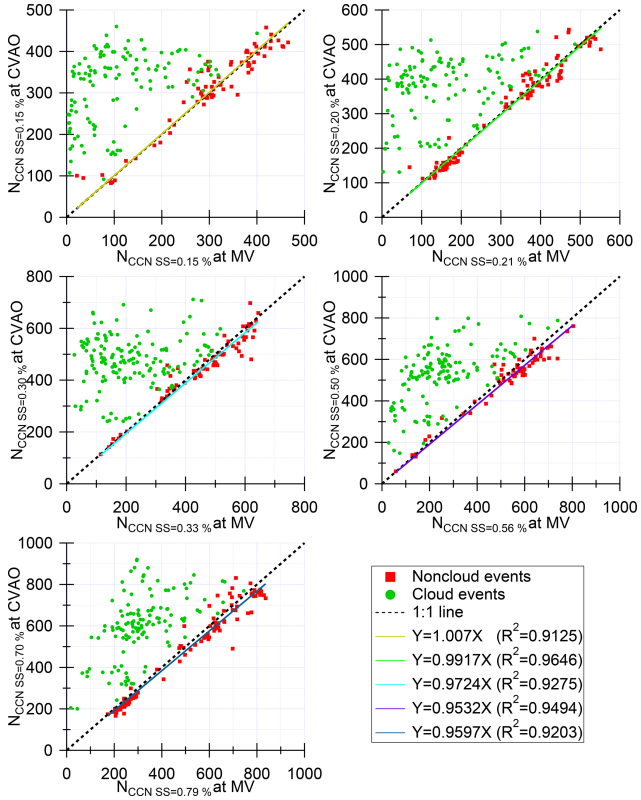

Figure 9. Scatter plots of N_{CCN} at CVAO against those at MV at different supersaturations. Slope and R^2 values for these fits are given in the legend.

PNSDs at CVAO and MV, i.e., particles are generally well mixed in the MBL.

To summarize Sect. 3.3, cloud events were observed at MV and can be identified based on the integrated concentrations between ground and cloud level. During the cloud events, larger particles (mainly accumulation and coarse mode) are activated to cloud droplets. Aitken mode particles starting with sizes of roughly 40 nm can also be activated to cloud droplets if the cloud is strong enough. During noncloud events, PNC, PNSD and N_{CCN} are similar at CVAO and MV. The aerosol particles measured at ground level (CVAO) can represent the aerosol particles at the cloud level (MV).

3.4 Particle hygroscopicity

In this section, we will focus on N_{CCN}, d_{crit} and κ measurements at CVAO. As outlined above, PNSDs and N_{CCN} measured at ground level are similar to those at cloud level. Therefore, measurements at CVAO can be representative of that at MV. Firstly, a thorough statistical analysis of N_{CCN}, d_{crit} and κ will be discussed. Secondly, the marine and dust aerosol contributions of particles to N_{CCN} and their κ values will be compared.

3.4.1 Statistical analysis of N_{CCN}, d_{crit} and κ

Figure 10a shows the time series of N_{total} and N_{CCN}, d_{crit} in Fig. 10b and κ in Fig. 10c, with different colors for different supersaturations. The error bars of d_{crit} show 1 standard deviation (SD), and error bars of κ show 1 geometric standard deviation (geoSD). Explanation of error bars can be found in Sect. 2.4 as well as in the Supplement. N_{CCN} shows large variability, e.g., $N_{CCN,0.30\,\%}$ varied from 106 to 884 cm^{-3}, with a median of 509 cm^{-3}. We observed highest $N_{CCN,0.30\,\%}$ of 503 cm^{-3} (median) during dust type2 periods, and lowest $N_{CCN,0.30\,\%}$ of 109 cm^{-3} (median) during marine periods. $N_{CCN,0.30\,\%}$ during different aerosol type periods are summarized in Table 2. Figure 11a shows the boxplot of N_{CCN} at different supersaturations during the whole campaign. As can be seen, N_{CCN} increases towards higher supersaturation, which is expected. The median of N_{CCN} at different supersaturations also exhibited large variability, varying from 327 (median) at a supersaturation of 0.15 % to 652 cm^{-3} (median) at a supersaturation of 0.70 %. Table 3 summarizes those numbers and shows additional details.

d_{crit} at supersaturations of 0.15 %, 0.20 %, 0.50 % and 0.70 % were almost constant throughout the campaign, as shown in Fig. 10b. The mean value of d_{crit} and its SD are summarized in Table 3. For the supersaturations of 0.70 % and 0.50 %, d_{crit} is below 80 nm, i.e., inside the Aitken mode. However, for the lower supersaturations of 0.15 % and 0.20 %, d_{crit} is located in the accumulation mode. Consequently, hygroscopicities derived at these supersaturations can be assumed to be representative of the Aitken (at supersaturations of 0.70 % and 0.50 %) and the accumulation modes (at supersaturation of 0.10 % and 0.20 %), respectively. d_{crit} at a supersaturation of 0.30 % ($d_{crit,0.30\,\%}$) is not as constant as it is at other supersaturations, and it is larger during the marine type period than during other periods. With a median of 79.7 nm, it is close to the Hoppel minimum. Therefore, the hygroscopicity derived at a supersaturation of 0.30 % can be assumed to be representative of the mixture of Aitken and accumulation particles.

The particle hygroscopicity, expressed as κ, can be seen as a measure for average particle chemical composition. κ values at different supersaturations show little variability over time (lower panel in Fig. 10), with geoSD lower than 0.12, i.e., there is no clear trend in κ over time during the campaign. A slightly increasing trend of κ was observed with decreasing supersaturations, as shown in Fig. 11c. At supersaturations of 0.70 % and 0.50 %, i.e., for Aitken mode particles, κ values are 0.18 and 0.25 (geomean), respectively. At the lowest supersaturation of 0.15 % and 0.20 %, i.e., for accumulation mode particles, κ values are 0.32 and 0.34 (geomean). Table 3 summarizes those numbers and shows additional details.

Figure 11d shows κ as a function of d_{crit} and error bars of κ and d_{crit} show geoSD and SD, respectively. A slightly increasing trend of κ over increasing d_{crit} is observed. It

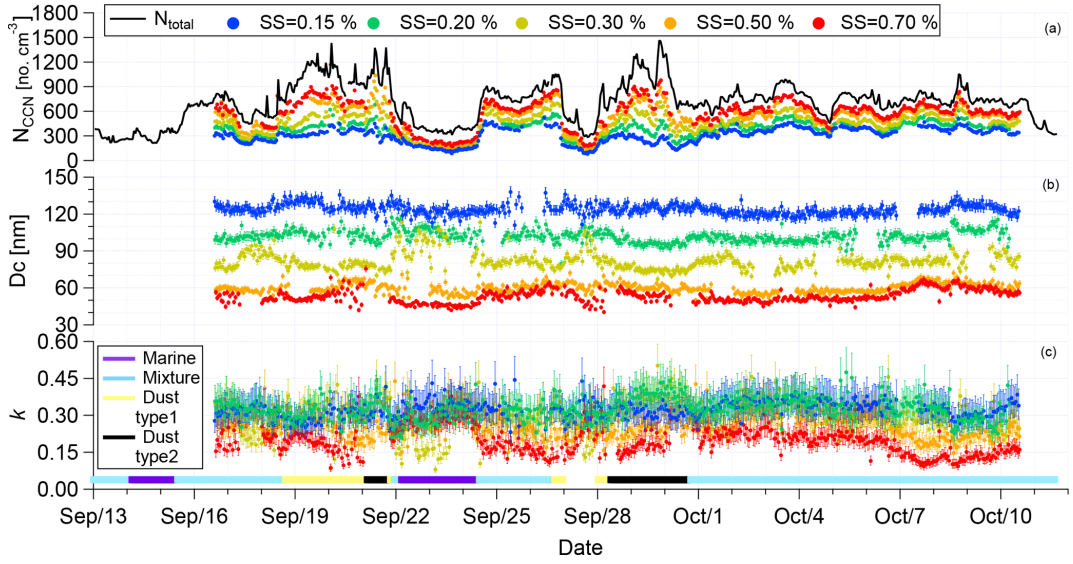

Figure 10. Time series of N_{CCN} in **(a)**, d_{crit} in **(b)** and κ in **(c)**. All of those are measured at CVAO. Error bars of d_{crit} and κ show 1 standard deviation and 1 geometric standard deviation. The color bar in **(c)** indicates the times of different aerosol type periods.

Table 3. Median and mean values of N_{CCN}, d_{crit}, κ, 1 standard deviation of d_{crit} and 1 geometric standard deviation of κ at different supersaturations.

	Supersaturation (%)	N_{CCN} (cm^{-3}) median, mean ± SD	d_{crit} (nm) mean ± SD	κ geomean, +geoSD, −geoSD*
Whole campaign	0.15	327, 320 ± 88	123.8 ± 8.9	0.32, 0.09, 0.07
	0.20	414, 400 ± 112	100.4 ± 7.7	0.34, 0.10, 0.08
	0.30	509, 495 ± 143	79.7 ± 8.4	0.30, 0.12, 0.08
	0.50	602, 593 ± 176	59.8 ± 6.9	0.25, 0.09, 0.07
	0.70	652, 638 ± 186	53.3 ± 6.5	0.18, 0.08, 0.06
Marine	0.15	146, 155 ± 37	121.2 ± 5.0	0.34, 0.08, 0.06
	0.20	166, 177 ± 43	103.5 ± 7.8	0.31, 0.10, 0.08
	0.30	190, 202 ± 49	87.8 ± 15.7	0.23, 0.17, 0.10
	0.50	191, 215 ± 70	56.9 ± 5.7	0.30, 0.12, 0.09
	0.70	235, 260 ± 72	46.1 ± 2.2	0.28, 0.06, 0.05
Dust type2	0.15	259, 242 ± 56	124.6 ± 4.7	0.32, 0.07, 0.06
	0.20	370, 357 ± 77	96.9 ± 4.2	0.37, 0.08, 0.07
	0.30	503, 501 ± 105	74.9 ± 3.6	0.36, 0.08, 0.06
	0.50	654, 636 ± 125	60.4 ± 3.2	0.25, 0.06, 0.05
	0.70	798, 764 ± 111	52.6 ± 5.5	0.19, 0.08, 0.06

* 1 geometric standard deviation

suggests that the soluble, likely inorganic, material added during cloud processing increases κ of the originally very organic-rich particles, which has also been observed in previous studies (Kalivitis et al., 2015; Kristensen et al., 2016). Overall, κ averaged 0.28. Pringle et al. (2010) used an atmospheric chemistry model to derive global distributions of effective particle hygroscopicity κ. For CVAO, this model resolved an annual cycle of monthly-mean κ values ranging from 0.25 in February to 0.60 in April. This annual circle of κ likely originated in a change of chemical composition of the aerosol throughout the year, related to different precursors and a higher organic content during times with higher algal activity. For September and October, the period of this study, values of 0.35 and 0.30 were reported, respectively, which is consistent with what we obtained during this campaign.

The Hoppel minimum diameter range of 70 to 100 nm for different aerosol types (mentioned in Sect. 3.2.2), together with the average κ of 0.28, can be used to obtain a rough estimate of maximum supersaturations present in trade wind clouds along the path of the sampled air masses. Resulting

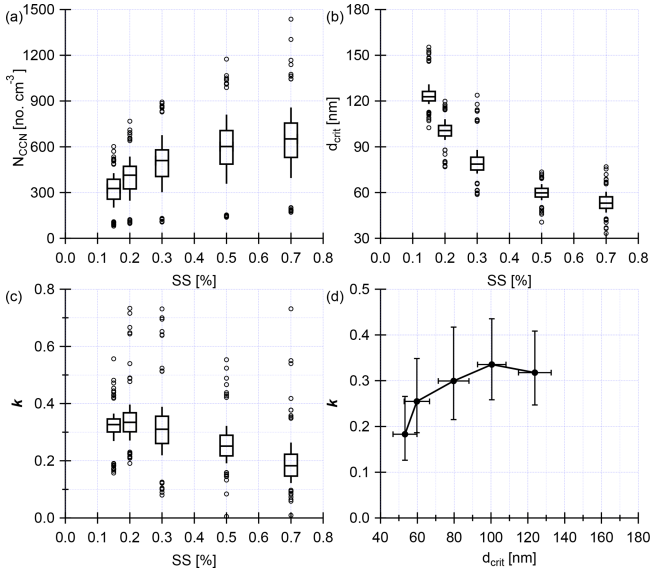

Figure 11. Boxplots of N_{CCN} **(a)**, d_{crit} **(b)** and κ **(c)** at different supersaturations (SS). Whiskers show the 10th to 90th percentiles. Circles show the outliers (1 %). **(d)** κ as a function of d_{crit}. Error bars of d_{crit} and κ show 1 standard deviation and 1 geometric standard deviation, respectively.

values are roughly 0.22 % to 0.37 % for dust type2 and marine air masses, respectively. These are close to an earlier estimate given in Clarke et al. (1996) of 0.35 %, and they can be interpreted as typical values for trade wind cumuli.

3.4.2 Dust and marine comparison

In this section, we will focus on examining the difference between the cleanest periods (marine type) and heaviest observed dust pollution periods (dust type2). Therefore, we compared N_{CCN} and κ during marine type and dust type2 periods. Figure 12a shows the boxplot of N_{CCN} as a function of supersaturation. As outlined above, during dust periods, the aerosol shows a great enhancement in the Aitken, accumulation and coarse mode particles; therefore, overall N_{CCN} increases at different supersaturations. It is clear that N_{CCN} during dust type2 periods is much higher than that during marine periods. For example, $N_{CCN,0.30\,\%}$ median values were 503 and 190 cm^{-3} during dust type2 and marine periods, respectively. During marine periods, N_{coarse}, i.e., SSA particles, accounted for roughly 3.7 % of $N_{CCN,0.30\,\%}$, for the range of wind speeds from 4 to 10 $m\,s^{-1}$ that were present during this study. This is relatively low compared to Wex et al. (2016), who found that the SSA particles accounted for up to 15 % of $N_{CCN,0.30\,\%}$ for wind speeds up to 14 $m\,s^{-1}$ for the marine aerosol on Barbados, and Modini et al. (2015), who found that SSA particles accounted for up to 16 % to 28 % (wind speeds up to 16 $m\,s^{-1}$) and 5 % to 10 % (wind speed from 4 to 10 $m\,s^{-1}$) of $N_{CCN,0.30\,\%}$. However, these fractions not only depend on the concentrations of SSA but

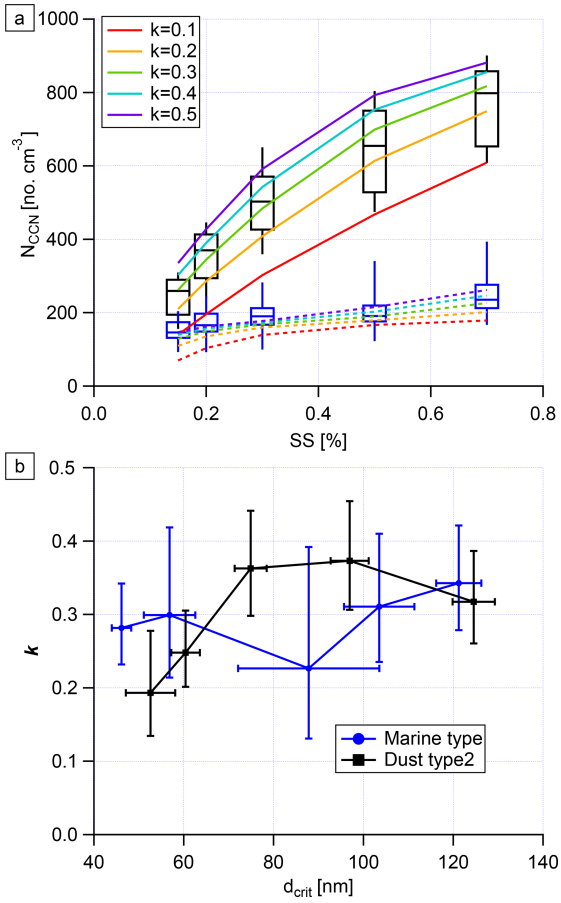

Figure 12. (a) Boxplots of N_{CCN} as a function of κ for marine type (blue) and dust type2 (black). Whiskers show the 10th to 90th percentiles. The predicted N_{CCN} based on median PNSD and different κ values (0.1, 0.2, 0.3, 0.4 and 0.5) are shown in solid (during dust type2 period) and dashed lines (during marine period). **(b)** κ as a function of d_{crit} for marine type (blue) and dust type2 (black). Error bars of d_{crit} and κ show 1 standard deviation and 1 geometric standard deviation, respectively.

also on those of particles in the accumulation mode, which have other sources. Still, the respective accumulation modes and related particle concentrations in Modini et al. (2015), Wex et al. (2016) and the present study resemble each other. Therefore the lower fractions of SSA particles in our study are likely connected to the low wind speeds (lower SSA number concentration) or, to some extent, to different accumulation mode particle number concentrations.

κ as a function of d_{crit} is shown in Fig. 12b. The error bars of d_{crit} and κ show SD and geoSD, respectively. During dust type2, slightly increasing κ with increasing d_{crit} was observed, similar to the overall trend we described above. κ featured lower values from 0.13 to 0.31 for Aitken mode particles, while higher values from 0.26 to 0.45 were found for accumulation mode particles. Until now, the only field measurement of particle hygroscopicity during a dust plume at

Cabo Verde was carried out by Schladitz et al. (2011a), who found that hygroscopic particles featured a κ value (based on hygroscopic growth factor of particles) from 0.35 to 0.65. Our CCN-derived κ values in this study for the aerosol influenced by dust are therefore comparable to the values reported by Schladitz et al. (2011a).

No clear trend of κ with d_{crit} was observed during marine type periods (as shown in Fig. 12), during which κ averaged 0.30. Larger error bars of κ and d_{crit} at the supersaturation of 0.30 % were observed, as in this case the d_{crit} is close to the Hoppel minimum, where a small change in N_{CCN} causes a comparably large change in d_{crit} (explained in the Supplement). Kristensen et al. (2016) found that, for the marine aerosol on Barbados in June and July 2013, values for κ of 0.2 to 0.5 were derived, which are consistent with this study. When considering the scatter observed in κ (see the error bars in Fig. 12), κ during the dust type2 period still agreed with that of the marine period within uncertainty. Therefore, no distinguishable differences in κ during marine and dust periods in the size range from 40 to 140 nm were found during this campaign.

We additionally derived N_{CCN} based on PNSDs. For that, we assumed values for κ of 0.1, 0.2, 0.3, 0.4 or 0.5, and we calculated the corresponding d_{crit} at different supersaturations. The integrated particle number concentrations in the size range larger than d_{crit} were derived from the median PNSDs during dust type2 and marine periods. These particle number concentrations also can be treated as the predicted N_{CCN} at different supersaturations, as shown in solid (dust type2) and dashed (marine type) lines with different colors (indicating different κ) in Fig. 12a. As expected, the thusly derived N_{CCN} values were within the measured N_{CCN} range. Comparing the solid and dashed lines, it can be seen that different aerosol types, i.e., different PNSDs, played an important role in N_{CCN} variation. When looking at the results from the different κ values, we found that the particle chemical composition did not control N_{CCN}, especially when the particle number concentration was very low. These colored solid and dashed lines connected the κ and N_{CCN}, which can be helpful for N_{CCN} predictions in modeling studies.

To summarize Sect. 3.4, overall there is a slight increase in κ with particle size, indicating the addition of soluble, likely inorganic, material during cloud processing. κ values in this study are comparable to previous model work and field measurements. N_{CCN} during the heaviest observed dust periods is much higher than that during marine periods, while κ values for these two periods show no significant difference.

4 Conclusions

The MarParCloud campaign took place in September and October 2017 on Cabo Verde to investigate the aerosols prevailing in the Atlantic Ocean. As the first in a series of publications to come from the MarParCloud campaign, this study provides a thorough characterization of the abundance, properties and sources of aerosol particles in general, and CCN in particular, close to both sea-level and cloud-level heights with measurements done at the Cape Verde Atmospheric Observatory (CVAO) and on the top of Monte Verde (MV), respectively.

N_{total} varied from ~ 200 to $\sim 1500\,cm^{-3}$, with a median of $\sim 700\,cm^{-3}$ at CVAO. A trimodal parameterization method was deployed to characterize PNC. Based on number concentrations in different aerosol modes, four well-separable types of PNSDs were found, i.e., the marine type, mixture type, dust type1 and dust type2. These different aerosol types originate from different regions. The marine type aerosol mainly originates from the Atlantic Ocean, while the dust type aerosol mainly comes from the Saharan region. During marine periods, the coarse mode can be attributed to sea spray aerosol, and the corresponding particle number concentration accounted for about 3.7 % of $N_{CCN,0.30\,\%}$ and for about 1.1 % to 4.4 % of N_{total}. Because of lower wind speeds that were present at CVAO, this value is lower than previous field measurements (Modini et al., 2015; Wex et al., 2016).

A thorough comparison of PNC, PNSDs and N_{CCN} at CVAO and MV clearly showed these parameters to be similar at both stations in the absence of clouds. Cloud events were observed at MV during roughly 58 % of the time. During the cloud events, larger particles (mainly accumulation and coarse mode) are activated to cloud droplets and our data suggest that the maximum supersaturation in the clouds is higher the cleaner the air mass gets, leading to a lower Hoppel minimum. Altogether, it was observed that the boundary layer is generally well mixed; therefore, CVAO can be used to describe the aerosol particles at cloud level.

Overall, κ averaged 0.28, suggesting the presence of organic material in particles. This is consistent with previous model work (Pringle et al., 2010) and field measurements of hygroscopic growth (Schladitz et al., 2011a) done for the location of Cabo Verde. There is a slight increase in κ with particle size, indicating the addition of soluble, likely inorganic, material during cloud processing. When looking at the two most different aerosol types, the marine type and dust type2, κ values for these periods show no significant difference. On the other hand, dust plumes enhanced particle concentrations in the Aitken, accumulation and coarse modes and therefore increased N_{CCN}; $N_{CCN,0.30\,\%}$ during the strongest observed dust periods is about 2.5 times higher than that during marine periods.

Data availability. The data are available through the World Data Center PANGAEA (https://doi.pangaea.de/10.1594/PANGAEA.905070, Gong et al., 2019).

Supplement. The supplement related to this article is available online at: https://doi.org/10.5194/acp-20-1431-2020-supplement.

Author contributions. XG wrote the article with contributions from HW, JV and MvP. KW and XG performed MPSS and APS measurements, and XG performed the data evaluation. KW calibrated MPSS and APS before, during, and after the campaign. FS, HW and XG performed the CCN measurements, and XG performed the data evaluation. SH calibrated CCN before and after the campaign. Balloon measurements and data evaluation were performed by JV and XG. XG, HW and FS discussed the results and further analysis after the campaign. All co-authors proofread and commented on the article.

Competing interests. The authors declare that they have no conflict of interest.

Special issue statement. This article is part of the special issue "Marine organic matter: from biological production in the ocean to organic aerosol particles and marine clouds (ACP/OS inter-journal SI)". It is not associated with a conference.

Acknowledgements. The work was carried out in the framework of the MarParCloud project. The authors acknowledge the Leibniz Association SAW funding for the project "Marine biological production, organic aerosol particles and marine clouds: a Process Chain (MarParCloud)" (SAW-2016-TROPOS-2). We are grateful to Lucy Carpenter and Katie Read, from the University of York and the Atmospheric Measurement and Observation Facility at the National Centre for Atmospheric Science (NCAS-AMOF), for kindly providing the meteorology data at CVAO.

Financial support. This research has been supported by the Leibniz Association SAW (MarParCloud (grant no. SAW-2016-TROPOS-2)).

The publication of this article was funded by the Open Access Fund of the Leibniz Association.

Review statement. This paper was edited by Kimitaka Kawamura and reviewed by two anonymous referees.

References

Albrecht, B. A.: Aerosols, cloud microphysics, and fractional cloudiness, Science, 245, 1227–1230, 1989.

Allan, J. D., Topping, D. O., Good, N., Irwin, M., Flynn, M., Williams, P. I., Coe, H., Baker, A. R., Martino, M., Niedermeier, N., Wiedensohler, A., Lehmann, S., Müller, K., Herrmann, H., and McFiggans, G.: Composition and properties of atmospheric particles in the eastern Atlantic and impacts on gas phase uptake rates, Atmos. Chem. Phys., 9, 9299–9314, https://doi.org/10.5194/acp-9-9299-2009, 2009.

Andreae, M. and Rosenfeld, D.: Aerosol–cloud–precipitation interactions. Part 1. The nature and sources of cloud-active aerosols, Earth-Sci. Rev., 89, 13–41, 2008.

Brooks, S. D. and Thornton, D. C.: Marine Aerosols and Clouds, Annu. Rev. Mar. Sci., 10, 289–313, https://doi.org/10.1146/annurev-marine-121916-063148, 2018.

Carpenter, L. J., Fleming, Z. L., Read, K. A., Lee, J. D., Moller, S. J., Hopkins, J. R., Purvis, R. M., Lewis, A. C., Müller, K., Heinold, B., Herrmann, H., Fomba, K. W., van Pinxteren, D., Müller, C., Tegen, I., Wiedensohler, A., Müller, T., Niedermeier, N., Achterberg, E. P., Patey, M. D., Kozlova, E. A., Heimann, M., Heard, D. E., Plane, J. M. C., Mahajan, A., Oetjen, H., Ingham, T., Stone, D., Whalley, L. K., Evans, M. J., Pilling, M. J., Leigh, R. J., Monks, P. S., Karunaharan, A., Vaughan, S., Arnold, S. R., Tschritter, J., Pöhler, D., Frieß, U., Holla, R., Mendes, L. M., Lopez, H., Faria, B., Manning, A. J., and Wallace, D. W. R.: Seasonal characteristics of tropical marine boundary layer air measured at the Cape Verde Atmospheric Observatory, J. Atmos. Chem., 67, 87–140, https://doi.org/10.1007/s10874-011-9206-1, 2010.

Christensen, M. W., Chen, Y.-C., and Stephens, G. L.: Aerosol indirect effect dictated by liquid clouds, J. Geophys. Res.-Atmos., 121, 14636–14650, https://doi.org/10.1002/2016JD025245, 2016.

Clarke, A. D., Li, Z., and Litchy, M.: Aerosol dynamics in the equatorial Pacific marine boundary layer: Microphysics, diurnal cycles and entrainment, Geophys. Res. Lett., 23, 733–736, https://doi.org/10.1029/96gl00778, 1996.

DeMott, P. J., Sassen, K., Poellot, M. R., Baumgardner, D., Rogers, D. C., Brooks, S. D., Prenni, A. J., and Kreidenweis, S. M.: African dust aerosols as atmospheric ice nuclei, Geophys. Res. Lett., 30, 1732, https://doi.org/10.1029/2003GL017410, 2003.

DeMott, P. J., Hill, T. C. J., McCluskey, C. S., Prather, K. A., Collins, D. B., Sullivan, R. C., Ruppel, M. J., Mason, R. H., Irish, V. E., Lee, T., Hwang, C. Y., Rhee, T. S., Snider, J. R., McMeeking, G. R., Dhaniyala, S., Lewis, E. R., Wentzell, J. J. B., Abbatt, J., Lee, C., Sultana, C. M., Ault, A. P., Axson, J. L., Diaz Martinez, M., Venero, I., Santos-Figueroa, G., Stokes, M. D., Deane, G. B., Mayol-Bracero, O. L., Grassian, V. H., Bertram, T. H., Bertram, A. K., Moffett, B. F., and Franc, G. D.: Sea spray aerosol as a unique source of ice nucleating particles, P. Natl. Acad. Sci. USA, 113, 5797–5803, https://doi.org/10.1073/pnas.1514034112, 2016.

Dusek, U., Frank, G., Hildebrandt, L., Curtius, J., Schneider, J., Walter, S., Chand, D., Drewnick, F., Hings, S., Jung, D., Borrmann, S., and Andreae, M. O.: Size matters more than chemistry for cloud-nucleating ability of aerosol particles, Science, 312, 1375–1378, 2006.

Fomba, K. W., Müller, K., van Pinxteren, D., and Herrmann, H.: Aerosol size-resolved trace metal composition in remote northern tropical Atlantic marine environment: case study Cape Verde islands, Atmos. Chem. Phys., 13, 4801–4814, https://doi.org/10.5194/acp-13-4801-2013, 2013.

Fomba, K. W., Müller, K., van Pinxteren, D., Poulain, L., van Pinxteren, M., and Herrmann, H.: Long-term chemical characterization of tropical and marine aerosols at the Cape Verde Atmospheric Observatory (CVAO) from 2007 to 2011, Atmos.

Chem. Phys., 14, 8883–8904, https://doi.org/10.5194/acp-14-8883-2014, 2014.

Fuentes, E., Coe, H., Green, D., and McFiggans, G.: On the impacts of phytoplankton-derived organic matter on the properties of the primary marine aerosol – Part 2: Composition, hygroscopicity and cloud condensation activity, Atmos. Chem. Phys., 11, 2585–2602, https://doi.org/10.5194/acp-11-2585-2011, 2011.

Gama, C., Tchepel, O., Baldasano, J. M., Basart, S., Ferreira, J., Pio, C., Cardoso, J. a., and Borrego, C.: Seasonal patterns of Saharan dust over Cape Verde – a combined approach using observations and modelling, Tellus B, 67, 24410, https://doi.org/10.3402/tellusb.v67.24410, 2015.

Garrison, V. H., Majewski, M. S., Foreman, W. T., Genualdi, S. A., Mohammed, A., and Massey Simonich, S. L.: Persistent organic contaminants in Saharan dust air masses in West Africa, Cape Verde and the eastern Caribbean, Sci. Total Environ., 468–469, 530–543, https://doi.org/10.1016/j.scitotenv.2013.08.076, 2014.

Ginoux, P., Chin, M., Tegen, I., Prospero, J. M., Holben, B., Dubovik, O., and Lin, S.-J.: Sources and distributions of dust aerosols simulated with the GOCART model, J. Geophys. Res.-Atmos., 106, 20255–20273, https://doi.org/10.1029/2000JD000053, 2001.

Ginoux, P., Prospero, J. M., Gill, T. E., Hsu, N. C., and Zhao, M.: Global-scale attribution of anthropogenic and natural dust sources and their emission rates based on MODIS Deep Blue aerosol products, Rev. Geophys., 50, RG3005, https://doi.org/10.1029/2012RG000388, 2012.

Gong, X., Wex, H., Voigtländer, J., Fomba, K. W., Weinhold, K., van Pinxteren, M., Henning, S., Müller, T., Herrmann, H., and Stratmann, F.: Ground-based measurements on aerosol particles at Cape Verde (Sep–Oct 2017), PANGAEA, https://doi.org/10.1594/PANGAEA.905070, 2019.

Gong, X., Wex, H., van Pinxteren, M., Triesch, N., Fomba, K. W., Lubitz, J., Stolle, C., Robinson, T.-B., Müller, T., Herrmann, H., and Stratmann, F.: Characterization of aerosol particles at Cabo Verde close to sea level and at the cloud level – Part 2: Ice-nucleating particles in air, cloud and seawater, Atmos. Chem. Phys., 20, 1451–1468, https://doi.org/10.5194/acp-20-1451-2020, 2020.

Goudie, A. S. and Middleton, N. J.: Saharan dust storms: nature and consequences, Earth-Sci. Rev., 56, 179–204, https://doi.org/10.1016/S0012-8252(01)00067-8, 2001.

Gysel, M. and Stratmann, F.: WP3 – NA3: In-situ chemical, physical and optical properties of aerosols, Deliverable D3.11: Standardized protocol for CCN measurements, Tech. rep., available at: http://www.actris.net/Publications/ACTRISQualityStandards/tabid/11271/language/en-GB/Default.aspx (last access: 4 February 2020), 2013.

Heinold, B., Tegen, I., Schepanski, K., Tesche, M., Esselborn, M., Freudenthaler, V., Gross, S., Kandler, K., Knippertz, P., Müller, D., Schladitz, A., Toledano, C., Weinzierl, B., Ansmann, A., Althausen, D., Müller, T., Petzold, A., and Wiedensohler, A.: Regional modelling of Saharan dust and biomass-burning smoke, Tellus B, 63, 781–799, https://doi.org/10.1111/j.1600-0889.2011.00570.x, 2011.

Herenz, P., Wex, H., Henning, S., Kristensen, T. B., Rubach, F., Roth, A., Borrmann, S., Bozem, H., Schulz, H., and Stratmann, F.: Measurements of aerosol and CCN properties in the Mackenzie River delta (Canadian Arctic) during spring–summer transition in May 2014, Atmos. Chem. Phys., 18, 4477–4496, https://doi.org/10.5194/acp-18-4477-2018, 2018.

Hoppel, W., Frick, G., and Larson, R.: Effect of nonprecipitating clouds on the aerosol size distribution in the marine boundary layer, Geophys. Res. Lett., 13, 125–128, https://doi.org/10.1029/GL013i002p00125, 1986.

Hoppel, W. A., Frick, G. M., Fitzgerald, J. W., and Larson, R. E.: Marine boundary layer measurements of new particle formation and the effects nonprecipitating clouds have on aerosol size distribution, J. Geophys. Res.-Atmos., 99, 14 443–14 459, https://doi.org/10.1029/94JD00797, 1994.

Huang, J., Lin, B., Minnis, P., Wang, T., Wang, X., Hu, Y., Yi, Y., and Ayers, J. K.: Satellite-based assessment of possible dust aerosols semi-direct effect on cloud water path over East Asia, Geophys. Res. Lett., 33, L19802, https://doi.org/10.1029/2006GL026561, 2006.

Jaenicke, R. and Schütz, L.: Comprehensive study of physical and chemical properties of the surface aerosols in the Cape Verde Islands region, J. Geophys. Res.-Oceans, 83, 3585–3599, https://doi.org/10.1029/JC083iC07p03585, 1978.

Kaaden, N., Massling, A., Schladitz, A., Müller, T., Kandler, K., Schütz, L., Weinzierl, B., Petzold, A., Tesche, M., Leinert, S., Deutscher, C., Ebert, M., Weinbruch, S., and Wiedensohler, A.: State of mixing, shape factor, number size distribution, and hygroscopic growth of the Saharan anthropogenic and mineral dust aerosol at Tinfou, Morocco, Tellus B, 61, 51–63, https://doi.org/10.1111/j.1600-0889.2008.00388.x, 2009.

Kalivitis, N., Kerminen, V.-M., Kouvarakis, G., Stavroulas, I., Bougiatioti, A., Nenes, A., Manninen, H. E., Petäjä, T., Kulmala, M., and Mihalopoulos, N.: Atmospheric new particle formation as a source of CCN in the eastern Mediterranean marine boundary layer, Atmos. Chem. Phys., 15, 9203–9215, https://doi.org/10.5194/acp-15-9203-2015, 2015.

Kandler, K., SchüTz, L., Deutscher, C., Ebert, M., Hofmann, H., JäCkel, S., Jaenicke, R., Knippertz, P., Lieke, K., Massling, A., Petzold, A., Schladitz, A., Weinzierl, B., Wiedensohler, A., Zorn, S., and Weinbruch, S.: Size distribution, mass concentration, chemical and mineralogical composition and derived optical parameters of the boundary layer aerosol at Tinfou, Morocco, during SAMUM 2006, Tellus B, 61, 32–50, https://doi.org/10.1111/j.1600-0889.2008.00385.x, 2009.

Kandler, K., Lieke, K., Benker, N., Emmel, C., Küpper, M., Müller-Ebert, D., Ebert, M., Scheuvens, D., Schladitz, A., Schütz, L., and Weinbruch, S.: Electron microscopy of particles collected at Praia, Cape Verde, during the Saharan Mineral Dust Experiment: particle chemistry, shape, mixing state and complex refractive index, Tellus B, 63, 475–496, https://doi.org/10.1111/j.1600-0889.2011.00550.x, 2011a.

Kandler, K., Schütz, L., Jäckel, S., Lieke, K., Emmel, C., Müller-Ebert, D., Ebert, M., Scheuvens, D., Schladitz, A., Šegvić, B., Wiedensohler, A., and Weinbruch, S.: Ground-based off-line aerosol measurements at Praia, Cape Verde, during the Saharan Mineral Dust Experiment: microphysical properties and mineralogy, Tellus B, 63, 459–474, https://doi.org/10.1111/j.1600-0889.2011.00546.x, 2011b.

Karydis, V. A., Kumar, P., Barahona, D., Sokolik, I. N., and Nenes, A.: On the effect of dust particles on global cloud condensation nuclei and cloud droplet number, J. Geophys. Res.-Atmos., 116, D23204, https://doi.org/10.1029/2011JD016283, 2011.

Köhler, H.: The nucleus in and the growth of hygroscopic droplets, T. Faraday Soc., 32, 1152–1161, 1936.

Kristensen, T. B., Müller, T., Kandler, K., Benker, N., Hartmann, M., Prospero, J. M., Wiedensohler, A., and Stratmann, F.: Properties of cloud condensation nuclei (CCN) in the trade wind marine boundary layer of the western North Atlantic, Atmos. Chem. Phys., 16, 2675–2688, https://doi.org/10.5194/acp-16-2675-2016, 2016.

Lieke, K., Kandler, K., Scheuvens, D., Emmel, C., Von Glahn, C., Petzold, A., Weinzierl, B., Veira, A., Ebert, M., Weinbruch, S., and Schütz, L.: Particle chemical properties in the vertical column based on aircraft observations in the vicinity of Cape Verde Islands, Tellus B, 63, 497–511, https://doi.org/10.1111/j.1600-0889.2011.00553.x, 2011.

Modini, R. L., Frossard, A. A., Ahlm, L., Russell, L. M., Corrigan, C. E., Roberts, G. C., Hawkins, L. N., Schroder, J. C., Bertram, A. K., Zhao, R., Lee, A. K. Y., Abbatt, J. P. D., Lin, J., Nenes, A., Wang, Z., Wonaschütz, A., Sorooshian, A., Noone, K. J., Jonsson, H., Seinfeld, J. H., Toom-Sauntry, D., Macdonald, A. M., and Leaitch, W. R.: Primary marine aerosol-cloud interactions off the coast of California, J. Geophys. Res.-Atmos., 120, 4282–4303, https://doi.org/10.1002/2014JD022963, 2015.

Nie, W., Ding, A., Wang, T., Kerminen, V.-M., George, C., Xue, L., Wang, W., Zhang, Q., Petäjä, T., Qi, X., Gao, X., Wang, X., Yang, X., Fu, C., and Kulmala, M.: Polluted dust promotes new particle formation and growth, Sci. Rep., 4, 6634, https://doi.org/10.1038/srep06634, 2014.

Petters, M. D. and Kreidenweis, S. M.: A single parameter representation of hygroscopic growth and cloud condensation nucleus activity, Atmos. Chem. Phys., 7, 1961–1971, https://doi.org/10.5194/acp-7-1961-2007, 2007.

Pfeifer, S., Müller, T., Weinhold, K., Zikova, N., Martins dos Santos, S., Marinoni, A., Bischof, O. F., Kykal, C., Ries, L., Meinhardt, F., Aalto, P., Mihalopoulos, N., and Wiedensohler, A.: Intercomparison of 15 aerodynamic particle size spectrometers (APS 3321): uncertainties in particle sizing and number size distribution, Atmos. Meas. Tech., 9, 1545–1551, https://doi.org/10.5194/amt-9-1545-2016, 2016.

Prather, K. A., Bertram, T. H., Grassian, V. H., Deane, G. B., Stokes, M. D., DeMott, P. J., Aluwihare, L. I., Palenik, B. P., Azam, F., Seinfeld, J. H., Moffet, R. C., Molina, M. J., Cappa, C. D., Geiger, F. M., Roberts, G. C., Russell, L. M., Ault, A. P., Baltrusaitis, J., Collins, D. B., Corrigan, C. E., Cuadra-Rodriguez, L. A., Ebben, C. J., Forestieri, S. D., Guasco, T. L., Hersey, S. P., Kim, M. J., Lambert, W. F., Modini, R. L., Mui, W., Pedler, B. E., Ruppel, M. J., Ryder, O. S., Schoepp, N. G., Sullivan, R. C., and Zhao, D.: Bringing the ocean into the laboratory to probe the chemical complexity of sea spray aerosol, P. Natl. Acad. Sci. USA, 110, 7550–7555, https://doi.org/10.1073/pnas.1300262110, 2013.

Pringle, K. J., Tost, H., Pozzer, A., Pöschl, U., and Lelieveld, J.: Global distribution of the effective aerosol hygroscopicity parameter for CCN activation, Atmos. Chem. Phys., 10, 5241–5255, https://doi.org/10.5194/acp-10-5241-2010, 2010.

Prospero, J. M., Ginoux, P., Torres, O., Nicholson, S. E., and Gill, T. E.: Environmental characterization of global sources of atmospheric soil dust identified with the nimbus 7 total ozone mapping spectrometer (TOMS) absorbing aerosol product, Rev. Geophys., 40, 2-1–2-31, https://doi.org/10.1029/2000RG000095, 2002.

Quinn, P. K., Collins, D. B., Grassian, V. H., Prather, K. A., and Bates, T. S.: Chemistry and Related Properties of Freshly Emitted Sea Spray Aerosol, Chem. Rev., 115, 4383–4399, https://doi.org/10.1021/cr500713g, 2015.

Quinn, P. K., Coffman, D. J., Johnson, J. E., Upchurch, L. M., and Bates, T. S.: Small fraction of marine cloud condensation nuclei made up of sea spray aerosol, Nat. Geosci., 10, 674, https://doi.org/10.1038/ngeo3003, 2017.

Roberts, G. C. and Nenes, A.: A Continuous-Flow Streamwise Thermal-Gradient CCN Chamber for Atmospheric Measurements, Aerosol Sci. Technol., 39, 206–221, https://doi.org/10.1080/027868290913988, 2005.

Rolph, G.: Real-time environmental applications and display system (READY) website, available at: https://www.ready.noaa.gov/index.php (last access: 4 February 2020), 2003.

Rosati, B., Gysel, M., Rubach, F., Mentel, T. F., Goger, B., Poulain, L., Schlag, P., Miettinen, P., Pajunoja, A., Virtanen, A., Klein Baltink, H., Henzing, J. S. B., Größ, J., Gobbi, G. P., Wiedensohler, A., Kiendler-Scharr, A., Decesari, S., Facchini, M. C., Weingartner, E., and Baltensperger, U.: Vertical profiling of aerosol hygroscopic properties in the planetary boundary layer during the PEGASOS campaigns, Atmos. Chem. Phys., 16, 7295–7315, https://doi.org/10.5194/acp-16-7295-2016, 2016a.

Rosati, B., Herrmann, E., Bucci, S., Fierli, F., Cairo, F., Gysel, M., Tillmann, R., Größ, J., Gobbi, G. P., Di Liberto, L., Di Donfrancesco, G., Wiedensohler, A., Weingartner, E., Virtanen, A., Mentel, T. F., and Baltensperger, U.: Studying the vertical aerosol extinction coefficient by comparing in situ airborne data and elastic backscatter lidar, Atmos. Chem. Phys., 16, 4539–4554, https://doi.org/10.5194/acp-16-4539-2016, 2016b.

Rose, D., Gunthe, S. S., Mikhailov, E., Frank, G. P., Dusek, U., Andreae, M. O., and Pöschl, U.: Calibration and measurement uncertainties of a continuous-flow cloud condensation nuclei counter (DMT-CCNC): CCN activation of ammonium sulfate and sodium chloride aerosol particles in theory and experiment, Atmos. Chem. Phys., 8, 1153–1179, https://doi.org/10.5194/acp-8-1153-2008, 2008.

Salvador, P., Artíñano, B., Molero, F., Viana, M., Pey, J., Alastuey, A., and Querol, X.: African dust contribution to ambient aerosol levels across central Spain: Characterization of long-range transport episodes of desert dust, Atmos. Res., 127, 117–129, https://doi.org/10.1016/j.atmosres.2011.12.011, 2013.

Salvador, P., Almeida, S. M., Cardoso, J., Almeida-Silva, M., Nunes, T., Cerqueira, M., Alves, C., Reis, M. A., Chaves, P. C., Artíñano, B., and Pio, C.: Composition and origin of PM_{10} in Cape Verde: Characterization of long-range transport episodes, Atmos. Environ., 127, 326–339, https://doi.org/10.1016/j.atmosenv.2015.12.057, 2016.

Sassen, K., DeMott, P. J., Prospero, J. M., and Poellot, M. R.: Saharan dust storms and indirect aerosol effects on clouds: CRYSTAL-FACE results, Geophys. Res. Lett., 30, 1633, https://doi.org/10.1029/2003GL017371, 2003.

Schladitz, A., Müller, T., Nordmann, S., Tesche, M., Groß, S., Freudenthaler, V., Gasteiger, J., and Wiedensohler, A.: In situ aerosol characterization at Cape Verde, Part 2: Parameterization of relative humidity- and wavelength-

dependent aerosol optical properties, Tellus B, 63, 549–572, https://doi.org/10.1111/j.1600-0889.2011.00568.x, 2011a.

Schladitz, A., Müller, T., Nowak, A., Kandler, K., Lieke, K., Massling, A., and Wiedensohler, A.: In situ aerosol characterization at Cape Verde, Part1: Particle number size distributions, hygroscopic growth and state of mixing of mrine and Saharan dust aerosol, Tellus B, 63, 531–548, https://doi.org/10.1111/j.1600-0889.2011.00569.x, 2011b.

Seinfeld, J. H. and Pandis, S. N.: Atmospheric chemistry and physics: from air pollution to climate change, John Wiley & Sons, 2016.

Shao, Y., Wyrwoll, K.-H., Chappell, A., Huang, J., Lin, Z., McTainsh, G. H., Mikami, M., Tanaka, T. Y., Wang, X., and Yoon, S.: Dust cycle: An emerging core theme in Earth system science, Aeolian Res., 2, 181–204, https://doi.org/10.1016/j.aeolia.2011.02.001, 2011.

Stein, A. F., Draxler, R. R., Rolph, G. D., Stunder, B. J. B., Cohen, M. D., and Ngan, F.: NOAA's HYSPLIT Atmospheric Transport and Dispersion Modeling System, B. Am. Meteorol. Soc., 96, 2059–2077, https://doi.org/10.1175/bams-d-14-00110.1, 2015.

Stocker, T.: Climate change 2013: the physical science basis: Working Group I contribution to the Fifth assessment report of the Intergovernmental Panel on Climate Change, Cambridge University Press, 2014.

Swap, R., Garstang, M., Greco, S., Talbot, R., and Kallberg, P.: Saharan dust in the Amazon Basin, Tellus B, 44, 133–149, https://doi.org/10.1034/j.1600-0889.1992.t01-1-00005.x, 1992.

Tanaka, T. Y. and Chiba, M.: A numerical study of the contributions of dust source regions to the global dust budget, Global Planet. Change, 52, 88–104, https://doi.org/10.1016/j.gloplacha.2006.02.002, 2006.

Tesche, M., Ansmann, A., Müller, D., Althausen, D., Engelmann, R., Freudenthaler, V., and Groß, S.: Vertically resolved separation of dust and smoke over Cape Verde using multiwavelength Raman and polarization lidars during Saharan Mineral Dust Experiment 2008, J. Geophys. Res.-Atmos., 114, D13202, https://doi.org/10.1029/2009JD011862, 2009.

Twomey, S.: Pollution and the planetary albedo, Atmos. Environ., 8, 1251–1256, 1974.

van Pinxteren, M., Fomba, K. W., Triesch, N., Stolle, C., Wurl, O., Bahlmann, E., Gong, X., Voigtländer, J., Wex, H., Robinson, T.-B., Barthel, S., Zeppenfeld, S., Hoffmann, E. H., Roveretto, M., Li, C., Grosselin, B., Daële, V., Senf, F., van Pinxteren, D., Manzi, M., Zabalegui, N., Frka, S., Gašparović, B., Pereira, R., Li, T., Wen, L., Li, J., Zhu, C., Chen, H., Chen, J., Fiedler, B., von Tümpling, W., Read, K. A., Punjabi, S., C. Lewis, A. C., Hopkins, J. R., Carpenter, L. J., Peeken, I., Rixen, T., Schulz-Bull, D., Monge, M. E., Mellouki, A., George, C., Stratmann, F., and Herrmann, H.: Marine organic matter in the remote environment of the Cape Verde Islands – An introduction and overview to the MarParCloud campaign, Atmos. Chem. Phys. Discuss., https://doi.org/10.5194/acp-2019-997, in review, 2019.

von der Weiden, S.-L., Drewnick, F., and Borrmann, S.: Particle Loss Calculator – a new software tool for the assessment of the performance of aerosol inlet systems, Atmos. Meas. Tech., 2, 479–494, https://doi.org/10.5194/amt-2-479-2009, 2009.

Warneck, P.: Chemistry of the natural atmosphere, 2nd Edn., vol. 71, ISBN 10 0127356320, Elsevier, Academic Press, London, UK, 1999.

Weinzierl, B., Petzold, A., Esselborn, M., Wirth, M., Rasp, K., Kandler, K., Schütz, L., Koepke, P., and Fiebig, M.: Airborne measurements of dust layer properties, particle size distribution and mixing state of Saharan dust during SAMUM 2006, Tellus B, 61, 96–117, https://doi.org/10.1111/j.1600-0889.2008.00392.x, 2009.

Wex, H., Dieckmann, K., Roberts, G. C., Conrath, T., Izaguirre, M. A., Hartmann, S., Herenz, P., Schäfer, M., Ditas, F., Schmeissner, T., Henning, S., Wehner, B., Siebert, H., and Stratmann, F.: Aerosol arriving on the Caribbean island of Barbados: physical properties and origin, Atmos. Chem. Phys., 16, 14107–14130, https://doi.org/10.5194/acp-16-14107-2016, 2016.

Wiedensohler, A.: An approximation of the bipolar charge distribution for particles in the submicron size range, J. Aerosol Sci., 19, 387–389, https://doi.org/10.1016/0021-8502(88)90278-9, 1988.

Wiedensohler, A., Birmili, W., Nowak, A., Sonntag, A., Weinhold, K., Merkel, M., Wehner, B., Tuch, T., Pfeifer, S., Fiebig, M., Fjäraa, A. M., Asmi, E., Sellegri, K., Depuy, R., Venzac, H., Villani, P., Laj, P., Aalto, P., Ogren, J. A., Swietlicki, E., Williams, P., Roldin, P., Quincey, P., Hüglin, C., Fierz-Schmidhauser, R., Gysel, M., Weingartner, E., Riccobono, F., Santos, S., Grüning, C., Faloon, K., Beddows, D., Harrison, R., Monahan, C., Jennings, S. G., O'Dowd, C. D., Marinoni, A., Horn, H.-G., Keck, L., Jiang, J., Scheckman, J., McMurry, P. H., Deng, Z., Zhao, C. S., Moerman, M., Henzing, B., de Leeuw, G., Löschau, G., and Bastian, S.: Mobility particle size spectrometers: harmonization of technical standards and data structure to facilitate high quality long-term observations of atmospheric particle number size distributions, Atmos. Meas. Tech., 5, 657–685, https://doi.org/10.5194/amt-5-657-2012, 2012.

Wiedensohler, A., Wiesner, A., Weinhold, K., Birmili, W., Hermann, M., Merkel, M., Müller, T., Pfeifer, S., Schmidt, A., Tuch, T., Velarde, F., Quincey, P., Seeger, S., and Nowak, A.: Mobility particle size spectrometers: Calibration procedures and measurement uncertainties, Aerosol Sci. Technol., 52, 146–164, https://doi.org/10.1080/02786826.2017.1387229, 2018.

Wilson, T. W., Ladino, L. A., Alpert, P. A., Breckels, M. N., Brooks, I. M., Browse, J., Burrows, S. M., Carslaw, K. S., Huffman, J. A., Judd, C., Kilthau, W. P., Mason, R. H., McFiggans, G., Miller, L. A., Najera, J. J., Polishchuk, E., Rae, S., Schiller, C. L., Si, M., Temprado, J. V., Whale, T. F., Wong, J. P. S., Wurl, O., Yakobi-Hancock, J. D., Abbatt, J. P. D., Aller, J. Y., Bertram, A. K., Knopf, D. A., and Murray, B. J.: A marine biogenic source of atmospheric ice-nucleating particles, Nature, 525, 234–238, https://doi.org/10.1038/nature14986, 2015.

Supplement of Atmos. Chem. Phys., 20, 1431–1449, 2020
https://doi.org/10.5194/acp-20-1431-2020-supplement

Atmospheric Chemistry and Physics
Open Access
EGU

Supplement of

Characterization of aerosol particles at Cabo Verde close to sea level and at the cloud level – Part 1: Particle number size distribution, cloud condensation nuclei and their origins

Xianda Gong et al.

Correspondence to: Xianda Gong (gong@tropos.de)

S1 Combined MPSS and APS PNSDs

The dry density of Saharan dust particles was determined in a range of ρ = 2450 - 2700 kg m^{-3} over the Cape Verde Islands (Haywood et al., 2001). The dry particle density of sodium chloride is known to be ρ = 2160 kg m^{-3}. The overall effective density of the dust and sea-salt fraction is approximately 2, as recommenced in Schladitz et al. (2011).

The dry dynamic shape factor χ of mineral dust is χ = 1.25 (Kaaden et al., 2009) for 1 μm particles, whereas the dynamic shape factor for sodium chloride is χ = 1.08 (Kelly and McMurry, 1992; Gysel and Stratmann, 2013). We used the average shape factor of 1.17 in this study.

Based on these, a conversion from aerodynamic to geometric diameters were done for the APS data, and particle number concentrations from the APS were used to correct the multiply charged particle concentrations in the upper size range where the MPSS measured.

S2 Accounting for particle losses

The particle losses related to the transport of aerosol particles within the inlet tube system are determined using the Particle Loss Calculator (PLC) (von der Weiden et al., 2009). Size-dependent particle losses due to diffusion, sedimentation, turbulent inertial deposition, inertial deposition in a bend, and inertial deposition in a contraction are accounted for. The resulting particle losses is shown in Fig. S1, which depicts particle loesses in % as a function of particle size.

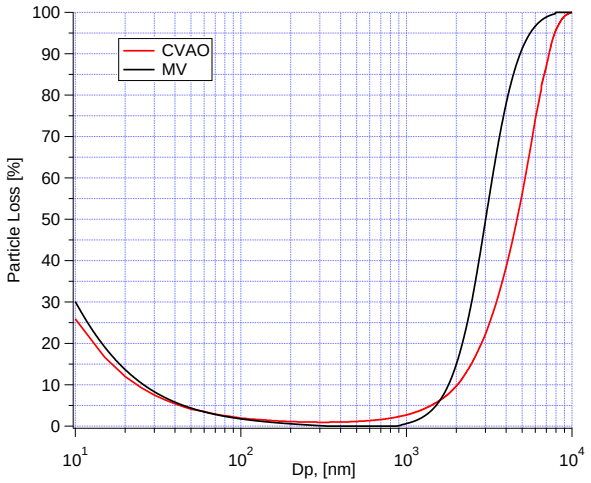

Figure S1. Size-dependent particle loss through the inlet at at the site close to sea level (CVAO) and on the mountaintop (MV).

S3 Monte Carlo simulation

The uncertainty in κ, which results from uncertainties of the PNSD measurements and the supersaturations of the CCNc, was determined by applying a Monte Carlo simulation (MCS) in a similar fashion as done by Kristensen et al. (2016) and Herenz et al. (2018).

The particle diameter which is selected with a differential mobility analyzer (DMA) has an uncertainty of 3.0% (corresponding to one standard deviation). The measured particle number concentration has an uncertainty of 5.0% (corresponding to one standard deviation). In addition, the effective supersaturation in CCNc has a relative uncertainty of 3.5% (corresponding to one standard deviation) for supersaturation above 0.20%. Below a supersaturation of 0.20%, the same absolute uncertainty as for a supersaturation of 0.20% can be assumed. These uncertainties have been inferred from several supersaturation calibrations that were performed at the Leibniz Institute for Tropospheric Research (TROPOS). All of the measurement uncertainties can be found in the ACTRIS protocol (Gysel and Stratmann, 2013). To consider the impact of these uncertainties on d_{crit} and κ in a realistic way, a Monte Carlo simulation (MCS) based on random normal distributions was used. This following general equation was applied:

$$s_{\text{MC}} = s + s * u * p \tag{S1}$$

where u is the relative uncertainty, p is a random number, s is the measured signal and s_{MC} is the resulting MCS signal. This was done for 10 000 random and normally distributed numbers p, with a mean of 0 and a standard deviation of 1, which then results in 10 000 values for s_{MC} with a variability that is characterized by u.

Firstly, the uncertainty in d_{crit} was obtained by a MCS based on one exemplary PNSDs, the related N_{CCN} and a 5.0% uncertainty in the particle number concentration. Eq. S1 was used to vary the particle number concentration of each size bin of the PNSD to calculate 10 000 d_{crit} values, of which a distribution is shown in Fig. S2(a). The mean and 1 standard deviation of these 10 000 d_{crit} values can be taken from this distribution, and the overall uncertainty in d_{crit} was derived from those values together with the 3.0% uncertainty in the particle sizing due to the DMA, using error propagation. This was then done for all PNSDs. The resulting uncertainties are shown as error bars in the middle panel of Fig. 10.

Secondly, κ and the corresponding error bars in the lower panel of Fig. 10 are inferred by means of Eq. 1. The effective supersaturation of the CCNc are 10 000 times Monte Carlo simulated (same procedure as for d_{crit}). Since the connection between κ and supersaturation is logarithmic, the resulting distribution of the 10 000 κ values is a log-normal distribution, as can be seen in Fig. S2(b) for one exemplary case. Consequently, our final inferred κ and its uncertainty are the geometric mean and the one standard geometric standard deviation of this distribution, respectively. The resulting uncertainties are shown as error bars in the lower panel of Fig. 10.

Lastly, we calculated d_{crit} and κ uncertainties in a certain period. Combining all d_{crit} values in a certain period, we could get the total d_{crit} distribution. In this case, we took all of the d_{crit} at a supersaturation of 0.50% during the whole campaign and the resulting distribution are shown in Fig. S2(c). The mean value and one standard deviation of d_{crit} can be taken from this distribution, which is shown in Fig. 11(d) and Fig. 12(b). Using the same way, we did the same distribution of κ values.

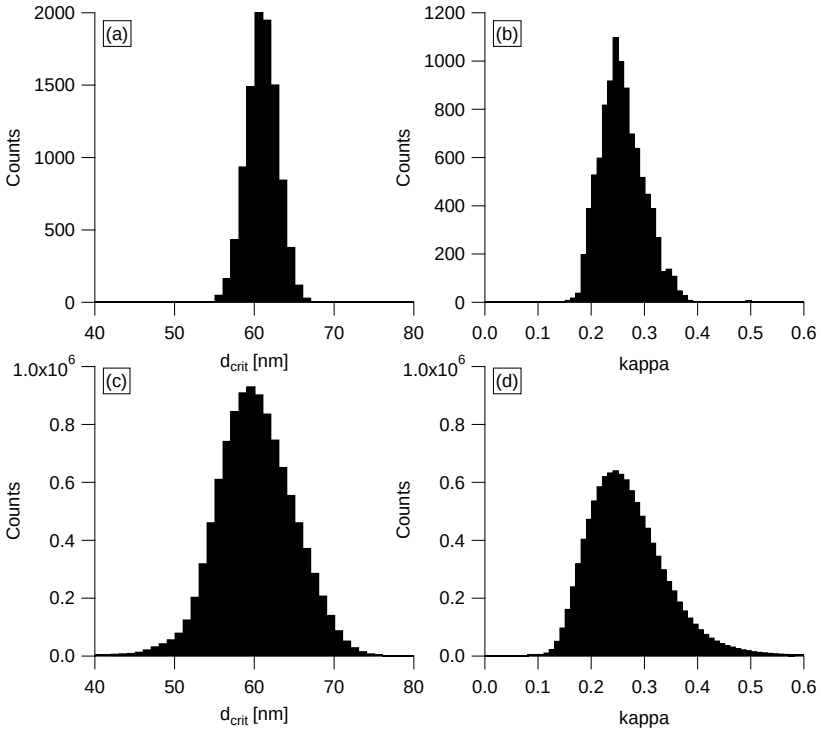

Figure S2. (a) Distribution of 10 000 d_{crit} values after applying the MCS. (b) Distribution of 10 000 κ values after applying the MCS. (c) Distribution of d_{crit} values over a certain period. (d) Distribution of κ values over a certain period.

The geometric mean value and one geometric standard deviation of κ can be taken from this distribution, which is shown in Fig. 11(d) and Fig. 12(b).

S4 Balloon measurement

Balloon measurements were carried out at CVAO. One example of the result from such a measurement at 14:30 UTC on 17 September is shown in Fig. S3, including vertical profile of temperature and relative humility. The weather condition at that moment is shown in Fig. S4.

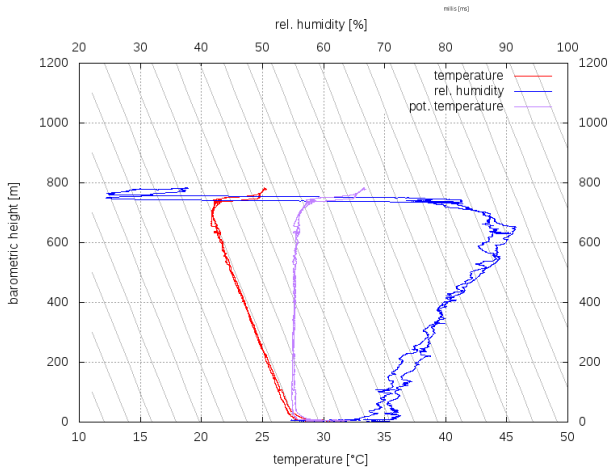

Figure S3. Vertical profile of temperature and relative humility at 14:30 UTC on 17 September. Profiles up to about 1200 m can be measured. From the measurements the inversion layer height was determined (here: ∼700 m).

Figure S4. Picture of weather condition at 14:30 UTC on 17 September.

S5 Particle classification

Fig. S5 shows the probability density function (PDF) of N_{coarse}. Two distinct modes of PDF were observed, i.e., small mode in the range from 0 to 25 cm^{-3}, large mode in the range large than 25 cm^{-3}. Based on a ground measurement at CVAO, Schladitz et al. (2011) found the particle number concentration of the coarse mode (N_{coarse}) is highly variable and the higher N_{coarse} originates from the Saharan desert. We assumed that $N_{\text{coarse}} > 25$ cm^{-3} is mainly contributed by dust aerosols.

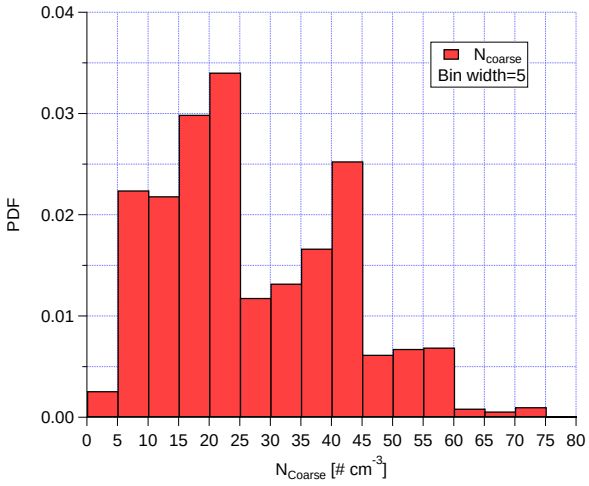

Figure S5. PDF of N_{coarse} during the whole campaign.

S6 Correlation of N_{coarse} with wind speed during marine period

Fig. S6 shows N_{coarse} as a function of wind speed during the marine type period. The coefficient of determination (R^2) is 0.69 and p value is <0.01, which means a good correlation between coarse mode number concentration and wind speed. This is consistent with the fact that these particles come from sea spray, i.e., are SSA (sea spray aerosol), generated from the process associated with the agitation of the sea surface by air moving above it.

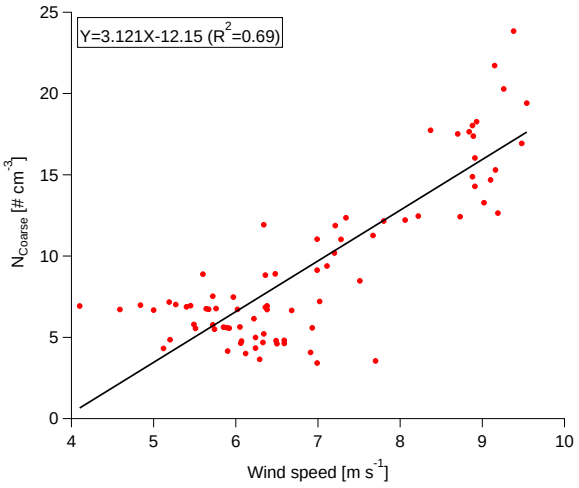

Figure S6. N_{coarse} as a function of wind speed during the marine type period. The liner fitting function and R^2 are given in the panel.

S7 Characterization of cloud events

Fig. S7 shows PDF of the ratio of $N^{\mathrm{MV}}_{\mathrm{accumulation}}$ to $N^{\mathrm{CVAO}}_{\mathrm{accumulation}}$ in the upper panel. Clearly, three modes were observed. The largest mode is located at the ratio of 1. The minimum between largest mode and smaller modes is at 0.85. Therefore, 0.85 can be used as a threshold to classify cloud events and non-cloud events. For the periods when the three-modal log-normal fitting function did not work (from 03:30 to 20:00 21 and 09:30 28 to 18:30 30 September), we used the ratio of $N^{\mathrm{MV}}_{\mathrm{80\text{-}800nm}}$ to $N^{\mathrm{CVAO}}_{\mathrm{80\text{-}800nm}}$ and the PDF of this ratio can be seen in the lower panel in Fig. S7. When the ratio is lower than 0.75, we assume that MV is in a cloud. These two ratios were derived separately for different cases with three- and bi-modal fitting and they are different.

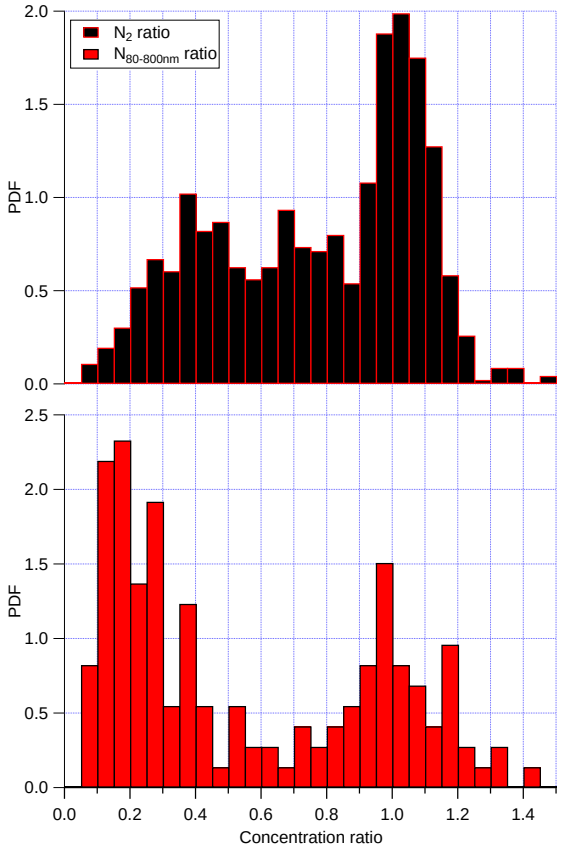

Figure S7. PDF of the ratio between $N^{\mathrm{MV}}_{\mathrm{accumulation}}$ and $N^{\mathrm{CVAO}}_{\mathrm{accumulation}}$ in the upper panel and the ratio between $N^{\mathrm{MV}}_{\mathrm{80\text{-}800nm}}$ and $N^{\mathrm{CVAO}}_{\mathrm{80\text{-}800nm}}$ in the lower panel.

The resulting times for the occurrence of cloud events is shown by red shadows in Fig. S8. Time series of RH at MV is shown by a black line in Fig. S8. It is clear that times with RH=100% are consistent with cloud events identified as described above, which verifies our identification of cloud events.

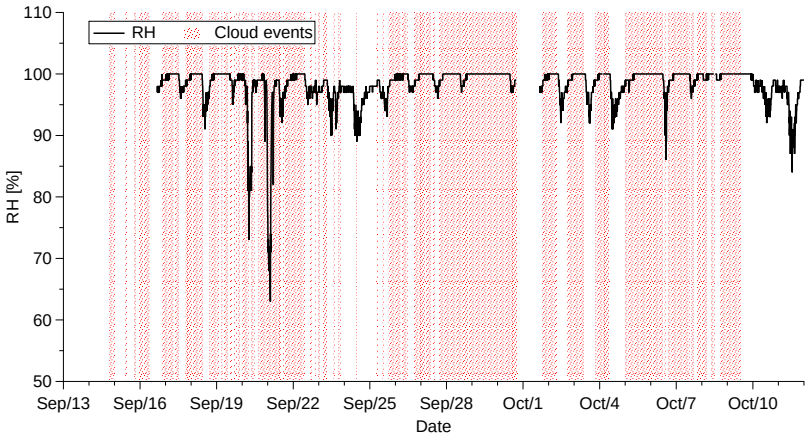

Figure S8. Time series of RH at MV is shown by black line. Cloud event times are shown by red shadows.

S8 Contour plots for PNSDs at CVAO and MV

Fig. S9 shows the contour plots for PNSDs in the size range between 10 to 800 nm at MV in the upper panel and at CVAO in the lower panel.

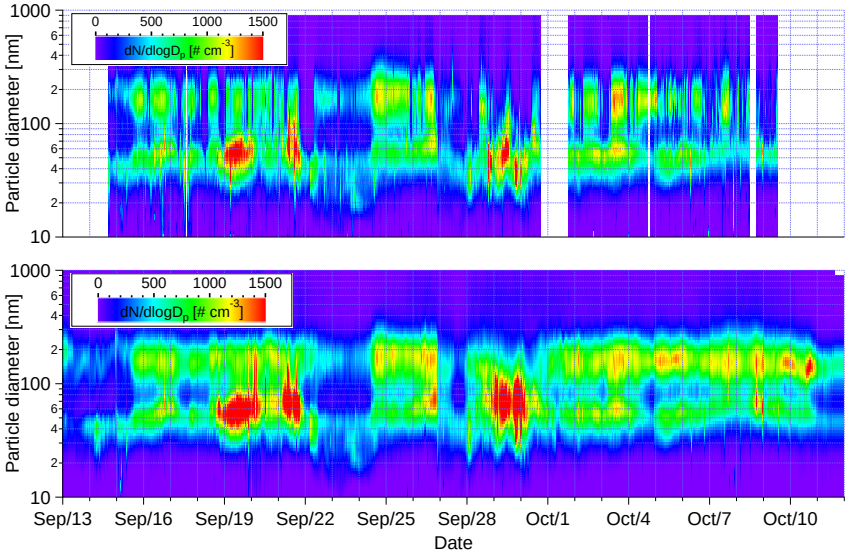

Figure S9. Contour plots for PNSDs in the size range between 10 to 800 nm at MV (upper panel) and at CVAO (lower panel). The color scale indicates dN/dlogDp in cm^{-3}.

S9 PNSDs at MV and CVAO during decoupled boundary layer period

Fig. S10 shows PNSDs at MV (red lines) and CVAO (black lines) from 10:30 to 11:00 16 September. This was a period during which a decoupled boundary layer was observed, and even in this case, PNSDs were similar at MV and CVAO.

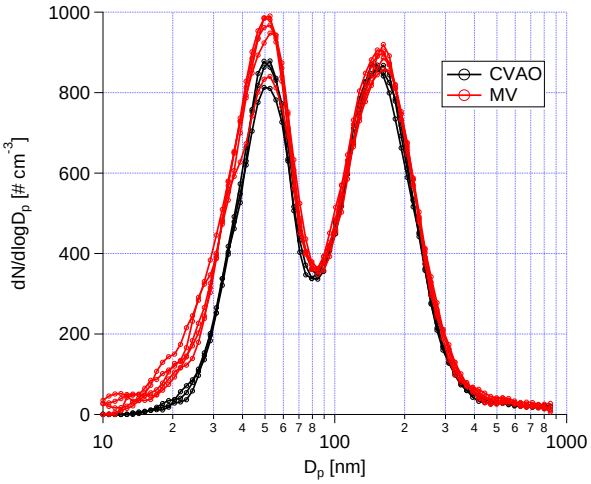

Figure S10. PNSDs at MV (in red) and CVAO (in black) from 10:30 to 11:00 16 September.

S10 Explanation of larger error bars for d_{crit} and κ at 0.30% during marine periods

At a supersaturation of 0.30% during the marine periods, κ and d_{crit} featured the largest observed variability. This can be seen from the larger error bars in Fig. 12. d_{crit} at 0.30% is close to the Hoppel minimum, and the particle number concentration (dN/dlogDp) around the Hoppel minimum is lower than 100 cm^{-3}. Assuming N_{CCN} varied 2% during each ~6-minute averaged period, the absolute number concentration can change around 5 cm^{-3}. The tiny variation of N_{CCN} can change d_{crit} by ~10 nm. Since κ is correlated to d_{crit}^3, the large error bar of κ results. To conclude, these larger error bars at a supersaturation of 0.30% are due to the measurement uncertainty.

References

Gysel, M. and Stratmann, F.: WP3 - NA3: In-situ chemical, physical and optical properties of aerosols, Deliverable D3.11: Standardized protocol for CCN measurements, Tech. rep., http://www.actris.net/Publications/ACTRISQualityStandards/tabid/11271/language/en-GB/Default.aspx, 2013.

Haywood, J. M., Francis, P. N., Glew, M. D., and Taylor, J. P.: Optical properties and direct radiative effect of Saharan dust: A case study of two Saharan dust outbreaks using aircraft data, Journal of Geophysical Research: Atmospheres, 106, 18 417–18 430, https://doi.org/10.1029/2000jd900319, https://agupubs.onlinelibrary.wiley.com/doi/abs/10.1029/2000JD900319, 2001.

Herenz, P., Wex, H., Henning, S., Kristensen, T. B., Rubach, F., Roth, A., Borrmann, S., Bozem, H., Schulz, H., and Stratmann, F.: Measurements of aerosol and CCN properties in the Mackenzie River delta (Canadian Arctic) during spring–summer transition in May 2014, Atmos. Chem. Phys., 18, 4477–4496, https://doi.org/10.5194/acp-18-4477-2018, https://www.atmos-chem-phys.net/18/4477/2018/, 2018.

Kaaden, N., Massling, A., Schladitz, A., Müller, T., Kandler, K., Schütz, L., Weinzierl, B., Petzold, A., Tesche, M., Leinert, S., Deutscher, C., Ebert, M., Weinbruch, S., and Wiedensohler, A.: State of mixing, shape factor, number size distribution, and hygroscopic growth of the Saharan anthropogenic and mineral dust aerosol at Tinfou, Morocco, Tellus B, 61, 51–63, https://doi.org/doi:10.1111/j.1600-0889.2008.00388.x, https://onlinelibrary.wiley.com/doi/abs/10.1111/j.1600-0889.2008.00388.x, 2009.

Kelly, W. P. and McMurry, P. H.: Measurement of Particle Density by Inertial Classification of Differential Mobility Analyzer–Generated Monodisperse Aerosols, Aerosol Science and Technology, 17, 199–212, https://doi.org/10.1080/02786829208959571, https://doi.org/10.1080/02786829208959571, 1992.

Kristensen, T. B., Müller, T., Kandler, K., Benker, N., Hartmann, M., Prospero, J. M., Wiedensohler, A., and Stratmann, F.: Properties of cloud condensation nuclei (CCN) in the trade wind marine boundary layer of the western North Atlantic, Atmos. Chem. Phys., 16, 2675–2688, https://doi.org/10.5194/acp-16-2675-2016, http://www.atmos-chem-phys.net/16/2675/2016/, 2016.

Schladitz, A., Müller, T., Nowak, A., Kandler, K., Lieke, K., Massling, A., and Wiedensohler, A.: In situ aerosol characterization at Cape Verde, Part1: Particle number size distributions, hygroscopic growth and state of mixing of mrine and Saharan dust aerosol, Tellus B, 63, 531–548, https://doi.org/10.1111/j.1600-0889.2011.00569.x, http://dx.doi.org/10.1111/j.1600-0889.2011.00569.x, 2011.

von der Weiden, S. L., Drewnick, F., and Borrmann, S.: Particle Loss Calculator - a new software tool for the assessment of the performance of aerosol inlet systems, Atmos. Meas. Tech., 2, 479–494, https://doi.org/10.5194/amt-2-479-2009, http://www.atmos-meas-tech.net/2/479/2009/, 2009.

3.3 Third Publication: Characterization of aerosol particles at Cabo Verde close to sea level and at the cloud level – Part 2: Ice-nucleating particles in air, cloud and seawater

The content of this section has already been published under the title "Characterization of aerosol particles at Cabo Verde close to sea level and at the cloud level – Part 2: Ice-nucleating particles in air, cloud and seawater" by Gong, X., Wex, H., van Pinxteren, M., Triesch, N., Fomba, K. W., Lubitz, J., Stolle, C., Robinson, T.-B., Müller, T., Herrmann, H., and Stratmann, F. In 2020, the paper was published under the Creative Commons Attribution 4.0 License in *Atmos. Chem. Phys.* with the doi: https://doi.org/10.5194/acp-20-1451-2020, 2020.

Reprinted with permission by the authors from *Atmos. Chem. Phys.*, 20, 1451–1468, 2020.

Atmos. Chem. Phys., 20, 1451–1468, 2020
https://doi.org/10.5194/acp-20-1451-2020

Atmospheric Chemistry and Physics
Open Access
EGU

Characterization of aerosol particles at Cabo Verde close to sea level and at the cloud level – Part 2: Ice-nucleating particles in air, cloud and seawater

Xianda Gong[1], Heike Wex[1], Manuela van Pinxteren[1], Nadja Triesch[1], Khanneh Wadinga Fomba[1], Jasmin Lubitz[1], Christian Stolle[2,3], Tiera-Brandy Robinson[3], Thomas Müller[1], Hartmut Herrmann[1], and Frank Stratmann[1]

[1]Leibniz Institute for Tropospheric Research, Leipzig, Germany
[2]Leibniz Institute for Baltic Sea Research Warnemünde (IOW), Rostock, Germany
[3]Institute for Chemistry and Biology of the Marine Environment, University of Oldenburg, Wilhelmshaven, Germany

Correspondence: Xianda Gong (gong@tropos.de)

Received: 14 August 2019 – Discussion started: 18 September 2019
Revised: 11 January 2020 – Accepted: 16 January 2020 – Published: 6 February 2020

Abstract. Ice-nucleating particles (INPs) in the troposphere can form ice in clouds via heterogeneous ice nucleation. Yet, atmospheric number concentrations of INPs (N_{INP}) are not well characterized, and, although there is some understanding of their sources, it is still unclear to what extend different sources contribute or if all sources are known. In this work, we examined properties of INPs at Cabo Verde (a.k.a. Cape Verde) from different environmental compartments: the oceanic sea surface microlayer (SML), underlying water (ULW), cloud water and the atmosphere close to both sea level and cloud level.

Both enrichment and depletion of N_{INP} in SML compared to ULW were observed. The enrichment factor (EF) varied from roughly 0.4 to 11, and there was no clear trend in EF with ice-nucleation temperature.

N_{INP} values in PM_{10} sampled at Cape Verde Atmospheric Observatory (CVAO) at any particular ice-nucleation temperature spanned around 1 order of magnitude below −15 °C, and about 2 orders of magnitude at warmer temperatures (> −12 °C). Among the 17 PM_{10} samples at CVAO, three PM_{10} filters showed elevated N_{INP} at warm temperatures, e.g., above 0.01 L^{-1} at −10 °C. After heating samples at 95 °C for 1 h, the elevated N_{INP} at the warm temperatures disappeared, indicating that these highly ice active INPs were most likely biological particles.

INP number concentrations in PM_1 were generally lower than those in PM_{10} at CVAO. About 83 ± 22 %, 67 ± 18 % and 77 ± 14 % (median±standard deviation) of INPs had a diameter > 1 µm at ice-nucleation temperatures of −12, −15 and −18 °C, respectively. PM_1 at CVAO did not show such elevated N_{INP} at warm temperatures. Consequently, the difference in N_{INP} between PM_1 and PM_{10} at CVAO suggests that biological ice-active particles were present in the supermicron size range.

N_{INP} in PM_{10} at CVAO was found to be similar to that on Monte Verde (MV, at 744 m a.s.l.) during noncloud events. During cloud events, most INPs on MV were activated to cloud droplets. When highly ice active particles were present in PM_{10} filters at CVAO, they were not observed in PM_{10} filters on MV but in cloud water samples instead. This is direct evidence that these INPs, which are likely biological, are activated to cloud droplets during cloud events.

For the observed air masses, atmospheric N_{INP} values in air fit well to the concentrations observed in cloud water. When comparing concentrations of both sea salt and INPs in both seawater and PM_{10} filters, it can be concluded that sea spray aerosol (SSA) only contributed a minor fraction to the atmospheric N_{INP}. This latter conclusion still holds when accounting for an enrichment of organic carbon in supermicron particles during sea spray generation as reported in literature.

1 Introduction

Ice particle formation in tropospheric clouds can affect cloud properties such as cloud lifetime, their radiative effects on the atmosphere and the formation of precipitation (Hoose

and Möhler, 2012; Murray et al., 2012). Ice crystals in the atmosphere can be formed either via homogeneous nucleation below −38 °C or via heterogeneous nucleation aided by aerosol particles known as ice-nucleating particles (INPs) at any temperature below 0 °C. Immersion freezing refers to the process when an INP becomes immersed in an aqueous solution, e.g., through the process of cloud droplet activation (Vali et al., 2015). Immersion freezing is suggested to be the most important freezing process for mixed-phase clouds (Ansmann et al., 2008; Westbrook and Illingworth, 2013), and is the process we will focus on in this study.

Submicron dust particles are recognized as effective INPs below −20 °C (Augustin-Bauditz et al., 2014), and supermicron dust particles were reported to be ice active even up to −10 °C (Hoose and Möhler, 2012; Murray et al., 2012). Laboratory studies on natural mineral dusts from different regions have been conducted to quantify the ability of particles to nucleate ice (Niemand et al., 2012; DeMott et al., 2015). Mineral dust particles from deserts are composed of a variety of minerals, and K-feldspar is supposed to be more active for ice nucleation than other minerals in the mixed-phase cloud temperature regime (Atkinson et al., 2013; Augustin-Bauditz et al., 2014; Niedermeier et al., 2015). Boose et al. (2016) found that ice activity of desert dust particles at temperatures between −35 and −28 °C can be attributed to the sum of the feldspar and quartz content. A high clay content, in contrast, was associated with lower ice-nucleating activity. In contrast to field measurements, in laboratory studies often separate types of mineral dusts are examined. Different parameterizations have been employed to summarize the mineral dust particle's ice-nucleating ability (Niemand et al., 2012; Ullrich et al., 2017).

A few field measurements have been carried out to quantify the ice-nucleation properties of desert dust. Based on airborne measurements, DeMott et al. (2003) found that ice-nucleating aerosol particles in air masses over Florida had sources from the north African desert. Chou et al. (2011) observed a good correlation between the number concentration of larger particles and INP number concentration (N_{INP}) during a Saharan dust event at Jungfraujoch in the Swiss Alps. Collecting airborne dust over the Sahara, Price et al. (2018) observed 2 orders of magnitude variability in N_{INP} at any particular temperature from ∼ −13 to ∼ −25 °C, which was related to the variability in atmospheric dust loading. This desert dust's ice-nucleating activity was only weakly dependent on differences in desert sources, i.e., on the differences in mineral composition that particles emitted from different locations in the desert may have. Schrod et al. (2017) found that mineral dust or a constituent related to dust was a major contributor to N_{INP} for the aerosol on Cyprus, and N_{INP} in elevated dust plumes was on average a factor of 10 higher than N_{INP} at ground level, where the dust loading was lower.

Ocean water can be a potential source of INPs (Brier and Kline, 1959). The source of INPs in ocean water might be associated with phytoplankton blooms (Schnell and Vali, 1976). Recently, Wilson et al. (2015) and Irish et al. (2017) found that organic material, with a diameter < 0.2 µm, is the major ice nucleator in the sea surface microlayer (SML). Based on a long-term measurement of INPs in the marine boundary layer to the south of and around Australia, Bigg (1973) suggested that INPs in ambient air were from a distant land source, from a stratospheric source, or brought to sea level by convective mixing and possible ocean sources. Schnell and Vali (1976) also suggested a marine source could explain the observations of Bigg (1973). DeMott et al. (2016) found that the ice-nucleating activity from laboratory-generated sea spray aerosol (SSA) aligned well with measurements from diverse regions over the oceans. Furthermore, a connection between marine biological activity and N_{INP} was uncovered in their laboratory study (DeMott et al., 2016). In pristine marine conditions, such as the Southern Ocean, SSA was the main source of the INP population, but N_{INP} was relatively low in the Southern Ocean as well as in the clean marine northeast Atlantic (McCluskey et al., 2018a, b). These field measurements are consistent with the model work by Burrows et al. (2013), which emphasizes the importance of SSA contribution to INPs in remote marine regions.

It is currently still uncertain whether the coarse mode particles or smaller particles are the major source of atmospheric INPs. Vali (1966) found that the diameters of INPs were mostly between 0.1 and 1 µm. On the high alpine research station Jungfraujoch, Mertes et al. (2007) found that ice residuals were as small as 300 nm, and they were mostly present in the submicron particle size range. Simultaneous measurements of N_{INP} and particle number size distributions were used to develop parameterizations in which N_{INP} depends on a temperature-dependent fraction of all particles with sizes above 500 nm (DeMott et al., 2010, 2015). Conen et al. (2017) found that INPs at −8 °C were equally distributed amongst the particles with sizes up to 2.5 µm and with sizes between 2.5 and 10 µm. Other field measurements reported that coarse mode particles were more efficient INPs, e.g., INPs (mainly bacterial aggregates and fungal spores) occurred in the size range of 2–6 µm (Huffman et al., 2013). Mason et al. (2016) found for Arctic aerosol that 91 ± 9 %, 79 ± 17 % and 63 ± 21 % (mean ± 1 standard deviation) of INPs had an aerodynamic diameter of > 1 µm at ice activation temperatures of −15, −20 and −25 °C, respectively. Creamean et al. (2018) also found that supermicron or coarse mode particles are the most proficient INPs at warmer temperatures in the Arctic boundary layer, and they might be biological INPs. Concerning biological INPs, it should be mentioned that it is well understood by now that these contain macromolecules of only some 10 nm in size at the most (Pummer et al., 2015). Some of them are easily separated from their carrier (e.g., from pollen and fungal spores; see, for example, Augustin et al., 2013; O'Sullivan et al., 2016, respectively), while others are embedded in the cell membrane (e.g., for bacteria; Hartmann et al., 2013), but based on the fact that most atmospheric INPs seem to be supermicron

in size, as observed in the above-cited literature, it seems that most of the biological ice-active macromolecules still occur together with their original carrier in the atmosphere.

Direct measurement of N_{INP} in the cloud water can be used to estimate concentrations of INPs in the air assuming that most INPs activate as CCN. Joly et al. (2014) measured total and biological (i.e., heat-sensitive) INPs between -5 and $-14\,^{\circ}C$ in cloud samples from the summit of Puy de Dôme (1465 m a.s.l., France). Petters and Wright (2015) summarized many INP spectra obtained from rain water, melted sleet, snow and hail samples at different sampling locations and reported a range of N_{INP} for these precipitation samples. Based on a shipborne measurement of the east coast of Nova Scotia, Canada, Schnell (1977) directly compared N_{INP} in the seawater to that in the fog water and found that N_{INP} in fog water and seawater appeared to vary quite independently of each other. As one part of the study presented here, these field measurement values will be compared with values obtained from our measurement campaign in the framework of the MarParCloud (Marine biological production, organic aerosol particles and marine clouds: a Process Chain) project.

During the MarParCloud project, samples collected for INP analysis include: SML and underlying water (ULW) from the ocean upwind of the island; quartz fiber filter samples of atmospheric aerosol, collected on a tower installed at the island shore (inlet height: 42 m a.s.l.) and on a mountaintop (inlet height: 746 m a.s.l.); and cloud water collected during cloud events on the mountaintop. In this study, we will first discuss N_{INP} in the SML and ULW. We will then discuss N_{INP} in the air, including a comparison of N_{INP} in PM_{10} and PM_1 and a comparison of N_{INP} close to both sea level and cloud level. Lastly, N_{INP} in the cloud water will be discussed. In addition, we will provide a feasible way to link N_{INP} in ambient air, ocean water and cloud water. This connection could be drawn only during times when there were cloud events on the mountaintop, together with data on number concentrations of cloud condensation nuclei (N_{CCN}). Respective information was derived and discussed in an accompanying paper (Gong et al., 2020). For more information about the campaign itself, we refer to an upcoming overview paper by van Pinxteren et al. (2019).

2 Experiment and methods

2.1 Sampling sites and sample types

2.1.1 Sampling site

The measurement campaign was carried out on São Vicente island at Cabo Verde from 13 September to 13 October 2017. We set up three measurement stations at Cabo Verde: at the Cape Verde Atmospheric Observatory (CVAO), on Monte Verde (MV) and an ocean station (OS). CVAO (16°51′49″ N, 24°52′02″ W) is located in the northeastern shore of the island of São Vicente, 70 m from the coastline about 10 m a.s.l. Filter samplers were installed on top of a 32 m tower. MV (16°52′11″ N, 24°56′02″ W) is located on a mountaintop (744 m a.s.l), ∼ 7 km away to the west of CVAO. Filter samplers were situated on the ground with the inlet 2 m above the bottom, upwind of any installation on the mountaintop. The OS covered an area at ∼ 16°53′30″ N, ∼ 24°54′00″ W, with a distance of at least 5 km from the island. Details on the measurement sites and the meteorological conditions can be found in the accompanying paper (Gong et al., 2020). In short, the conditions at Cabo Verde were quite stable, with temperature of on average 26.6 °C at CVAO and 21.2 °C at MV and wind speeds between 0.6 and 9.7 m s^{-1} with directions from the northeast.

In the following, the different samples collected during the campaign are described in detail. All of these samples were stored at $-20\,^{\circ}C$ right after sampling. After the campaign, the long-term storage and transport of the collected samples from Cabo Verde to the Leibniz Institute for Tropospheric Research (TROPOS), Germany, was carried out in a cooled container at $-20\,^{\circ}C$. At TROPOS, all samples were again stored frozen at $-20\,^{\circ}C$ until analysis was done. Measurement sites, locations, sample types and additional information are summarized in Table 1.

Following the description of the sampling, we will briefly introduce the measurement methods related to INPs, including freezing devices, N_{INP} calculation and measurement uncertainties. Note that all the times presented here are in UTC (corresponding to LT+1). For better comparison, all ambient particle number concentrations in this study are given for standard temperature and pressure (STP, 0 °C and 1013.25 hPa).

2.1.2 Seawater sampling

Seawater samples were taken at the OS by using a fishing boat at a distance of at least 5 km from the coast (offshore samples). The SML samples were collected using a glass plate sampler (Harvey and Burzell, 1972; Irish et al., 2017; van Pinxteren et al., 2017). The glass plate had a surface area of 2000 cm^{-2} and was immersed vertically into the ocean; it was then withdrawn at a slow rate (between 5 and 10 cm s^{-1}) and allowed to drain for less than 5 s. The surface film adhering to the surface of the glass was scraped off from both sides of the glass plate with a framed Teflon wiper into a 1 L glass bottle. For each SML sample, several liters were collected and 1 L required ∼ 55 dips. Based on the amount of material collected, the number of dips and the area of the plate, the average thickness of the layer collected was calculated as ∼ 91.0 µm. ULW samples were collected at the same time and location as the SML samples. ULW was collected from a depth of 1 m by a glass bottle mounted on a telescopic rod in order to monitor sampling depth. The bottle was opened underwater at the intended sampling depth with

Table 1. Measurement sites, locations, sample types and measurement instruments.

Measurement site	Location	Sample type	Instrument
CVAO	16°51′49″ N, 24°52′02″ W inlet height: 42 m a.s.l.	PM_1 quartz fiber filter PM_{10} quartz fiber filter	INDA INDA
MV	16°52′11″ N, 24°56′02″ W inlet height: 746 m a.s.l.	PM_{10} quartz fiber filter Cloud water	INDA LINA, INDA
OS	∼ 16°53′30″ N, ∼ 24°54′00″ W	SML ULW	LINA, INDA LINA, INDA

a specifically designed seal opener. After collection, the glass bottles containing both the SML and ULW samples were kept in a freezer at −20 °C until analysis. During the campaign, nine SML and nine ULW samples were collected for INP analysis. Details of SML and ULW samples, including the sampling time, location, salinity and additional information, are provided in the Supplement (Table S1).

2.1.3 Aerosol particle sampling

Particle sampling was done using high-volume samplers with either a PM_{10} inlet and or a PM_1 inlet (Digitel filter sampler DHA-80, Walter Riemer Messtechnik, Germany) operating with an average flow rate of ∼ 500 L min^{-1} for 24 h sampling periods. The high-volume samples were collected on 150 mm in diameter quartz fiber filters (Munktell, MK 360) with an effective sampling area of 140 mm in diameter. The filters were preheated in our laboratory at 110 °C for 24 h to remove the organic carbon background. After sampling, the filters were transported to a freezer where they were kept at −20 °C. For INP analysis, a circular piece of these filters of 2 cm in diameter was used from which then smaller pieces were punched out for the analysis (see Sect. 2.2). From CVAO, there were 17 and 19 filters from PM_{10} and PM_1 collection (CVAO PM_{10} and CVAO PM_1), respectively, and at MV 17 filters were collected for PM_{10} (MV PM_{10}). Field blind filters were obtained by inserting clean filters into the Digitel sampler for a period of 24 h without loading them. Three blind filters were collected during this campaign. Details of filter samples, including sampling time, duration, total volume and additional information can be found in the Supplement (Table S2 (CVAO PM_{10}), Table S3 (CVAO PM_1) and Table S4 (MV PM_{10})).

2.1.4 Cloud water sampling

During the campaign, MV was in clouds roughly 58 % of the time (a detailed analysis on this can be found in Gong et al., 2020). Cloud water was collected with CASCC2 (Caltech Active Strand Cloud Collector Version 2) at MV. All cloud drop sizes were collected in one bulk sample. Drops were collected by inertial impaction on Teflon strands with a diameter of 508 µm. The 50 % lower size cut for the CASCC2 was approximately 3.5 µm diameter. The flow rate through the CASCC2 was approximately 5.8 m^3 min^{-1}. The CASCC2 is described in more detail in Demoz et al. (1996). Between cloud events, the cloud water sampler was cleaned with a large amount (∼ 5 L) of ultrapure water. Once the collector was cleaned, a blank was taken by spraying about 200 mL of ultrapure water into the collection strands in the collector and subsequent sampling of this water. After collection, the cloud water samples were kept in a freezer at −20 °C. During the campaign, 13 cloud samples were collected for INP analysis. The details of cloud samples, including sampling time, duration, volume and additional information are provided in the Supplement (Table S5).

2.2 Freezing devices

Two droplet freezing devices called LINA (Leipzig Ice Nucleation Array) and INDA (Ice Nucleation Droplet Array) have been set up at TROPOS in Germany. The design of LINA was inspired by Budke and Koop (2015). Briefly, 90 droplets with a volume of 1 µL were pipetted from the samples onto a thin hydrophobic glass slide, with each droplet being placed separately into its own compartment. After pipetting, the compartments were sealed at the top with another glass slide to prevent the droplets from evaporation and to prevent ice seeding from neighboring droplets. The droplets were cooled on a Peltier element with a cooling rate of 1 K min^{-1} down to −35 °C, while the setup was illuminated by a circular light source from above. Once the cooling started, pictures were taken every 6 s by a camera. The number of frozen versus unfrozen droplets was derived automatically by an image identification program in Python. LINA was employed to measure SML, ULW and cloud water samples in this study. More detailed parameters and the temperature calibration of LINA and its application can be found in previous studies (Chen et al., 2018; Gong et al., 2019a).

The design of INDA was inspired by Conen et al. (2012) but uses PCR (polymerase chain reaction) trays instead of separate tubes. For quartz fiber filters, circular pieces with a diameter of 1 mm were punched out. Each of the 96 wells of a PCR tray were filled with the filter piece together with 50 µL of ultrapure water. For SML, ULW and cloud water samples, 50 µL of the water samples was filled into each PCR tray. Af-

ter sealing by a transparent foil, the PCR tray was placed on a sample holder and immersed into a bath thermostat, where it was illuminated from below with a LED light source. The bath thermostat then decreased the temperature with a cooling rate of approximately 1 K min^{-1}. Real-time images of the PCR tray were recorded every 6 s by a CCD (charge-coupled device) camera. Frozen droplets can be identified based on the brightness change during the freezing process. A program recorded the actual temperature of the cooling bath and related it to the real-time images from the CCD camera. The temperature in the PCR trays had been calibrated. More detailed parameters and information of temperature calibration of INDA and its application can be found in previous studies (Chen et al., 2018; Hartmann et al., 2019).

2.3 Deriving N_{INP}

2.3.1 Basic calculation

Based on Vali (1971), the cumulative concentration of INPs (N_{INP}) as a function of temperature per air or water volume can be calculated by

$$N_{INP}(\theta) = \frac{-\ln(1 - f_{ice}(\theta))}{V} \quad (1)$$

with

$$f_{ice}(\theta) = \frac{N(\theta)}{N_{total}}, \quad (2)$$

where N_{total} is the number of droplets and $N(\theta)$ is the number of frozen droplets at temperature θ. Equation (1) accounts for the possibility of the presence of multiple INPs in one vial by assuming that INPs are Poisson distributed. This way, the cumulative number of INPs active at any temperature will be obtained, although only the most ice-active INPs (nucleating ice at the highest temperature) present in each droplet or well will be observed. As for the quartz fiber filters, V is the volume of air collected onto one circular 1 mm filter piece placed in each well, resulting in airborne N_{INP}. Information on the air volume can be found in the Supplement (Tables S2, S3 and S4). As for the SML, ULW and cloud water, V is the volume of droplet or well ($V_{LINA} = 1\,\mu L$, $V_{INDA} = 50\,\mu L$), resulting in N_{INP} per volume of water. Compared to the droplets examined in a LINA measurement, INDA measurements have a larger volume of water in each well. The larger volume of water corresponds to a higher probability of the presence of INPs in each well; therefore, INDA can detect INPs at warmer temperatures, where INPs are more scarce. In this study, the derived N_{INP} values from LINA and INDA measurements were combined when both instruments were deployed.

2.3.2 Uncertainty and background

Because the number of INPs present in the water is usually small (some single up to a few tens of INPs per examined droplet or well), and the number of droplets or wells considered in our measurements is limited, statistical errors need to be considered in the data evaluation. Therefore, confidence intervals for f_{ice} were determined using the method suggested by Agresti and Coull (1998). These confidence intervals were estimated according to the improved Wald interval, which implicitly assumes a normal approximation for binomially distributed measurement errors. Previous studies (McCluskey et al., 2018a; Suski et al., 2018; Gong et al., 2019a) used the same method to calculate the measurement uncertainties of the freezing devices.

For the quartz fiber filters, a background freezing signal resulting from the field blind filters was determined by doing a regular INDA measurement with these filters. Measured N_{INP} from the sampled filters was corrected by subtracting the averaged background concentrations determined for the blind filters, as explained in Wex et al. (2019). All values for airborne N_{INP} presented in the following are background corrected. A detailed description of the background subtraction method and background values is provided in the Supplement. For those samples that were already collected in a liquid state (ULW, SML and cloud water), a background correction was not done.

2.3.3 Salinity correction of SML and ULW

SML and ULW samples were adjusted to account for the freezing depression caused by dissolved salts in sea water. Based on Kreidenweis et al. (2005), the water activity can be calculated by

$$a_w = \frac{n_{water}}{n_{water} + i \cdot n_{solute}}, \quad (3)$$

where the n_{solute} and n_{water} are the number of moles of solute and water in solution, respectively. i is the van 't Hoff factor (Pruppacher and Klett, 2010). We assumed sea salt to be mainly sodium chloride, for which the van 't Hoff factor is 2. The freezing depression temperature as a function of a_w was taken from Koop and Zobrist (2009). In our study, this was roughly a correction by 2.2 °C.

2.4 Active surface site density

A thorough analysis of particle number size distributions (PNSDs) has been presented in Gong et al. (2020), and based on these PNSDs we derived the particle surface area size distributions (PASDs) for use in this study (to be seen in the Supplement, Fig. S14). These PASDs were used to determine the temperature-dependent cumulative active surface site density (n_s) for aerosol particles. The n_s is a measure of how well an aerosol acts as a seed surface for ice nucleation. The n_s can be calculated as

$$n_s = \frac{N_{INP}(\theta)}{A_{total}}, \quad (4)$$

where A_{total} is the concentration of the total particle surface area.

For cases where a single type of aerosol, such as one type of mineral dust, is examined in laboratory studies, A_{total} can be the total particle surface area. However, when field experiments are done, using the total particle surface area of the atmospheric aerosol assumes that all particles contribute to INPs and have the same n_s, but the vast majority of these particles will not even be an INP. On the other hand, singling out the contribution of separate INP types in the atmospheric aerosol and relating n_s only to them by using their contribution to the total surface area is at least demanding if not often impossible. This has to be kept in mind when interpreting heterogeneous ice nucleation in terms of n_s. An example of separating the n_s for dust and marine ambient air can be found in Cornwell et al. (2019).

3 Results

3.1 INPs in SML and ULW

Based on Eq. (1), the derived N_{INP} in seawater as a function of temperature is shown in Fig. 1, for both SML and ULW. Note that for each sample a separate INP spectrum is shown. Error bars show the 95 % confidence interval. For completeness, f_{ice} of all seawater samples is shown in the Supplement (Fig. S1 (measured by LINA) and Fig. S2 (measured by INDA)). The variation in N_{INP} at any particular temperature is within 1 order of magnitude. Included in Fig. 1 are previous studies of N_{INP} measured east of Greenland in the Arctic (shown as a red box) and east of North America in the North Atlantic Ocean (shown as a black box) from Wilson et al. (2015).

The concentration range detected for ULW in Wilson et al. (2015) (both in the Arctic and the North Atlantic Ocean) roughly agrees with our data. In Wilson et al. (2015), N_{INP} in the SML in the North Atlantic Ocean is at the lower end of that found in the Arctic. A possible reason for this difference could be the biological activity of the ocean water. Wilson et al. (2015) found that organic material was correlated to N_{INP} in SML, and that N_{INP} values per gram of total organic carbon in the Arctic and the North Atlantic Ocean were comparable. A recent study found that the SML at Cabo Verde was oligotrophic, which is supported by the low Chlorophyll-*a* and transparent exopolymer particle concentrations found during the MarParCloud campaign (Robinson et al., 2019). The low biological activity in the SML around Cabo Verde could be the reason why N_{INP} in SML in this study is lower than those reported in Wilson et al. (2015).

To better quantify the enrichment or depletion of N_{INP} in SML to ULW, we derived an enrichment factor (EF). An enrichment might be expected as organic material is known to attach to air bubbles rising to the ocean surface. The EF in SML was calculated by dividing N_{INP} in SML ($N_{INP,\,SML}$) by the respective N_{INP} measured in ULW ($N_{INP,\,ULW}$), as the equation below shows:

$$EF = \frac{N_{INP,\,SML}}{N_{INP,\,ULW}}. \quad (5)$$

Enrichment of N_{INP} in the SML is indicated when $EF > 1$, while depletion is indicated when $EF < 1$. Figure 2 shows the EF as a function of the temperature at which N_{INP} was determined in the freezing devices. Both enrichment and depletion were observed, but there is no clear trend in the EF with temperature. Most of the variation seen here is likely caused by measurement uncertainties, which are indicated in Fig. S3 in the Supplement. EF varied from 0.36 to 11.40 at −15 °C and from 0.36 to 7.11 at −20 °C. By comparing T_{10} (the temperature at which 10 % of droplets had frozen) for the SML and ULW, Wilson et al. (2015) observed higher enrichment of INPs in SML in both the Arctic and the North Atlantic Ocean. However, Irish et al. (2017) observed both enrichment and depletion of INPs in SML in the Arctic, similar to the observation made in the present study.

These differences in EF between studies might partially be due to differences in the techniques deployed and different SML thicknesses in our and the other studies. SML

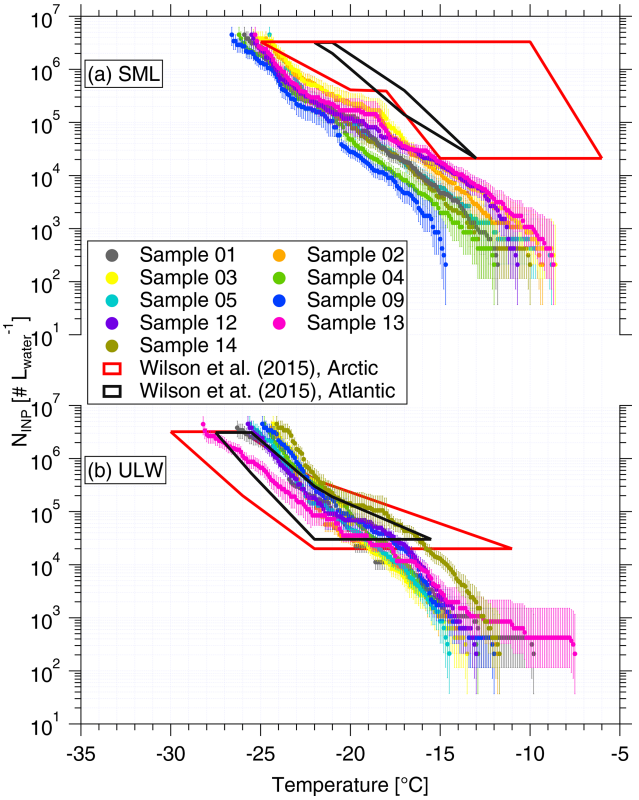

Figure 1. N_{INP} as a function of temperature in SML **(a)** and ULW **(b)**. Error bars show the 95 % confidence interval. Previous field measurements of N_{INP} in seawater by Wilson et al. (2015) are compared, as shown by red and black boxes.

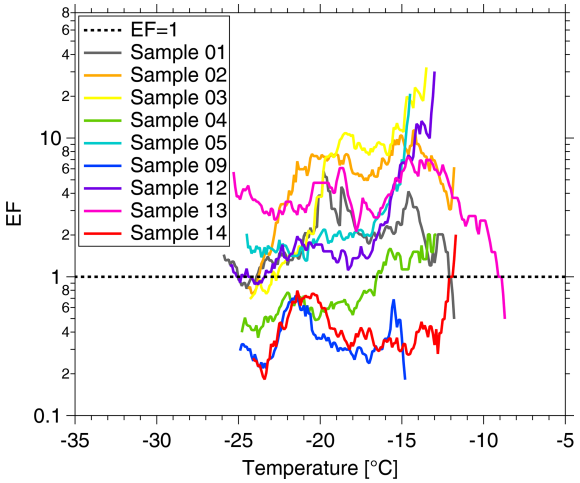

Figure 2. Enrichment factor (EF) as a function of ice-nucleation temperature. The EF = 1 result is shown by the dashed line.

samples were estimated to be about ∼ 91.0 µm thick in this study, while for Wilson et al. (2015) they were between 6 and 83 µm. It is interesting to note that we used glass dipping for the samples analyzed herein, while both glass dipping and a rotating drum sampler were used in Wilson et al. (2015). Previous studies pointed out that the rotating drum sampler and the glass dipping method probe different thicknesses of the SML, thus making a direct comparison of both SML thickness as well as enrichment factors generally difficult (Agogué et al., 2004; Aller et al., 2017).

3.2 N_{INP} in air

Three different sets of filter samples were collected at CVAO and MV, i.e., CVAO PM_{10}, CVAO PM_1 and MV PM_{10}. In this section, we will discuss N_{INP} at CVAO for the two different size classes and compare N_{INP} from close to the sea level (CVAO) to that at cloud level (MV).

3.2.1 N_{INP} close to sea level

CVAO PM_{10}

N_{INP} values as a function of temperature from CVAO PM_{10} filters and CVAO PM_1 filters are shown in Fig. 3a and b. Error bars show the 95 % confidence interval. The respective values of f_{ice} are shown in the Supplement (Fig. S4 (CVAO PM_{10}) and Fig. S8 (CVAO PM_1)), together with the results from the blind filters. The CVAO PM_{10} filter samples were all active at −11.3 °C and the highest freezing temperature was found to be −5.0 °C. Filter samples collected in Cabo Verde over the period 2009–2013 for INP measurement were reported by Welti et al. (2018), and they are shown as a gray background in Fig. 3a. The measured N_{INP} in this study is within the N_{INP} range presented by Welti et al. (2018).

N_{INP} values at any particular temperature span around 1 order of magnitude below −15 °C and about 2 orders of magnitude at warmer temperatures. This is consistent with the previous studies from O'Sullivan et al. (2018) and Gong et al. (2019a), who carried out field measurement in northwestern Europe and the eastern Mediterranean, respectively. A few samples (CVAO 1596, CVAO 1641 and CVAO 1643) showed elevated concentrations above 0.01 L^{-1} at −10 °C. Biological particles usually contribute to INPs at this moderate supercooling temperature (Kanji et al., 2017; O'Sullivan et al., 2018).

Biological INPs contain specific ice-nucleating proteins. These proteins are disrupted and denatured by heating, which causes them to lose their ice-nucleating ability. However, the inorganic ice-nucleating material, such as dust particles, is insensitive to heat (Wilson et al., 2015; O'Sullivan et al., 2018). Therefore, a commonly used heat treatment was deployed to assess the contribution of biological INPs to the total INPs in this study. Samples CVAO 1596, CVAO 1641 and CVAO 1643 were heated to 95 °C for 1 h, and the resulting N_{INP} data are shown in Fig. S6. A clear comparison of before and after heating f_{ice} is shown in Fig. S7. A large reduction of more than 1 order of magnitude in N_{INP} at $T > -15$ °C was observed in the samples after heating. The reductions in N_{INP} became smaller at colder temperature and were, for example, less than 1 order of magnitude at $T = -20$ °C. This shows that biological aerosol contributed a large fraction of total INPs in PM_{10} at $T > -20$ °C.

The correlation of N_{INP} at different temperatures within one sample was calculated by comparing each N_{INP} at each temperature to that at each other temperature at which a measurement had been made. That was done separately for each of the samples. For temperature steps of 0.1 °C, N_{INP} at every temperature was correlated to that at every other temperature in the measurement range. With increasing difference in temperatures, the variation in N_{INP} at two temperatures become less correlated. As long as the examined temperature difference was less than 2 °C, N_{INP} were correlated. But when looking at this in a broader picture, in the temperature region down to ∼ −16.8 °C, N_{INP} at all temperatures correlated well with that at all other temperatures, with coefficient of determination $(R^2) > 0.8$ and $p < 0.01$. The same was true for N_{INP} in the temperatures region < −18.4 °C. In between these two temperature regimes (between > −16.8 °C and < −18.4 °C), the correlation of N_{INP} was clearly lower. Therefore, it might be expected that INPs that are active in these two temperature regimes originated from different sources.

CVAO PM_1 in comparison to CVAO PM_{10}

N_{INP} values in PM_1 filters are also determined in this study (as shown in Fig. 3b). An initial inspection of the data shows that the bulk of the data of N_{INP} for CVAO PM_1 is below that

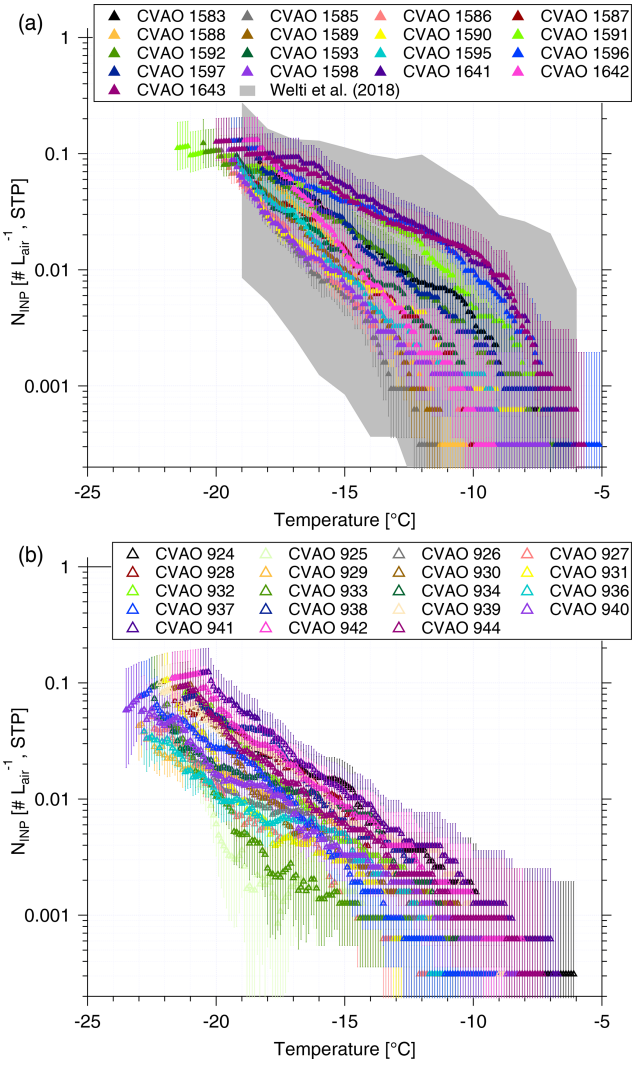

Figure 3. N_{INP} as a function of temperature from CVAO PM_{10} filters **(a)** and CVAO PM_1 filters **(b)**. The field measurement of N_{INP} in PM_{10} by Welti et al. (2018) is shown by gray shading in panel **(a)**. Error bars show the 95 % confidence interval.

for CVAO PM_{10}. Comparing N_{INP} for PM_1 and PM_{10}, two key features are evident:

1. Larger particles, i.e., supermicron ones, were more efficient INPs, which is independent of temperature in the examined range.

2. Smaller particles, i.e., submicron ones, exhibited an equal spread of about 1 order of magnitude in N_{INP} for the whole temperature range (see Fig. 3b). The elevated N_{INP} values at warm temperatures, which are seen for CVAO PM_{10}, are not observed for CVAO PM_1.

As for the first feature, we calculated the ratio of N_{INP} in supermicron size range to N_{INP} in PM_{10} during the same time period and found that 83 ± 22 %, 67 ± 18 % and 77 ± 14 % (median $\pm$ standard deviation) of INPs had a diameter of $>$ 1 µm at ice activation temperatures of -12, -15 and -18 °C, respectively. On average, over all temperatures, this INP number fraction for supermicron particles is roughly 70 % (shown for a higher temperature resolution in Fig. 4), and it is almost independent of temperature. Mason et al. (2016) and Creamean et al. (2018) also found that the majority of INPs is in the supermicron size range. However, they see even increasing fractions towards higher temperatures. For the present study, as said above, only 3 of the examined 17 filters showed clearly elevated N_{INP} at high temperatures, so overall such an increase was not observed.

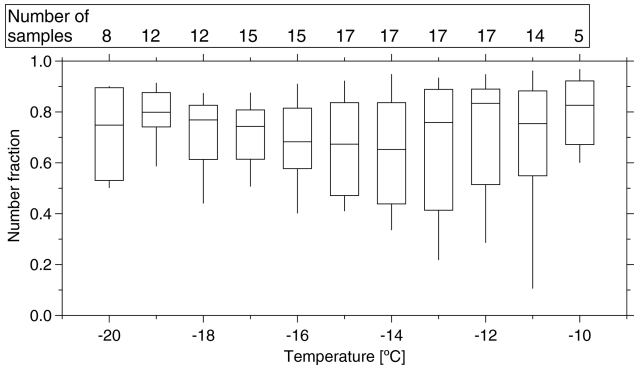

Figure 4. Boxplot of number fraction of INPs in the size range of $>$ 1 µm as a function of temperature. The boxes represent the interquartile range. Whiskers represent 10th and 90th percentiles. The number of samples indicated at the top of the figure shows how many different samples contributed at the different temperatures.

As for the second feature, looking at Fig. 3b, we found that N_{INP} spread about 1 order of magnitude at any temperature from -12 to -20 °C. As outlined above, a few PM_{10} samples showed elevated concentrations at warm temperatures, showing up as a "bump" in the freezing curves at higher temperatures. This bump at warm temperatures was not observed for the CVAO PM_1 filters. N_{INP} values of CVAO 932, CVAO 942 and CVAO 944 (sampled at the same time as CVAO 1596, CVAO 1641 and CVAO 1643) are all below 0.001 L^{-1} at -10 °C. As mentioned above, INPs active at comparably high temperatures were found to be biological in origin in this study, and the comparison between PM_{10} and PM_1 samples shows that there are biological INPs in the CVAO PM_{10} samples that are absent in the CVAO PM_1 samples, i.e., that the detected biological INPs are supermicron in size. This suggests that these biological INPs might originate from long-range transport, as marine biological INPs were usually reported to be submicron in size (Wilson et al., 2015; Irish et al., 2017). The contribution of SSA to INPs will be discussed further in Sect. 3.4.

3.2.2 N_{INP} at cloud level

In the companion paper (Gong et al., 2020), we discussed PNSD and CCN number concentration (N_{CCN}) at CVAO and MV. We found that particles are mainly well mixed in the marine boundary layer, and we derived the periods with cloud events, with a time resolution of ~ 30 min, at MV. In the present study, N_{INP} values in PM_{10} at CVAO and MV are compared. The fraction of time during which there was a cloud event to the total sampling time (cloud time fraction) for each filter is summarized in the Supplement (Table S4). All of the filters were affected by cloud events with a cloud time fraction from 4.17 % to 100 %, with two filters being affected only a little (cloud time fraction < 10 %), i.e., MV 1602 and MV 1603. When comparing results from these two filters to those from filters sampled at the same time at CVAO (see Fig. 5a), we found that N_{INP} values are quite similar close to sea level (CVAO) and cloud level (MV). This is in line with what was discussed in the companion paper (Gong et al., 2020), i.e., the marine boundary is often well mixed at Cabo Verde.

Figure 5b compares N_{INP} values at CVAO and MV when MV filters were mostly collected during cloud events with cloud time fractions > 90 %. During the cloud events, the filters did not collect droplets larger than 10 µm because of the inlet cutoff. It is obvious from Fig. 5 that for these cases, N_{INP} at MV is much lower than that at CVAO, implying that particularly INPs that were ice active above ~ -17 °C were activated to cloud droplets to a large degree. But note that even when filters have a cloud time fraction of 100 % (MV 1615 and MV 1616), the respective filters still had clearly more INPs on them than the field blind filters (see Supplement, Fig. S9). This might indicate that either not all INPs are activated to cloud droplets, or, on the other hand, that some INPs were only recently activated to a cloud droplet, and the droplet size was smaller than 10 µm. These observations are consistent with results by Siebert and Shaw (2017), who observed broad cloud droplet size distributions in a size range from ~ 5 to 25 µm in shallow cumulus clouds, with the maximum of the distribution still being below 10 µm.

Concerning the supermicron particles of likely biological origin that activated ice already at -10 °C and above, it is observed that the related corresponding bump is not seen in the corresponding data from MV (MV 1610, MV 1614 and MV 1616 – to be seen in the Supplement, Fig. S10). This indicates that these INPs were all activated to cloud droplets during the cloud events, and we will come back to this below.

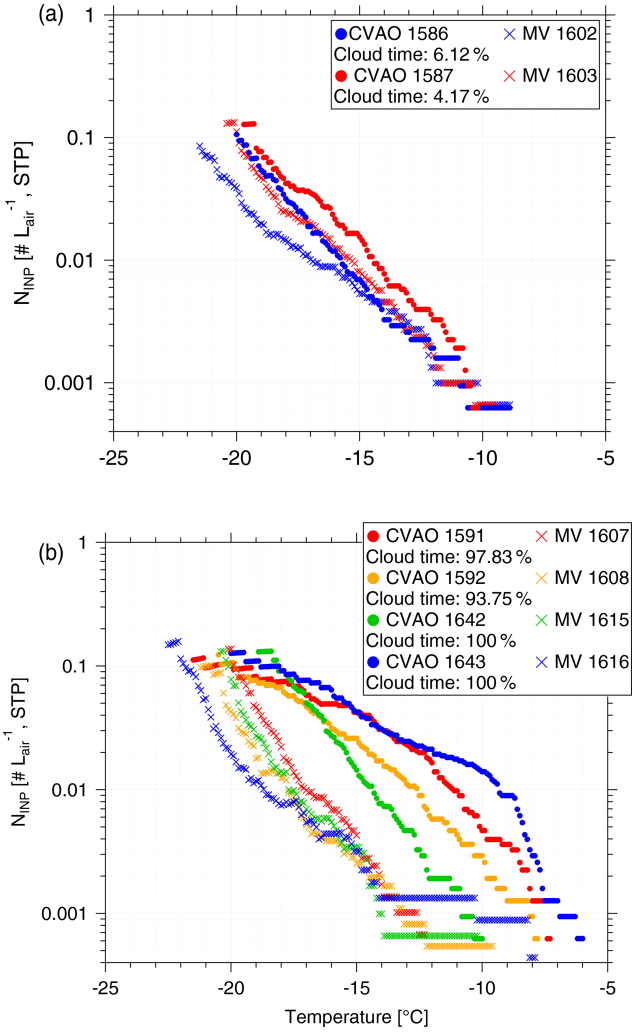

Figure 5. N_{INP} as a function of temperature from CVAO PM_{10} filters and MV PM_{10} filters during **(a)** less (cloud time fraction < 10 %) cloud effected periods and **(b)** highly (cloud time fraction > 90 %) cloud effected periods.

3.3 INPs in cloud water

3.3.1 Main characteristics and N_{INP} in cloud water

Thirteen cloud water samples were collected during cloud events in this study. Sampling durations varied from 2.5 to 13 h and volumes varied from 78 to 544 mL. The most abundant inorganic species were Na^+ and Cl^-, followed by SO_4^{2-}, NO_3^- and Mg^{2+}. For example, the mass concentration of Na^+ and Cl^- varied from 5.00 to 46.11 mg L^{-1} and 9.27 to 70.30 mg L^{-1}, with a mean value of 17.31 and 28.86 mg L^{-1}, respectively. Somewhat different values, which are still roughly in the same range, were reported by Gioda et al. (2009), who found in Puerto Rico the Na^+ and Cl^- concentration in the cloud water varied from 3.79 to 15.53 mg L^{-1} and 5.90 to 23.20 mg L^{-1}, with a mean of 10.74 and 15.67 mg L^{-1}, respectively. All of the abovementioned parameters are summarized in the Supplement (Table S5).

Based on Eq. (1), the derived N_{INP} as a function of temperature is shown in Fig. 6. Error bars represent the 95 % confidence interval. For completeness, f_{ice} for cloud water is shown in the Supplement (Fig. S12 (measured by LINA) and

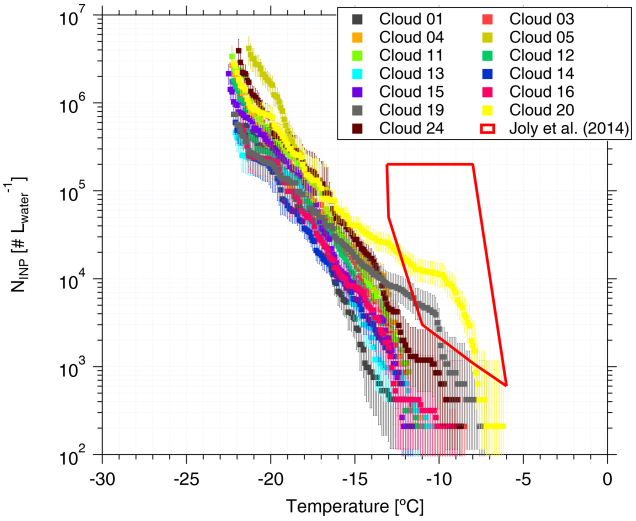

Figure 6. N_{INP} in cloud water as a function of temperature. Error bars show the 95 % confidence interval. Previous field measurements of N_{INP} in cloud water by Joly et al. (2014) are shown as a red box for comparison.

Fig. S13 (measured by INDA)). N_{INP} values at any particular temperature span less than 1 order of magnitude below −15 °C, while they span 2 orders of magnitude at warmer temperatures. We observed elevated N_{INP} in the cloud water at warm temperatures (above 1000 L^{-1} at −10 °C), particularly for the Cloud 19, Cloud 20 and Cloud 24 samples. Joly et al. (2014) measured the total and biological (i.e., heat-sensitive) INPs between −5 and −14 °C from the summit of Puy de Dôme (1465 m a.s.l., France), as shown in the red box in Fig. 6. Joly et al. (2014) observed very high concentrations of both biological particles and N_{INP}. Agreement of N_{INP} in cloud water all over the world was not expected, since the sources of INPs are different in different locations.

When highly ice active particles were present for CVAO PM_{10} filters (CVAO 1596, CVAO 1641 and CVAO 1643), they were not observed for MV PM_{10} (MV 1610, MV1614 and MV 1616, which had cloud time fractions of 52, 87 and 100 %, respectively), but instead they were found in cloud water samples (Cloud 19, Cloud 20 and Cloud 24). This is in line with what was outlined in Sect. 3.2.2: these highly ice active particles were activated to cloud droplets during cloud events. Periods during which clouds were present at MV, together with the sampling periods of all cloud water samples and selected CVAO PM_{10} filters (those that had higher N_{INP} at warm temperatures; CVAO 1596, CVAO 1641 and CVAO 1643) can be checked in the Supplement (Fig. S11).

3.3.2 Connecting INPs in the cloud water with these in the air

In the following, N_{INP} in the cloud water will be compared to that in the air. To be able to do this, we used measured values of N_{CCN} to calculate cloud droplet number concentrations. These, together with an assumption on cloud droplet size (d_{drop}), yield the volume of cloud water per volume of air, given as F_{cloud_air} in Eq. (6):

$$F_{cloud\_air} = N_{CCN} \cdot \pi/6 \cdot d_{drop}^3. \quad (6)$$

For the calculation, we used N_{CCN} measured at CVAO at a supersaturation of 0.30 % (Gong et al., 2020). N_{CCN} was averaged for the different periods when each cloud water sample was collected. The chosen supersaturation corresponds to a critical diameter of roughly 80 nm, which is at the Hoppel minimum of the respective particle number size distributions (Gong et al., 2020), indicating that this is indeed the relevant supersaturation occurring in the prevailing clouds. Based on previous studies (Miles et al., 2000; Bréon et al., 2002; Igel and Heever, 2017; Siebert and Shaw, 2017), we assumed that d_{drop} varies between 7 and 20 µm, and we did separate estimates for these two values and additionally for 15 µm. The calculation based on this size range of cloud droplets should cover all that can be expected to occur.

Following this approach, F_{cloud_air} varied from 4.2×10^{-7} to 1.1×10^{-6}, with a median of 8.5×10^{-7} $m_{water}^3\, m_{air}^{-3}$. To see how reliable these values are, we also examined the following: assuming all sodium chloride particles were activated to cloud droplets, F_{cloud_air} can be also estimated from the ratio of sodium chloride mass concentration in air to that in cloud water. This ratio varied from 1.1×10^{-7} to 4.4×10^{-7} $m_{water}^3\, m_{air}^{-3}$, which is at the lower end but still comparable to F_{cloud_air} as we derived it above. Previous studies used the liquid water content (LWC), which is a measure of the mass of the water in a cloud in a specified amount of dry air. Typical ranges for LWC in thicker clouds are between 0.2 and 0.8 g m^{-3} (Rangno and Hobbs, 2005; Petters and Wright, 2015), corresponding to F_{cloud_air} between 2×10^{-7} and 8×10^{-7} $m_{water}^3\, m_{air}^{-3}$, which again agreed well with the above given values derived for this study.

With this F_{cloud_air}, N_{INP} in the respective volume of air can be compared to N_{INP} in this volume of cloud water when assuming that all INPs are CCN, which, based on the supermicron size of most of the INPs alone, is likely. To do so, N_{INP} obtained for cloud water was multiplied by F_{cloud_air} (for the three different assumptions on d_{drop}) to yield N_{INP} in the air ($N_{INP,air}$), given in Eq. (7):

$$N_{INP,air} = F_{cloud\_air} \cdot N_{INP,cloud}. \quad (7)$$

Figure 7 shows the measured N_{INP} in the air as a function of temperature with square symbols. Derived $N_{INP,air}$ from cloud water (calculated with a d_{drop} of 15 µm) are shown with triangle symbols. The samples with comparatively high numbers of INPs active at warm temperatures are shown in different colors. CVAO 1596, CVAO 1641 and CVAO 1643 are shown by green squares (the rest are shown with blue squares) and derived $N_{INP,air}$ values from samples collected for Cloud 19, Cloud 20 and Cloud 24 are shown by brown

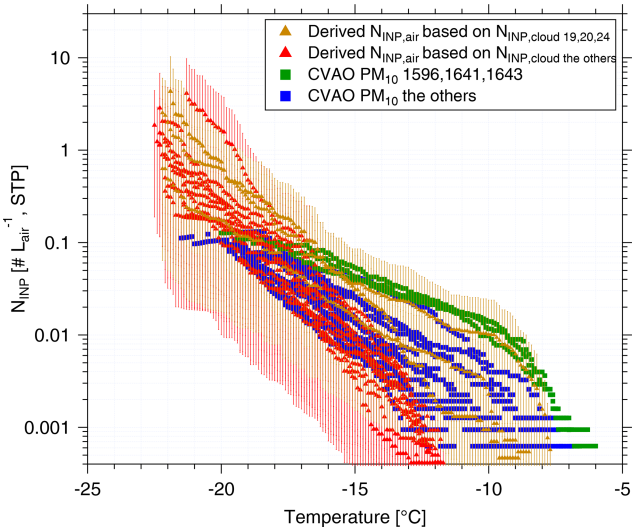

Figure 7. The measured atmospheric N_{INP} values as a function of ice-nucleation temperature are shown as squares. The derived N_{INP} in the air ($N_{INP,air}$) based on INP concentrations measured for cloud water are shown as triangles. The samples with highly ice active INPs at warm temperatures are shown in a different color than the others: CVAO 1596, CVAO 1641 and CVAO 1643 are shown as green squares and derived $N_{INP,air}$ based on Cloud 19, Cloud 20 and Cloud 24 are shown as brown triangles. The uncertainty range indicated for the derived $N_{INP,air}$ originates from calculations with 7 and 20 µm cloud droplet size.

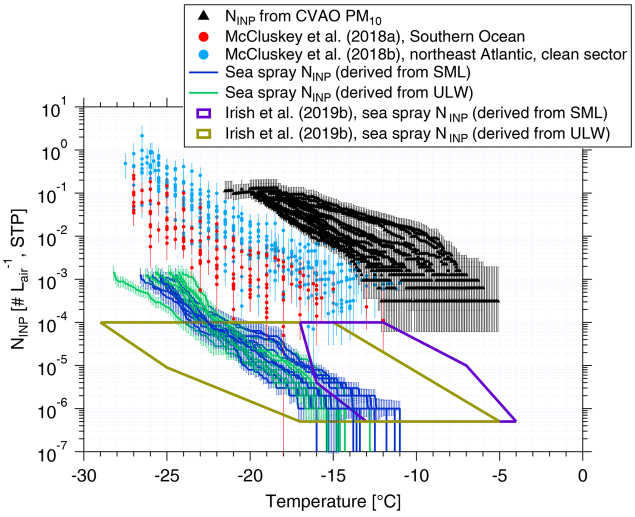

Figure 8. Atmospheric N_{INP} values are shown as a function of temperature from PM_{10} filters (black triangles), together with error bars showing the 95 % confidence interval. N_{INP} values as a function of temperature from McCluskey et al. (2018a, b) are shown by red and light blue dots, respectively. Error bars show the 95 % confidence interval. N_{INP} values in the air originating from sea spray ($N_{INP}^{\text{sea spray, air}}$) from this study are shown by blue (derived from SML) and green lines (derived from ULW). $N_{INP}^{\text{sea spray, air}}$ values from Irish et al. (2019b) are shown by purple (derived from SML) and brown (derived from ULW) boxes.

triangles (the rest shown by red triangles). The range of values indicated for $N_{INP,air}$ was obtained by using 7 and 20 µm cloud droplet size, with 7 µm droplets yielding the lower boundary and 20 µm the upper one.

There is general agreement between measured and derived N_{INP} in air but with some variation where the values derived from cloud water samples are somewhat lower. This might be connected to a less-than-optimal sampling efficiency of the cloud water sampler, which has a 50 % collection efficiency at 3.5 µm. Also the spread in the derived values, originating from the different assumed d_{drop}, is rather large. Nevertheless, it is striking that at least within an order of magnitude, based on our comparably simple assumptions, an agreement between concentrations of INPs in the air and in cloud water is found.

3.4 INPs originating from sea spray

In the following section, it will briefly be discussed whether SSA contributed noticeably to INPs in the air. Assuming sea salt and INPs to be similarly distributed in both seawater and air (i.e., assuming that INPs would not be enriched during the production of sea spray), N_{INP} in the air originating from sea spray ($N_{INP}^{\text{sea spray, air}}$) can be calculated based on Eq. (8):

$$N_{INP}^{\text{sea spray,air}} = \frac{\text{NaCl}_{\text{mass,air}}}{\text{NaCl}_{\text{mass,seawater}}} \cdot N_{INP}^{\text{seawater}}, \quad (8)$$

where $\text{NaCl}_{\text{mass,air}}$ and $\text{NaCl}_{\text{mass,seawater}}$ are sodium chloride mass concentrations in air and seawater, respectively. $N_{INP}^{\text{seawater}}$ is the INP number concentration in the seawater (this calculation can be done similarly for both SML and ULW).

$\text{NaCl}_{\text{mass,air}}$ and $\text{NaCl}_{\text{mass,seawater}}$ data can be found in the Supplement (Tables S1 and S2). $\text{NaCl}_{\text{mass,seawater}}$ was very stable, with a median value of $\sim 31\,\text{g L}^{-1}$. $\text{NaCl}_{\text{mass,air}}$ showed large variability from 3.40 to 17.76 µg m^{-3}, with a median of 13.08 µg m^{-3}. Based on Eq. (8), the resulting $N_{INP}^{\text{sea spray, air}}$ values are shown in blue (derived from SML) and green (derived from ULW) in Fig. 8. Irish et al. (2019b) used the same method to get $N_{INP}^{\text{sea spray, air}}$ in the Arctic (without considering enrichment of INPs in sea salt particles during sea spray generation), as shown by purple (derived from SML) and brown (derived from ULW) boxes in Fig. 8. As discussed in Sect. 3.1, N_{INP} values from ULW at Cabo Verde are comparable to the Arctic, and the NaCl ratios were close to 10^{-10} in both studies; therefore, $N_{INP}^{\text{sea spray, air}}$ values (derived from ULW) are also comparable. A high enrichment of N_{INP} in SML to ULW was observed in the Arctic (Irish et al., 2019b). Therefore, $N_{INP}^{\text{sea spray, air}}$ (derived from SML) in the Arctic was also higher than in this study.

Figure 8 includes N_{INP} from PM_{10} in this study (shown by black triangles). These values are roughly 4 orders of magnitude above our $N_{INP}^{\text{sea spray, air}}$. But Fig. 8 also shows airborne

N_{INP} as derived for the Southern Ocean (McCluskey et al., 2018a) and the northeast Atlantic (only clean sector; McCluskey et al., 2018b), which are all above our $N_{INP}^{sea\ spray,\ air}$. As mentioned above, we did not consider a possible enrichment of INPs in SSA compared to the SML or ULW samples. Previous studies found an enrichment of organic carbon in submicron sea spray particles of about 10^4 to 10^5 (Keene et al., 2007; van Pinxteren et al., 2017), and this value decreased to 10^2 for supermicron particles (Keene et al., 2007; Quinn et al., 2015). It is not clear if INPs are included in the organic carbon for which the enrichment was observed. Also, the INPs we detected in this study were mostly in the supermicron size range. If we increased $N_{INP}^{sea\ spray,\ air}$ by about 2 orders of magnitude in agreement with the enrichment observed for supermicron organic carbon, the resulting $N_{INP}^{sea\ spray,\ air}$ becomes comparable to sea spray INPs measured in the Southern Ocean (McCluskey et al., 2018a) and the northeast Atlantic (McCluskey et al., 2018b). But even when considering such an enrichment of INPs, INPs originating from sea spray would only explain a small fraction of all INPs contributing to the measured airborne N_{INP} in the air at Cabo Verde.

4 Discussion

N_{INP} values close to sea level and cloud level were compared. One major point of interest is to know whether ground-based measurements can be used to infer aerosol properties at the cloud level. In this study, we found that N_{INP} values are quite similar close to sea level (CVAO) and cloud level (MV) during noncloud events. But it should still be noted that we only have a small number of filter samples representing noncloud events in this study. During the observed cloud events, most INPs at MV are activated to cloud droplets. The above findings are in line with what was discussed in the companion paper (Gong et al., 2020): (1) the marine boundary layer is often well mixed at Cabo Verde and PNSDs and N_{CCN} are similar both near sea level and at the cloud level; (2) during cloud events, larger particles are activated to cloud droplets.

Most INPs are in the supermicron size range at Cabo Verde. We found that about 70 % of INPs had a diameter of $> 1\,\mu m$ at ice activation temperatures between -10 and $-20\,^{\circ}C$. Mason et al. (2016) and Creamean et al. (2018) also found that the majority of INPs is in the supermicron size range in the Arctic, in agreement with the results we obtained here.

Above we derived that N_{INP} contributed from SSA only accounted for a minor fraction of total N_{INP} in the air, as well as in the cloud water at Cabo Verde. This still holds even when considering a possible enrichment of INPs in SSA up to 10^2, which is an enrichment as given in literature for supermicron organic particles (Keene et al., 2007; Quinn et al., 2015). On the other hand, mineral dust is associated with a factor of 1000 higher ice surface site density (a measure to describe the ice activity per particle surface area), compared to SSA (Niemand et al., 2012; DeMott et al., 2016; McCluskey et al., 2018a). In our study, the supermicron particles that make up a large fraction of the INPs we observed were mainly mineral dust, as described in the accompanying study (Gong et al., 2020). The comparably high ice activity of supermicron mineral dust and the presence of mainly dust particles in the supermicron size range in our study again support that indeed most INPs observed in this study were not from sea spray. This is in line with results from Si et al. (2018) and Irish et al. (2019a), both done in the Arctic, where it was also concluded that SSA only contributed a little to the INP population. The commonality of these two studies from the Arctic and the present study is that land was still close enough, so that terrestrial sources can have contributed to the observed INPs.

While the above arguments suggest that INPs in our study were mostly mineral dust particles, there were also some measurements with comparably high INP concentrations at temperatures of $-10\,^{\circ}C$ and above. Although it can not be ruled out that desert dust particles might be ice active at such high temperatures, by examining the reaction of some highly ice active samples to heating, described in Sect. 3.2.1, we found that the most highly ice active INPs on these samples were biological particles. It is an open question as to where these biological INPs originated. The times during which these highly ice active INPs were observed were times when air masses came from southern Europe, traveling along the African coast and meanwhile crossing over the region of the Canary Islands. Therefore, for these specific samples, a contribution of INPs from these land sources might be assumed.

In the following, we will compare n_s derived from our data with that from literature. In Fig. 9, we show the surface site density derived for N_{INP} from CVAO PM_{10} filters (as shown by black boxes) following Niemand et al. (2012) (details on the surface area are given in the Supplement, Fig. S14), together with parameterizations for n_s given by Niemand et al. (2012), Ullrich et al. (2017) and McCluskey et al. (2018b), and the measured n_s given by DeMott et al. (2016) and Price et al. (2018). Niemand et al. (2012) derived n_s from a laboratory study, based on aerosol consisting purely of desert dust particles. It is therefore reasonable that these mineral dust-related n_s values are the largest values shown in Fig. 9, as they are purely related to the mineral dust surface area of an aerosol. All other values shown in Fig. 9 were derived for atmospheric measurements, and the surface area used to derive n_s was always based on measured particle number concentrations. Price et al. (2018) carried out airborne measurements in dust-laden air over the tropical Atlantic. Parameterizations from McCluskey et al. (2018b) were done for pristine SSA over the northeast Atlantic, and both laboratory and atmospheric measurements of SSA were the base for the n_s parameterization given in DeMott et al. (2016). These available n_s parameterizations from previous literature may not be representative of Cabo Verde, but we will still compare

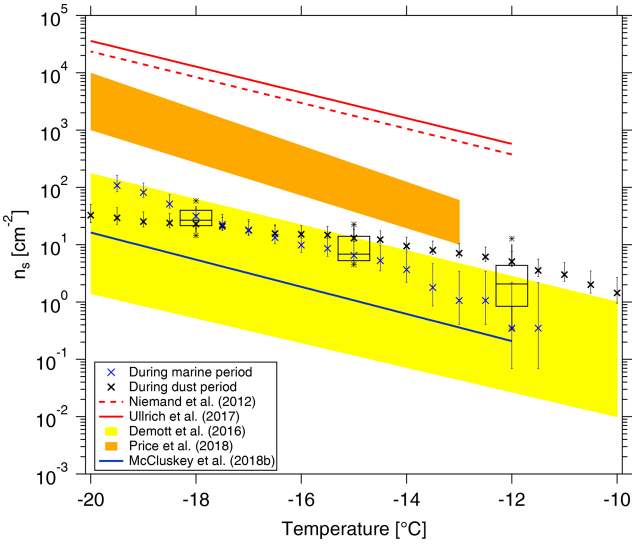

Figure 9. Cumulative n_s as a function of temperature in this study is shown by black boxes. The boxes represent the interquartile range. Whiskers represent 10th and 90th percentiles. Data not included between the whiskers are plotted as an outlier with a star. Two n_s parameterizations (Niemand et al., 2012; Ullrich et al., 2017) for pure desert dust are shown in dashed and solid red lines, respectively. n_s parameterizations from McCluskey et al. (2018b) for pristine SSA over the northeast Atlantic are shown as a solid blue line. We also make comparisons to recent data from airborne measurements in a dust layer by Price et al. (2018) in brown shading and from nascent laboratory-generated and ambient SSA by DeMott et al. (2016) in yellow shading, respectively. n_s during the cleanest marine (CVAO 1585) and dustiest (CVAO 1591) periods are shown as blue and black crosses, respectively.

them here. n_s values derived for our study coincide with the upper range of parameterizations that are otherwise reported for SSA but are clearly lower than values reported for atmospheric desert dust aerosol. This is striking since, as discussed above, INPs observed in this study most likely do not originate from sea spray but are dominated by supermicron dust and/or biological particles.

CVAO is a place where marine and dust particles strongly intersect, and both particle types contribute to the surface area. In the companion paper, we have classified the aerosol at CVAO into four different types. Here, in addition to looking at average values as presented above, we selected the cleanest marine (CVAO 1585) and dustiest (CVAO 1591) samples for a separate calculation of n_s, and we added the results to Fig. 9. The n_s is clearly higher for the sample collected during the dusty period than during the marine period at higher temperatures (roughly $> -16\,^{\circ}\mathrm{C}$). However, at temperatures below $-18\,^{\circ}\mathrm{C}$ it is the other way around. In general, results for these vastly different cases are both still close to the upper limit of the parameterizations reported for SSA.

These comparisons to literature raise the questions of if and how n_s should be used to parameterize atmospheric INP measurements, which, however, is a question far too prominent to be answered in this study. In general, it is still an open issue as to what extent N_{INP} can be parameterized, based on one or a few parameters, to reliably describe N_{INP} for different locations around the globe. It might prove necessary to develop separate parameterizations for different locations or air masses, as it was already started for parameterizations based on particle number concentrations (see DeMott et al., 2010, 2015; Tobo et al., 2013).

5 Summary and conclusions

The MarParCloud campaign took place in September and October 2018 on the islands of Cabo Verde to investigate aerosols prevailing in the Atlantic Ocean. In addition to a thorough analysis of the atmospheric aerosol particles and CCN in a companion paper (Gong et al., 2020), samples collected for INP analysis in this study include the following: sea surface microlayer (SML) and underlying water (ULW) from the ocean upwind of the island; quartz fiber filter samples of atmospheric aerosol, collected on a tower installed at the island shore and on a 744 m high mountaintop; and cloud water collected during cloud events on the mountaintop. N_{INP} values were measured offline with two types of freezing devices, yielding results in the temperature range from roughly -5 to $-25\,^{\circ}\mathrm{C}$.

Both enrichment and depletion of N_{INP} in SML to ULW were observed. The enrichment factors (EF) varied from 0.36 to 11.40 and from 0.36 to 7.11 at -15 and $-20\,^{\circ}\mathrm{C}$, respectively, and they were generally independent of the freezing temperature at which N_{INP} was determined in the freezing devices.

A few CVAO PM_{10} filter samples (CVAO 1596, CVAO 1641 and CVAO 1643) showed elevated N_{INP} at high temperatures, e.g., above $0.01\,\mathrm{L}^{-1}$ at $-10\,^{\circ}\mathrm{C}$. These elevated values disappeared after heating the samples at 95 °C for 1 h. Therefore, biological particles appear to contribute to INPs at these moderate supercooling temperatures. About $83 \pm 22\,\%$, $67 \pm 18\,\%$ and $77 \pm 14\,\%$ (median $\pm$ standard deviation) of INPs had a diameter $> 1\,\mu\mathrm{m}$ at ice activation temperatures of -12, -15 and $-18\,^{\circ}\mathrm{C}$, respectively; over the whole examined temperature range, on average roughly 70 % of all INPs were supermicron, independent of the temperature. The highly ice active INPs were not found on the CVAO PM_1 filters, which suggests that most of these likely biological INPs are in the supermicron size range.

As MV was in clouds most of the time, only two filters could be collected on MV that were affected by cloud for less than 10 % of the sampling time. For these, N_{INP} values were similar at CVAO and MV. During cloud events, most INPs at MV were activated into cloud droplets. These findings aligned very well with the companion paper, i.e., during

noncloud events, PNSDs and N_{CCN} are similar at CVAO and MV, while during cloud events larger particles at MV are activated to clouds (see Fig. 8 in the companion paper, Gong et al., 2020). When highly ice active particles were present on CVAO PM_{10} filters, they were not observed on MV PM_{10} filters, but they were instead observed in the respective cloud water samples. This shows that these INPs are activated into cloud droplets during cloud events.

By comparing N_{INP} values derived for the different examined samples, it was found that values in air and in cloud water agreed well. We also compared atmospheric N_{INP} to those in SML and ULW, based on the ratio of sodium chloride concentrations measured for the atmosphere and for SML and ULW. From that we concluded that marine INPs from sea spray can only explain a small fraction of all atmospheric INPs at Cabo Verde, unless there would be an enrichment of INPs from SML to the atmosphere by at least a factor of 10^4. Such an enrichment, however, is higher than anything observed for organic compounds in supermicron particles so far. Summarizing, it can be assumed that most atmospheric INPs detected in the present study were mainly contributed by the dust particles at cold temperatures and possibly with a few contributions from biological particles at warmer temperatures.

Data availability. The data are available through the World Data Center PANGAEA (https://doi.org/10.1594/PANGAEA.906946; Gong et al., 2019b).

Supplement. The supplement related to this article is available online at: https://doi.org/10.5194/acp-20-1451-2020-supplement.

Author contributions. XG wrote the article with contributions from HW and MvP. CS, NT and BR collected ocean water samples. XG, MvP and NT collected filter samples. KWF collected cloud water samples. XG and JL performed INP measurements. XG preformed data evaluation. XG, HW and FS discussed the results and further analysis after the campaign. All co-authors proofread and commented on the article.

Competing interests. The authors declare that they have no conflict of interest.

Special issue statement. This article is part of the special issue "Marine organic matter: from biological production in the ocean to organic aerosol particles and marine clouds (ACP/OS inter-journal SI)". It is not associated with a conference.

Acknowledgements. The works were carried out in the framework of the MarParCloud project. The authors acknowledge the Leibniz Association SAW funding for the project "Marine biological production, organic aerosol particles and marine clouds: a Process Chain (MarParCloud)", SAW-2016-TROPOS-2.

Financial support. This research has been supported by the Leibniz Association SAW (MarParCloud (grant no. SAW-2016-TROPOS-2)).

The publication of this article was funded by the Open Access Fund of the Leibniz Association.

Review statement. This paper was edited by Paul Zieger and reviewed by two anonymous referees.

References

Agogué, H., Casamayor, E. O., Joux, F., Obernosterer, I., Dupuy, C., Lantoine, F., Catala, P., Weinbauer, M. G., Reinthaler, T., Herndl, G. J., and Lebaron, P.: Comparison of samplers for the biological characterization of the sea surface microlayer, Limnol. Oceanogr.-Meth., 2, 213–225, https://doi.org/10.4319/lom.2004.2.213, 2004.

Agresti, A. and Coull, B. A.: Approximate is Better than "Exact" for Interval Estimation of Binomial Proportions, Am. Stat., 52, 119–126, https://doi.org/10.1080/00031305.1998.10480550, 1998.

Aller, J. Y., Radway, J. C., Kilthau, W. P., Bothe, D. W., Wilson, T. W., Vaillancourt, R. D., Quinn, P. K., Coffman, D. J., Murray, B. J., and Knopf, D. A.: Size-resolved characterization of the polysaccharidic and proteinaceous components of sea spray aerosol, Atmos. Environ., 154, 331–347, https://doi.org/10.1016/j.atmosenv.2017.01.053, 2017.

Ansmann, A., Tesche, M., Althausen, D., Müller, D., Seifert, P., Freudenthaler, V., Heese, B., Wiegner, M., Pisani, G., Knippertz, P., and Dubovik, O.: Influence of Saharan dust on cloud glaciation in southern Morocco during the Saharan Mineral Dust Experiment, J. Geophys. Res.-Atmos., 113, D04210, https://doi.org/10.1029/2007jd008785, 2008.

Atkinson, J. D., Murray, B. J., Woodhouse, M. T., Whale, T. F., Baustian, K. J., Carslaw, K. S., Dobbie, S., O'Sullivan, D., and Malkin, T. L.: The importance of feldspar for ice nucleation by mineral dust in mixed-phase clouds, Nature, 498, 355, https://doi.org/10.1038/nature12278, 2013.

Augustin, S., Wex, H., Niedermeier, D., Pummer, B., Grothe, H., Hartmann, S., Tomsche, L., Clauss, T., Voigtländer, J., Ignatius, K., and Stratmann, F.: Immersion freezing of birch pollen washing water, Atmos. Chem. Phys., 13, 10989–11003, https://doi.org/10.5194/acp-13-10989-2013, 2013.

Augustin-Bauditz, S., Wex, H., Kanter, S., Ebert, M., Niedermeier, D., Stolz, F., Prager, A., and Stratmann, F.: The immersion mode ice nucleation behavior of mineral dusts: A comparison of different pure and surface modified dusts, Geophys. Res. Lett., 41, 7375–7382, https://doi.org/10.1002/2014gl061317, 2014.

Bigg, E. K.: Ice Nucleus Concentrations in Remote Areas, J. Atmos. Sci., 30, 1153–1157, https://doi.org/10.1175/1520-0469(1973)030<1153:INCIRA>2.0.CO;2, 1973.

Boose, Y., Welti, A., Atkinson, J., Ramelli, F., Danielczok, A., Bingemer, H. G., Plötze, M., Sierau, B., Kanji, Z. A., and Lohmann, U.: Heterogeneous ice nucleation on dust particles sourced from nine deserts worldwide – Part 1: Immersion freezing, Atmos. Chem. Phys., 16, 15075–15095, https://doi.org/10.5194/acp-16-15075-2016, 2016.

Bréon, F.-M., Tanré, D., and Generoso, S.: Aerosol Effect on Cloud Droplet Size Monitored from Satellite, Science, 295, 834–838, https://doi.org/10.1126/science.1066434, 2002.

Brier, G. W. and Kline, D. B.: Ocean Water as a Source of Ice Nuclei, Science, 130, 717–718, https://doi.org/10.1126/science.130.3377.717, 1959.

Budke, C. and Koop, T.: BINARY: an optical freezing array for assessing temperature and time dependence of heterogeneous ice nucleation, Atmos. Meas. Tech., 8, 689–703, https://doi.org/10.5194/amt-8-689-2015, 2015.

Burrows, S. M., Hoose, C., Pöschl, U., and Lawrence, M. G.: Ice nuclei in marine air: biogenic particles or dust?, Atmos. Chem. Phys., 13, 245–267, https://doi.org/10.5194/acp-13-245-2013, 2013.

Chen, J., Wu, Z., Augustin-Bauditz, S., Grawe, S., Hartmann, M., Pei, X., Liu, Z., Ji, D., and Wex, H.: Ice-nucleating particle concentrations unaffected by urban air pollution in Beijing, China, Atmos. Chem. Phys., 18, 3523–3539, https://doi.org/10.5194/acp-18-3523-2018, 2018.

Chou, C., Stetzer, O., Weingartner, E., Jurányi, Z., Kanji, Z. A., and Lohmann, U.: Ice nuclei properties within a Saharan dust event at the Jungfraujoch in the Swiss Alps, Atmos. Chem. Phys., 11, 4725–4738, https://doi.org/10.5194/acp-11-4725-2011, 2011.

Conen, F., Henne, S., Morris, C. E., and Alewell, C.: Atmospheric ice nucleators active $\geq -12\,^{\circ}\mathrm{C}$ can be quantified on PM10 filters, Atmos. Meas. Tech., 5, 321–327, https://doi.org/10.5194/amt-5-321-2012, 2012.

Conen, F., Eckhardt, S., Gundersen, H., Stohl, A., and Yttri, K. E.: Rainfall drives atmospheric ice-nucleating particles in the coastal climate of southern Norway, Atmos. Chem. Phys., 17, 11065–11073, https://doi.org/10.5194/acp-17-11065-2017, 2017.

Cornwell, G. C., McCluskey, C. S., Levin, E. J. T., Suski, K. J., DeMott, P. J., Kreidenweis, S. M., and Prather, K. A.: Direct Online Mass Spectrometry Measurements of Ice Nucleating Particles at a California Coastal Site, J. Geophys. Res.-Atmos., 124, 12157–12172, https://doi.org/10.1029/2019jd030466, 2019.

Creamean, J. M., Kirpes, R. M., Pratt, K. A., Spada, N. J., Maahn, M., de Boer, G., Schnell, R. C., and China, S.: Marine and terrestrial influences on ice nucleating particles during continuous springtime measurements in an Arctic oilfield location, Atmos. Chem. Phys., 18, 18023–18042, https://doi.org/10.5194/acp-18-18023-2018, 2018.

DeMott, P. J., Sassen, K., Poellot, M. R., Baumgardner, D., Rogers, D. C., Brooks, S. D., Prenni, A. J., and Kreidenweis, S. M.: African dust aerosols as atmospheric ice nuclei, Geophys. Res. Lett., 30, 1732, https://doi.org/10.1029/2003GL017410, 2003.

DeMott, P. J., Prenni, A. J., Liu, X., Kreidenweis, S. M., Petters, M. D., Twohy, C. H., Richardson, M. S., Eidhammer, T., and Rogers, D. C.: Predicting global atmospheric ice nuclei distributions and their impacts on climate, P. Natl. Acad. Sci. USA, 107, 11217–11222, https://doi.org/10.1073/pnas.0910818107, 2010.

DeMott, P. J., Prenni, A. J., McMeeking, G. R., Sullivan, R. C., Petters, M. D., Tobo, Y., Niemand, M., Möhler, O., Snider, J. R., Wang, Z., and Kreidenweis, S. M.: Integrating laboratory and field data to quantify the immersion freezing ice nucleation activity of mineral dust particles, Atmos. Chem. Phys., 15, 393–409, https://doi.org/10.5194/acp-15-393-2015, 2015

DeMott, P. J., Hill, T. C. J., McCluskey, C. S., Prather, K. A., Collins, D. B., Sullivan, R. C., Ruppel, M. J., Mason, R. H., Irish, V. E., Lee, T., Hwang, C. Y., Rhee, T. S., Snider, J. R., McMeeking, G. R., Dhaniyala, S., Lewis, E. R., Wentzell, J. J. B., Abbatt, J., Lee, C., Sultana, C. M., Ault, A. P., Axson, J. L., Diaz Martinez, M., Venero, I., Santos-Figueroa, G., Stokes, M. D., Deane, G. B., Mayol-Bracero, O. L., Grassian, V. H., Bertram, T. H., Bertram, A. K., Moffett, B. F., and Franc, G. D.: Sea spray aerosol as a unique source of ice nucleating particles, P. Natl. Acad. Sci. USA, 113, 5797–5803, https://doi.org/10.1073/pnas.1514034112, 2016.

Demoz, B. B., Collett, J. L., and Daube, B. C.: On the Caltech Active Strand Cloudwater Collectors, Atmos. Res., 41, 47–62, https://doi.org/10.1016/0169-8095(95)00044-5, 1996.

Gioda, A., Mayol-Bracero, O. L., Morales-García, F., Collett, J., Decesari, S., Emblico, L., Facchini, M. C., Morales-De Jesús, R. J., Mertes, S., Borrmann, S., Walter, S., and Schneider, J.: Chemical Composition of Cloud Water in the Puerto Rican Tropical Trade Wind Cumuli, Water Air Soil Poll., 200, 3–14, https://doi.org/10.1007/s11270-008-9888-4, 2009.

Gong, X., Wex, H., Müller, T., Wiedensohler, A., Höhler, K., Kandler, K., Ma, N., Dietel, B., Schiebel, T., Möhler, O., and Stratmann, F.: Characterization of aerosol properties at Cyprus, focusing on cloud condensation nuclei and ice-nucleating particles, Atmos. Chem. Phys., 19, 10883–10900, https://doi.org/10.5194/acp-19-10883-2019, 2019a.

Gong, X., Wex, H., van Pinxteren, M., Triesch, N., Fomba, K. W., Lubitz, J., Stolle, C., Robinson, T.-B., Müller, T., Herrmann, H., and Stratmann, F.: Ice nucleating particles measured in air, cloud and seawater at the Cape Verde Atmospheric Observatory (CVAO), PANGAEA, https://doi.org/10.1594/PANGAEA.906946, 2019b.

Gong, X., Wex, H., Voigtländer, J., Fomba, K. W., Weinhold, K., van Pinxteren, M., Henning, S., Müller, T., Herrmann, H., and Stratmann, F.: Characterization of aerosol particles at Cabo Verde close to sea level and at the cloud level – Part 1: Particle number size distribution, cloud condensation nuclei and their origins, Atmos. Chem. Phys., 20, 1431–1449, https://doi.org/10.5194/acp-20-1431-2020, 2020.

Hartmann, M., Blunier, T., Brügger, S., Schmale, J., Schwikowski, M., Vogel, A., Wex, H., and Stratmann, F.: Variation of Ice Nucleating Particles in the European Arctic Over the Last Centuries, Geophys. Res. Lett., 46, 4007–4016, https://doi.org/10.1029/2019gl082311, 2019.

Hartmann, S., Augustin, S., Clauss, T., Wex, H., Šantl-Temkiv, T., Voigtländer, J., Niedermeier, D., and Stratmann, F.: Immersion freezing of ice nucleation active protein complexes, Atmos. Chem. Phys., 13, 5751–5766, https://doi.org/10.5194/acp-13-5751-2013, 2013.

Harvey, G. W. and Burzell, L. A.: A simple microlayer method for small samples, Limnol. Oceanogr., 17, 156–157, https://doi.org/10.4319/lo.1972.17.1.0156, 1972.

Hoose, C. and Möhler, O.: Heterogeneous ice nucleation on atmospheric aerosols: a review of results from labo-

ratory experiments, Atmos. Chem. Phys., 12, 9817–9854, https://doi.org/10.5194/acp-12-9817-2012, 2012.

Huffman, J. A., Prenni, A. J., DeMott, P. J., Pöhlker, C., Mason, R. H., Robinson, N. H., Fröhlich-Nowoisky, J., Tobo, Y., Després, V. R., Garcia, E., Gochis, D. J., Harris, E., Müller-Germann, I., Ruzene, C., Schmer, B., Sinha, B., Day, D. A., Andreae, M. O., Jimenez, J. L., Gallagher, M., Kreidenweis, S. M., Bertram, A. K., and Pöschl, U.: High concentrations of biological aerosol particles and ice nuclei during and after rain, Atmos. Chem. Phys., 13, 6151–6164, https://doi.org/10.5194/acp-13-6151-2013, 2013.

Igel, A. L. and Heever, S. C. v. d.: The Importance of the Shape of Cloud Droplet Size Distributions in Shallow Cumulus Clouds. Part II: Bulk Microphysics Simulations, J. Atmos. Sci., 74, 259–273, https://doi.org/10.1175/jas-d-15-0383.1, 2017.

Irish, V. E., Elizondo, P., Chen, J., Chou, C., Charette, J., Lizotte, M., Ladino, L. A., Wilson, T. W., Gosselin, M., Murray, B. J., Polishchuk, E., Abbatt, J. P. D., Miller, L. A., and Bertram, A. K.: Ice-nucleating particles in Canadian Arctic sea-surface microlayer and bulk seawater, Atmos. Chem. Phys., 17, 10583–10595, https://doi.org/10.5194/acp-17-10583-2017, 2017.

Irish, V. E., Hanna, S. J., Willis, M. D., China, S., Thomas, J. L., Wentzell, J. J. B., Cirisan, A., Si, M., Leaitch, W. R., Murphy, J. G., Abbatt, J. P. D., Laskin, A., Girard, E., and Bertram, A. K.: Ice nucleating particles in the marine boundary layer in the Canadian Arctic during summer 2014, Atmos. Chem. Phys., 19, 1027–1039, https://doi.org/10.5194/acp-19-1027-2019, 2019a.

Irish, V. E., Hanna, S. J., Xi, Y., Boyer, M., Polishchuk, E., Ahmed, M., Chen, J., Abbatt, J. P. D., Gosselin, M., Chang, R., Miller, L. A., and Bertram, A. K.: Revisiting properties and concentrations of ice-nucleating particles in the sea surface microlayer and bulk seawater in the Canadian Arctic during summer, Atmos. Chem. Phys., 19, 7775–7787, https://doi.org/10.5194/acp-19-7775-2019, 2019b.

Joly, M., Amato, P., Deguillaume, L., Monier, M., Hoose, C., and Delort, A.-M.: Quantification of ice nuclei active at near 0 °C temperatures in low-altitude clouds at the Puy de Dôme atmospheric station, Atmos. Chem. Phys., 14, 8185–8195, https://doi.org/10.5194/acp-14-8185-2014, 2014.

Kanji, Z. A., Ladino, L. A., Wex, H., Boose, Y., Burkert-Kohn, M., Cziczo, D. J., and Krämer, M.: Overview of Ice Nucleating Particles, Meteorol. Mon., 58, 1.1–1.33, https://doi.org/10.1175/amsmonographs-d-16-0006.1, 2017.

Keene, W. C., Maring, H., Maben, J. R., Kieber, D. J., Pszenny, A. A. P., Dahl, E. E., Izaguirre, M. A., Davis, A. J., Long, M. S., Zhou, X., Smoydzin, L., and Sander, R.: Chemical and physical characteristics of nascent aerosols produced by bursting bubbles at a model air-sea interface, J. Geophys. Res.-Atmos., 112, D21202, https://doi.org/10.1029/2007jd008464, 2007.

Koop, T. and Zobrist, B.: Parameterizations for ice nucleation in biological and atmospheric systems, Phys. Chem. Chem. Phys., 11, 10839–10850, https://doi.org/10.1039/B914289D, 2009.

Kreidenweis, S. M., Koehler, K., DeMott, P. J., Prenni, A. J., Carrico, C., and Ervens, B.: Water activity and activation diameters from hygroscopicity data – Part I: Theory and application to inorganic salts, Atmos. Chem. Phys., 5, 1357–1370, https://doi.org/10.5194/acp-5-1357-2005, 2005.

Mason, R. H., Si, M., Chou, C., Irish, V. E., Dickie, R., Elizondo, P., Wong, R., Brintnell, M., Elsasser, M., Lassar, W. M., Pierce, K. M., Leaitch, W. R., MacDonald, A. M., Platt, A., Toom-Sauntry, D., Sarda-Estève, R., Schiller, C. L., Suski, K. J., Hill, T. C. J., Abbatt, J. P. D., Huffman, J. A., DeMott, P. J., and Bertram, A. K.: Size-resolved measurements of ice-nucleating particles at six locations in North America and one in Europe, Atmos. Chem. Phys., 16, 1637–1651, https://doi.org/10.5194/acp-16-1637-2016, 2016.

McCluskey, C. S., Hill, T. C. J., Humphries, R. S., Rauker, A. M., Moreau, S., Strutton, P. G., Chambers, S. D., Williams, A. G., McRobert, I., Ward, J., Keywood, M. D., Harnwell, J., Ponsonby, W., Loh, Z. M., Krummel, P. B., Protat, A., Kreidenweis, S. M., and DeMott, P. J.: Observations of Ice Nucleating Particles Over Southern Ocean Waters, Geophys. Res. Lett., 45, 11989–11997, https://doi.org/10.1029/2018GL079981, 2018a.

McCluskey, C. S., Ovadnevaite, J., Rinaldi, M., Atkinson, J., Belosi, F., Ceburnis, D., Marullo, S., Hill, T. C. J., Lohmann, U., Kanji, Z. A., O'Dowd, C., Kreidenweis, S. M., and DeMott, P. J.: Marine and Terrestrial Organic Ice-Nucleating Particles in Pristine Marine to Continentally Influenced Northeast Atlantic Air Masses, J. Geophys. Res.-Atmos., 123, 6196–6212, https://doi.org/10.1029/2017JD028033, 2018b.

Mertes, S., Verheggen, B., Walter, S., Connolly, P., Ebert, M., Schneider, J., Bower, K. N., Cozic, J., Weinbruch, S., Baltensperger, U., and Weingartner, E.: Counterflow Virtual Impactor Based Collection of Small Ice Particles in Mixed-Phase Clouds for the Physico-Chemical Characterization of Tropospheric Ice Nuclei: Sampler Description and First Case Study, Aerosol Sci. Tech., 41, 848–864, https://doi.org/10.1080/02786820701501881, 2007.

Miles, N. L., Verlinde, J., and Clothiaux, E. E.: Cloud Droplet Size Distributions in Low-Level Stratiform Clouds, J. Atmos. Sci., 57, 295–311, https://doi.org/10.1175/1520-0469(2000)057<0295:cdsdil>2.0.co;2, 2000.

Murray, B. J., O'Sullivan, D., Atkinson, J. D., and Webb, M. E.: Ice nucleation by particles immersed in supercooled cloud droplets, Chem. Soc. Rev., 41, 6519–6554, https://doi.org/10.1039/C2CS35200A, 2012.

Niedermeier, D., Augustin-Bauditz, S., Hartmann, S., Wex, H., Ignatius, K., and Stratmann, F.: Can we define an asymptotic value for the ice active surface site density for heterogeneous ice nucleation?, J. Geophys. Res.-Atmos., 120, 5036–5046, https://doi.org/10.1002/2014JD022814, 2015.

Niemand, M., Möhler, O., Vogel, B., Vogel, H., Hoose, C., Connolly, P., Klein, H., Bingemer, H., DeMott, P., Skrotzki, J., and Leisner, T.: A Particle-Surface-Area-Based Parameterization of Immersion Freezing on Desert Dust Particles, J. Atmos. Sci., 69, 3077–3092, https://doi.org/10.1175/jas-d-11-0249.1, 2012.

O'Sullivan, D., Murray, B. J., Ross, J. F., and Webb, M. E.: The adsorption of fungal ice-nucleating proteins on mineral dusts: a terrestrial reservoir of atmospheric ice-nucleating particles, Atmos. Chem. Phys., 16, 7879–7887, https://doi.org/10.5194/acp-16-7879-2016, 2016.

O'Sullivan, D., Adams, M. P., Tarn, M. D., Harrison, A. D., Vergara-Temprado, J., Porter, G. C. E., Holden, M. A., Sanchez-Marroquin, A., Carotenuto, F., Whale, T. F., McQuaid, J. B., Walshaw, R., Hedges, D. H. P., Burke, I. T., Cui, Z., and Murray, B. J.: Contributions of biogenic material to the atmospheric ice-nucleating particle population in North Western Europe, Sci.

Rep.-UK, 8, 13821, https://doi.org/10.1038/s41598-018-31981-7, 2018.

Petters, M. and Wright, T.: Revisiting ice nucleation from precipitation samples, Geophys. Res. Lett., 42, 8758–8766, https://doi.org/10.1002/2015GL065733, 2015.

Price, H. C., Baustian, K. J., McQuaid, J. B., Blyth, A., Bower, K. N., Choularton, T., Cotton, R. J., Cui, Z., Field, P. R., Gallagher, M., Hawker, R., Merrington, A., Miltenberger, A., Neely III, R. R., Parker, S. T., Rosenberg, P. D., Taylor, J. W., Trembath, J., Vergara-Temprado, J., Whale, T. F., Wilson, T. W., Young, G., and Murray, B. J.: Atmospheric Ice-Nucleating Particles in the Dusty Tropical Atlantic, J. Geophys. Res.-Atmos., 123, 2175–2193, https://doi.org/10.1002/2017JD027560, 2018.

Pruppacher, H. and Klett, J.: Microphysics of Clouds and Precipitation, Vol. 18, Springer Science & Business Media, D. Reidel, Dordrecht, 2010.

Pummer, B. G., Budke, C., Augustin-Bauditz, S., Niedermeier, D., Felgitsch, L., Kampf, C. J., Huber, R. G., Liedl, K. R., Loerting, T., Moschen, T., Schauperl, M., Tollinger, M., Morris, C. E., Wex, H., Grothe, H., Pöschl, U., Koop, T., and Fröhlich-Nowoisky, J.: Ice nucleation by water-soluble macromolecules, Atmos. Chem. Phys., 15, 4077–4091, https://doi.org/10.5194/acp-15-4077-2015, 2015.

Quinn, P. K., Collins, D. B., Grassian, V. H., Prather, K. A., and Bates, T. S.: Chemistry and Related Properties of Freshly Emitted Sea Spray Aerosol, Chem. Rev., 115, 4383–4399, https://doi.org/10.1021/cr500713g, 2015.

Rangno, A. L. and Hobbs, P. V.: Microstructures and precipitation development in cumulus and small cumulonimbus clouds over the warm pool of the tropical Pacific Ocean, Q. J. Roy. Meteor. Soc., 131, 639–673, https://doi.org/10.1256/qj.04.13, 2005.

Robinson, T.-B., Stolle, C., and Wurl, O.: Depth is relative: the importance of depth for transparent exopolymer particles in the near-surface environment, Ocean Sci., 15, 1653–1666, https://doi.org/10.5194/os-15-1653-2019, 2019.

Schnell, R. C.: Ice Nuclei in Seawater, Fog Water and Marine Air off the Coast of Nova Scotia: Summer 1975, J. Atmos. Sci., 34, 1299–1305, https://doi.org/10.1175/1520-0469(1977)034<1299:INISFW>2.0.CO;2, 1977.

Schnell, R. C. and Vali, G.: Biogenic Ice Nuclei: Part I. Terrestrial and Marine Sources, J. Atmos. Sci., 33, 1554–1564, https://doi.org/10.1175/1520-0469(1976)033<1554:BINPIT>2.0.CO;2, 1976.

Schrod, J., Weber, D., Drücke, J., Keleshis, C., Pikridas, M., Ebert, M., Cvetković, B., Nickovic, S., Marinou, E., Baars, H., Ansmann, A., Vrekoussis, M., Mihalopoulos, N., Sciare, J., Curtius, J., and Bingemer, H. G.: Ice nucleating particles over the Eastern Mediterranean measured by unmanned aircraft systems, Atmos. Chem. Phys., 17, 4817–4835, https://doi.org/10.5194/acp-17-4817-2017, 2017.

Si, M., Irish, V. E., Mason, R. H., Vergara-Temprado, J., Hanna, S. J., Ladino, L. A., Yakobi-Hancock, J. D., Schiller, C. L., Wentzell, J. J. B., Abbatt, J. P. D., Carslaw, K. S., Murray, B. J., and Bertram, A. K.: Ice-nucleating ability of aerosol particles and possible sources at three coastal marine sites, Atmos. Chem. Phys., 18, 15669–15685, https://doi.org/10.5194/acp-18-15669-2018, 2018.

Siebert, H. and Shaw, R. A.: Supersaturation Fluctuations during the Early Stage of Cumulus Formation, J. Atmos. Sci., 74, 975–988, https://doi.org/10.1175/jas-d-16-0115.1, 2017.

Suski, K. J., Hill, T. C. J., Levin, E. J. T., Miller, A., DeMott, P. J., and Kreidenweis, S. M.: Agricultural harvesting emissions of ice-nucleating particles, Atmos. Chem. Phys., 18, 13755–13771, https://doi.org/10.5194/acp-18-13755-2018, 2018.

Tobo, Y., Prenni, A. J., DeMott, P. J., Huffman, J. A., McCluskey, C. S., Tian, G., Pöhlker, C., Pöschl, U., and Kreidenweis, S. M.: Biological aerosol particles as a key determinant of ice nuclei populations in a forest ecosystem, J. Geophys. Res.-Atmos., 118, 10100–10110, https://doi.org/10.1002/jgrd.50801, 2013.

Ullrich, R., Hoose, C., Möhler, O., Niemand, M., Wagner, R., Höhler, K., Hiranuma, N., Saathoff, H., and Leisner, T.: A New Ice Nucleation Active Site Parameterization for Desert Dust and Soot, J. Atmos. Sci., 74, 699–717, https://doi.org/10.1175/JAS-D-16-0074.1, 2017.

Vali, G.: Sizes of Atmospheric Ice Nuclei, Nature, 212, 384–385, https://doi.org/10.1038/212384a0, 1966.

Vali, G.: Quantitative Evaluation of Experimental Results an the Heterogeneous Freezing Nucleation of Supercooled Liquids, J. Atmos. Sci., 28, 402–409, https://doi.org/10.1175/1520-0469(1971)028<0402:qeoera>2.0.co;2, 1971.

Vali, G., DeMott, P. J., Möhler, O., and Whale, T. F.: Technical Note: A proposal for ice nucleation terminology, Atmos. Chem. Phys., 15, 10263–10270, https://doi.org/10.5194/acp-15-10263-2015, 2015.

van Pinxteren, M., Barthel, S., Fomba, K. W., Müller, K., Von Tümpling, W., and Herrmann, H.: The influence of environmental drivers on the enrichment of organic carbon in the sea surface microlayer and in submicron aerosol particles–measurements from the Atlantic Ocean, Elementa, 5, 35, https://doi.org/10.1525/elementa.225, 2017.

van Pinxteren, M., Fomba, K. W., Triesch, N., Stolle, C., Wurl, O., Bahlmann, E., Gong, X., Voigtländer, J., Wex, H., Robinson, T.-B., Barthel, S., Zeppenfeld, S., Hoffmann, E. H., Roveretto, M., Li, C., Grosselin, B., Daële, V., Senf, F., van Pinxteren, D., Manzi, M., Zabalegui, N., Frka, S., Gašparović, B., Pereira, R., Li, T., Wen, L., Li, J., Zhu, C., Chen, H., Chen, J., Fiedler, B., von Tümpling, W., Read, K. A., Punjabi, S., C. Lewis, A. C., Hopkins, J. R., Carpenter, L. J., Peeken, I., Rixen, T., Schulz-Bull, D., Monge, M. E., Mellouki, A., George, C., Stratmann, F., and Herrmann, H.: Marine organic matter in the remote environment of the Cape Verde Islands – An introduction and overview to the MarParCloud campaign, Atmos. Chem. Phys. Discuss., https://doi.org/10.5194/acp-2019-997, in review, 2019.

Welti, A., Müller, K., Fleming, Z. L., and Stratmann, F.: Concentration and variability of ice nuclei in the subtropical maritime boundary layer, Atmos. Chem. Phys., 18, 5307–5320, https://doi.org/10.5194/acp-18-5307-2018, 2018.

Westbrook, C. D. and Illingworth, A. J.: The formation of ice in a long-lived supercooled layer cloud, Q. J. Roy. Meteor. Soc., 139, 2209–2221, https://doi.org/10.1002/qj.2096, 2013.

Wex, H., Huang, L., Zhang, W., Hung, H., Traversi, R., Becagli, S., Sheesley, R. J., Moffett, C. E., Barrett, T. E., Bossi, R., Skov, H., Hünerbein, A., Lubitz, J., Löffler, M., Linke, O., Hartmann, M., Herenz, P., and Stratmann, F.: Annual variability of ice-nucleating particle concentrations at differ-

ent Arctic locations, Atmos. Chem. Phys., 19, 5293–5311, https://doi.org/10.5194/acp-19-5293-2019, 2019.

Wilson, T. W., Ladino, L. A., Alpert, P. A., Breckels, M. N., Brooks, I. M., Browse, J., Burrows, S. M., Carslaw, K. S., Huffman, J. A., Judd, C., Kilthau, W. P., Mason, R. H., McFiggans, G., Miller, L. A., Najera, J. J., Polishchuk, E., Rae, S., Schiller, C. L., Si, M., Temprado, J. V., Whale, T. F., Wong, J. P. S., Wurl, O., Yakobi-Hancock, J. D., Abbatt, J. P. D., Aller, J. Y., Bertram, A. K., Knopf, D. A., and Murray, B. J.: A marine biogenic source of atmospheric ice-nucleating particles, Nature, 525, 234–238, https://doi.org/10.1038/nature14986, 2015.

Supplement of Atmos. Chem. Phys., 20, 1451–1468, 2020
https://doi.org/10.5194/acp-20-1451-2020-supplement

Atmospheric Chemistry and Physics
Open Access
EGU

Supplement of

Characterization of aerosol particles at Cabo Verde close to sea level and at the cloud level – Part 2: Ice-nucleating particles in air, cloud and seawater

Xianda Gong et al.

Correspondence to: Xianda Gong (gong@tropos.de)

S1 Seawater samples

Table S1. The information of seawater samples at ocean station, including sample number, start time, end time, location, salinity, sodium chloride (NaCl) mass concentration, PH value and water temperature.

Sample Number	Start Time yyyy/mm/dd hh:mm:ss	End Time yyyy/mm/dd hh:mm:ss	Location	Salinity [g L^{-1}]	NaCl [g L^{-1}]	PH value	Temperature [°C]
SML01	2017/09/18 12:35:00	2017/09/18 13:00:00	-	-	-	-	-
ULW01	2017/09/18 12:35:00	2017/09/18 13:00:00	-	34.1	29.23	8.14	25.0
SML02	2017/09/20 09:32:00	2017/09/20 10:54:00	16°53′20 N, 24°54′22 W	36.2	31.03	8.11	26.7
ULW02	2017/09/20 09:32:00	2017/09/20 10:54:00	16°53′20 N, 24°54′22 W	36.3	31.11	8.12	26.7
SML03	2017/09/25 10:45:00	2017/09/25 11:48:00	16°53′46 N, 24°54′19 W	36.4	31.20	8.14	25.5
ULW03	2017/09/25 10:45:00	2017/09/25 11:48:00	16°53′46 N, 24°54′19 W	36.4	31.20	8.15	26.0
SML04	2017/09/26 11:05:00	2017/09/26 11:51:00	16°53′50 N, 24°54′27 W	36.1	30.94	8.12	26.4
ULW04	2017/09/26 11:05:00	2017/09/26 11:51:00	16°53′50 N, 24°54′27 W	36.3	31.11	8.15	25.1
SML05	2017/09/27 09:50:00	2017/09/27 11:00:00	16°53′38 N, 24°54′16 W	36.3	31.11	8.15	23.7
ULW05	2017/09/27 09:50:00	2017/09/27 11:00:00	16°53′38 N, 24°54′16 W	36.4	31.20	8.14	24.0
SML09	2017/10/04 09:15:00	2017/10/04 10:00:00	-	-	-	-	-
ULW09	2017/10/04 09:15:00	2017/10/04 10:00:00	-	36.2	31.03	8.23	23.7
SML12	2017/10/07 10:22:00	2017/10/07 11:35:00	16°53′25 N, 24°54′18 W	36.7	31.46	8.22	21.2
ULW12	2017/10/07 10:22:00	2017/10/07 11:35:00	16°53′25 N, 24°54′18 W	36.4	31.20	8.22	21.8
SML13	2017/10/09 09:30:00	2017/10/09 10:17:00	16°53′42 N, 24°54′08 W	36.6	31.37	8.19	21.5
ULW13	2017/10/09 09:30:00	2017/10/09 10:17:00	16°53′42 N, 24°54′08 W	36.4	31.20	8.13	23.6
SML14	2017/10/10 09:30:00	2017/10/10 10:30:00	16°53′43 N, 24°54′13 W	36.4	31.20	8.19	21.7
ULW14	2017/10/10 09:30:00	2017/10/10 10:30:00	16°53′43 N, 24°54′13 W	36.3	31.11	8.18	22.4

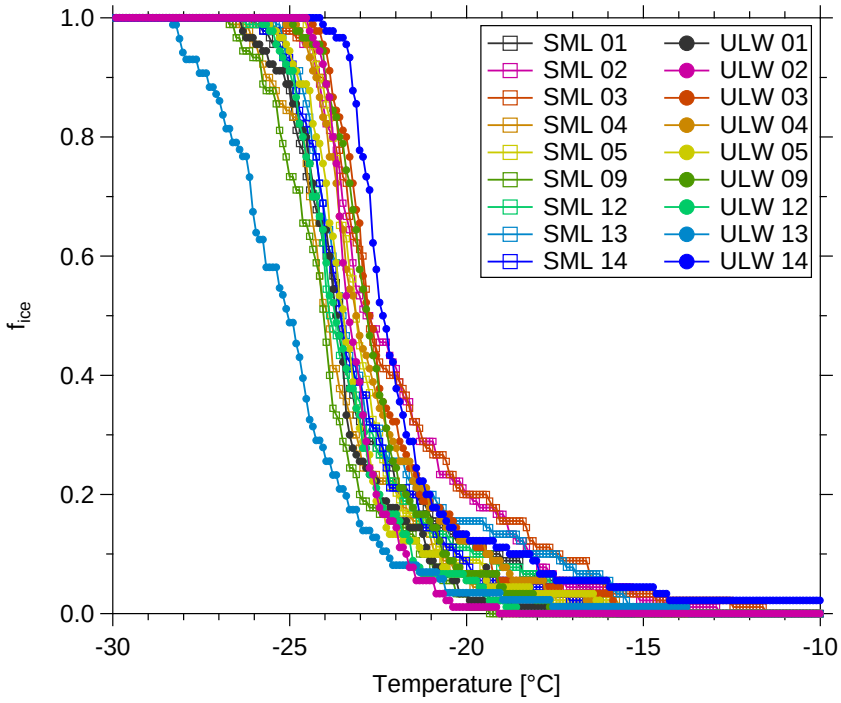

Figure S1. Frozen fraction (f_{ice}) measured by LINA (Leipzig Ice Nucleation Array) as a function of temperature in sea surface microlayer (SML) and underlying water (ULW). All temperatures have been corrected for freezing point depression.

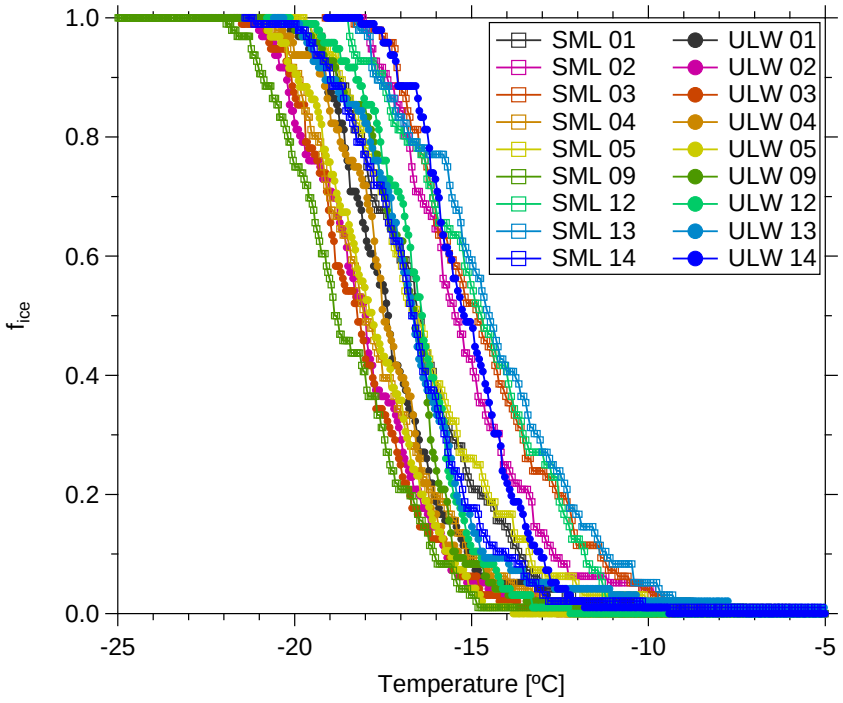

Figure S2. f_{ice} measured by INDA (Ice Nucleation Droplet Array) as a function of temperature in SML and ULW. All temperatures have been corrected for freezing point depression.

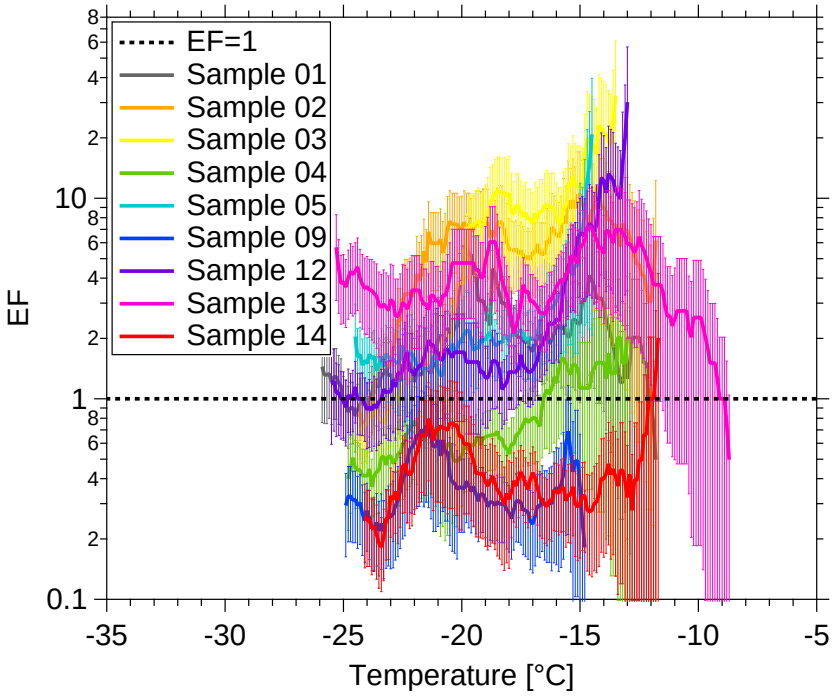

Figure S3. Enrichment factor (EF) as function of ice nucleation temperature. The EF=1 is shown by dashed line. Error bars show the measurement uncertainty.

S2 Filter samples

S2.1 Background subtraction

INP number concentration (N_{INP}) from the field blanks was then subtracted from that of the filter samples, and the result was converted to background corrected atmospheric INP number concentrations, as the below equation shows:

$$N_{\mathrm{INP}} = (-ln(1 - f_{\mathrm{ice,s}}) + ln(1 - f_{\mathrm{ice,b}}))/V \quad \text{(S1)}$$

The corrected atmospheric INP number concentration is N_{INP}, the frozen fractions measured for the filter samples and the field blanks are $f_{\mathrm{ice,s}}$ and $f_{\mathrm{ice,b}}$, respectively, and V is the volume of air sampled in each well.

S2.2 CVAO $\mathbf{PM_{10}}$

Table S2. The information of PM_{10} filter samples at Cape Verde Atmospheric Observatory (CVAO), including sample number, start time, end time, duration, total sampling volume, sampling volume per well, sodium (Na^+) and chloride (Cl^-) mass concentration, total particle surface area concentration (A_{total}) and sample type.

Sample Number	Start Time yyyy/mm/dd hh:mm:ss	End Time yyyy/mm/dd hh:mm:ss	Duration [minute]	Total Volume [std m^3]	Volume Per Well [std L]	Na^+ $\mu g\ m^{-3}$	Cl^- $\mu g\ m^{-3}$	A_{total} $\mu m^2\ cm^{-3}$	Type
CVAO1583	2017/09/19 21:00:00	2017/09/20 21:00:00	1439.34	660.289	33.6882	4.40	6.19	370	PM_{10}
CVAO1585	2017/09/22 16:00:00	2017/09/23 16:00:00	1439.34	660.289	33.6882	3.09	4.97	89	PM_{10}
CVAO1586	2017/09/23 16:00:00	2017/09/24 16:00:00	1439.34	660.289	33.6882	2.36	3.36	78	PM_{10}
CVAO1587	2017/09/24 16:00:00	2017/09/25 16:00:00	1439.34	660.289	33.6882	2.83	3.54	158	PM_{10}
CVAO1588	2017/09/25 16:00:00	2017/09/26 16:00:00	1438.90	660.792	33.7139	3.32	4.98	277	PM_{10}
CVAO1589	2017/09/26 16:00:00	2017/09/27 16:00:00	1439.61	661.462	33.7481	1.41	1.99	159	PM_{10}
CVAO1590	2017/09/27 16:00:00	2017/09/28 16:00:00	1439.71	661.644	33.7573	1.77	2.70	198	PM_{10}
CVAO1591	2017/09/28 16:00:00	2017/09/29 16:00:00	1439.73	661.420	33.7459	5.04	8.41	325	PM_{10}
CVAO1592	2017/09/29 16:00:00	2017/09/30 16:00:00	1439.73	660.289	33.6882	6.49	11.26	297	PM_{10}
CVAO1593	2017/09/30 16:00:00	2017/10/01 16:00:00	1439.73	660.821	33.7153	5.32	8.99	238	PM_{10}
CVAO1594	2017/09/29 16:00:00	2017/09/30 16:00:00							Blind filter
CVAO1595	2017/10/01 16:00:00	2017/10/02 16:00:00	1439.36	659.330	33.6393	4.52	6.67	172	PM_{10}
CVAO1596	2017/10/02 16:00:00	2017/10/03 16:00:00	1439.71	660.629	33.7056	3.71	6.49	171	PM_{10}
CVAO1597	2017/10/03 16:00:00	2017/10/04 16:00:00	1439.71	660.629	33.7056	-	-	169	PM_{10}
CVAO1598	2017/10/05 16:00:00	2017/10/06 16:00:00	1439.55	659.264	33.6359	2.58	3.33	162	PM_{10}
CVAO1641	2017/10/06 16:00:00	2017/10/07 16:00:00	1439.73	658.670	33.6056	4.67	6.91	244	PM_{10}
CVAO1642	2017/10/07 16:00:00	2017/10/08 16:00:00	1439.71	661.187	33.7341	5.46	8.54	271	PM_{10}
CVAO1643	2017/10/08 16:00:00	2017/10/09 16:00:00	1439.71	659.785	33.6625	5.22	7.98	230	PM_{10}
CVAO1644	2017/10/07 17:00:00	2017/10/08 17:00:00							Blind filter

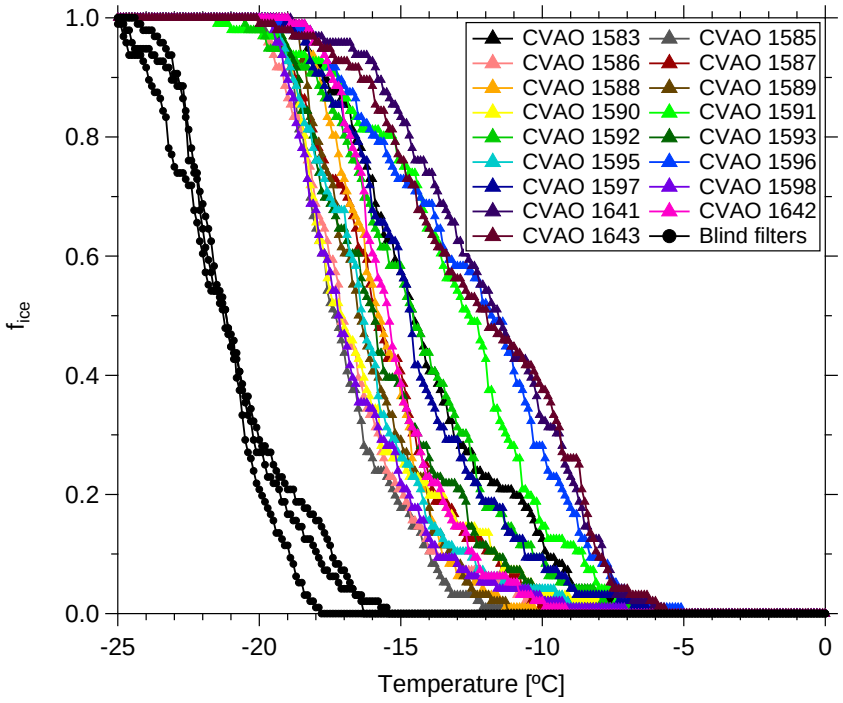

Figure S4. f_{ice} measured by INDA (without background subtraction) as a function of temperature in CVAO PM_{10} filters. f_{ice} of blind filters are shown by black dots.

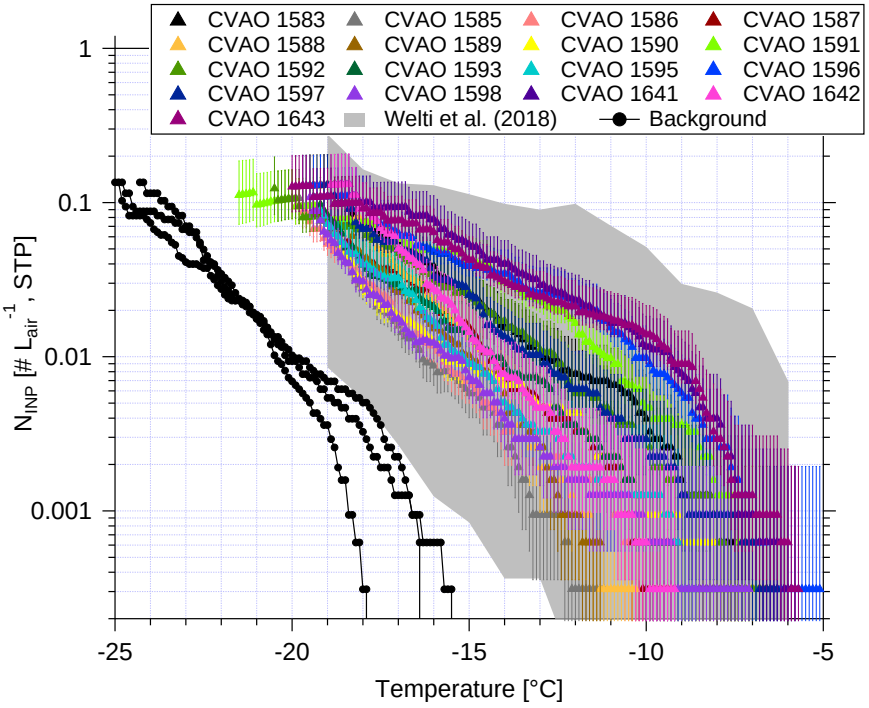

Figure S5. N_{INP} as a function of temperature from CVAO PM_{10} filters. Background correction of N_{INP} is included for these filter samples. The field measurement of N_{INP} in PM_{10} by Welti et al. (2018) is shown by gray shadow. Error bars show the 95% confidence interval. Black dots show the measurement background.

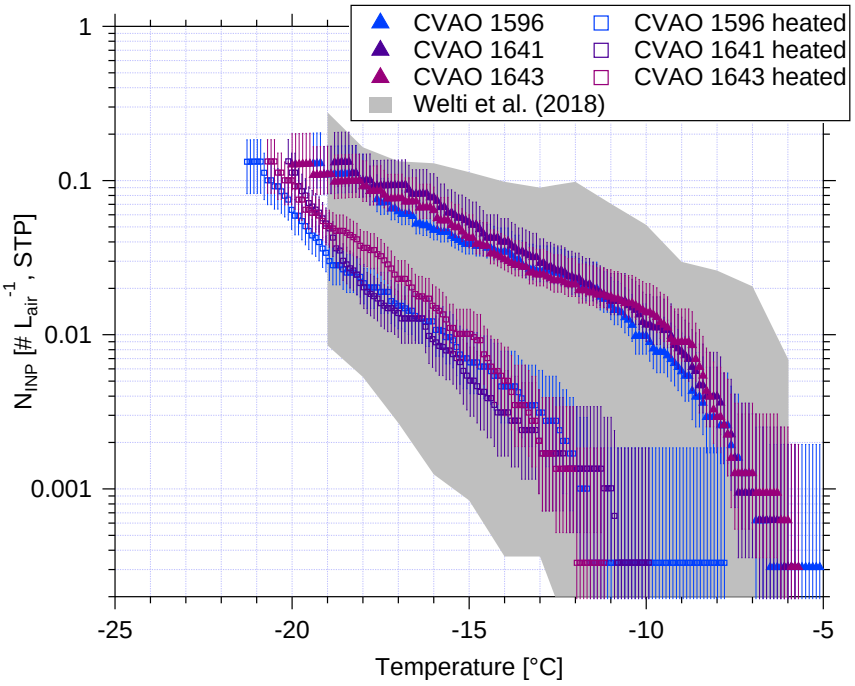

Figure S6. Comparison of N_{INP} as a function of temperature from CVAO 1596, CVAO 1641 and CVAO 1643 before and after heating (CVAO PM_{10} filters). The field measurement of N_{INP} in PM_{10} by Welti et al. (2018) is shown by gray shadow. Error bars show the 95% confidence interval. Background correction of N_{INP} is included for these filter samples.

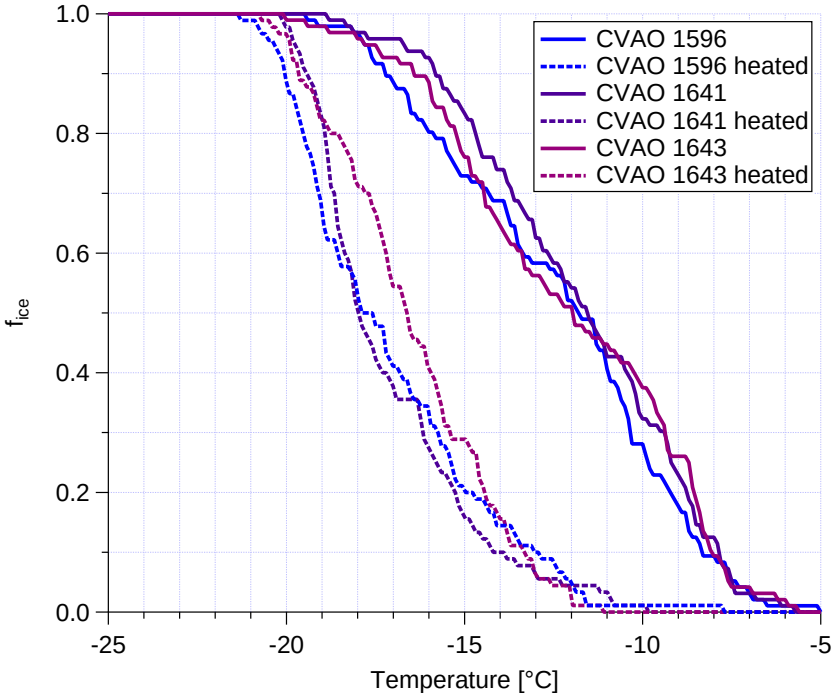

Figure S7. Comparison of f_{ice} measured by INDA (without background subtraction) as a function of temperature from CVAO 1596, CVAO 1641 and CVAO 1643 before and after heating (CVAO PM_{10} filters).

S2.3 CVAO PM_1

Table S3. The information of PM_1 filter samples at CVAO, including sample number, start time, end time, duration, total sampling volume, sampling volume per well and sample type.

Sample Number	Start Time yyyy/mm/dd hh:mm:ss	End Time yyyy/mm/dd hh:mm:ss	Duration [minute]	Total Volume [std m^3]	Volume Per Well [std L]	Type
CVAO924	2017/09/19 21:00:00	2017/09/20 21:00:00	1439.36	661.200	33.7347	PM_1
CVAO925	2017/09/21 21:00:00	2017/09/22 21:00:00	1439.36	661.200	33.7347	PM_1
CVAO926	2017/09/22 16:00:00	2017/09/23 16:00:00	1439.36	661.200	33.7347	PM_1
CVAO927	2017/09/23 16:00:00	2017/09/24 16:00:00	1439.36	661.200	33.7347	PM_1
CVAO928	2017/09/24 16:00:00	2017/09/25 16:00:00	1439.36	661.200	33.7347	PM_1
CVAO929	2017/09/25 16:00:00	2017/09/26 16:00:00	1439.21	664.115	33.8834	PM_1
CVAO930	2017/09/26 16:00:00	2017/09/27 16:00:00	1439.36	661.200	33.7347	PM_1
CVAO931	2017/09/27 16:00:00	2017/09/28 16:00:00	1439.36	661.200	33.7347	PM_1
CVAO932	2017/09/28 16:00:00	2017/09/29 16:00:00	1439.36	661.200	33.7347	PM_1
CVAO933	2017/09/29 16:00:00	2017/09/30 16:00:00	1439.36	661.200	33.7347	PM_1
CVAO934	2017/09/30 16:00:00	2017/10/01 16:00:00	1439.36	661.200	33.7347	PM_1
CVAO935	2017/09/29 16:00:00	2017/09/30 16:00:00				Blind filter
CVAO936	2017/10/01 16:00:00	2017/10/02 16:00:00	1438.53	659.798	33.6632	PM_1
CVAO937	2017/10/02 16:00:00	2017/10/03 16:00:00	1439.55	660.255	33.6865	PM_1
CVAO938	2017/10/03 16:00:00	2017/10/04 16:00:00	1439.36	661.200	33.7347	PM_1
CVAO939	2017/10/04 16:00:00	2017/10/05 16:00:00	1439.36	661.200	33.7347	PM_1
CVAO940	2017/10/05 16:00:00	2017/10/06 16:00:00	1439.18	661.071	33.7281	PM_1
CVAO941	2017/10/06 16:00:00	2017/10/07 16:00:00	1439.58	662.336	33.7927	PM_1
CVAO942	2017/10/07 16:00:00	2017/10/08 16:00:00	1439.58	662.122	33.7817	PM_1
CVAO944	2017/10/08 16:00:00	2017/10/09 16:00:00	1439.55	660.377	33.6927	PM_1

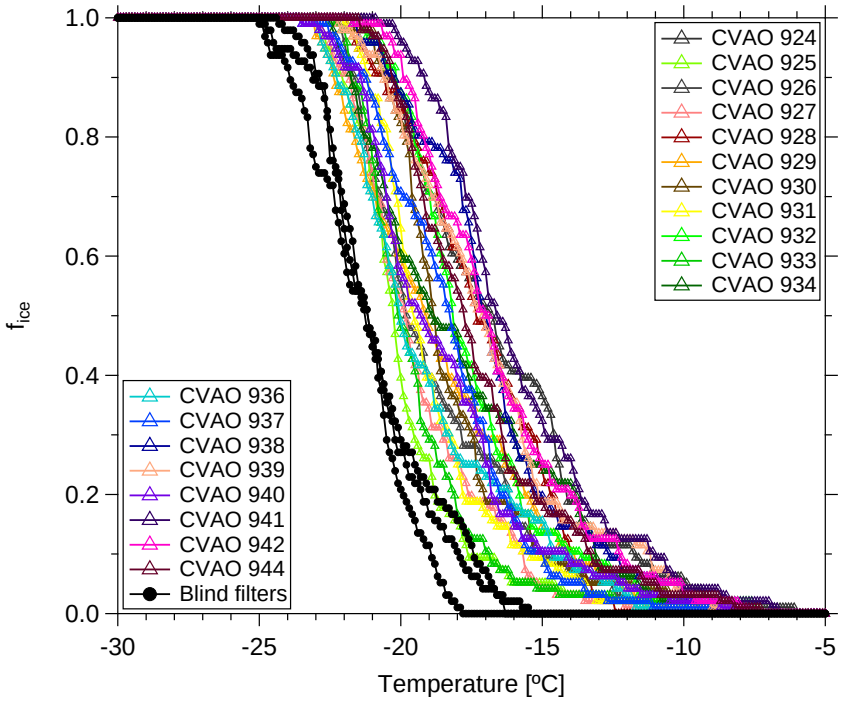

Figure S8. f_{ice} measured by INDA (without background subtraction) as a function of temperature in CVAO PM_1 filters. f_{ice} of blind filters are shown by black dots.

S2.4 MV PM_{10}

Table S4. The information of PM_{10} filter samples at MV, including sample number, start time, end time, duration, total sampling volume, sampling volume per well, cloud time (percent of the time MV was in cloud during the filter was sampled) and sample type.

Sample Number	Start Time yyyy/mm/dd hh:mm:ss	End Time yyyy/mm/dd hh:mm:ss	Duration [minute]	Total Volume [std m^3]	Volume Per Well [std L]	Cloud time [%]	Type
MV1600	2017/09/21 16:39:00	2017/09/22 16:23:00	1382.86	601.870	30.7077	67.44%	PM_{10}
MV1601	2017/09/22 16:23:00	2017/09/23 15:59:00	1418.31	615.998	31.4285	17.39%	PM_{10}
MV1602	2017/09/23 15:59:00	2017/09/24 16:01:00	1440.60	625.035	31.8896	6.12%	PM_{10}
MV1603	2017/09/24 16:01:00	2017/09/25 16:11:00	1449.61	629.660	32.1255	4.17%	PM_{10}
MV1604	2017/09/25 16:13:00	2017/09/26 16:19:00	1444.90	627.655	32.0232	61.70%	PM_{10}
MV1605	2017/09/26 16:20:00	2017/09/27 16:23:00	1440.58	627.381	32.0092	65.96%	PM_{10}
MV1606	2017/09/27 16:23:00	2017/09/28 16:59:00	1464.99	637.541	32.5276	79.59%	PM_{10}
MV1607	2017/09/28 17:01:00	2017/09/29 16:28:00	1406.21	611.922	31.2205	97.83%	PM_{10}
MV1608	2017/09/29 16:30:00	2017/09/30 16:28:00	1676.36	760.265	38.7890	93.75%	PM_{10}
MV1609	2017/10/01 19:02:00	2017/10/02 17:09:00	1326.63	576.405	29.4084	47.73%	PM_{10}
MV1610	2017/10/02 17:09:00	2017/10/03 17:09:00	1439.36	624.715	31.8732	52.08%	PM_{10}
MV1611	2017/10/03 17:10:00	2017/10/04 16:27:00	1396.11	606.390	30.9383	50.00%	PM_{10}
MV1612	2017/10/04 16:27:00	2017/10/05 16:00:00	1408.61	613.421	31.2970	69.05%	PM_{10}
MV1613	2017/10/05 16:00:00	2017/10/06 16:01:00	1441.46	627.486	32.0146	79.59%	PM_{10}
MV1614	2017/10/06 16:03:00	2017/10/07 16:02:00	1439.46	625.832	31.9302	87.23%	PM_{10}
MV1615	2017/10/07 16:02:00	2017/10/08 18:12:00	1439.36	627.485	32.0145	100.00%	PM_{10}
MV1616	2017/10/08 18:13:00	2017/10/09 12:04:00	1071.60	467.526	23.8534	100.00%	PM_{10}

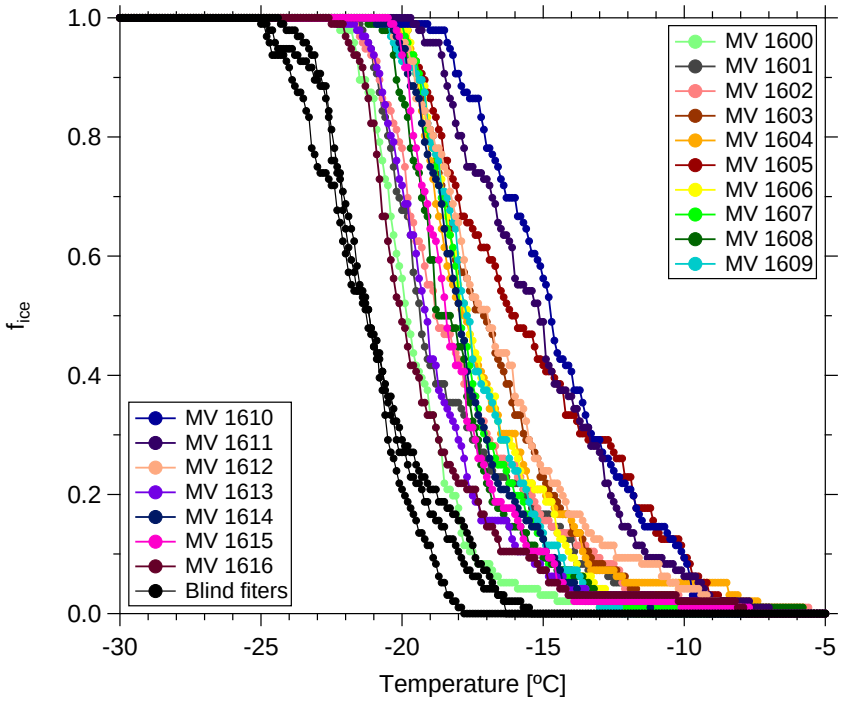

Figure S9. f_{ice} measured by INDA (without background subtraction) as a function of temperature in MV PM_{10} filters. f_{ice} of blind filters are shown by black dots.

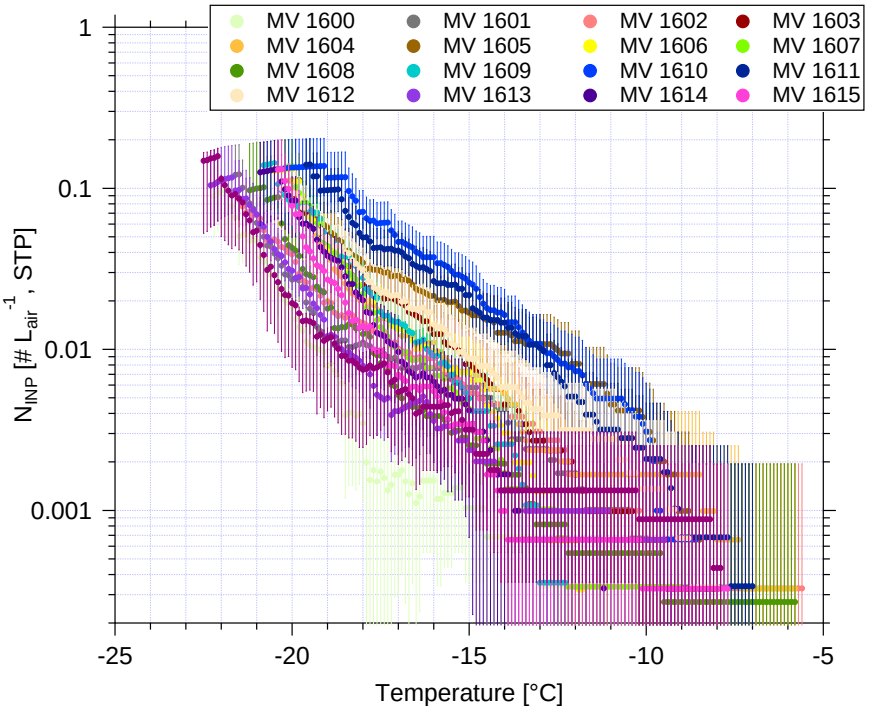

Figure S10. N_{INP} as function of temperature in MV PM_{10} filters. N_{INP} are background-corrected. Error bars show the 95% confidence interval.

S3 Cloud samples

Table S5. The information of cloud water samples, including sample number, start time, end time, duration, volume, sodium (Na^+) and chloride (Cl^-) mass concentration and $N_{CCN,0.30\%}$.

Sample Number	Start Time yyyy/mm/dd hh:mm:ss	End Time yyyy/mm/dd hh:mm:ss	Duration (h) [h]	Volume [mL]	Na^+ mg L^{-1}	Cl^- mg L^{-1}	$N_{CCN,0.30\%}$ cm^{-3}
Cloud01	2017/09/20 14:25:00	2017/09/20 19:20:00	4.92	185	8.44	15.51	551
Cloud03	2017/09/26 20:00:00	2017/09/27 09:00:00	13.00	435	8.32	14.15	387
Cloud04	2017/09/27 20:00:00	2017/09/28 08:30:00	12.50	544	5.00	9.27	239
Cloud05	2017/09/28 20:00:00	2017/09/29 08:30:00	12.50	537	14.18	24.57	560
Cloud11	2017/10/04 20:00:00	2017/10/05 08:30:00	12.50	150	46.11	70.30	481
Cloud12	2017/10/05 08:45:00	2017/10/05 18:38:00	9.88	78	22.75	36.99	494
Cloud13	2017/10/05 18:40:00	2017/10/05 21:10:00	2.50	133	16.97	25.23	442
Cloud14	2017/10/05 21:10:00	2017/10/06 00:30:00	3.33	131	17.31	24.36	473
Cloud15	2017/10/06 00:30:00	2017/10/06 05:00:00	4.50	120	21.85	31.95	491
Cloud16	2017/10/06 05:05:00	2017/10/06 09:00:00	3.92	120	16.87	19.77	445
Cloud19	2017/10/06 20:00:00	2017/10/07 08:30:00	12.50	537	18.34	29.10	482
Cloud20	2017/10/07 08:48:00	2017/10/07 12:48:00	4.00	88	28.19	41.54	510
Cloud24	2017/10/08 20:00:00	2017/10/09 08:00:00	12.00	537	24.54	32.46	625

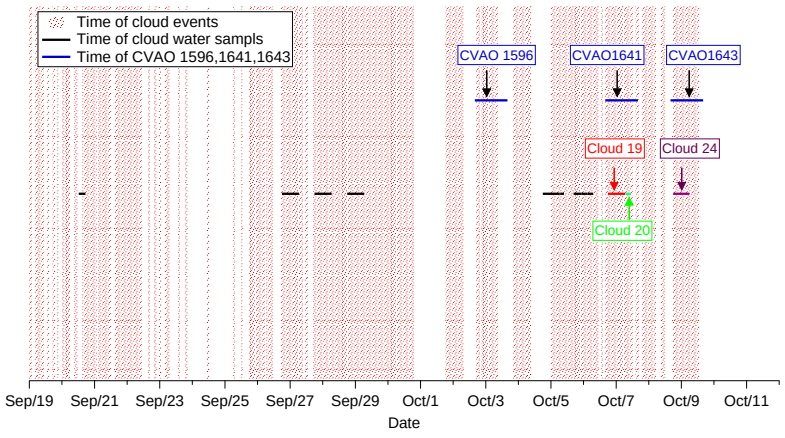

Figure S11. Times during which MV was in clouds (in red shadows) and the sampling time of all cloud water and that of some selected CVAO PM_{10} filters.

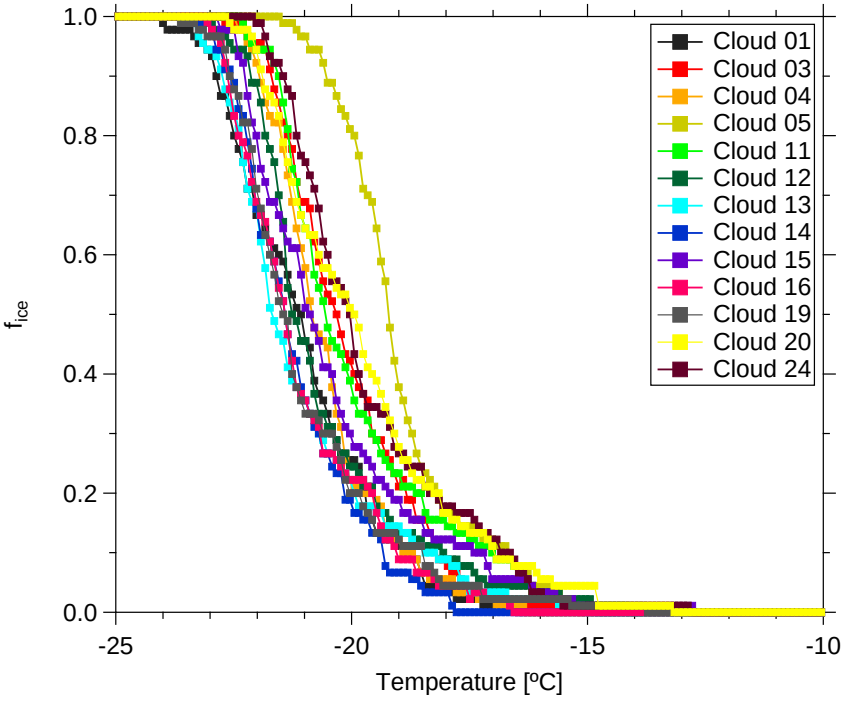

Figure S12. f_{ice} measured by LINA as a function of temperature in cloud water.

S4 Particle surface area size distribution

A thorough aerosol characterization has been done during the measurement campaign, and is described in detail in Gong et al. (2019). Fig. S14 shows the median particle surface area size distribution (PASD) for the whole campaign. Error bars show the 75th and 25th percentiles. Two different modes were observed, i.e., a small mode (30-500 nm) and a larger mode (500 nm-10 μm). The larger mode particle surface area is about 3 times higher than the small mode. Based on the PASD, the concentrations for the total surface area of the particles were calculated. The total particle surface area concentration (A_{total}) varied from 35 to 824 μm^2 cm^{-3}, with a median of 116 μm^2 cm^{-3}. The averaged A_{total} during each CVAO PM_{10} sampling period varied from 78 to 370 μm^2 cm^{-3} (summarized in Tab. S2). Based on airborne measurements in the Saharan dust layer, Price et al. (2018) found A_{total} mainly above 100 with a maximum of 688 μm^2 cm^{-3}, which is higher than values found for this study, likely due to the fact that Cape Verde is at some distance to the Sahara and also that less strong dust events were sampled.

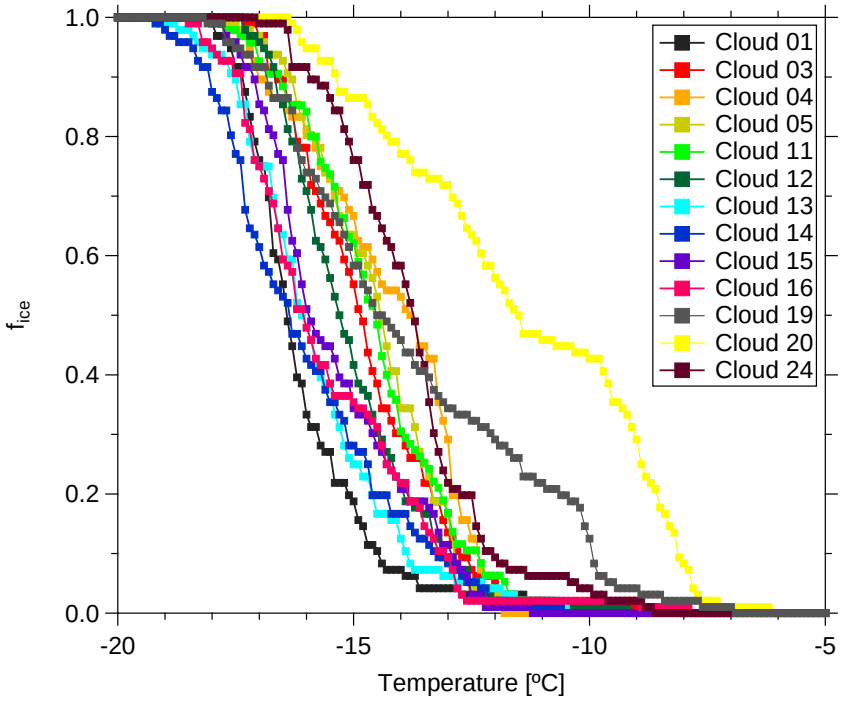

Figure S13. f_{ice} measured by INDA as a function of temperature in cloud water.

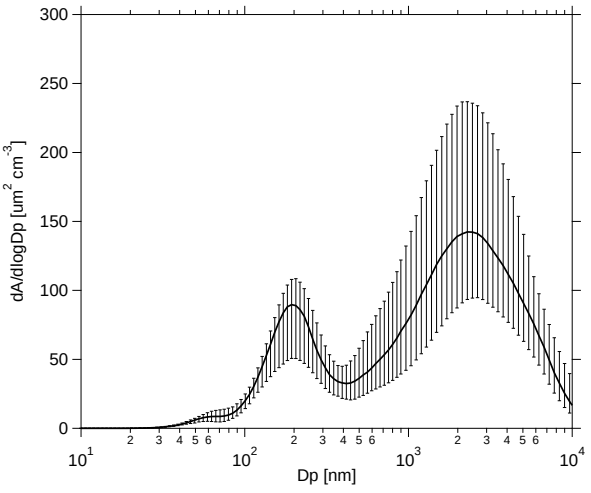

Figure S14. The median PASD during the whole campaign. The error bar indicates the range between the 75th and 25th percentiles.

References

Gong, X., Wex, H., Voigtländer, J., Fomba, K. W., Weinhold, K., van Pinxteren, M., Henning, S., Müller, T., Herrmann, H., and Stratmann, F.: Characterization of aerosol particles at Cape Verde close to sea and cloud level heights – Part 1: particle number size distribution, cloud condensation nuclei and their origins, Atmos. Chem. Phys. Discuss., 2019, 1–31, https://doi.org/10.5194/acp-2019-585, https://www.atmos-chem-phys-discuss.net/acp-2019-585/, 2019.

Price, H. C., Baustian, K. J., McQuaid, J. B., Blyth, A., Bower, K. N., Choularton, T., Cotton, R. J., Cui, Z., Field, P. R., Gallagher, M., Hawker, R., Merrington, A., Miltenberger, A., Neely III, R. R., Parker, S. T., Rosenberg, P. D., Taylor, J. W., Trembath, J., Vergara-Temprado, J., Whale, T. F., Wilson, T. W., Young, G., and Murray, B. J.: Atmospheric Ice-Nucleating Particles in the Dusty Tropical Atlantic, Journal of Geophysical Research: Atmospheres, 123, 2175–2193, https://doi.org/doi:10.1002/2017JD027560, https://agupubs.onlinelibrary.wiley.com/doi/abs/10.1002/2017JD027560, 2018.

Welti, A., Müller, K., Fleming, Z. L., and Stratmann, F.: Concentration and variability of ice nuclei in the subtropical maritime boundary layer, Atmospheric Chemistry and Physics, 18, 5307–5320, 2018.

4 Summary and Conclusions

In the present thesis, we dealt with the aerosol particles, their properties (size distribution, hygroscopicity), sources and contributions to CCN and INPs over tropical and subtropical regions in the northern hemisphere. Two field campaigns were carried out in two representative locations, i.e., anthropogenic polluted environment at Cyprus (A-LIFE project) and marine-dust intersect environment at Cabo Verde (MarParCloud project). On-line aerosol physical measurements were performed and samples from different environmental compartments: the oceanic sea surface microlayer (SML), underlying water (ULW), cloud water and atmospheric filters close to both sea and cloud levels were collected for INP measurement with off-line freezing devices in our lab. Data were analyzed, interpreted and published on Gong et al. [53], Gong et al. [54] and Gong et al. [55].

A-LIFE project The A-LIFE campaign took place in April 2017 on the island of Cyprus to investigate the aerosols prevailing in the eastern Mediterranean region. As part of the A-LIFE campaign, ground-based measurements were carried out in Paphos, Cyprus, to characterize the abundance, properties (size distribution, hygroscopicity, ice activity), and sources of aerosol particles in general, CCN and INP in particular.

During this campaign, new particle formation events with subsequent growth of the particles into the CCN size range were observed. Aitken mode particles contained high fraction of organic material (hygroscopicity parameter κ values of 0.21 to 0.29). Accumulation mode particles contained sulfate and maybe sea salt mixed with organic (κ value of 0.57). Super-micron particles originated mainly from sea-spray aerosol and partly from mineral dust.

INP number concentrations were measured in the temperature range from -6.5 to -26.5 °C. INP number concentration at any particular temperature span around 1 order of magnitude below -20 °C and about 2 orders of magnitude at warmer temperatures (T>-18 °C). Few samples showed elevated concentrations at temperatures >-15 °C, which suggests a significant contribution of biological particles to the INP population. Both measured temperature spectra and INP number concentration probability density functions indicate that the observed INP (ice active in the temperature range between -15 and -20 °C) might originate from long-range transport.

There was no correlation between INP number concentration and particle number concentration in the size range > 500 nm. Parameterizations based on particle number concentration in the size range > 500 nm were found to overestimate INP number concentration by about 1 to 2 orders of magnitude. There was also no correlation between INP number concentration and particle surface area concentration. The ice active surface site density (n_S, a measure to describe the ice activity per particle surface area) for the polluted aerosol encountered in the eastern Mediterranean in this study is about 1 to 3 orders of magnitude lower than the n_S found for dust aerosol particles in previous studies. Anthropogenic polluted aerosol particles contributed to a high concentration of $N_{>500\ \mathrm{nm}}$ and surface area, but they are relatively inefficient INPs compared to dust particles. Therefore, the derived INP number concentration probability density function in this study could be a better choice for modeling INP number concentration if the aerosol particle composition is unknown or uncertain.

MarParCloud project The MarParCloud (**Mar**ine biological production, organic aerosol **par**ticles and marine **cloud**s: a process chain) campaign took place in September and October 2017 on the Cabo Verde islands to investigate the mixed marine-dust type aerosols prevailing in this region of the Atlantic Ocean. A thorough characterization of the abundance, properties, and sources of aerosol particles, CCN and INPs was done at the Cape Verde Atmospheric Observatory (CVAO, sea level height) and on the top of Monte Verde (MV, cloud level height), respectively.

During times without clouds, we found that aerosol properties (particle number concentration, particle number size distribution as well as, CCN and INP number concentrations) to be similar at CVAO and MV and the boundary layer generally to be well mixed. Therefore, data obtained at CVAO are representative for the aerosol properties at cloud level. Cloud events were observed at MV during roughly 58% of the time and during these, a large fraction of particles were activated to cloud droplets.

A trimodal parameterization method was deployed to characterize particle number concentration at CVAO. Based on number concentrations in different aerosol modes, four well separable types of PNSDs were found, which were named the marine type, mixture type, dust type1 and dust type2. Aerosol particles differ depending on their origins. When the air masses came from the Atlantic Ocean, sea spray can be assumed to be one source for particles, besides for NPF. For these air masses, PNSDs featured the lowest number concentration in Aitken, accumulation and coarse mode. Particle number concentrations for the sea spray aerosol (i.e., the coarse mode for these air masses) accounted for a limited portion of CCN number concentration at supersaturation of 0.30% (about 3.7%) and total particle number concentration (about 1.1% to 4.4%). When the air masses came from the Sahara, we observed

enhanced Aitken, accumulation and coarse mode particle number concentrations and overall increased CCN number concentration. CCN number concentration at supersaturation of 0.30% (proxy for the supersaturation encountered in clouds) during the strongest observed dust periods is about 2.5 times higher than that during marine periods. However, the CCN-derived hygroscopicity for marine and dust periods shows no significant difference and is generally similar, independent of air mass.

For INPs in collected seawater samples, both enrichment and depletion of INP number concentration in SML compared to ULW were observed. The enrichment factor varied from roughly 0.4 to 11, and there was no clear trend in EF with ice nucleation temperature.

INP number concentration in the atmospheric PM_{10} samples at CVAO spanned around 1 order of magnitude below -15 °C, and about 2 orders of magnitude at warmer temperatures (> -12 °C). Among the 17 PM_{10} samples at CVAO, three PM_{10} filters showed elevated INP number concentration at warm temperatures. These highly ice active INPs were most likely biological particles because the elevated INP number concentration at the warm temperatures were significant reduced after heating samples at 95 °C for 1 hour.

INP number concentration in PM_1 were generally lower than those in PM_{10} at CVAO. About 83±22%, 67±18% and 77±14% (median±standard deviation) of INPs had a diameter >1 μm at ice nucleation temperatures of -12, -15, and -18 °C, respectively. PM_1 at CVAO did not show such elevated INP number concentration at warm temperatures. Consequently, the difference in INP number concentration between PM_1 and PM_{10} at CVAO suggests that biological ice active particles were present in the super-micron size range.

INP number concentration in PM_{10} at CVAO was found to be similar to that on MV during non-cloud events. During cloud events, most INPs on MV were activated to cloud droplets. When highly ice active particles were present in PM_{10} filters at CVAO, they were not observed in PM_{10} filters on MV, but in cloud water samples, instead. This is direct evidence that these INPs which are likely biological are activated to cloud droplets during cloud events.

For the observed air masses, INP number concentration in air fit well to the concentrations observed in cloud water. When comparing atmospheric concentrations of INPs to those found in seawater samples, it can be concluded that sea spray aerosol only contributed a minor fraction to the atmospheric INP population at Cabo Verde. This latter conclusion still holds when accounting for an enrichment of

organic carbon in super-micron particles during sea spray generation as reported in literature.

The data and knowledge concerning CCN and INPs gained in this thesis will help to better understand the interactions between aerosol particles and clouds and represent highly valuable information for evaluating, driving and constraining atmospheric model simulations.

5 Outlook

In recent years, considerable progress has been made in understanding the chemical composition of aerosols, their microphysical properties, and the factors that enable them to act as CCN and INPs. However, our understanding of CCN and INP on a global level is still limited. Here I point out some aspects towards future work concerning CCN and INP studies, respectively.

For CCN studies Quantification of the global budget of CCN is an essential step towards a complete understanding of global clouds and climate. Up to date, large uncertainties still exist for quantitative assessment of CCN sources, especially the contribution of CCN from the submicron part of marine particles and anthropogenic particles. Quantifying the CCN population in remote area, such as in the Southern Ocean, can help us understand the baseline of atmospheric CCN concentrations. Furthermore, many CCN measurements are made in short campaigns of typically a month duration [89, 72, 73, 90]. Short-term measurements are not representative because the real world has large spatial heterogeneity and temporal variability. It has therefore been recommended, that long-term measurement should be performed for a better constraint of modeling efforts [91].

For INP studies

1. During the campaign in Cyprus, we found that INP concentrations might not be influenced directly by urban pollution, at least not down to roughly -25 °C. This is consistent to previous study by Chen et al. [45] in Beijing. The urban pollution is one of the most important particle sources in most developing countries. It is worth to investigate the ice nucleating ability of anthropogenic aerosol particles in the colder temperature range below -25 °C.

2. SSA particles are relatively inefficient as INPs compared to mineral dust and biological particles. However, due to the vast coverage of the Earth's surface by oceans, it is necessary to clarify the quantity and role of SSA and marine organic particles to INPs. A target campaign should focus on identifying sources of marine INPs, particularly in regions lacking a strong influence from dust, e.g. the South Ocean. Such a campaign should combine ship-based and, ideally, airborne measurements of air, seawater and cloud water, using recent state-of-the art instruments to measure INP concentra-

tions and composition. Such examinations already have started to be under way (e.g. SOCRATES, https://www.eol.ucar.edu/content/socrates-project-overview), and results from this and further alike campaigns will be highly valuable.

3. Previous studies found an enrichment of organic carbon in submicron sea spray particles of about 10^4 to 10^5 in mass [92, 76], and this value decreased to 10^2 for super-micron particles [92, 27]. It is not clear if INPs are included in the organic carbon in which the enrichment was observed. A targeted field campaign in the clean marine environment (e.g. in the Southern Ocean) or laboratory study (e.g. bring the ocean water into the tank) will be necessary to understand the INPs production mechanism and quantify the abundance of SSA INPs.

4. To establish robust empirical correlations between ice nucleating properties and physical characteristics (number concentration, size distribution, surface area) of atmospheric aerosol has been a challenge for decades. If the correlation was found, it might allow us to predict INPs from aerosol data. However, parametrizations [93, 94] based on particle number concentration in the size range >500 nm were found to overestimate INP number concentartion by about 1 to 2 orders of magnitude at Cyprus. Parametrizations [19, 31, 95, 37] based on particle surface area was not representative for Cabo Verde. These comparisons to literature raise the question if and how particle number concentration and particle surface area should be used to parameterize atmospheric INP measurements. In general, it is still an open issue to which extent INP number concentration can be parameterized, based on one or a few parameters, to reliably describe INP number concentration for different locations around the globe.

Appendix A

A.1 Paper Included in This Doctoral Thesis and Author's Contribution

I **Gong, X.**, Wex, H., Müller, T., Wiedensohler, A., Höhler, K., Kandler, K., Ma, N., Dietel, B., Schiebel, T., Möhler, O., and Stratmann, F.: Characterization of aerosol properties at Cyprus, focusing on cloud condensation nuclei and ice-nucleating particles, Atmos. Chem. Phys., 19, 10883-10900, https://doi.org/10.5194/acp-19-10883-2019, 2019.

X. Gong wrote the manuscript with contributions from H. Wex, F. Stratmann, K. Höhler, K. Kandler, T. Müller and A. Wiedensohler. N. Ma and T. Müller performed particle number size distribution measurement and X. Gong performed data evaluation. Chemical composition measurements and data evaluation were performed by K. Kandler. CCN measurements and data analysis were performed by X. Gong. LINA measurements and data evaluation were performed by X. Gong. INSEKT measurements and data evaluation were performed by B. Dietel, T. Schiebel, K. Höhler and X. Gong. X. Gong, H. Wex and F. Stratmann discussed the results and further analysis after the campaign. All co-authors proofread and commented the manuscript.

II **Gong, X.**, Wex, H., Voigtlälnder, J., Fomba, K. W., Weinhold, K., van Pinxteren, M., Henning, S., Mülller, T., Herrmann, H., and Stratmann, F.: Characterization of aerosol particles at Cabo Verde close to sea level and at the cloud level – Part 1: Particle number size distribution, cloud condensation nuclei and their origins , Atmos. Chem. Phys., 20, 1431-1449, https://doi.org/10.5194/acp-20-1431-2020, 2020.

X. Gong wrote the manuscript with contributions from H. Wex, J. Voigtländer and M. van Pinxteren. K. Weinhold and X. Gong performed MPSS and APS measurements and X. Gong performed data evaluation. K. Weinhold calibrated MPSS and APS before, during and after the campaign. F. Stratmann, H. Wex and X. Gong performed the CCN measurements and X. Gong performed data evaluation. S. Henning calibrated CCN before and after the campaign. Balloon measurements and data evaluation were performed by J.Voigtländer and X. Gong. X. Gong, H. Wex and

F. Stratmann discussed the results and further analysis after the campaign. All co-authors proofread and commented the manuscript.

III **Gong, X.**, Wex, H., van Pinxteren, M., Triesch, N., Fomba, K. W., Lubitz, J., Stolle, C., Robinson, T.-B., Müller, T., Herrmann, H., and Stratmann, F.: Characterization of aerosol particles at Cabo Verde close to sea level and at the cloud level - Part 2: Ice-nucleating particles in air, cloud and seawater, Atmos. Chem. Phys., 20, 1451-1468, https://doi.org/10.5194/acp-20-1451-2020, 2020.

X. Gong wrote the manuscript with contributions from H. Wex and M. van Pinxteren. C. Stolle, N. Triesch and B. Robinson collected ocean water samples. X. Gong, M. van Pinxteren and N. Triesch collected filter samples. K. W. Fomba collected cloud water samples. X. Gong and J. Lubitz performed INP measurements. X. Gong preformed data evaluation. X. Gong, H. Wex and F. Stratmann discussed the results and further analysis after the campaign. All co-authors proofread and commented the manuscript.

A.2 Co-authorship Publication During PhD

I Wendisch, M., A. Macke, A. Ehrlich, C. Lüpkes, M. Mech, D. Chechin, K. Dethloff, C.B. Velasco, H. Bozem, M. Brückner, H. Clemen, S. Crewell, T. Donth, R. Dupuy, K. Ebell, U. Egerer, R. Engelmann, C. Engler, O. Eppers, M. Gehrmann, **X. Gong,** M. Gottschalk, C. Gourbeyre, H. Griesche, J. Hartmann, M. Hartmann, B. Heinold, A. Herber, H. Herrmann, G. Heygster, P. Hoor, S. Jafariserajehlou, E. Jäkel, E. Järvinen, O. Jourdan, U. Kästner, S. Kecorius, E.M. Knudsen, F. Köllner, J. Kretzschmar, L. Lelli, D. Leroy, M. Maturilli, L. Mei, S. Mertes, G. Mioche, R. Neuber, M. Nicolaus, T. Nomokonova, J. Notholt, M. Palm, M. van Pinxteren, J. Quaas, P. Richter, E. Ruiz-Donoso, M. Schäfer, K. Schmieder, M. Schnaiter, J. Schneider, A. Schwarzenböck, P. Seifert, M.D. Shupe, H. Siebert, G. Spreen, J. Stapf, F. Stratmann, T. Vogl, A. Welti, H. Wex, A. Wiedensohler, M. Zanatta, and S. Zeppenfeld, 2019: The Arctic Cloud Puzzle: Using ACLOUD/PASCAL Multiplatform Observations to Unravel the Role of Clouds and Aerosol Particles in Arctic Amplification. Bull. Amer. Meteor. Soc., 100, 841–871, https://doi.org/10.1175/BAMS-D-18-0072.1

For this publication, I contributed with the cloud condensation nuclei and ice-nucleating particles measurements on Polarstern cruise for two months.

II Kecorius, S., Vogl, T., Paasonen, P., Lampilahti, J., Rothenberg, D., Wex, H., Zeppenfeld, S., van Pinxteren, M., Hartmann, M., Henning, S., **Gong, X.**, Welti, A., Kulmala, M., Stratmann, F., Herrmann, H., and Wiedensohler, A.: New particle formation and its effect on cloud condensation nuclei abundance in the summer Arctic: a case study in the Fram Strait and Barents Sea, Atmos. Chem. Phys., 19, 14339–14364, https://doi.org/10.5194/acp-19-14339-2019, 2019.

For this publication, I contributed with the cloud condensation nuclei measurement on Polarstern cruise for two months.

III Brilke, S., Fölker, N., Müller, T., Kandler, K., Gong, X., Peischl, J., Weinzierl, B., and Winkler, P. M.: New particle formation and sub-10nm size distribution measurements during the A-LIFE field experiment in Paphos, Cyprus, Atmos. Chem. Phys., 20, 5645-5656, https://doi.org/10.5194/acp-2005645-2020, 2020.

For this publication, I contributed with the particle number size distribution measurement and analyzed the data.

IV van Pinxteren, M., Fomba, K. W., Triesch, N., Stolle, C., Wurl, O., Bahlmann, E., **Gong, X.**, Voigtländer, J., Wex, H., Robinson, T.-B., Barthel, S., Zeppenfeld, S., Hoffmann, E. H., Roveretto, M., Li, C., Grosselin, B., Daële, V., Senf, F., van Pinxteren, D., Manzi, M., Zabalegui, N., Frka, S., Gašparović, B., Pereira, R., Li, T., Wen, L., Li, J., Zhu, C., Chen, H., Chen, J., Fiedler, B., von Tümpling, W., Read, K. A., Punjabi, S., C. Lewis, A. C., Hopkins, J. R., Carpenter, L. J., Peeken, I., Rixen, T., Schulz-Bull, D., Monge, M. E., Mellouki, A., George, C., Stratmann, F., and Herrmann, H.: Marine organic matter in the remote environment of the Cape Verde islands – an introduction and overview to the MarParCloud campaign, Atmos. Chem. Phys., 20, 6921–6951, https://doi.org/10.5194/acp-20-6921-2020, 2020.

For this publication, I contributed with the particle number size distribution and cloud condensation nuclei measurements. I wrote Sect. 5.1.1 Physical aerosol characterization and provided the particle number size distribution plot (Fig. 8 and Fig. 9). I contributed with the ice-nucleating particle measurement. I wrote Sect. 5.7.4 Ice-nucleating particles and provided the ice-nucleating particle number concentration plot (Fig. 21).

V Welti, A., Bigg, E. K., DeMott, P. J., **Gong, X.**, Hartmann, M., Harvey, M., Henning, S., Herenz, P., Hill, T. C. J., Hornblow, B., Leck, C., Löffler, M., McCluskey, C. S., Rauker, A. M., Schmale, J., Tatzelt, C., van Pinxteren, M., and Stratmann, F.: Ship-based measurements of ice nuclei concentrations over the Arctic, Atlantic, Pacific

and Southern Ocean, Atmos. Chem. Phys. Discuss., https://doi.org/10.5194/acp-2020-466, in review, 2020.

For this publication, I contributed with the ice nucleating particles' measurement on Polarstern cruise for two months.

A.3 Conference Abstracts as Lead Author

I **X. Gong**, T. Müller, H Wex, N. Ma, A. Wiedensohler, F. Stratmann,: In-situ measurement of Cloud Condensation Nuclei and Ice Nucleating Particles in Cyprus. EGU General Assembly Conference, 2018.

II **X. Gong**, H. Wex, L. Huang, H. Hung, R. Traversi, RJ. Sheesley, CE. Moffett,: Annual cycles in ice nucleating particle concentrations at four Arctic locations. AGU Fall Meeting, 2018.

III **X. Gong**, H. Wex, M. Van Pinxteren, N. Triesch, C. Stolle, F. Stratmann,: Connecting in-situ measurements of Ice Nucleating Particles in air and in ocean and cloud water for the region of the Cape Verde islands. AGU Fall Meeting, 2018.

IV **X. Gong**, H. Wex, M. van Pinxteren, N. Triesch, C. Stolle, F. Stratmann,: In-situ Measurements of Ice Nucleating Particles in Tropical Marine Boundary Layer and in Ocean and Warm Cloud Water. European Aerosol Conference, 2019.

A.4 PhD Commission

Prof. Dr. Alfred Wiedensohler (Chairman)
Department Experimental Aerosol and Cloud Microphysics, Leibniz Institute for Tropospheric Research, Leipzig, Germany
ali@tropos.de

Prof. Dr. Johannes Quaas
Institute for Meteorology, University of Leipzig, Leipzig, Germany
johannes.quaas@uni-leipzig.de

Prof. Dr. Andreas Macke (Supervisor)
Department Remote Sensing of Atmospheric Processes, Leibniz Institute for Tropospheric Research, Leipzig, Germany
andreas.macke@tropos.de

A.5 Supervisor Committee

Dr. Frank Stratmann
Department Experimental Aerosol and Cloud Microphysics, Leibniz Institute for Tropospheric Research, Leipzig, Germany
frank.stratmann@tropos.de

Dr. Heike Wex
Department Experimental Aerosol and Cloud Microphysics, Leibniz Institute for Tropospheric Research, Leipzig, Germany
wex@tropos.de

Dr. Manuela van Pinxteren
Department Chemistry of the Atmosphere, Leibniz Institute for Tropospheric Research, Leipzig, Germany
manuela.vanpinxteren@tropos.de

Bibliography

[1]Thomas Stocker. *Climate change 2013: the physical science basis: Working Group I contribution to the Fifth assessment report of the Intergovernmental Panel on Climate Change*. Cambridge University Press, 2014 (cit. on p. 1).

[2]S Twomey. „Pollution and the planetary albedo“. In: *Atmospheric Environment (1967)* 8.12 (1974), pp. 1251–1256 (cit. on p. 1).

[3]Bruce A Albrecht. „Aerosols, cloud microphysics, and fractional cloudiness“. In: *Science* 245.4923 (1989), pp. 1227–1230 (cit. on p. 1).

[4]Matthew W Christensen, Yi-Chun Chen, and Graeme L Stephens. „Aerosol indirect effect dictated by liquid clouds“. In: *Journal of Geophysical Research: Atmospheres* 121.24 (2016) (cit. on p. 1).

[5]G. Vali, P. J. DeMott, O. Möhler, and T. F. Whale. „Technical Note: A proposal for ice nucleation terminology“. In: *Atmos. Chem. Phys.* 15.18 (2015), pp. 10263–10270 (cit. on p. 1).

[6]A. Ansmann, M. Tesche, D. Althausen, et al. „Influence of Saharan dust on cloud glaciation in southern Morocco during the Saharan Mineral Dust Experiment“. In: *Journal of Geophysical Research: Atmospheres* 113.D4 (2008) (cit. on p. 1).

[7]C. D. Westbrook and A. J. Illingworth. „The formation of ice in a long-lived supercooled layer cloud“. In: *Quarterly Journal of the Royal Meteorological Society* 139.677 (2013), pp. 2209–2221 (cit. on p. 1).

[8]Paul Ginoux, Mian Chin, Ina Tegen, et al. „Sources and distributions of dust aerosols simulated with the GOCART model“. In: *Journal of Geophysical Research: Atmospheres* 106.D17 (2001), pp. 20255–20273 (cit. on p. 1).

[9]Jianping Huang, Bing Lin, Patrick Minnis, et al. „Satellite-based assessment of possible dust aerosols semi-direct effect on cloud water path over East Asia“. In: *Geophysical Research Letters* 33.19 (2006) (cit. on p. 1).

[10]Taichu Y. Tanaka and Masaru Chiba. „A numerical study of the contributions of dust source regions to the global dust budget“. In: *Global and Planetary Change* 52.1 (2006), pp. 88–104 (cit. on p. 1).

[11]A. S. Goudie and N. J. Middleton. „Saharan dust storms: nature and consequences“. In: *Earth-Science Reviews* 56.1 (2001), pp. 179–204 (cit. on p. 1).

[12]Yaping Shao, Karl-Heinz Wyrwoll, Adrian Chappell, et al. „Dust cycle: An emerging core theme in Earth system science“. In: *Aeolian Research* 2.4 (2011), pp. 181–204 (cit. on p. 1).

[13] Kenneth Sassen, Paul J. DeMott, Joseph M. Prospero, and Michael R. Poellot. „Saharan dust storms and indirect aerosol effects on clouds: CRYSTAL-FACE results“. In: *Geophysical Research Letters* 30.12 (2003) (cit. on p. 1).

[14] Paul J. DeMott, Kenneth Sassen, Michael R. Poellot, et al. „African dust aerosols as atmospheric ice nuclei“. In: *Geophysical Research Letters* 30.14 (2003), n/a–n/a (cit. on p. 1).

[15] V. A. Karydis, P. Kumar, D. Barahona, I. N. Sokolik, and A. Nenes. „On the effect of dust particles on global cloud condensation nuclei and cloud droplet number“. In: *Journal of Geophysical Research: Atmospheres* 116.D23 (2011), n/a–n/a (cit. on p. 1).

[16] S. Augustin-Bauditz, H. Wex, S. Kanter, et al. „The immersion mode ice nucleation behavior of mineral dusts: A comparison of different pure and surface modified dusts“. In: *Geophysical Research Letters* 41.20 (2014), pp. 7375–7382 (cit. on p. 2).

[17] C. Hoose and O. Möhler. „Heterogeneous ice nucleation on atmospheric aerosols: a review of results from laboratory experiments“. In: *Atmos. Chem. Phys.* 12.20 (2012), pp. 9817–9854 (cit. on p. 2).

[18] B. J. Murray, D. O'Sullivan, J. D. Atkinson, and M. E. Webb. „Ice nucleation by particles immersed in supercooled cloud droplets“. In: *Chemical Society Reviews* 41.19 (2012), pp. 6519–6554 (cit. on p. 2).

[19] Monika Niemand, Ottmar Möhler, Bernhard Vogel, et al. „A Particle-Surface-Area-Based Parameterization of Immersion Freezing on Desert Dust Particles“. In: *Journal of the Atmospheric Sciences* 69.10 (2012), pp. 3077–3092 (cit. on pp. 2, 20, 132).

[20] P. J. DeMott, A. J. Prenni, G. R. McMeeking, et al. „Integrating laboratory and field data to quantify the immersion freezing ice nucleation activity of mineral dust particles“. In: *Atmos. Chem. Phys.* 15.1 (2015), pp. 393–409 (cit. on p. 2).

[21] James D. Atkinson, Benjamin J. Murray, Matthew T. Woodhouse, et al. „The importance of feldspar for ice nucleation by mineral dust in mixed-phase clouds“. In: *Nature* 498 (2013), p. 355 (cit. on p. 2).

[22] Dennis Niedermeier, Stefanie Augustin-Bauditz, Susan Hartmann, et al. „Can we define an asymptotic value for the ice active surface site density for heterogeneous ice nucleation?“ In: *Journal of Geophysical Research: Atmospheres* 120.10 (2015), pp. 5036–5046 (cit. on p. 2).

[23] Y. Boose, A. Welti, J. Atkinson, et al. „Heterogeneous ice nucleation on dust particles sourced from nine deserts worldwide - Part 1: Immersion freezing“. In: *Atmospheric Chemistry and Physics* 16.23 (2016), pp. 15075–15095 (cit. on p. 2).

[24] Peter Warneck. *Chemistry of the natural atmosphere*. Vol. 71. Elsevier, 1999 (cit. on p. 2).

[25] R. L. Modini, A. A. Frossard, L. Ahlm, et al. „Primary marine aerosol-cloud interactions off the coast of California“. In: *Journal of Geophysical Research: Atmospheres* 120.9 (2015), pp. 4282–4303 (cit. on p. 2).

[26] Kimberly A. Prather, Timothy H. Bertram, Vicki H. Grassian, et al. „Bringing the ocean into the laboratory to probe the chemical complexity of sea spray aerosol“. In: *Proceedings of the National Academy of Sciences* 110.19 (2013), pp. 7550–7555 (cit. on p. 2).

[27]Patricia K. Quinn, Douglas B. Collins, Vicki H. Grassian, Kimberly A. Prather, and Timothy S. Bates. „Chemistry and Related Properties of Freshly Emitted Sea Spray Aerosol“. In: *Chemical Reviews* 115.10 (2015), pp. 4383–4399 (cit. on pp. 2, 132).

[28]E. Fuentes, H. Coe, D. Green, and G. McFiggans. „On the impacts of phytoplankton-derived organic matter on the properties of the primary marine aerosol – Part 2: Composition, hygroscopicity and cloud condensation activity“. In: *Atmos. Chem. Phys.* 11.6 (2011), pp. 2585–2602 (cit. on p. 2).

[29]MO Andreae and D Rosenfeld. „Aerosol–cloud–precipitation interactions. Part 1. The nature and sources of cloud-active aerosols“. In: *Earth-Science Reviews* 89.1-2 (2008), pp. 13–41 (cit. on p. 2).

[30]Theodore W. Wilson, Luis A. Ladino, Peter A. Alpert, et al. „A marine biogenic source of atmospheric ice-nucleating particles“. In: *Nature* 525.7568 (2015), pp. 234–238 (cit. on p. 2).

[31]Paul J. DeMott, Thomas C. J. Hill, Christina S. McCluskey, et al. „Sea spray aerosol as a unique source of ice nucleating particles“. In: *Proceedings of the National Academy of Sciences* 113.21 (2016), pp. 5797–5803 (cit. on pp. 2, 132).

[32]P. K. Quinn, D. J. Coffman, J. E. Johnson, L. M. Upchurch, and T. S. Bates. „Small fraction of marine cloud condensation nuclei made up of sea spray aerosol“. In: *Nature Geoscience* 10 (2017), p. 674 (cit. on p. 2).

[33]Glenn W. Brier and Dwight B. Kline. „Ocean Water as a Source of Ice Nuclei“. In: *Science* 130.3377 (1959), pp. 717–718 (cit. on p. 2).

[34]R. C. Schnell and Gabor Vali. „Biogenic Ice Nuclei: Part I. Terrestrial and Marine Sources“. In: *Journal of the Atmospheric Sciences* 33.8 (1976), pp. 1554–1564 (cit. on p. 2).

[35]V. E. Irish, P. Elizondo, J. Chen, et al. „Ice-nucleating particles in Canadian Arctic sea-surface microlayer and bulk seawater“. In: *Atmos. Chem. Phys.* 17.17 (2017), pp. 10583–10595 (cit. on pp. 2, 13).

[36]C. S. McCluskey, T. C. J. Hill, R. S. Humphries, et al. „Observations of Ice Nucleating Particles Over Southern Ocean Waters“. In: *Geophysical Research Letters* 45.21 (2018), pp. 11,989–11,997 (cit. on pp. 2, 18).

[37]Christina S. McCluskey, Jurgita Ovadnevaite, Matteo Rinaldi, et al. „Marine and Terrestrial Organic Ice-Nucleating Particles in Pristine Marine to Continentally Influenced Northeast Atlantic Air Masses“. In: *Journal of Geophysical Research: Atmospheres* 123.11 (2018), pp. 6196–6212 (cit. on pp. 2, 132).

[38]S. M. Burrows, C. Hoose, U. Pöschl, and M. G. Lawrence. „Ice nuclei in marine air: biogenic particles or dust?“ In: *Atmos. Chem. Phys.* 13.1 (2013), pp. 245–267 (cit. on p. 2).

[39]J. Sciare, H. Bardouki, C. Moulin, and N. Mihalopoulos. „Aerosol sources and their contribution to the chemical composition of aerosols in the Eastern Mediterranean Sea during summertime“. In: *Atmos. Chem. Phys.* 3.1 (2003), pp. 291–302 (cit. on p. 2).

[40]S. Sandrini, D. van Pinxteren, L. Giulianelli, et al. „Size-resolved aerosol composition at an urban and a rural site in the Po Valley in summertime: implications for secondary aerosol formation“. In: *Atmos. Chem. Phys.* 16.17 (2016), pp. 10879–10897 (cit. on p. 3).

[41]N. Kalivitis, V. M. Kerminen, G. Kouvarakis, et al. „Atmospheric new particle formation as a source of CCN in the eastern Mediterranean marine boundary layer“. In: *Atmos. Chem. Phys.* 15.16 (2015), pp. 9203–9215 (cit. on p. 3).

[42]A. Bougiatioti, A. Nenes, C. Fountoukis, et al. „Size-resolved CCN distributions and activation kinetics of aged continental and marine aerosol“. In: *Atmos. Chem. Phys.* 11.16 (2011), pp. 8791–8808 (cit. on p. 3).

[43]D. A. Knopf, B. Wang, A. Laskin, R. C. Moffet, and M. K. Gilles. „Heterogeneous nucleation of ice on anthropogenic organic particles collected in Mexico City“. In: *Geophysical Research Letters* 37.11 (2010) (cit. on p. 3).

[44]J. C. Corbin, P. J. G. Rehbein, G. J. Evans, and J. P. D. Abbatt. „Combustion particles as ice nuclei in an urban environment: Evidence from single-particle mass spectrometry“. In: *Atmospheric Environment* 51 (2012), pp. 286–292 (cit. on p. 3).

[45]J. Chen, Z. Wu, S. Augustin-Bauditz, et al. „Ice-nucleating particle concentrations unaffected by urban air pollution in Beijing, China“. In: *Atmos. Chem. Phys.* 18.5 (2018), pp. 3523–3539 (cit. on pp. 3, 15, 16, 131).

[46]R Chester, M Nimmo, M Alarcon, et al. „Defining the chemical character of aerosols from the atmosphere of the Mediterranean-Sea and surrounding regions“. In: *Oceanologica Acta* 16.3 (1993), pp. 231–246 (cit. on p. 3).

[47]J. Piazzola and S. Despiau. „Contribution of marine aerosols in the particle size distributions observed in Mediterranean coastal zone“. In: *Atmospheric Environment* 31.18 (1997), pp. 2991–3009 (cit. on p. 3).

[48]J. Lelieveld, H. Berresheim, S. Borrmann, et al. „Global Air Pollution Crossroads over the Mediterranean“. In: *Science* 298.5594 (2002), pp. 794–799 (cit. on p. 3).

[49]Carla Gama, Oxana Tchepel, José María Baldasano, et al. „Seasonal patterns of Saharan dust over Cape Verde – a combined approach using observations and modelling“. In: *Tellus B: Chemical and Physical Meteorology* 67.1 (2015), p. 24410 (cit. on p. 4).

[50]P. Salvador, S. M. Almeida, J. Cardoso, et al. „Composition and origin of PM10 in Cape Verde: Characterization of long-range transport episodes“. In: *Atmospheric Environment* 127 (2016), pp. 326–339 (cit. on p. 4).

[51]K. W. Fomba, K. Müller, D. van Pinxteren, et al. „Long-term chemical characterization of tropical and marine aerosols at the Cape Verde Atmospheric Observatory (CVAO) from 2007 to 2011“. In: *Atmos. Chem. Phys.* 14.17 (2014), pp. 8883–8904 (cit. on p. 4).

[52]K. Kandler, K. Lieke, N. Benker, et al. „Electron microscopy of particles collected at Praia, Cape Verde, during the Saharan Mineral Dust Experiment: particle chemistry, shape, mixing state and complex refractive index“. In: *Tellus B* 63.4 (2011), pp. 475–496 (cit. on p. 4).

[53]X. Gong, H. Wex, T. Müller, et al. „Characterization of aerosol properties at Cyprus, focusing on cloud condensation nuclei and ice-nucleating particles“. In: *Atmos. Chem. Phys.* 19.16 (2019), pp. 10883–10900 (cit. on pp. 4, 15, 127).

[54]X. Gong, H. Wex, J. Voigtländer, et al. „Characterization of aerosol particles at Cabo Verde close to sea level and at the cloud level - Part 1: Particle number size distribution, cloudcondensation nuclei and their origins“. In: *Atmos. Chem. Phys.* 20.3 (2020), pp. 1431–1449 (cit. on pp. 4, 127).

[55]X. Gong, H. Wex, M. van Pinxteren, et al. „Characterization of aerosol particles at Cabo Verde close to sea level and at the cloud level - Part 2: Ice-nucleating particles in air, cloud and seawater“. In: *Atmos. Chem. Phys.* 20.3 (2020), pp. 1451–1468 (cit. on pp. 4, 127).

[56]A. Wiedensohler, W. Birmili, A. Nowak, et al. „Mobility particle size spectrometers: harmonization of technical standards and data structure to facilitate high quality long-term observations of atmospheric particle number size distributions“. In: *Atmos. Meas. Tech.* 5.3 (2012), pp. 657–685 (cit. on pp. 6, 7).

[57]TSI. *Aerodynamic Particle Sizer Spectrometer Model 3321, Instruction Manual*. TSI Inc., 2004 (cit. on p. 8).

[58]A. Wiedensohler. „An approximation of the bipolar charge distribution for particles in the submicron size range“. In: *Journal of Aerosol Science* 19.3 (1988), pp. 387–389 (cit. on p. 7).

[59]S. Pfeifer, T. Müller, K. Weinhold, et al. „Intercomparison of 15 aerodynamic particle size spectrometers (APS 3321): uncertainties in particle sizing and number size distribution“. In: *Atmos. Meas. Tech.* 9.4 (2016), pp. 1545–1551 (cit. on p. 7).

[60]N. Kaaden, A. Massling, A. Schladitz, et al. „State of mixing, shape factor, number size distribution, and hygroscopic growth of the Saharan anthropogenic and mineral dust aerosol at Tinfou, Morocco“. In: *Tellus B* 61.1 (2009), pp. 51–63 (cit. on p. 7).

[61]W. P. Kelly and P. H. McMurry. „Measurement of Particle Density by Inertial Classification of Differential Mobility Analyzer–Generated Monodisperse Aerosols“. In: *Aerosol Science and Technology* 17.3 (1992), pp. 199–212 (cit. on p. 7).

[62]M. Gysel, E. Weingartner, and U. Baltensperger. „Hygroscopicity of Aerosol Particles at Low Temperatures. 2. Theoretical and Experimental Hygroscopic Properties of Laboratory Generated Aerosols“. In: *Environmental Science & Technology* 36.1 (2002), pp. 63–68 (cit. on p. 7).

[63]James M. Haywood, Peter N. Francis, Martin D. Glew, and Jonathan P. Taylor. „Optical properties and direct radiative effect of Saharan dust: A case study of two Saharan dust outbreaks using aircraft data“. In: *Journal of Geophysical Research: Atmospheres* 106.D16 (2001), pp. 18417–18430 (cit. on p. 7).

[64]Alexander Schladitz, Thomas Müller, Andreas Nowak, et al. „In situ aerosol characterization at Cape Verde“. In: *Tellus B* 63.4 (2011), pp. 531–548 (cit. on p. 7).

[65]S. L. von der Weiden, F. Drewnick, and S. Borrmann. „Particle Loss Calculator - a new software tool for the assessment of the performance of aerosol inlet systems“. In: *Atmos. Meas. Tech.* 2.2 (2009), pp. 479–494 (cit. on p. 7).

[66]A. Wiedensohler, A. Wiesner, K. Weinhold, et al. „Mobility particle size spectrometers: Calibration procedures and measurement uncertainties“. In: *Aerosol Science and Technology* 52.2 (2018), pp. 146–164 (cit. on p. 7).

[67]G. C. Roberts and A. Nenes. „A Continuous-Flow Streamwise Thermal-Gradient CCN Chamber for Atmospheric Measurements“. In: *Aerosol Science and Technology* 39.3 (2005), pp. 206–221 (cit. on p. 8).

[68]DMT. *Cloud Condensation Nuclei Counter Manual for Single-Column CCNs DOC-0086 Revision I-2.* Droplet Measurement Technologies, Inc., 2012 (cit. on p. 9).

[69] M. Gysel and F. Stratmann. „WP3 - NA3: In-situ chemical, physical and optical properties of aerosols, Deliverable D3.11: Standardized protocol for CCN measurements“. In: *Tech. rep.* (2013) (cit. on p. 8).

[70] Hilding Köhler. „The nucleus in and the growth of hygroscopic droplets“. In: *Transactions of the Faraday Society* 32 (1936), pp. 1152–1161 (cit. on p. 9).

[71] M. D. Petters and S. M. Kreidenweis. „A single parameter representation of hygroscopic growth and cloud condensation nucleus activity“. In: *Atmos. Chem. Phys.* 7.8 (2007), pp. 1961–1971 (cit. on p. 9).

[72] T. B. Kristensen, T. Müller, K. Kandler, et al. „Properties of cloud condensation nuclei (CCN) in the trade wind marine boundary layer of the western North Atlantic“. In: *Atmos. Chem. Phys.* 16.4 (2016), pp. 2675–2688 (cit. on pp. 10, 131).

[73] P. Herenz, H. Wex, S. Henning, et al. „Measurements of aerosol and CCN properties in the Mackenzie River delta (Canadian Arctic) during spring–summer transition in May 2014“. In: *Atmos. Chem. Phys.* 18.7 (2018), pp. 4477–4496 (cit. on pp. 10, 131).

[74] D. Rose, S. S. Gunthe, E. Mikhailov, et al. „Calibration and measurement uncertainties of a continuous-flow cloud condensation nuclei counter (DMT-CCNC): CCN activation of ammonium sulfate and sodium chloride aerosol particles in theory and experiment“. In: *Atmos. Chem. Phys.* 8.5 (2008), pp. 1153–1179 (cit. on p. 12).

[75] George W. Harvey and Linden A. Burzell. „A simple microlayer method for small samples“. In: *Limnology and Oceanography* 17.1 (1972), pp. 156–157 (cit. on p. 13).

[76] Manuela Van Pinxteren, Stefan Barthel, Khanneh Wadinga Fomba, et al. „The influence of environmental drivers on the enrichment of organic carbon in the sea surface microlayer and in submicron aerosol particles–measurements from the Atlantic Ocean“. In: *Elementa: Science of the Anthropocene* 5 (2017), p. 35 (cit. on pp. 13, 132).

[77] B. B. Demoz, J. L. Collett, and B. C. Daube. „On the Caltech Active Strand Cloudwater Collectors“. In: *Atmospheric Research* 41.1 (1996), pp. 47–62 (cit. on p. 14).

[78] C. Budke and T. Koop. „BINARY: an optical freezing array for assessing temperature and time dependence of heterogeneous ice nucleation“. In: *Atmos. Meas. Tech.* 8.2 (2015), pp. 689–703 (cit. on p. 15).

[79] F. Conen, S. Henne, C. E. Morris, and C. Alewell. „Atmospheric ice nucleators active $\geq$-12°C can be quantified on PM_{10} filters“. In: *Atmos. Meas. Tech.* 5.2 (2012), pp. 321–327 (cit. on p. 16).

[80] Thomas C. J. Hill, Bruce F. Moffett, Paul J. Demott, et al. „Measurement of ice nucleation-active bacteria on plants and in precipitation by quantitative PCR“. In: *Applied and environmental microbiology* 80.4 (2014), pp. 1256–1267 (cit. on p. 16).

[81] H. Wex, L. Huang, W. Zhang, et al. „Annual variability of ice-nucleating particle concentrations at different Arctic locations“. In: *Atmos. Chem. Phys.* 19.7 (2019), pp. 5293–5311 (cit. on p. 16).

[82] Naruki Hiranuma, Stefanie Augustin-Bauditz, Heinz Bingemer, et al. „A comprehensive laboratory study on the immersion freezing behavior of illite NX particles: a comparison of 17 ice nucleation measurement techniques“. In: *Atmospheric Chemistry and Physics* 15.5 (2015), pp. 2489–2518 (cit. on p. 16).

[83]Gabor Vali. „Quantitative Evaluation of Experimental Results an the Heterogeneous Freezing Nucleation of Supercooled Liquids“. In: *Journal of the Atmospheric Sciences* 28.3 (1971), pp. 402–409 (cit. on p. 18).

[84]K. J. Suski, T. C. J. Hill, E. J. T. Levin, et al. „Agricultural harvesting emissions of ice-nucleating particles“. In: *Atmos. Chem. Phys.* 18.18 (2018), pp. 13755–13771 (cit. on p. 18).

[85]Alan Agresti and Brent A. Coull. „Approximate is Better than “Exact” for Interval Estimation of Binomial Proportions“. In: *The American Statistician* 52.2 (1998), pp. 119–126 (cit. on p. 18).

[86]SM Kreidenweis, K Koehler, PJ DeMott, et al. „Water activity and activation diameters from hygroscopicity data-Part I: Theory and application to inorganic salts“. In: *Atmospheric Chemistry and Physics* 5.5 (2005), pp. 1357–1370 (cit. on p. 19).

[87]HR Pruppacher and JD Klett. *Microphysics of Clouds and Precipitation*. Vol. 18. Springer Science & Business Media, 2010 (cit. on p. 19).

[88]Thomas Koop and Bernhard Zobrist. „Parameterizations for ice nucleation in biological and atmospheric systems“. In: *Physical Chemistry Chemical Physics* 11.46 (2009), pp. 10839–10850 (cit. on p. 19).

[89]H. Wex, K. Dieckmann, G. C. Roberts, et al. „Aerosol arriving on the Caribbean island of Barbados: physical properties and origin“. In: *Atmos. Chem. Phys.* 16.22 (2016), pp. 14107–14130 (cit. on p. 131).

[90]P. Herenz, H. Wex, A. Mangold, et al. „CCN measurements at the Princess Elisabeth Antarctica research station during three austral summers“. In: *Atmos. Chem. Phys.* 19.1 (2019), pp. 275–294 (cit. on p. 131).

[91]C. L. Reddington, K. S. Carslaw, P. Stier, et al. „The Global Aerosol Synthesis and Science Project (GASSP): Measurements and Modeling to Reduce Uncertainty“. In: *Bulletin of the American Meteorological Society* 98.9 (2017), pp. 1857–1877 (cit. on p. 131).

[92]William C. Keene, Hal Maring, John R. Maben, et al. „Chemical and physical characteristics of nascent aerosols produced by bursting bubbles at a model air-sea interface“. In: *Journal of Geophysical Research: Atmospheres* 112.D21 (2007) (cit. on p. 132).

[93]P. J. DeMott, A. J. Prenni, X. Liu, et al. „Predicting global atmospheric ice nuclei distributions and their impacts on climate“. In: *Proceedings of the National Academy of Sciences* 107.25 (2010), pp. 11217–11222 (cit. on p. 132).

[94]Yutaka Tobo, Anthony J. Prenni, Paul J. DeMott, et al. „Biological aerosol particles as a key determinant of ice nuclei populations in a forest ecosystem“. In: *Journal of Geophysical Research: Atmospheres* 118.17 (2013), pp. 10,100–10,110 (cit. on p. 132).

[95]H. C. Price, K. J. Baustian, J. B. McQuaid, et al. „Atmospheric Ice-Nucleating Particles in the Dusty Tropical Atlantic“. In: *Journal of Geophysical Research: Atmospheres* 123.4 (2018), pp. 2175–2193 (cit. on p. 132).

List of Figures

2.1 Schematic of the measurement system, including (a) sampling inlet and (b) on-line instruments TROPOS-type mobility particle size spectrometer (MPSS), aerodynamic particle sizer (APS) and cloud condensation cuclei counter (CCNC). 5

2.2 Schematic sketch of the TROPOS-type MPSS. MPSS consists of a sequential setup of a bipolar diffusion charger (neutralizer), a DMA, and a CPC, with some auxiliary flow and temperature controller and filters. This picture is taken from Wiedensohler et al. [56]. 7

2.3 Schematic sketch of the TSI APS model 3321. APS mainly contains nozzles and a optics chamber, with some auxiliary flow and temperature controller and filters. The picture is taken from the TSI APS model 3321 instruction manual [57]. 8

2.4 (a) Schematic sketch of the DMT CCNC and (b) the main part of CCNC, i.e., cylindrical continuous-flow thermal-gradient diffusion chamber. The picture is taken from DMT CCNC manual [68]. 9

2.5 The connection between the PNSD, a corresponding N_{CCN} and the resulting d_{crit}. The critical diameter d_{crit} is determined by the integration of a PNSD starting from the largest diameter til it is equal to the value of a simultaneous measured N_{CCN}. 10

2.6 (a) Distribution of 10 000 d_{crit} values after applying the MCS. (b) Distribution of 10 000 κ values after applying the MCS. (c) Distribution of d_{crit} values during the whole MarParCloud campaign. (d) Distribution of κ values during the whole MarParCloud campaign. 12

2.7 Schematic diagram of the sample collection strategy during MarParCloud campaign, including the sample collection of SML, ULW, filters of atmospheric aerosol and cloud water, and the corresponding sampling techniques. 13

2.8 (a) Picture of LINA setup. (b) Image recording of a droplet freeze assay. 16

2.9 (a) Picture of INDA setup. (b) Image recording of a PCR tray. 17

List of Tables

2.1 Sample type, treatment method, instrumentation and sample location. 17

Colophon

In its PDF form, this thesis was typeset with LaTeX. It uses the *Clean Thesis* style `http://cleanthesis.der-ric.de/`.

The MatLab (version R2016a) and Python 3.7 were used for data analysis in this study.

The IGOR Pro was used for plotting in this study.

Declaration of Independence

Hereby I, Xianda Gong, declare that I prepared this PhD Thesis without inadmissible aid and only by the usage of the specified resources. I also declare, that I marked the directly or indirectly adopted ideas from external references.

I insure that I do not get any assistance benefits from other persons in selection and evaluation of the material as well as in the preparation of the manuscript.

Furthermore I insure that no further persons were participated in the intellectual creation process of this PhD dissertation. In particular, I insure that I did not make a claim on the aid of a doctoral consultant. Also I insure that no one has gained, from me or from other persons on behalf on me, immediately or indirectly pecuniary advantages, which are related to the content of this PhD dissertation.

Hereby I insure that this PhD Thesis was not submitted, neither in Germany nor in other countries, in an identical or similar design to another examination office for the purpose of a graduation or another examination procedure. Besides, I confirm the non-release/publication of this whole PhD Thesis.

Hereby I state that I have not been involved in another PhD procedure.

Leipzig, 22 June 2020

Xianda Gong